Coupled Theoretical and Experimental Methods to Understand Growth and Remodeling of *In Situ* Engineered Vascular Grafts in Young and Aged Hosts

by

Piyusha S. Gade

B.E. Mechanical Engineering, University of Pune, 2012

M.S. Biomedical Engineering, University of Iowa, 2014

Submitted to the Graduate Faculty of

Swanson School of Engineering in partial fulfillment

of the requirements for the degree of

Doctor of Philosophy

University of Pittsburgh

2019

UNIVERSITY OF PITTSBURGH

SWANSON SCHOOL OF ENGINEERING

This dissertation was presented

by

Piyusha S. Gade

It was defended on

July 8, 2019

and approved by

Yadong Wang, Ph.D., Professor, Department of Biomedical Engineering, Cornell University

Steven Abramowitch, Ph.D., Associate Professor, Department of Bioengineering

Ian Sigal, Ph.D., Assistant Professor, Department of Opthalmology

Spandan Maiti, Ph.D., Assistant Professor, Department of Bioengineering

Dissertation Director: Anne M. Robertson, Ph.D., William Kepler Whiteford Professor of Engineering, Department of Mechanical Engineering and Materials Science, Bioengineering, McGowan Institute for Regenerative Medicine

Coupled Theoretical and Experimental Methods to Understand Growth and Remodeling of *In Situ* Engineered Vascular Grafts in Young and Aged Hosts

Piyusha S. Gade, PhD

University of Pittsburgh, 2019

In 1975, Rodbard introduced the concept of mechanical homeostasis; that arteries have an inherent capacity to maintain homeostatic stress states by altering their morphology through a negative feedback mechanism in response to mechanical loads. More recently, this capacity has been leveraged to develop acellular, *in situ* tissue-engineered vascular grafts (iTEVGs) which promote host growth and remodeling (G&R) to develop new arteries (neoarteries) in the tissue's functional site (*in situ*). These grafts offer a much-needed option to address the lack of viable autologous conduits, difficulties in scaling traditional tissue engineered grafts, and the rising demand for bypass grafting in an aging population. One such acellular, poly (glycerol sebacate) (PGS) iTEVG developed by Wang et al. has demonstrated *in situ* mature elastin and collagen formation in young hosts. However, the trial and error nature of graft design, coupled with the lack of knowledge of fundamental mechanisms guiding neoarterial G&R impedes efforts to translate these successes across age and species.

In this work, we take a coupled theoretical and experimental approach to understanding salient mechanisms guiding neoartery formation in young and aged hosts. We developed a mathematical model of graft degradation based on *in vitro* assessment of enzymatic degradation. Next, we translated successful neoartery development from a rat aorta to the substantially smaller, rat carotid artery. We determined that after three-months of remodeling, the neoartery has similar mechanical properties to those of the clinical gold standard, vein graft. We then successfully

translated the iTEVG to an aged murine carotid model and assessed differences in mechanical, microstructural, and biological stages of neoarterial G&R in young versus aged hosts over the course of six months. Subsequently, a constrained mixture model-based G&R tool was developed, informed with these experimental data, and used to predict long-term neoarterial G&R response in both age groups. Finally, we identified a common mode of adverse remodeling in neoarteries - rupture and calcification. Motivated by these results, we developed new techniques to analyze calcification in a parallel, model system exhibiting similar modes of adverse remodeling - cerebral aneurysms. These results provide insights for future work developing strategies necessary to optimally design iTEVGs.

Table of Contents

List of Tables

List of Figures

Acknowledgement

My time at Pitt under the mentorship of Dr. Anne M. Robertson has been one of growth, learning and personal development. I owe my sincerest gratitude to Dr. Robertson, not only for her scientific guidance, but also for her continued support and freedom to explore different projects and make mistakes. She has been instrumental in the development of not only my technical acumen but has also helped me understand the importance of skills like communication and professional development. She has been an exceptional mentor who has inculcated a sense of collaboration, work ethic, creativity, and commitment. I will carry these values with me throughout my career, for which I will be forever grateful.

A special thank you to my committee members, Dr. Abramowitch, Dr. Wang, Dr. Maiti and Dr. Sigal for their guidance and support throughout my doctoral studies. This work would not have been possible without them.

I would also like to thank my lab mates, past and present. Xinjie, Chao, Fang, Mike, Sarah, Yas, and Eliisa have been instrumental in providing me insights when I was stuck, having great conversations and being wonderful people to work with. My PhD experience has been a fantastic one, thanks in large part, to them. I would like to thank Deb, from whom I have always tried to learn organizational skills. I have also had the good fortune of working with exceptional master's and undergraduate researchers. I appreciate the diligence and passion with which Blaise, Andy, Abe, and Arthur executed projects that helped take my work to the next level.

I cannot thank my Pittsburgh friends enough. Chelsea, Daniel, Kevin, Beth, Anvay, and Abhi are my family away from home. Thank you, guys, for your thought-provoking discussions, moral support, and companionship through the ups and downs of graduate school.

I have been extremely lucky to have found two constant sources of joy, love, trust, and complete understanding. Rhuta and Nimesha, your friendship has made everything I do in life possible. It’s a cliché, but I would not have been able to do this without you.

Last but not the least I would like to thank my family, my husband Piyush, my brother Saket, and my parents, Sanjay and Surekha Gade. Piyush has always been the voice of reason, the calmness to my frenzied brain and the best partner I could have ever asked for. My parents have led by example and instilled values that I try to uphold every day. I would not be here without you guys. Thank you for your unwavering trust, love, and support.

1.0 Introduction

1.1 The Need for Small Diameter Vascular Grafts

"Operating on the edge of cardiovascular disease" --- Edward Lakatta [1]

Cardiovascular disease (CVD) remains the leading cause of morbidity and mortality, globally, and in the United States [2]. Atherosclerosis induced coronary heart disease alone accounts for 31% of global deaths and 45% of deaths in the U.S. Another 8.5 million people in the U.S. and 202 million worldwide suffer from atherosclerosis-derived peripheral artery disease [3]. Furthermore, this situation is expected to worsen as the world population is aging. Globally, the population aged 60 or above is growing at a rate of about 3% year, and by 2050, a quarter of the population in every country will be over 60 years old [4]. In the U.S., the prevalence of CVD in the aged population is about 80% in people over 80 years old [2]. Although epidemiological studies have shown that lifestyle, lipid levels, genetics and hypertension are risk factors for CVD, age remains the biggest contributor to this disease [5].

Despite advances in endovascular treatments, bypass grafting remains the only suitable alternative for revascularization in many patients suffering from coronary heart disease (Figure 1). Furthermore, there is an increased need for revascularization in the older population since studies have also shown that aging is associated with increased thickening and dilatation of arterial walls even in the absence of atherosclerosis [6]. In the U.S. alone, 400,000 coronary artery bypasses and 460,000 peripheral artery bypasses are performed annually [2], [3]. Furthermore, another 110,000 receive arteriovenous fistulae for hemodialysis access annually in the U.S.[7]. The clinical gold standard for bypassing small diameter (< 6mm) arteries like the coronaries is the vein graft.

However, expanded indications for the procedure, shift to elderly population and increased number of re-operations limits the availability of suitable autologous grafts for bypass grafting[8]. The lack of viable autologous conduits has led to the widely recognized need for off-the-shelf, functional, small diameter vascular graft substitutes, the demand for which continues to increase with an aging population.

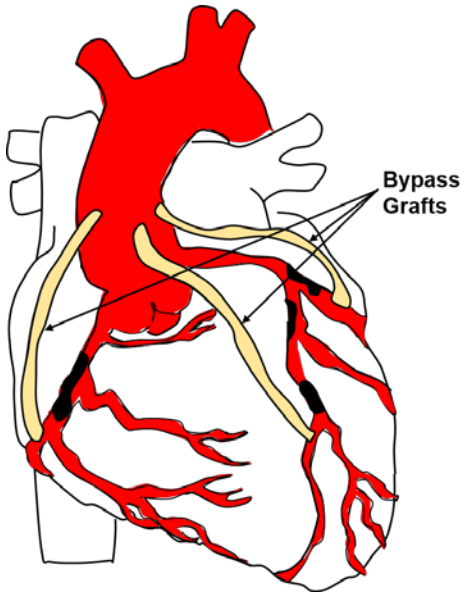

Figure 1: Schematic of vascular bypass grafting.

1.2 Cardiovascular Soft Tissue: Arteries

"…the old who enjoy good health die through lack of sustenance, and this is brought about by the continuous narrowing of the passage of the mesenteric vessels by thickening of the coats of these vessels" --- Leonardo da Vinci, Notes on the death of a centenarian, 1508 [9]

That normal functioning of arteries is crucial to the overall health of an individual is uncontested. In order to design alternative conduits to replace dysfunctional arteries, there is first a need to understand the normal structural and functional requirements of the arterial wall.

1.2.1 Designing the Arterial Wall: Gross Morphology

140 milliliters of nearly incompressible blood are ejected during the systolic phase of each cardiac cycle in the human body. In order to accommodate this volume of blood, the arterial network must, first and foremost, be compliant. Secondly, there is a limit on the strain that an arterial wall can undergo. These constraints arise since arterial cells can undergo undesirable phenotypic changes with increased strain. Furthermore, arteries need to be sufficiently reinforced to withstand periods of elevated blood pressure [10]. In order to meet these design requirements, a typical, normal, healthy arterial wall is comprised of three main layers – tunica intima, tunica media, and the tunica externa (Figure 2).

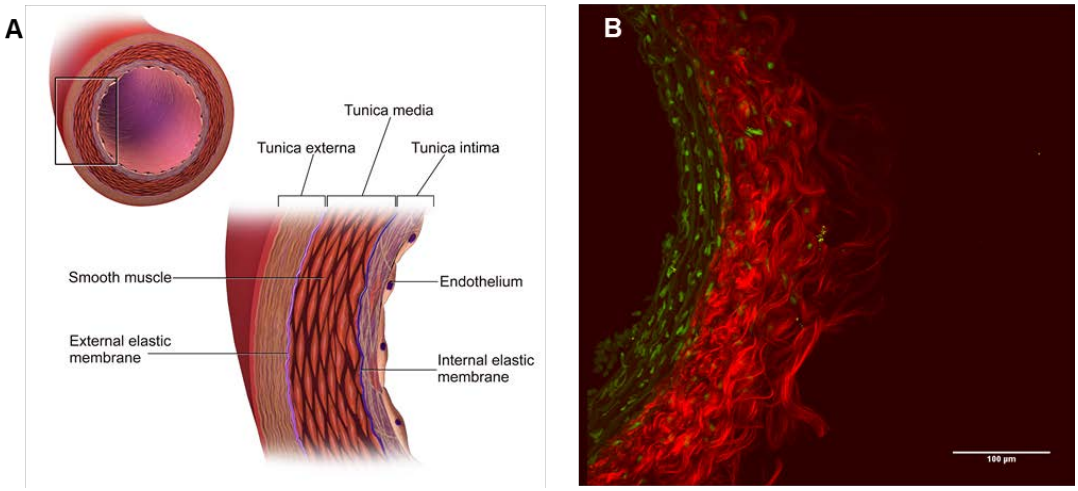

Figure 2: Arterial wall structure.

Schematic depicting the three layers – tunica intima, tunica media, and tunica externa, of the arterial wall [11]. (B) Second harmoic generation image of a cross-section of a young rat carotid artery (unpublished, created following protocol outlined in Appendix B). Elastic lamellae flouresce in green, collagen autoflouresces in red and nuclei are in green.

The healthy tunica intima consists of a fully confluent endothelial cell layer, a highly sensitive lining between the arterial wall and the circulating fluid that regulates wall shear stress. The tunica media is primarily comprised of circumferentially aligned vascular smooth muscle cells (VSMCs) embedded within a matrix composed of elastic lamellae and collagen fibers. The outermost layer, the tunica externa, is comprised of collagen fibers along with fibroblast cells. The sheets of elastin, called elastic lamellae, are primarily responsible for the complaint behavior of arteries, especially in the low-strain regime. Mechanically, collagen is the main load bearing protein, especially in high-strain regimes, limiting the expansion of the arterial wall through mechanisms of fiber re-orientation and straightening [12].

1.2.2 Designing the Arterial Wall: Microstructural Architecture

Proteoglycans, extracellular matrix (ECM) proteins, and vascular cells are the main constituents of the arterial wall. Proteoglycans consist of a core protein to which glycosaminoglycans (GAGs) are attached. The highly negatively charged GAG chains enable the proteoglycans to function as lubricants and dampers due to their ability to sequester water [13]. Extracellular proteins like collagen and elastin are the main load-bearing entities in the wall. Collagen is composed of three polypeptide α chains that form a triple helical structure. The most abundant collagen types present in the arterial wall are fibrillar type collagens I and III that constitute approximately 60% and 30% of total arterial collagen respectively [10]. However, it must be noted that the relative amount of each type changes as a function of age and location in the arterial tree. Collagen III fibers in the wall are typically thinner with an average diameter of 0.5-1.5μm, while type I fibers have diameters in the range of 2-10μm [14]. As can be seen in Figure 2B, collagen fibers in the arterial wall have a crimped wavy structure in the unloaded state in both the medial and adventitial layers of the wall. These fibers are straightened out during loading; a feature of collagen fibers that contributes to the nonlinearity observed in the typical mechanical stress-strain response of arteries [12]. The other main load bearing protein in the arterial wall is elastin. Elastin is a highly stable and extremely hydrophobic protein that stores elastic energy, and is the primary component that confers the arterial wall its flexibility. It is widely believed that a majority of the elastin is laid down during development and that the body has a limited capacity to produce elastin after puberty [15]. In contrast, collagen fibers are constantly degraded and produced with a half-life of 60-70 days [16] in order to maintain ECM integrity over time, in normal, diseased, and physiologically altered conditions. Cellular components of the arterial wall primarily include endothelial cells, VSMCs, and fibroblasts. Endothelial cells form

the inner lining of the arterial tree and are responsible for sensing and maintaining a constant wall shear stress in arteries. VSMCs constitute the “active” component of the arterial wall, in that they regulate arterial diameter through their contractile ability. These cells are partially contracted in the homeostatic state and impart a basal tone to arteries. In conjunction with endothelial cells, VSMCs regulate the blood vessel diameter to maintain homeostatic blood flow in the body. While VSMCs in arteries are primarily contractile, they can exhibit a spectrum of phenotypic changes. For example, VSMCs display a synthetic phenotype during remodeling and repair. Fibroblasts, located mostly in the adventitial (external) layer of the arteria wall are the main source of collagen production within the wall [17]. It has been estimated that each fibroblast can synthesize approximately 3.5 million procollagen molecules/cell/day [18]. Fibroblasts therefore play a major role in regulating collagen homeostasis by controlling the balance of collagen degradation and production.

1.2.3 Mechanical Properties of the Arterial Wall

The mechanical behavior of soft tissues like arteries greatly depends on the composition and organization of its ECM and cellular components. Constitutive models provide a mathematical formulation that best predicts salient features of the material response of a system. As discussed in previous sections, the arterial wall is a composite material made of passive load bearing structures like collagen and elastin, and active cellular component like VSMCs. There is extensive literature on constitutive modeling of arteries which can briefly be described in three categories – structural models, phenomenological models and structurally motivated models. Structural models include explicit constitutive equations for each individual component in the composite material. Due to this, these models can provide insights into the mechanisms of load-

bearing in the material, albeit, at the cost of adding complexity to the governing equations. Furthermore, it is practically impossible to make measurements for the properties of individual components. Phenomenological models described the gross mechanical response of the material without taking individual constituents into question. Structurally motivated models present a compromise between the two extremes by considering the role of certain load bearing constituents like collagen fiber straightening, re-orientation without modeling each mechanical properties of each individual component.

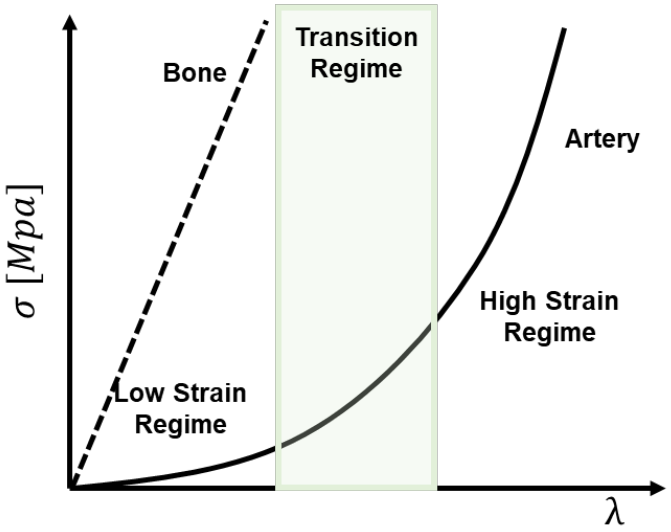

Figure 3: Schematic of a typical nonlinear stress-stretch curve of arterial walls as compared to the linear response in bones[10].

Seminal works by Roach and Burton posited that arteries exhibit a nonlinear stress-strain response as seen in Figure 3 due to the elastic response of highly compliant elastin in the low strain regime and recruitment (straightening) of stiff, wavy collagen fibers in the high strain regime [19]. Hill et al. confirmed this by imaging collagen fibers under various loading conditions and observing that collagen recruitment initiates at finite strains [12]. The transition regime in the curve is the region wherein most collagen fibers are recruited for load-bearing thereby transferring load from elastin alone to a combination of both elastin and collagen fibers. Under certain conditions it is sufficient to assume that the arterial wall can be modeled as a hyperelastic material with the following general strain energy function for the passive mechanical response

$$W = W_{iso} + W_{aniso} \qquad \textbf{Equation 1-1}$$

Where W_{iso} is isotropic strain energy function which describes the response of primarily, elastin and GAGs. W_{aniso} represents the strain energy function of collagen and is often defined using recruitment models that describe the gradual recruitment of collagen fibers [12]. Other approaches also describe fiber distribution models either as a continuous probability density function [20], [21] or in the form of two [22], four-fiber family [23] models that model fibers in discrete dominant directions.

From the strain energy function in Equation 1-1, the Cauchy stress tensor can be calculated as

$$\boldsymbol{T} = -pI + 2\boldsymbol{F}\frac{\partial W_{iso}}{\partial \boldsymbol{C}}\boldsymbol{F}^T + 2\boldsymbol{F}\frac{\partial W_{aniso}}{\partial \boldsymbol{C}}\boldsymbol{F}^T \qquad \textbf{Equation 1-2}$$

Where p is the Lagrange multiplier that arises out of the incompressibility constraint, **F** is the deformation gradient and $\boldsymbol{C = F^T F}$, is the right Cauchy Green tensor.

1.3 *In Situ* Tissue Engineered Vascular Grafts

"Seducing the Body to Regenerate" --- Martin Stoddart [24]

The most common prosthetic vascular grafts are made from expanded polytetrafluoroethylene (ePTFE, a.k.a. Gore-Tex) and woven polyethylene terephthalate (PET, a.k.a Dacron). While these grafts are relatively inexpensive and have long shelf-lives, they perform poorly in small diameter applications due to poor mechanical characteristics, thrombosis, stenosis, and infection [8], [25]. As an alternative, various tissue-engineered strategies have been suggested in recent years. These can broadly be classified into four major categories—ECM-derived cellular [26], ECM-derived acellular [27], [28], synthetic cellular [29], [30] and synthetic acellular grafts [31]. While ECM-derived strategies have shown remarkable in-host remodeling with some even reaching Phase II clinical trials [27], they are associated with complicated and high production times along with significant production costs, which serve as a barrier to clinical translation. Furthermore, applications have been limited to large diameter and high flow conditions.

In situ tissue engineered vascular grafts (iTEVGs) are a disruptive, state-of-the-art technology, wherein a synthetic degradable graft transforms within the host body into a functional new artery (neoartery). Conceptually, iTEVGs are acellular, biodegradable, polymeric conduits that harness host growth and remodeling (G&R) to deposit ECM proteins like elastin and collagen to develop a neoartery in place of the existing graft (Figure 4) [25].

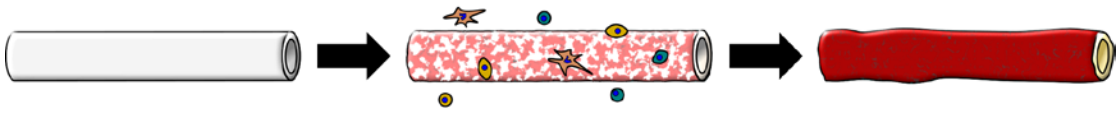

Figure 4: Schematic of iTEVG tranformation into a neoartery

An acellular, polymeric graft is implanted. Host cells invade the graft, degrade the polymer, proliferate, and synthesize new ECM. The artificial graft is replaced by a neoartery. Figure adapted with permission from [25].

The goal of iTEVGs is to develop a structurally and functionally sound neoartery that exhibits the general characteristics of a native artery (outlined in chapters 1.2.1 1.2.2 1.2.3) and can integrate and grow within the host body. iTEVGs offer a much-needed alternative for treating atherosclerosis due to their ease of fabrication, reduced regulatory burden and the ability to form an adaptive tissue that is capable of G&R within the host. Specifically, the work in this thesis focuses on an iTEVG developed by Wang et al [31]. This iTEVG is a bi-layered graft made of a poly (glycerol sebacate) (PGS) inner core and polycaprolactone (PCL) outer sheath. The iTEVG has demonstrated the capacity for neoartery formation with mature elastin, collagen and nerve formation in the rat aorta of young animals [31]. If successful in humans, this technology would have the advantages of both autologous and synthetic grafts, making them attractive candidates for commercial use. Notwithstanding their remarkable success, the main barrier to clinical translation of these grafts remains the trial and error nature of graft design with emphasis on avoiding early graft rupture, thrombosis and compliance matching alone. While these criteria are absolutely necessary for successful implantation, they are not sufficient for long term biological and functional integration of the iTEVG with surrounding tissue. Thus, there is a need to understand

the fundamental mechanisms guiding neoarterial remodeling to enable translation of iTEVGs to the clinically relevant aged population. The rationale is that once we have mechanistic understanding of evolving graft and neoarterial properties, we can develop mechanism-based functional forms in our G&R computational tool and combine them with global optimization strategies to design TEVG's for older animals.

1.4 Arterial Adaptation: Growth and Remodeling with Age

"Inside every old person is a young person wondering what happened." --- Anonymous

Section 1.2 described the morphology and function of normal, healthy arteries. However, arteries are constantly being subjected to a variety of forces and bio-chemo-mechanical cues which require them to remodel and grow. Pioneering works by Wolinsky and Glagov have shown that arteries maintain tensional homeostasis in order to sustain constant levels of transmural stress [32]. They showed that the average tension per lamellar unit of an aortic media was constant across species. Following this, Langille et al. (e.g. [33], [34]) showed that arteries in young species have an inherent capacity for altering their morphology in response to mechanical stimuli. This ability of arteries to undergo G&R enables them to maintain mechanical homeostasis - a constant, preferred mechanical state - despite altered mechanical loading. Young arteries respond to changes in flow, pressure and longitudinal tension to maintain a constant homeostatic mechanical environment. A decrease in blood flow leads to a reduction in diameter [35], whereas hypertension leads to wall thickening [36]. Furthermore, an increase in longitudinal strain is normalized by an increase in endothelial cell replication rates, and increased collagen and elastin deposition[37]. It

must, however, be noted that arteries are not adept at restoring homeostatic conditions under reduced longitudinal strains [38].

While arteries are highly adept at G&R in response to mechanical stimuli, this response is highly dependent on age. For example, carotid arteries of aged Fischer rats were not able to remodel in response to reduced flow potentially due to altered eNOS activity [39]. Aging also reduces cell proliferation rates, leads to endothelial cell dysfunction [40], and is associated with a dilatation and stiffening of arteries [41]. It also widely known that aging has a significant impact on regeneration and healing. There has been a growing consensus that aging delays wound healing [42], regeneration [43] and the host response to implants [44]. iTEVGs fundamentally leverage the G&R capability of the host body to develop neoateries. Hence, there is a need to understand the role of aging on the biomechanics of iTEVGs.

1.5 Theoretical Models of Growth and Remodeling

"All models are wrong but some are useful" --- George Box

While the fundamental form of biological tissue is encoded in the genes, its final structure and functionality are optimized according to its mechanobiological environment. A known example is the loss of bone mass and muscles atrophy due to weightlessness. G&R is a fundamental component of living systems. Living tissues continuously change and adapt through changes in mass and geometry (growth), rearrangement of the microstructure (remodeling) and shape (morphogenesis). These organisms grow and shrink, and become stronger or weaker at very small timescales. As discussed in Section 1.4, the constituents in the arterial wall can change in

time due to orchestrated production and removal of ECM. For example, the mass of individual components in the wall can increase due to the production of ECM components by the cells (e.g. fibroblasts and VSMCs) and also decrease due to their breakdown by matrix metalloproteases (MMPs). These changes require the body to adapt to a new set of mechanical conditions. The main component mediating mechanical homeostasis during these altered conditions is ECM turnover. ECM turnover refers to combined process of synthesis and degradation of ECM components. It is well known that increased mechanical loading leads to increased ECM synthesis [45]–[48] as well as ECM degradation [49]. These changes allow the body to not only change shape but also alter its mechanical properties.

Theoretical frameworks that model this phenomenon can be used to gain insights into G&R mechanics and the mechanisms that drive them. In the context of these models, growth specifically refers to change in mass while remodeling refers to changes in the organization of the material (for example fiber orientation, recruitment etc.) leading to changes in anisotropy, stiffness and strength. Since the seminal works of D'Arcy Thompson describing the mathematical and physical aspects of growth and form [50], and Skalak's formal description of G&R using a volumetric growth-based continuum mechanics framework [51], various groups have extended these approaches to describe G&R in soft and hard tissues. Skalak et al. assumed that the original stress-free body can be divided fictitiously into small parts that can "grow" independently. These individual parts can then be assembled to obtain the final configuration. The final stress in the body is dependent on deformations due to this assembly and applied loads but not due to "growth". This approach is based on the idea of growth as a change of form. Among others, Rodriguez et al. [52], Taber et al. [53], and Rachev et al.[54] have used this concept of volumetric growth to model left ventricular hypertrophy, the development of arteries as well as their response to hypertension in maturity.

Growth is modeled through the multiplicative decomposition of the deformation gradient into a growth tensor ($\boldsymbol{F}_g$) and an elastic tensor ($\boldsymbol{F}_e$). Epstein et al. presented a theory of growth that viewed growth as a local rearrangement of material inhomogeneities [55]. Drawing from theories of plasticity, Eckart first introduced the concept of multiple natural configurations and provided a mathematical formulation for the same [56]. Rajagopal et al., along with Wineman, then extended this formulation to provide a unified framework to study metal plasticity [57], twinning [58], and, viscoelastic fluids [59]. Ambrosi et al. then applied this framework of volumetric growth with evolving natural configurations to model biological tumor growth [60]. More recently Kuhl et al. [61] have used this theory to explain the mechanism of folding in the brain, and the mechanobiology [62] and expansion of skin in reconstructive surgery [63].

While these models describe the consequences of growth and predict G&R responses with reasonable accuracy, they do not necessarily describe the cause of G&R. Kinematic growth is described by prescribing evolution equations for the expansion of fictitious stress-free elements. However, G&R mostly occurs in a stressed configuration and is accompanied by a production or removal of constituents. In order to overcome these limitations, and drawing from the continuum theory of mixtures [64], Humphrey and Rajagopalan [65] introduced the constrained mixture theory based model of G&R. This theory is based on a few key assumptions:

1. That soft tissues can be modeled as a mixture of different constituents (e.g. collagen, elastin etc.).
2. The mixture is constrained; all constituents in a material point are subject to the same motion.
3. The mass per unit current volume is assumed to be constant along the G&R process.

This theory has been successfully used for predicting time-courses of arterial adaptations and disease progression in diverse cases. Initial studies by the authors focused on arterial adaptation to changes in mechanical stimuli in young healthy arteries. It was shown that this theory was able to capture key morphological changes in response to mechanical forces; dilatation in response to increased flow [66], hypertension induced wall thickness [67], and axial force induced G&R [68]. Qualitative features of disease progression due to aging [69] and unbounded growth, i.e. aneurysm growth could also be predicted [70]. Watton et al. employed a simpler membrane, rate-based formulation of this approach to predict the growth of cerebral aneurysms [71] and further refined it with mechanobiological equations to model the effect of various drug therapies on aneurysm G&R [72]. This theory has recently been extended to understand the effect of vascular interventional strategies like stentplasty for vasospam [73], and venous bypass grafting for treating atherosclerosis [74]. Since this theory is based on the knowledge that vascular tissues adapt their structure and function to achieve a certain homeostatic stress state, there is a need to understand the final homeostatic condition for the application under consideration. Thus, translating this theory to modeling *i*TEVGs for arterial circulation requires experimental data to determine their homeostatic state. Furthermore, since each constituent is modeled explicitly, there is an inherent need for biological and mechanical data to understand application-specific mass kinetics equations in order to use this model not only for qualitative, but quantitative predictions. Therefore, in order to understand the fundamental mechanisms guiding iTEVG formation across age and develop a G&R based approach to guide rational design of these constructs, we designed the following specific aims.

1.6 Specific Aims

Since the first clinical use of a tissue engineered product (the epithelium) in 1981 [75], there has been very little change in the trial and error nature of tissue engineering product design. In this work we propose a new paradigm for vascular graft design which will not only accelerate clinical translation of grafts but can also be used for design of other mechanobiology based tissue engineered devices. It has long been known that mechanical stimuli influence not only gross morphological [76], [77] and protein remodeling [38],[39] but also stem cell lineage differentiation [80], [81]. While mature arteries are extremely quiescent with cell proliferation rates of 0.01- 1% per day, both physiological and pathological changes can elicit a significant remodeling response involving ECM synthesis, degradation and turnover [82]. As noted by Zilla et al. [83], there needs to be a focus on clinically relevant models when designing TEVG's to improve success rates to translation. Since older populations are the target audience for therapy, these grafts need to be designed for the older demographic. Unfortunately, translating results between animal models is not a trivial task since not only do the graft parameters have to be optimized for a new model but the model itself reacts very differently to diverse mechanobiological cues. The overall goal of this dissertation is to understand the fundamental mechanisms guiding iTEVG formation and rationally design neoarteries in an aged murine model. In order to achieve these goals, we will take a combined *in vivo*, *ex vivo* and *in silico* approach.

1.6.1 Specific Aim 1

Determine changes in graft material properties during degradation. Successful neoartery development is contingent on the effective interplay between graft degradation and ECM deposition. Our hypothesis is that both *in vitro* and *in vivo* degradation are governed by the same passive degradation mechanism. Thus, in this aim our objective is to improve the predictive capability of our G&R tool by developing physics-based functional forms for changes in graft properties during degradation by conducting *in vitro* degradation experiments.

1.6.2 Specific Aim 2

Determine structure-function and biological evolution equations for neoartery formation in young rats. Understanding the mechanism of G&R in young rats as a function of initial graft properties is a fundamental requirement for developing grafts for other models. In order to develop this mechanistic understanding, we will track biological and mechanical remodeling in young rats implanted with our successful bi-layered grafts at three time points post-implant; using the data to assess its performance relative to clinical gold standard - vein grafts.

1.6.3 Specific Aim 3

Develop a data-driven computational G&R tool for iTEVG modeling for both young and aged hosts. Translating the success of iTEVGs from young to old animals, across species, or even across different sites in the body is not a trivial task due to the large number of graft (porosity,

degradation rate, wall thickness etc.) and system parameters (cellular infiltration, rate of ECM deposition etc.) governing the remodeling response. Hence, there is an unmet need for a sophisticated approach to iTEVG design that can reduce the time and cost for clinical translation. In this aim we will modify the theory of constrained mixtures to incorporate an iTEVG component in the reference configuration to develop a tool that can be used for guiding experimental design of iTEVGs. The rationale behind the proposed work is that it is only with a mechanistic G&R model, coupled with our rich experimental dataset, that it will be possible to rationally design optimal iTEVG properties for various animal models and ultimately human clinical trials.

1.6.4 Specific Aim 4

Determine effect of age on neoartery formation. We hypothesize that the rate of formation of ECM proteins in both young and old animals is governed by the same mechanobiological cues but with altered rates of productions. We will identify and quantify the differences in neoartery formation between young and old rats by obtaining biological and mechanical data. We will obtain these data by implanting grafts in both young and old animals and tracking biological and mechanical evolution over time. We will then use this data to tailor, validate, and use our G&R model to predict the salient mechanisms guiding neoarterial remodeling.

1.6.5 Specific Aim 5

Determine the prevalence and role of calcification in a parallel model system of adverse remodeling. G&R is a natural mechanism of adaptation to diverse mechanobiological cues developed by the body. However, not all G&R leads to the recapitulation of the native environment. Calcification is thought to be one of the principal manifestations of adverse remodeling in the arterial wall, especially in diseases like atherosclerosis. Understanding the role of calcification in the biology and mechanics of soft tissues is a first step toward designing strategies to prevent the occurrence or strategically use its presence for robust G&R. In order to understand the potential role of calcification in soft tissues, we will investigate its role in a parallel model system that exhibits similar modes of failure – cerebral aneurysms. In this aim, our goal is to understand the prevalence and role of calcification in cerebral aneurysms in order to guide G&R strategies. We will also develop tools and techniques to simultaneously image ECM components along with calcification. These methods will enable us to better understand pathological G&R and develop strategies to mitigate adverse remodeling. This in turn will guide iTEVG design, while providing a fundamental understanding of the interaction of calcification with ECM.

2.0 Degradation and Erosion Mechanisms of Acellular Bioresorbable Porous Vascular

The work in this chapter is largely reproduced with permission from the following manuscript:

Gade, Piyusha S., Keewon Lee, Blaise N. Pfaff, Yadong Wang, and Anne M. Robertson. "Degradation and erosion mechanisms of bioresorbable porous acellular vascular grafts: an in vitro investigation." *Journal of The Royal Society Interface* 14, no. 132 (2017): 20170102.

2.1 Introduction

A fundamental mechanism of *in situ* tissue regeneration from biodegradable synthetic acellular vascular grafts is the effective interplay between graft degradation, erosion and the production of ECM. Degradation studies on PGS have been focused on solid PGS *in vivo* [84], [85] or base-accelerated degradation *in vitro* [86], with the aim of understanding rate of mass loss as a function of degradation. However, no studies have investigated the effect of degradation and erosion on porous small diameter PGS grafts. Since the efficacy of the G&R tool depends on well-formulated functional forms, there is a much-cited [74], [87], [88] need in the field of biomechanics for experimental data to develop these functional forms. Furthermore, our preliminary computational studies showed the time constants associated with graft erosion and degradation are critical for remodeling, with fusiform aneurysms forming if the degradation rate was too fast. The objective of this aim is to understand the degradation and erosion mechanisms of porous PGS grafts while also formulating mechanism-based functional forms to inform the G&R tool and

improve robustness of its predictions. The working hypothesis is that both *in vitro* and *in vivo* degradation are governed by passive degradation mechanisms. Thus, mechanistic functional forms can be used by adjusting rate constants and boundary conditions for the *in vivo* model. The rationale for this aim is that improved understanding of graft degradation will not only improve the G&R tools robustness but will also enable us to have a mechanistic understanding of the process. This knowledge is critical for future translational work in mature and large animal models.

Developments in biomechanics have led to formulation of continuum mechanics based, mixture theory-driven G&R computational models that predict vascular G&R response to altered physiological conditions [68], [89], [90]. These models have been useful in predicting G&R response in diseased conditions like aneurysms [91]–[94] and are being extended to model the *in vivo* development of neo- tissue from a degrading TEVG in venous circulation [95]. In our prior work, we used this G&R model to conduct a parametric study to understand the effect of degradation rates on long-term neoarterial development [96]. Briefly, we postulate the following strain energy function to model the evolving neoartery using a constrained mixture model [65]:

Equation 2-1

$$W(s) = \sum_{\alpha=1}^{k} W^{\alpha}(s) = \sum_{\alpha=1}^{k} \frac{\rho^{\alpha}(0)}{\rho(s)} Q^{\alpha}(s) \bar{W}^{\alpha}\left(\boldsymbol{C}^{\alpha}_{n(0)}(s)\right) + \int_{0}^{s} \frac{m^{\alpha}(\tau)}{\rho(s)} q^{s-\tau} \bar{W}^{\alpha}\left(\boldsymbol{C}^{\alpha}_{n(\tau)}(s)\right) d\tau$$

where $W(s)$ is the total strain energy of the mixture, $\rho^{\alpha}(0)$ is the density of constituent at time $s = 0$, $Q^{\alpha}(s)$ is the survival function that represents remaining mass and $\bar{W}^{\alpha}\left(\boldsymbol{C}^{\alpha}_{n(0)}(s)\right)$ represents the evolving strain energy function of the degrading constituent. $\bar{W}^{\alpha}\left(\boldsymbol{C}^{\alpha}_{n(\tau)}(s)\right)$ and $m^{\alpha}(\tau)$ represent the strain energy function and rate of deposition of constituents respectively, where $\left(\boldsymbol{C}^{\alpha}_{n(\tau)}(s)\right)$ is the right Cauchy–Green tensor at current time *s*, defined relative to the configuration at time t. The detailed description of this theory has been presented in chapter 4.0. The survival function and changing mechanical properties are phenomenological equations which can be tuned to refine the predictive capability of the tool. There is a much-cited need in the field of biomechanics for experimental data to develop these constitutive equations and obtain the requisite rate constants [65], [74], [87], [96]. Our prior computational work with this model showed that the time constants associated with graft erosion and degradation are critical for the remodeling process, with fusiform aneurysms forming if the degradation rate was too fast. It must be noted that while degradation is defined as the deleterious change in properties due to scission of polymer chains into monomers [97], we are primarily concerned with the manifestation of these changes in the context of mechanical properties. Erosion of the grafts is defined as the reduction in mass through surface or volumetric (bulk) erosion.

While there is a critical need to understand the erosion and degradation process of TEVGs, the only data available are based on studies of solid PGS erosion *in vivo* [84] and base- accelerated degradation *in vitro* [86], with no data on degradation or erosion of porous small diameter PGS TEVGs.

In this study, we address this need by investigating the degradation and erosion mechanisms of porous PGS TEVGs used for *in situ* neoartery formation [98]. We acquire experimental data by conducting an *in vitro* analysis of the porous grafts used in our *in vivo* studies

exposed to enzymatic degradation and provide a constitutive equation (functional form) for mass loss and mechanical property change as a function of degradation time. Furthermore, we use these data to develop a diffusion-based erosion model for predicting mass loss. This mechanistic, physics-based explanation allows formulation of erosion as a boundary-value problem and can be used for modeling the phenomena under different boundary conditions. To our knowledge, this is the first investigation that studies the degradation and erosion process for porous PGS TEVGs and provides a mechanistic framework to model erosion with validation against experimental data. These results provide physical insights into the mechanisms of degradation and erosion and will be of great value for G&R frameworks as the basis of predictive tools for rational design of TEVGs.

PGS is a widely used elastomer in the field of tissue engineering due to its biocompatibility and fast degradability. It has been used in myocardial engineering [99]–[101], vascular graft and microvasculature fabrication [31], [102], bone and cartilage engineering [103], [104] and nerve guide development [105]–[107], to name a few. These applications require an understanding of the degradation and erosion process of the polymer as it guides load transfer and remodeling response. Hence, understanding these mechanisms will have translational benefits by providing the necessary information to tune properties of PGS (like curing time, temperature, porosity) to achieve desired degradation rates. This work also has broader applicability to other elastomers manufactured by salt leaching [108]–[110] as they exhibit a similar porous morphology which we have found to play a major role in degradation.

This work is broadly divided into two parts—modeling erosion as pertaining to mass loss and modelling degradation as manifested by change in mechanical properties. Section 2 outlines the methods used to investigate the enzymatic degradation of grafts *in vitro* followed by outlining

the analytical solution of the erosion boundary value problem and predicting mass loss through this process. Section 3 provides constitutive relationships of mass loss based on *in vitro* enzymatic degradation assays and outlines the relative contribution of bulk versus surface erosion. Results from the mathematical modelling of erosion are presented in the context of theoretical as compared to the experimental mass loss. Furthermore, we investigated the changes in mechanical properties of the degrading grafts and introduced a scalar damage function with an explicit time-dependence to represent the weakening of mechanical properties over degradation time s. Finally, we analyze the results in the context of TEVG development and refinement of G&R tools for guiding graft design.

2.2 Materials and Methods

2.2.1 Graft Fabrication

The PGS prepolymer was synthesized as previously described [85]. Briefly, 20 grafts were fabricated from a solvent casting/ salt leaching method using 25–32 mm ground salts as porogens [111]. Salts were packed into the mold, which consisted of a stainless-steel rod (outer diameter = 0.8mm) as a mandrel and a Teflon outer tubing (inner diameter = 1.58mm, length = 20mm). The salt mold was then fused in humidified chamber at 37ºC for 90 min. Salt templates were released from the mold. PGS prepolymer was dissolved with tetrahydrofuran to prepare 20% (w/v) solution. The volume of PGS solution was adjusted as 3:1 mass ratio of salt: PGS, and added to salt templates. Salt templates were placed in a fume hood for 1 h to evaporate solvent, and cured in a vacuum oven at 150ºC for 24 h. After curing, grafts were placed in a series of two water baths

(first bath for 24 h and second bath for 48 h) to remove residual salts and then lyophilized (Figure 5).

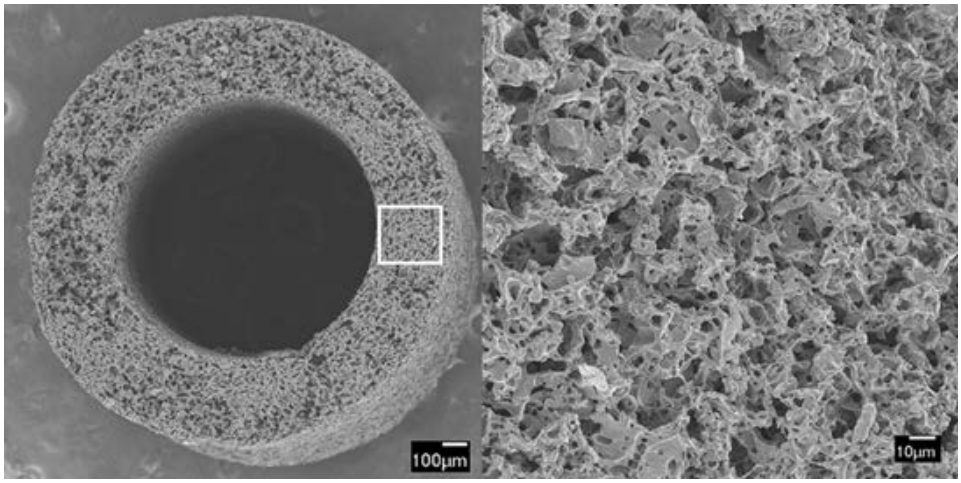

Figure 5 Scanning electron microscopy image of salt-leached PGS core.

2.2.2 Enzymatic Degradation

Since graft mechanics cannot directly be studied *in vivo* due to the growth of neotissue upon graft degradation, we conducted an *in vitro* analysis of the effect of enzymatic degradation on graft properties to understand the physics of degradation and erosion of these grafts. Cholesterol esterase was the enzyme of choice for the study as it has been reported to be the primary enzyme responsible for catalysis of PGS degradation by hydrolysis of ester groups *in vivo* [112]. Fabricated PGS samples (n = 4 at each of the 4 time points) were immersed in 1 ml solution of phosphate buffered saline with 0.2 units μg^{-1} PGS of cholesterol esterase (Sigma-Aldrich) kept in an incubator at 37ºC maintained at a pH of 7.4. Enzyme concentration was chosen through preliminary experiments that iteratively determined the concentration required to achieve complete *in vitro* mass loss by three weeks, a time constant found to match *in vivo* observed rates of mass loss [113].

Initial enzyme concentration for this process was obtained from Chen et al. [114]. The medium was replaced every 2 days to maintain enzyme activity. Mass loss, change in volume fraction, morphology and mechanical properties were recorded at days 1, 4, 7 and 10 after which the grafts lost most of their structural integrity.

2.2.3 Dry Mass Loss

The mass of each sample was recorded before immersion in degradation media and at every time point post-degradation. Wet samples at every time-point were thoroughly dried by lyophilization for 24 h. Each sample was then weighed and mass loss was calculated as

$$\Delta m(\%) = \frac{m(s) - m(0)}{m(0)} \times 100 \qquad \textbf{Equation 2-2}$$

where $m(s)$ is the dry mass after degradation time s and $m(0)$is the initial dry mass.

2.2.4 Change in Volume Fraction

Porosity and pore size of grafts were measured using a sub micrometer resolution (0.35 mm) Skyscan 1272 (Bruker Corporation) 11 Mp micro-computed tomography (microCT) instrument. Samples were scanned before immersion in degradation media for baseline measurements. Following enzymatic degradation, samples were lyophilized at predetermined time

points and dry samples were scanned to measure change in porosity and pore size over time. Briefly, samples were mounted on a brass stub with a Styrofoam holder (Figure 6a) and scanned using the following settings: camera pixel size of 7.4 mm, image pixel size of 2.8 mm, frame averaging of 10, rotation step size of 0.18 and scanned 180 degrees around the vertical axis. *In vitro* volume fraction of PGS was defined as

$$\phi_{PGS}(s) = \frac{V_{PGS}(s)}{V_{graft}(s)} \quad \textbf{Equation 2-3}$$

where $\phi_{PGS}(s)$ is the *in vitro* volume fraction (also called porosity) of PGS, $V_{PGS}(s)$ is the volume of PGS and $V_{graft}(s)$ is the total graft volume as calculated using microCT at time s. To obtain volume fraction, a three-dimensional image was reconstructed as a stack of 2 mm average thick sections in the axial plane using NRecon (Bruker Corporation). Volume fraction was calculated by using CT-Analyser (Bruker Corporation). Briefly, a region of interest (ROI) was defined along the length of the graft followed by identifying a threshold value to obtain a binary image with air as the background (Figure 6c). These binary images were then used to obtain overall dimensions and a three-dimensional morphometric analysis was conducted to obtain metrics of volume fractions and to create a surface mesh using the marching cubes algorithm (Figure 6d). We calculated the per cent change in *in vitro* porosity over time of the degrading grafts as

$$\Delta\phi_{PGS}(\%) = \frac{\phi_{PGS}(s) - \phi_{PGS}(0)}{\phi_{PGS}(0)} \times 100 \quad \textbf{Equation 2-4}$$

where $\phi_{PGS}(0)$ and $\phi_{PGS}(s)$ are the porosities of the scaffolds at time $s = 0$ and current time, respectively.

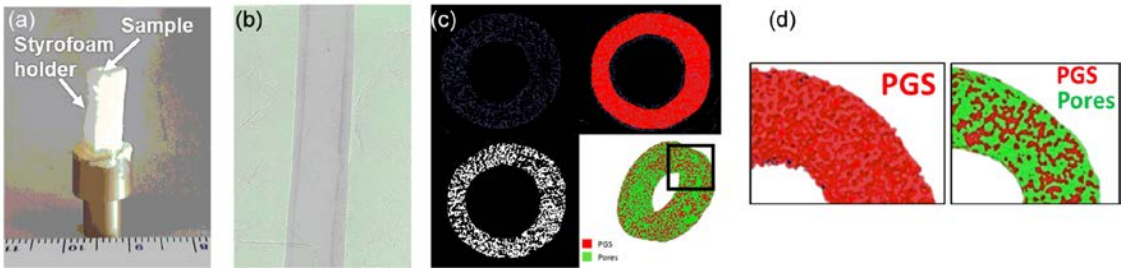

Figure 6 Methodology of obtaining PGS volume fraction.

(a) Image of PGS graft mounted on brass stub in styrofoam holder, (b) scanned CT image, (c) reconstructed surface mesh with (d) PGS in red and pores in green.

2.2.5 Apparent Density

The balance of mass equation in mixture theory allows formulation of mass exchange between different constituents. This exchange leads to mass deposition/removal which can occur as a surface or volume erosion process. Surface erosion constitutes evolution of the entire boundary of the species and volume erosion is surface erosion at a microscopic level (at pore surface) throughout the bulk of the body [115]. Looked at another way, pure surface erosion requires that the apparent density of the body remains constant, whereas volume erosion leads to a change in apparent density, where the apparent density of PGS (ρ_a^{PGS}) is defined as the mass of PGS per unit total TEVG volume. The apparent density can also be defined in terms of graft porosity as follows:

$$\rho_{a_{PGS}} = \rho_T^{PGS} \times \phi_{PGS}(s) \quad \textbf{Equation 2-5}$$

where ρ_T^{PGS} is the true material density of PGS.

2.2.6 Change in Bulk Morphology

Three-dimensional images obtained from microCT reconstruction were used to calculate the changes in inner and outer diameter as functions of time exposed to enzymatic degradation. These were measured at every 0.2 mm and averaged across the length of the sample followed by normalization to its initial dimensions to calculate per cent change in diameter as

$$\Delta d(\%) = \frac{d(s) - d(0)}{d(0)} \times 100 \quad \textbf{Equation 2-6}$$

where $d(0)$ and $d(s)$ are the diameters of the scaffolds at time $s = 0$ and current time, respectively.

2.2.7 Mechanical Testing

PGS grafts were assumed to be isotropic as they were fabricated using the method of salt-leaching. Uniaxial tensile testing was performed on each sample to calculate the change in

mechanical properties as a function of time exposed to enzymatic degradation. The wet length, diameter and thickness of each sample was recorded before mounting the sample. Each sample was tested uniaxially to failure on a custom-designed biaxial inflation testing machine. For this purpose, only axial tension was applied since grafts were porous and could not be pressurized. Briefly, the device consists of mounting points for various gauge cannulae (Zephyrtronics Inc.) which are used to mount specimens. A bath is provided for submerging samples in desired solution at 37ºC (Figure 7). Samples can be stretched axially at a controlled strain rate via a computer-controlled actuator (Aero- tech Inc., Model ANT-25LA) under a video camera (Edmund Optics, model EO-5012C) capturing images which are analyzed using custom written MATLAB (MathWorks, Natick, USA) code to obtain local strain measurements.

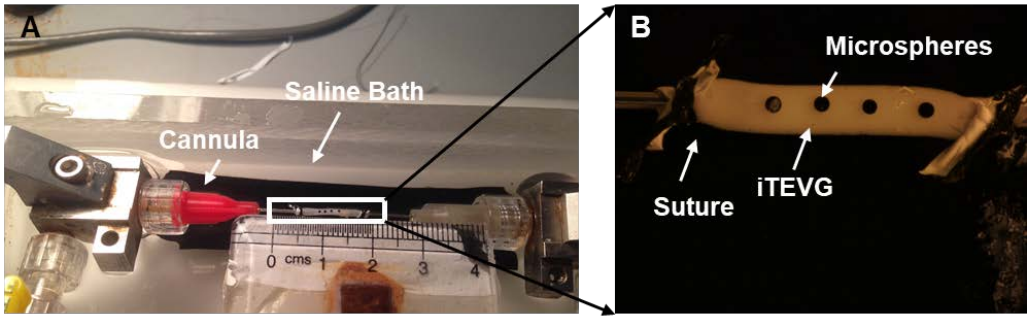

Figure 7: Biaxial-inflation mechanical testing device setup.

The load is recorded by a load cell (Transducer Techniques, model MDB-5) affixed to one of the mounts of the device. In this case, samples were stretched uniaxially to failure to obtain their mechanical properties. Samples were mounted on gauge 27 cannulae followed by lightly gluing 250 mm silica microspheres (Whitehouse Scientific Ltd) on the surface for local strain

measurements. Four preconditioning cycles were performed by stretching the samples to 10% of their initial length at a strain rate of 0.005mm/s. This was followed by stretching the samples to failure. Cauchy stress and stretch were calculated as follows:

$$\sigma_z = \frac{f}{\pi(r_o(t)^2 - r_i(t)^2)} \quad and \quad \lambda_z = \frac{l(t)}{l(0)} \qquad \textbf{Equation 2-7}$$

where f is the force recorded by the load cell, $r_o(t)$ and $r_i(t)$ are the outer and inner radii, respectively, at current time (t), calculated assuming isovolumetric deformations. $l(0)$ and $l(t)$ are the initial and current lengths, respectively. This data was fit to a standard neo-Hookean model with a time-dependent material coefficient

$$\bar{W}^{PGS}(s) = \frac{\beta(s)}{2}[I_1 - 3] \qquad \textbf{Equation 2-8}$$

where s represents the G&R time and I_1 is the first invariant of the right Cauchy–Green tensor, namely the trace of $\boldsymbol{C}^{\alpha}_{n(\tau)}(s)$.

2.2.8 Mathematical Modeling of Surface Erosion

In this section, we discuss the analytical solution for the mass loss from a graft subjected to enzymatic degradation. We hypothesized that the mechanism of TEVG mass loss is through a

time evolving concentration gradient set up by diffusion of the eroded PGS from the exposed graft surface. This diffusion-driven mass loss can occur in the volume occupied by the solvent (degradation media) which serves as the transport medium for the eroded solute. We model the graft as a thick walled, circular cylinder and define a cylindrical coordinate system (r, θ, z) with the z-axis coincident with the centerline of the graft. We consider an initial value problem, where at time $s = 0$, the graft is placed in an impermeable cylinder of radius R_3 that represents the beaker in the experiment. Ω_1 and Ω_2 denote the inner solvent region $(0 \leq r \leq R_1(s), 0 \leq \theta \leq 2\pi, 0 \leq z \leq L)$ and outer solvent region $R_2(s) \leq r \leq R_3, 0 \leq \theta \leq 2\pi, 0 \leq z \leq L$, respectively (figure 3). In this work, we approximate these moving boundaries Γ_1 and Γ_2 as independent of time, based on our perturbation analysis of the moving boundary problem [116]. It follows from the perturbation analysis that this approximation is valid when the ratio $\frac{c_s}{\rho_a^{\alpha}} \ll 1$. In this study, $\frac{c_s}{\rho_a^{PGS}} = 8.77 \times 10^{-4}$, supporting the fixed boundary approximation.

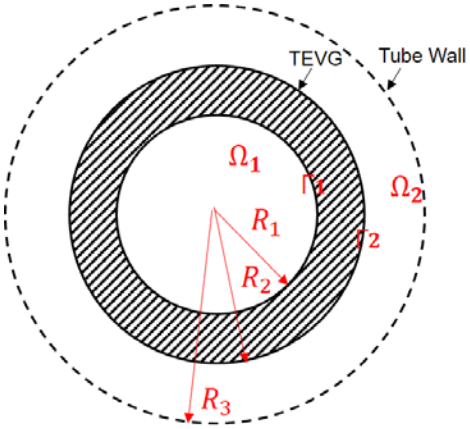

Figure 8 Schematic of cross section of TEVG submerged in degradation media. Diffusion of eroded PGS occurs in the domains Ω_1 and Ω_2. Γ_1 and Γ_2 represent the inner and outer surfaces of the PGS graft, respectively. Γ_3 represents the impermeable outer tube wall.

The eroded PGS (solute) sets up a concentration gradient in both these domains and Fick's law in conjunction with conservation of mass can be used to model the rate of change of concentration gradient. Figure 3 shows a representative two-dimensional cross section of the hollow cylinder (TEVG) submerged in degradation media. We employ Fick's law of isotropic diffusion in both fluid domains,

$$\boldsymbol{F} = -D\nabla \mathrm{c} \qquad \text{in } \Omega_1, \Omega_2 \qquad \textbf{Equation 2-9}$$

Where $\boldsymbol{F}$ is the mass flux and D is the coefficient of diffusion, a scalar material constant. For convenience, it is assumed that all materials we consider are isotropic with respect to diffusion and that D is uniform and independent of C. Accordingly, Fick's second law is given by

$$\frac{\partial c}{\partial s} = D\nabla^2 c \qquad \textbf{Equation 2-10}$$

The diffusion is modelled as axisymmetric and independent of axial position, so that Equation 2-10 reduces to

$$\frac{\partial c}{\partial s} = D\frac{1}{r}\frac{\partial}{\partial r}\left(r\frac{\partial c}{\partial r}\right), \qquad \Omega_1, \Omega_2 \qquad \textbf{Equation 2-11}$$

We impose the standard Noyes–Whitney equation [117] to describe the rate of dissolution of the graft at its inner and outer surfaces, Γ_1 and Γ_2, respectively

$$\boldsymbol{n}.\boldsymbol{F} = h(c_s - c) \quad or \quad \frac{\partial c}{\partial n} = -\frac{h}{D}(c_s - c) \quad on \quad \Gamma_1, \Gamma_2, s > 0 \qquad \textbf{Equation 2-12}$$

Where h is a material coefficient, c is the molar concentration and c_s is the saturation limit for the solute (eroded PGS) in the solvent (enzymatic media). We assume the concentration is initially zero in both fluid regions,

$$c(r, 0) = 0 \quad in \quad \Omega_1, \Omega_2 \qquad \textbf{Equation 2-13}$$

2.2.8.1 Solution in the Inner Domain, $\boldsymbol{\Omega_1}$

At the inner surface of the graft (Γ_1), where $r = R_1$ and $\boldsymbol{n} = -e_r$, Equation 2-12 takes the form,

$$\frac{\partial c}{\partial r} = \frac{h}{D}(c_s - c) \quad r = R_1, \quad s > 0 \qquad \textbf{Equation 2-14}$$

The classical method of separation of variables can be used to obtain the solution $c(r,s)$ to Equation 2-11 subject to the boundary condition Equation 2-14 and initial condition Equation 2-13 [118]. It is convenient to first introduce the nondimensionalization,

$$\hat{u} = 1 - \frac{c}{c_s} \quad \hat{r} = r\frac{h}{D} \quad \hat{s} = s\frac{D}{R_1^2} \quad \hat{\beta} = h\frac{R_1}{D} \qquad \textbf{Equation 2-15}$$

Using the definitions in Equation 2-15, the equation for radial diffusion (Equation 2-11), the boundary condition on Γ_1 (Equation 2-14), and the initial condition (Equation 2-13) can be written as,

$$\begin{cases} \dfrac{\partial \hat{u}}{\partial \hat{s}} = \hat{\beta}^2 \dfrac{1}{\hat{r}} \dfrac{\partial}{\partial\, \hat{r}} \left(\hat{r} \dfrac{\partial \hat{u}}{\partial \hat{r}} \right) & \hat{r} \in [0, \hat{\beta}] & \hat{s} > 0, \\ \dfrac{\partial \hat{u}}{\partial \hat{r}} = -\hat{u} & at\ \hat{r} = \hat{\beta}, & \hat{s} > 0, \\ \hat{u}(\hat{r}, 0) = 1 & \hat{r} \in [0, \hat{\beta}], & \hat{s} > 0 \end{cases} \qquad \textbf{Equation 2-16}$$

Using standard methods of separation of variables (see, for example, Carslaw and Jaeger [118]), we look for a factorized solution $\hat{u} = \hat{T}(\hat{s})R(\hat{r})$ for (Equation 2-16), from which it follows, that $\hat{T}(\hat{s})$ and $\hat{R}(\hat{r})$ must satisfy

$$\hat{T}' + \alpha^2 \hat{\beta}^2 \hat{T} = 0, \quad \hat{R}'' + \frac{1}{\hat{r}} \hat{R}' + \alpha^2 \hat{R} = 0, \qquad \textbf{Equation 2-17}$$

For $\hat{s} > 0$ and $\hat{r}\,\epsilon\,[0, \hat{\beta}]$, where α^2 is a positive, real constant and we have used the "′" notation to denote differentiation with respect to the independent variable. The well-known solutions to (Equation 2-17) are

$$\hat{T} = Ae^{-\alpha^2 \hat{\beta}^2 \hat{s}}, \quad \hat{R}' = BJ_0(\alpha\,\hat{r}) \qquad \textbf{Equation 2-18}$$

where we have imposed the boundedness of the solution at $\hat{r} = 0$. The equation for $\hat{R}(\hat{r})$ in (Equation 2-17) is a (singular), Sturm-Liouville problem, where

$$L[\hat{R}] \equiv (\hat{r}\hat{R}')' \qquad \textbf{Equation 2-19}$$

with corresponding differential equation and boundary conditions,

$$\begin{Bmatrix} L[\hat{R}] = -\alpha^2 \hat{r}\hat{R} & \hat{r}\,\epsilon\,[0, \hat{\beta}] \\ \hat{R}' + \hat{R} = 0 & at\ \hat{r} = \hat{\beta} \end{Bmatrix} \qquad \textbf{Equation 2-20}$$

The Lagrange identity holds for this singular problem (Equation 2-20) (e.g. page 659 Boyce and DiPrima) [119], and we therefore have the completeness of the set of eigenfunctions $\hat{R}(\hat{r})$ in the appropriate function space, so the solution $\hat{u}$ can be represented as the following series

$$\hat{u} = \sum_{n=1}^{\infty} A_n e^{-\alpha_n^2 \widehat{\beta^2} \hat{s}} J_0(\alpha_n \hat{r})$$ **Equation 2-21**

Applying the boundary condition given in (Equation 2-16) on surface $\Gamma_1(\hat{r} = \hat{\beta})$, we obtain,

$$\sum_{n=1}^{\infty} A_n e^{-\alpha_n^2 \widehat{\beta^2} \hat{s}} [J_0(\alpha_n \hat{\beta}) - \alpha_n J_1(\alpha_n \hat{\beta})] = 0$$ **Equation 2-22**

And therefore, α_n, are the roots of

$$[J_0(\alpha_n \hat{\beta}) - \alpha_n J_1(\alpha_n \hat{\beta})] = 0 \quad n = 1,2,3 \ldots$$ **Equation 2-23**

Using the initial condition $\hat{u} = 1$ at $\hat{s} = 0$ in (Equation 2-21), it follows that,

$$\sum_{n=1}^{\infty} A_n J_0(\alpha_n \hat{r}) = 1$$ **Equation 2-24**

And therefore,

$$\sum_{n=1}^{\infty}\int_0^{\hat{\beta}} A_n J_0(\alpha_n\hat{r})J_0(\alpha_m\hat{r})\hat{r}d\hat{r} = \int_0^{\hat{\beta}} J_0(\alpha_m\hat{r})\hat{r}d\hat{r}, \quad m = 1,2,3 \ldots \qquad \textbf{Equation 2-25}$$

Using the well-known orthogonality properties of the solution with (Equation 2-23),

$$\int_0^{\hat{\beta}} J_0(\alpha_n\hat{r})J_0(\alpha_m\hat{r})\hat{r}d\hat{r} = \begin{cases} 0 & m \neq n \\ \dfrac{\hat{\beta}^2(1+\alpha_n^2)}{2\alpha_n^2}J_0^2(\alpha_m\hat{\beta}) & m = n \end{cases} \qquad \textbf{Equation 2-26}$$

Hence,

$$A_n = \int_0^{\hat{\beta}} J_0(\alpha_n\hat{r})\,\hat{r}d\hat{r} \Big/ \int_0^{\hat{\beta}} J_0^2(\alpha_n\hat{r})\,\hat{r}d\hat{r} \qquad \textbf{Equation 2-27}$$

It follows from standard integral results for Bessel functions and (Equation 2-23) that

$$\int_0^{\hat{\beta}} J_0(\alpha_n\hat{r})\,\hat{r}d\hat{r} = \frac{\hat{\beta}}{\alpha_n}J_1(\alpha_n\hat{\beta}) = \frac{\hat{\beta}}{\alpha_n^2}J_0(\alpha_n\hat{\beta}) \qquad \textbf{Equation 2-28}$$

Using this last result with (Equation 2-26) in (Equation 2-27), we obtain the solution for $\hat{u}$ in Ω_1 (see, e.g. page 201 of Carslaw and Jaeger) [118],

$$\hat{u} = \sum_{n=1}^{\infty} \frac{2J_0(\alpha_n \hat{r})}{\hat{\beta}(1+\alpha_n^2)J_0(\alpha_n \hat{\beta})} e^{-\alpha_n^2 \widehat{\beta^2} \hat{s}} \quad \hat{r} \in [0, \hat{\beta}] \; and \; \hat{s} > 0$$ **Equation 2-29**

Substituting $\hat{u} = 1 - \frac{c}{c_s}$ in Equation 2-29 we get

$$\frac{c}{c_s} = 1 - \sum_{n=1}^{\infty} \frac{2J_0(\alpha_n \hat{r})}{\hat{\beta}(1+\alpha_n^2)J_0(\alpha_n \hat{\beta})} e^{-\alpha_n^2 \widehat{\beta^2} \hat{s}} \quad \hat{r} \in [0, \hat{\beta}] \; and \; \hat{s} > 0$$ **Equation 2-30**

Using Equation 2-12 and Equation 2-30, mass loss in the inner domain can then be calculated as follows

$$\Delta \hat{m} = 2\pi R_1 l \int_0^s h(c - c_s) dt$$ **Equation 2-31**

$$\Delta \hat{m} = 4\pi \frac{R_1^2 l c_s}{\hat{\beta}^2} \sum_{n=1}^{\infty} \left[\frac{1 - e^{-\alpha_n^2 \widehat{\beta^2} \hat{s}}}{(1+\alpha_n^2)\alpha_n^2} \right]$$

2.2.8.2 Solution in the Outer Domain, Ω_2

At the outer surface of the graft (Γ_2), where $r = R_2$ and $\boldsymbol{n} = -e_r$, Equation 2-12 takes the form,

$$\frac{\partial c}{\partial r} = \frac{h}{D}(c_s - c) \quad r = R_2, \quad s > 0 \qquad \textbf{Equation 2-32}$$

At the surface of the outer tube (Γ_3), where $r = R_3$ and $\boldsymbol{n} = -e_r$, the zero-flux condition becomes,

$$\frac{\partial c}{\partial r} = 0 \quad r = R_3, \quad s > 0 \qquad \textbf{Equation 2-33}$$

The classical method of separation of variables can be used to obtain the solution $c(r, s)$ to Equation 2-11 subject to the boundary conditions (Equation 2-32) and (Equation 2-33), with the initial condition (Equation 2-13). It is convenient to first introduce the nondimensionalization,

$$\hat{u} = 1 - \frac{c}{c_s} \quad \hat{r} = r\frac{h}{D} \quad \hat{s} = s\frac{D}{R_1^2} \quad \hat{\beta} = h\frac{R_1}{D} \quad \Upsilon = \frac{R_2}{R_3} \qquad \textbf{Equation 2-34}$$

the system of equations for the outer domain can be written as,

$$\frac{\partial \hat{u}}{\partial \hat{s}} = \hat{\beta}^2 \frac{1}{\hat{r}} \frac{\partial}{\partial \hat{r}} \left(\hat{r} \frac{\partial \hat{u}}{\partial \hat{r}} \right) \qquad \hat{r} \in \left[\hat{\beta}, \frac{\hat{\beta}}{\Upsilon} \right] \qquad \hat{s} > 0, \tag{Equation 2-35}$$

$$\frac{\partial \hat{u}}{\partial \hat{r}} = -\hat{u} \qquad at\ \hat{r} = \hat{\beta}, \qquad \hat{s} > 0,$$

$$\frac{\partial \hat{u}}{\partial \hat{r}} = 0 \qquad at\ \hat{r} = \frac{\hat{\beta}}{\Upsilon} \qquad \hat{s} > 0,$$

$$\hat{u}(\hat{r}, 0) = 1 \qquad \hat{r} \in [0, \hat{\beta}],$$

As for the solution in the inner domain, the classical method of separation of variables is used and we look for a factorized solution of the form $\hat{u} = \hat{T}(\hat{s})R(\hat{r})$. It follows from Equation 2-35, that,

$$\hat{T}(t) = Ae^{-\alpha^2 \widehat{\beta^2} \hat{s}}, \quad \hat{R}(\hat{r}) = AJ_0(\alpha \hat{r}) + BY_0(\alpha\, \hat{r}) \tag{Equation 2-36}$$

where α is once again a real, positive constant. Hence, the solution for $\hat{u}$ in the outer domain is

$$\hat{u} = \sum_{n=1}^{\infty} [A_n J_0(\alpha_n \hat{r}) + B_n Y_0(\alpha_n \hat{r})]\, e^{-\alpha_n^2 \widehat{\beta^2} \hat{s}} \tag{Equation 2-37}$$

applying the boundary condition at the outer boundary, $\Gamma_3(\hat{r} = \hat{\beta}/\Upsilon)$, we obtain

$$A_n \alpha_n J_1\left(\frac{\alpha_n \hat{\beta}}{\Upsilon}\right) + B_n \alpha_n Y_1\left(\frac{\alpha_n \hat{\beta}}{\Upsilon}\right) = 0, \quad n = 1,2,3 \ldots$$

Equation 2-38

It is useful to define the function, $\varphi_0(\alpha_n \hat{r})$, as a linear combination of $J_0(\alpha_n \hat{r})$ and $Y_0(\alpha_n \hat{r})$

$$\phi_0(\alpha_n \hat{r}) = J_0(\alpha_n \hat{r}) Y_1\left(\frac{\alpha_n \hat{\beta}}{\Upsilon}\right) - Y_0(\alpha_n \hat{r}) J_1\left(\frac{\alpha_n \hat{\beta}}{\Upsilon}\right)$$

Equation 2-39

Using Equation 2-38 to eliminate B_n in Equation 2-37 and using the notation in Equation 2-39, we have

$$\hat{u} = \sum_{n=1}^{\infty} [C_n \phi_0(\alpha_n \hat{r})]\, e^{-\alpha_n^2 \widehat{\beta^2} \hat{s}}$$

Equation 2-40

It follows from Equation 2-40 and Equation 2-35, that $\phi_0(\alpha_n \hat{r})$ are eigenfunctions that satisfy

$$\begin{Bmatrix} (\hat{r}\phi_0')' = -\alpha^2 \hat{r} \phi_0 & \hat{r} \in \left[\hat{\beta}, \frac{\hat{\beta}}{\Upsilon}\right] \\ \phi_0' - \phi_0 = 0 & \hat{r} = \hat{\beta} \\ \phi_0' = 0 & \hat{r} = \hat{\beta}/\gamma \end{Bmatrix}$$

Equation 2-41

Applying the boundary condition at $\Gamma_2(\hat{r} = \hat{\beta})$ given in Equation 2-41 with Equation 2-39, we obtain the equation for the eigenvalues α_n as roots of,

$$\alpha_n J_1(\alpha_n\hat{\beta})Y_1\left(\frac{\alpha_n\hat{\beta}}{\Upsilon}\right) - \alpha_n Y_1(\alpha_n\hat{\beta})J_1\left(\frac{\alpha_n\hat{\beta}}{\Upsilon}\right) = J_0(\alpha_n\hat{\beta})Y_1\left(\frac{\alpha_n\hat{\beta}}{\Upsilon}\right) - Y_0(\alpha_n\hat{\beta})J_1\left(\frac{\alpha_n\hat{\beta}}{\Upsilon}\right) \quad \textbf{Equation 2-42}$$

Applying the initial condition $\hat{u} = 1$ at $t = 0$ to the solution Equation 2-40

$$\sum_{n=1}^{\infty} C_n\phi_0(\alpha_n\hat{r}) = 1 \quad \textbf{Equation 2-43}$$

Therefore, from Equation 2-43

$$\sum_{n=1}^{\infty}\int_{\widehat{\beta}}^{\widehat{\beta/\gamma}} C_n\phi_0(\alpha_n\hat{r})\phi_0(\alpha_m\hat{r})\hat{r}d\hat{r} = \int_{\widehat{\beta}}^{\widehat{\beta/\gamma}} \phi_0(\alpha_m\hat{r})\hat{r}d\hat{r}, \quad m = 1,2,3 \ldots \quad \textbf{Equation 2-44}$$

The eigenfunctions $\phi_0(\alpha_n\hat{r})$ are linear combinations of Bessel functions $J_0(\alpha_n\hat{r})$ and $Y_0(\alpha_n\hat{r})$ and are orthogonal, so that, from Equation 2-44,

$$C_n = \int_{\hat{\beta}}^{\widehat{\beta/\gamma}} \phi_0(\alpha_n \hat{r})\hat{r}d\hat{r} \Big/ \int_{\hat{\beta}}^{\widehat{\beta/\gamma}} \phi_0^2(\alpha_n \hat{r})\hat{r}d\hat{r} \qquad \textbf{Equation 2-45}$$

Making use of Equation 2-41, the following simplifications follow for the integral in Equation 2-45

$$\int_{\hat{\beta}}^{\widehat{\beta/\gamma}} \phi_0(\alpha_n \hat{r})\hat{r}d\hat{r} = -\frac{1}{\alpha_n^2}\int_{\hat{\beta}}^{\frac{\hat{\beta}}{\gamma}} (\hat{r}\phi_0')'d\hat{r} \qquad \textbf{Equation 2-46}$$

$$= -\frac{1}{\alpha_n^2}\left[\frac{\hat{\beta}}{\gamma}\phi_0'\left(\frac{\alpha_n\hat{\beta}}{\Upsilon}\right) - \hat{\beta}\phi_0'(\alpha_n\hat{\beta})\right] = \frac{\hat{\beta}}{\alpha_n^2}\phi_0(\alpha_n\hat{\beta})$$

And, after multiplying Equation 2-41 by the quantity $2r\phi'$, rearranging terms and integrating over the domain, we obtain,

$$\int_{\hat{\beta}}^{\widehat{\beta/\gamma}} \phi_0^2(\alpha_n \hat{r})\hat{r}d\hat{r} = \left[\frac{\hat{r}^2}{2\alpha_n^2}\left(\left(\phi_0'(\alpha_n\hat{r})\right)^2 + \alpha_n^2\phi_0^2(\alpha_n\hat{r})\right)\right]_{\hat{\beta}}^{\hat{\beta}/\gamma} = \qquad \textbf{Equation 2-47}$$

$$\frac{\hat{\beta}}{2}\left[\frac{1}{\gamma^2}\phi_0^2\left(\frac{\alpha_n\hat{\beta}}{\Upsilon}\right) - \phi_0^2(\alpha_n\hat{\beta})(1 + 1/\alpha_n^2)\right]$$

Using the last two results with Equation 2-45, it follows that the solution for $\hat{u}$ in the outer domain Ω_2 is

$$\hat{u} = \sum_{n=1}^{\infty} C_n \phi_0(\alpha_n \hat{r}) e^{-\alpha_n^2 \widehat{\beta^2} \hat{s}}$$ **Equation 2-48**

With

$$C_n = \frac{2\phi_0(\alpha_n \hat{\beta})}{\hat{\beta}\left[\frac{\alpha_n^2 \phi_0^2\left(\frac{\alpha_n \hat{\beta}}{\Upsilon}\right)}{\gamma^2} - (1+\alpha_n^2)\phi_0^2(\alpha_n \hat{\beta})\right]}$$ **Equation 2-49**

where it should be recalled that α_n can be determined through Equation 2-42 and $\phi_n(\alpha_n \hat{r})$ is defined in Equation 2-39

Using this result, the mass loss in the outer domain can be obtained by using equations Equation 2-12 and Equation 2-48, applied at Γ_2,

$$\Delta \hat{m} = 2\pi R_2 l \int_0^s h(c - c_s) dt$$ **Equation 2-50**

$$\Delta \hat{m} = 2\pi \frac{R_2^2 l c_s}{\hat{\beta}} \sum_{n=1}^{\infty} \left[\frac{C_n}{\alpha_n^2} \phi_0(\alpha_n \hat{\beta})(1 - e^{-\alpha_n^2 \widehat{\beta^2} \hat{s}}) \right]$$ **Equation 2-51**

2.2.9 Determination of Degradation Constants

Mass loss was theoretically calculated through the above boundary value problem using two degradation constants. The experimental condition required change of degradation media every two days which changed the solute concentration. This process was modelled by repeatedly solving the dimensional form of equation Equation 2-51 at each two-day time point, after which the solute concentration in the solution was returned to zero. For this analysis, we let $c_s = 0.25gl^{-1}$ [120] as the degradation products of PGS are sebacic acid and glycerol, with glycerol being miscible in the media. D and h are obtained by fitting dimensional form of equation Equation 2-51 to only the first experimental mass loss time point. These values of h and D are then used to predict mass loss at all other subsequent times. These predicted values were validated against the experimentally observed mass loss at each time point.

2.3 Results

2.3.1 Baseline Graft Evaluation

The fabricated grafts (n = 20) had an average outer diameter of 1.51 ± 0.02 mm, inner diameter of 0.85 ± 0.13mm and length of 9.62 ± 0.36 mm. Porosity of 72.76 ± 1.89% and pore size of 25–32 mm with 99.99% interconnectivity of pores were observed. MicroCT analysis was conducted to assess heterogeneity within samples before exposing them to enzymatic degradation. Equation 2-7a shows the variation in porosity along the length and Equation 2-7b shows the pore size of a representative sample. All samples showed consistent porosity of 71.84 ± 1.76 across their

length and 75% of these pores lie within 16–35 mm for all samples, as expected from porogen size.

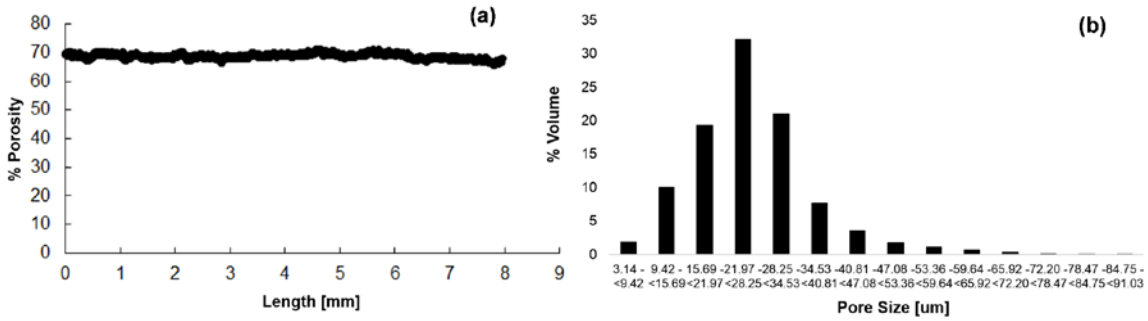

Figure 9: Baseline graft porosity and pore size.

Variation in (a) porosity and (b) pore size of PGS sample at time *s* = 0. No significant axial variation in porosity was observed.

2.3.2 Erosion of Tissue Engineered Vascular Grafts

Changes in mass, volume fraction and bulk morphology were assessed as a function of time exposed to enzymatic degradation. These are important parameters that indicate the extent of erosion of these grafts. They are also valuable in understanding and modelling the mechanism of erosion in these porous TEVGs.

2.3.2.1 Survival Function: Best-fit to Experimental Mass Loss

Rate of mass loss is of fundamental importance for understanding and modelling degradation of these grafts. Equation 2-8 shows the *in vitro* rate of mass loss of these porous grafts

when exposed to enzymatic degradation. In the constrained mixture model, mass loss of the degrading TEVGs is captured by the survival function $Q^{PGS}(s)$ which is defined as:

$$Q^{PGS}(s) = 1 - \frac{\Delta m(s)}{100} \qquad \textbf{Equation 2-52}$$

where $\Delta m(s)$ is defined in Equation 2-2. In order to obtain the functional form of the survival function for these porous grafts, we performed nonlinear regression on mass loss as a function of time exposed to enzymatic degradation *in vitro*. Figure 10 shows the experimental mass loss with the best-fit exponential form of the survival function. Rate constant Q_2 specifies the rate of degradation. The form of this survival function is generally assumed to be sigmoidal [96] due to lack of experimental data in the literature. However, it is clear from our experimental data that an exponential function is better suited to model mass loss (R^2 value of 0.99), than the sigmoidal function (R^2 =0.03), Table 1.

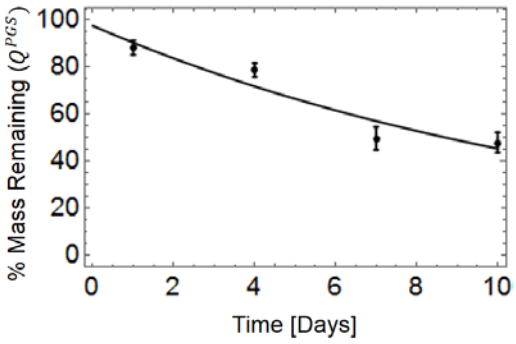

Figure 10: Mass remaining (survival function) as a function of time exposed to enzymatic degradation. Data are presented as mean±standard deviation (n=4, each time point)

Table 1: Functional forms for survival function with best-fit values and goodness of fit

Functional Form	Equation	Parameter Values	R^2
Exponential	$Q^{PGS}(s) = Q_1 e^{-Q_2 s}$	$Q_1 = 97.74, Q_2 = 0.07d^{-1}$	0.99
Linear	$Q^{PGS}(s) = \dot{m}s + m(0)$	$\dot{m} = -5.02d^{-1}, m(0) = 93.8$	0.88
Sigmoidal	$Q^{PGS}(s) = \left[1 + e^{k_p(s-offset)}\right]^{-1}$	$k_p = 1.42d^{-1}, offset = 27d$	0.03

2.3.2.2 Mass Loss is Surface Erosion Driven

The mass loss of TEVGs can be due to a range of mechanisms, from pure surface erosion to pure volume erosion. There was a 20% reduction in outer diameter at day 10 with a negligible change in the inner diameter, Figure 11. The small change in inner radius can be attributed to saturation of the inner domain and will be explained in detail in later sections. Also, the apparent density of the grafts (as normalized with the original apparent density to account for between sample variations) also remains fairly constant as seen in Figure 12 over the duration of degradation. Therefore, mass loss is nearly completely due to erosion of the outer diameter, thus showing that these TEVGs primarily undergo surface erosion, rather than a combination of bulk and surface erosion.

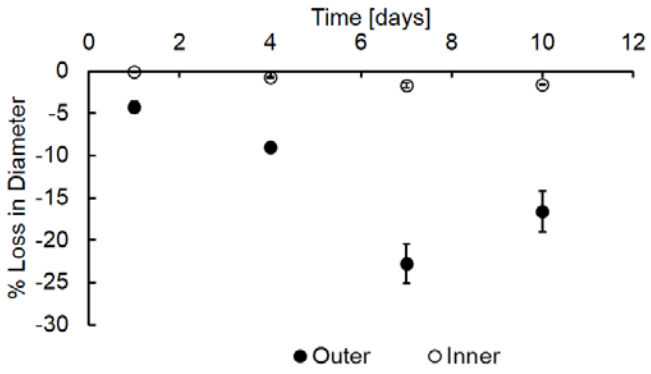

Figure 11: Loss of inner and outer diameter as a function of time exposed to enzymatic degradation

Surface erosion is characterized by reduction in diameter of sample. This plot shows the reduction in inner and outer diameters as a function of time exposed to enzymatic degradation. Data are presented as mean±s.d. (n = 4 each time point).

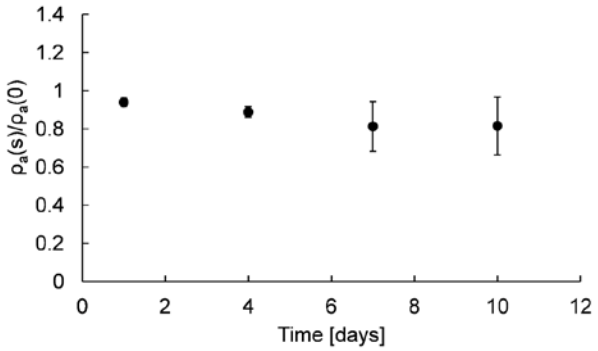

Figure 12: Time course of apparent density normalized to initial density of each sample exposed to enzymatic degradation.

A value of 1 represents no change in apparent density of the sample, consistent with minimal volume erosion. Data are presented as mean±s.d. (n = 4 each time point).

2.3.3 Mathematical Modeling of Tissue-Engineered Vascular Graft Erosion

A simple mass balance shows that saturation of the inner domain causes at most a 0.044% reduction in inner radius of the grafts as follows:

$$\begin{Bmatrix} c_s \pi R_1^2 = \pi(R_1(s)^2 - R_1(0)^2)\rho_a, \\ \frac{\Delta R_1}{R_1(0)} = \frac{c_s}{2\rho_a} \times 100 \\ \frac{\Delta R_1}{R_1(0)} = 0.044\% \end{Bmatrix}$$ **Equation 2-53**

This is consistent with the result that no discernible change in inner radius is observed. As the inner core saturates, the observed surface erosion can be attributed to reduction in outer diameter. Based on the observation that TEVG erosion was primarily driven by a concentration gradient as seen by the negligible loss in inner diameter, we developed a concentration gradient-driven mass diffusion equation to model this mass loss process. Using Equation 2-51 and the approach elucidated earlier for the outer domain, we determined that the best-fit values of h and D are $1.053 \times 10^{-6}\ mm/s$ and $2.123 \times 10^{-6}\ \frac{mm^2}{s}$ respectively. Using these values obtained by fitting to the first experimental time point, and the roots of Equation 2-42 outlined in Table 2, we can predict mass loss at the subsequent times.

Table 2: Roots of equation 2.25

n	1	2	3	4	5	6	7
Roots	0.2919	1.7824	3.2043	4.6504	6.1131	7.5859	9.0649

Figure 13 shows the experimental and predicted mass loss from the mechanistic model in the outer domain. The first experimental time point was used to fit h, D required in Equation 2-51. As can be seen, the predictions at later time points closely follow the experimentally observed mass loss which suggests that the analytical approach accurately models TEVG mass loss.

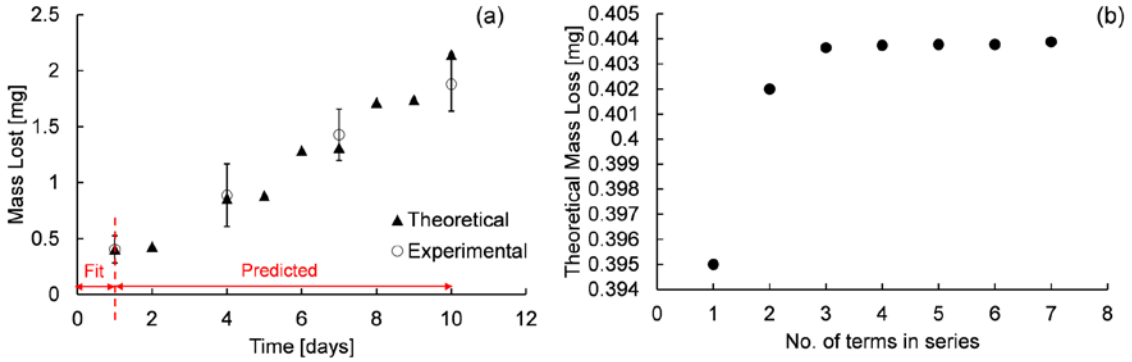

Figure 13: Mathematical modeling of graft erosion.

(a) Graph of experimental and theoretically predicted mass loss. Predicted mass loss is obtained by fitting dimensional form of equation (2.28) to day 1 experimental data. (b) The analytical solution is an infinite series; at least three terms of equation (2.28) are required to achieve a good fit.

Observing the spatial distribution of concentration at the experimental time points of 1 and 2 days show that saturation is observed at day 1 and the saturation front increases over time (Figure 14). As noted in section Material and methods, after 2 days, the degradation medium was replaced in the beaker to maintain enzyme activity and prevent complete saturation. Through the use of three terms in the series Equation 2-51, this analytical approach models the experimental phenomena and re-establishes the concentration gradient which can be seen by the increase in rate of mass loss after 2 days following a period of reduction in rate of mass loss, Figure 13.This method therefore reliably mimics the experimental conditions.

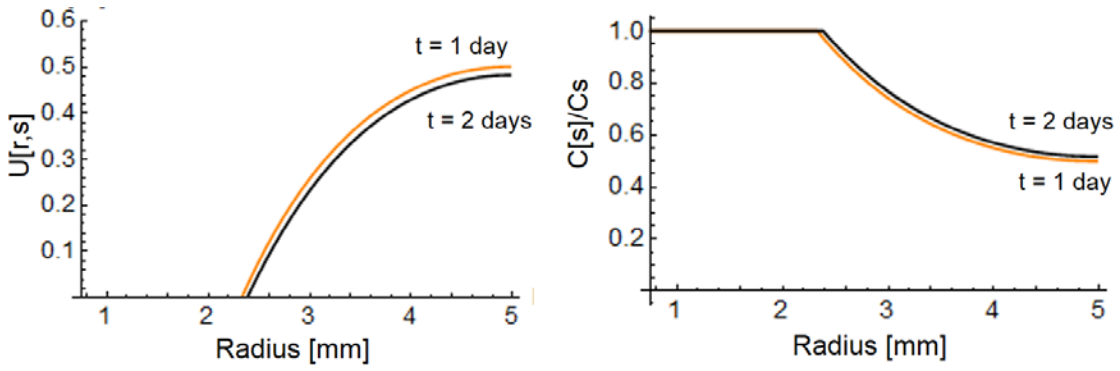

Figure 14: Predicted evolution of concentration with time.

Graph of (a) non-dimensional concentration $\hat{u}(r,s)$ and (b) concentration c normalized to c_s as a function of radius $R_2 \leq r \leq R_3$ at 1 day (orange) and 2 days (black). Almost 50% radial saturation was observed at day 1 and increased slightly with time.

2.3.4 Degradation of Tissue-Engineered Vascular Grafts

2.3.4.1 Change in Mechanical Properties

Change in mechanical properties due to degradation is a crucial component of *in situ* host-remodeling. Degradation of polymer alters mechanical properties of the grafts, which causes a transfer of load from the degrading graft to the surrounding cells under *in vivo* conditions. In order to capture this phenomenon accurately in our G&R tool, we need to obtain the functional form and rate constants associated with the evolving material properties. Figure 15 shows the stress–stretch data fitted to a neo-Hookean model (Equation 2-8) at each degradation time point with an $R^2 > 0.97$ for each sample.

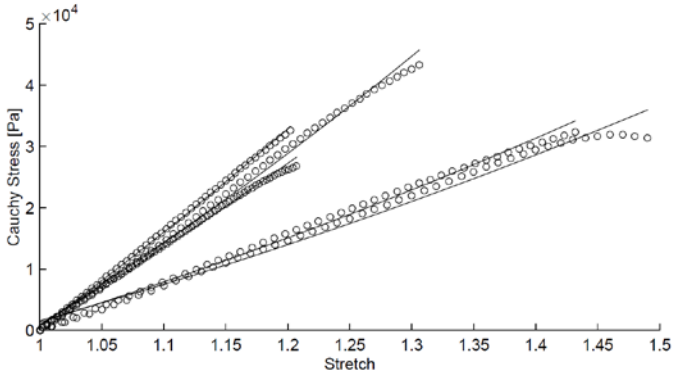

Figure 15: Cauchy stress–stretch curves (circles) as a function of time exposed to enzymatic degradation. Fit for $\boldsymbol{\beta}(\boldsymbol{s})$ in the neo-Hookean model (solid lines) (equation (2.7)).

Section 2.3.2.2 shows that the TEVG mass loss is primarily surface driven; however, the mechanical properties are not. Specifically, the mechanical properties of the grafts do not scale with density. We introduce an explicit time dependence of mechanical properties to the existing G&R models by introducing a scalar damage function $\zeta(s)$such that $0 \leq \zeta(s) \leq 1$. This damage

function ‘softens’ the material over degradation time s. A value of one for the damage function signifies zero damage and a value of zero represents complete loss of mechanical properties. Hence, the mechanical properties of the degrading graft can then be represented as

$$W^{PGS}(s) = \frac{\beta(s)}{2}[I_1 - 3] = \zeta(s)\left[\frac{\beta_0^{PGS}}{2}(I_1 - 3)\right] \quad \textbf{Equation 2-54}$$

where $\beta_0^{PGS} = 34.43\ kPa$

The damage function is obtained by a nonlinear regression fit of $\zeta(s)$ normalized to the shear modulus at $s = 0$ (Figure 16). It can be seen from Table 3 that an exponential fit to the normalized $\zeta(s)$ values yielded an R^2 value of 0.96. In summary, the experimental data provided by the *in vitro* enzymatic degradation study conducted on these porous TEVGs enable the formulation of data-driven functional forms of the survival function and changing material properties.

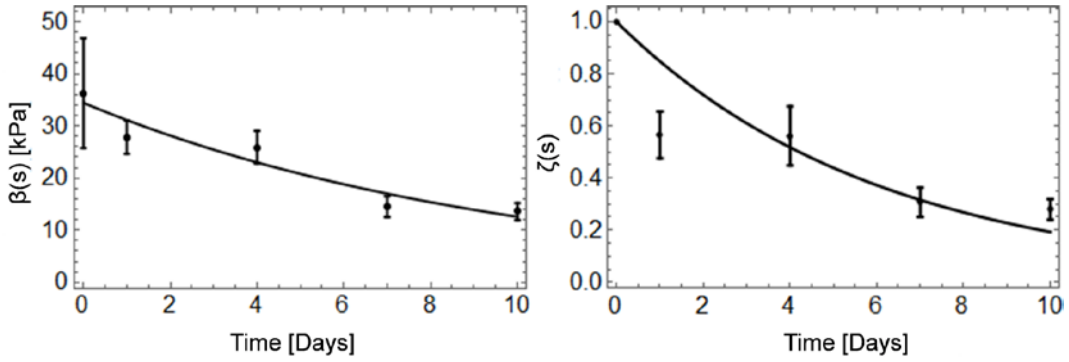

Figure 16: Mechanical parameters.

(a) Neo-Hookean parameter fit as a function of time. (b) $\zeta(s)$ fit as a function of time, to model damage-like phenomena in changing mech- anical properties of grafts exposed to enzymatic degradation. Data are shown as mean±s.d. (n = 4 each time point).

Recall the strain energy function for the entire mixture

$$W(s) = \sum_{\alpha=1}^{n} W^{\alpha}(s) \qquad \textbf{Equation 2-55}$$

$$= \sum_{\alpha=1}^{n} \frac{\rho^{\alpha}(0)}{\rho(s)} Q^{\alpha}(s) \bar{W}^{\alpha}\left(\boldsymbol{C}^{\alpha}_{n(0)}(s)\right)$$

$$+ \int_{0}^{s} \frac{m^{\alpha}(\tau)}{\rho(s)} q^{\alpha}(s-\tau) \bar{W}^{\alpha}\left(\boldsymbol{C}^{\alpha}_{n(0)}(s)\right) d\tau$$

For the TEVG component in question

$$\alpha = PGS \quad m^{PGS}(\tau) = 0$$

since PGS is only degrading and is not deposited over time. Therefore,

$$W(s) = W^{PGS}(s) = \frac{\rho^{PGS}(0)}{\rho(s)} Q^{PGS}(s) \bar{W}^{\alpha}\left(\boldsymbol{C}^{\alpha}_{n(0)}(s)\right) \qquad \textbf{Equation 2-56}$$

Substituting the form of the survival function and evolving material properties into Equation 2-56 gives

$$W^{PGS}(s) = \frac{\rho^{PGS}(0)}{\rho(s)} Q_1 e^{Q_2 s} \zeta(s) \left[\frac{\beta_0^{PGS}}{2}(I_1 - 3)\right]$$

where values of Q_1 and Q_2 are given in Table 1.

Table 3: Functional forms for time-evolving neo-Hookean parameter with best fit values and goodness of fit.

Functional Form	Equation	Parameter Values	R^2
Exponential	$\zeta(s) = \zeta_1 e^{-\zeta_2 s}$	$\zeta_1 = 1, \zeta_2 = 0.164$	0.96
Linear	$\zeta(s) = \zeta s \dot{+} \zeta_0$	$\zeta = -0.0\dot{8}6, \zeta_0 = 1$	0.89

2.4 Discussion

Successful G&R elicited by porous acellular TEVGs rests on the effective interplay between PGS degradation, erosion and ECM deposition. Computational G&R tools have proven to be sources of predictive capabilities that guide rational design of TEVGs. However, this predictive capability depends on the knowledge of certain properties that can be prescribed through experimental data or mechanistic models. Two such material properties that are the focus of this study are degradation and erosion rates of grafts. It has been postulated that the main mechanism of ECM deposition is through the stress driven mechanobiological response of ECM-producing cells which requires accurate modeling of load transfer from the graft. Since graft mechanics cannot directly be studied *in vivo* due to the growth of neotissue upon graft degradation, we conducted an *in vitro* analysis of the effect of enzymatic degradation on graft properties.

We took two approaches to modeling the mass loss due to erosion of these TEVGs based on experimental data. Firstly, we obtained functional forms and rate constants of the survival function by providing a best-fit to mass loss over time. While most previous models assume a sigmoidal mass loss [95], we observe that an exponential model provides a better fit in this context. Another significant finding was that despite the porous nature of these grafts, most mass loss occurs at the surface of these TEVGs. This was evidenced by the little change in density, pore size and inner diameter of the grafts over degradation time. Based on these results, we formulated a mathematical model of graft erosion and validated the proposed theoretical model with experimental data. The boundary value problem formulated herein, enables the prediction of mass loss through two degradation constants h and D. Furthermore, differences between the *in vivo* and *in vitro* setting can be included in this framework by changing the rate constants and boundary conditions while using the same functional forms of the equations. For example, the inner

boundary condition can be changed to a convection boundary condition to account for blood flow in the lumen *in vivo*. Cell infiltration *in vivo* is expected to alter the rate constants for degradation and erosion and not the functional forms themselves. These rate constants can be tuned for *in vivo* applications based on measurements of neoartery formation. For example, the parameters h and D can be tuned for *in vivo* mass loss through a parametric evaluation guided by observations from experiments. The rate of degradation could additionally be affected *in vivo* by strains experienced by the graft. However, due to the nature of graft implantation, there is no axial strain at implantation and the presence of the PCL sheath restricts circumferential strain to be less than 4%. The influence of larger strains on degradation rates can be evaluated, if needed, in future studies.

Another important aspect of the in-host remodeling process is the changing load bearing contribution of the degrading TEVG which guides cellular response over time. We observed that while mass loss is largely surface driven, mechanical properties are not. Herein, we provided a constitutive relationship for the `weakening' of material properties due to degradation over time by introducing a damage function. This key finding ensures that mechanical properties are extracted from the dependence on mass loss alone and are explicitly modeled as functions of degradation time; an improvement to existing G&R models.

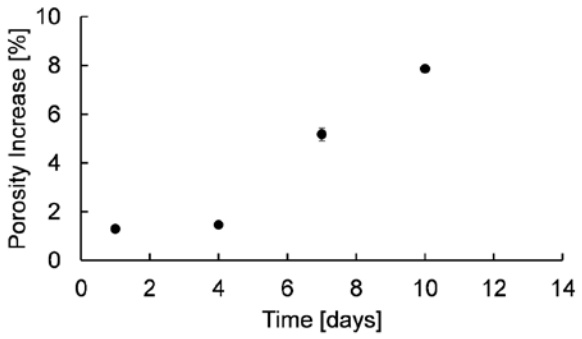

Figure 17: Per cent change in porosity as a function of time exposed to enzymatic degradation. Very small increase in porosity suggests little volumetric degradation. Data are shown as mean±s.d. (n = 4 each time point).

It must be noted that while erosion was primarily observed on the outer surface of the grafts, we did observe some minor volume degradation at the pores. Figure 17 shows that there was an 8% increase in porosity at day 10 which corresponds to only a 3% mass loss. We also modeled mechanical properties of the graft using an assumption of isochoric deformation for an incompressible material. This assumption is often made in models of the artery wall and vascular grafts [68], [121], and future studies can explore the importance of modeling the graft using a two-parameter coupled compressible Neo-Hooken model [122].

These findings not only provide an understanding of the fundamental process of PGS degradation and erosion, but also provide broader insights into the *in vivo* remodeling process. The finding that graft surface erosion is dominated by an evolving concentration gradient implies that the pores in these grafts saturate which is consistent with data found here on mass loss. This has implications in the inflammatory response of cells; a crucial first response that guides further remodeling [123]. Furthermore, since pore size is one of the major determinants of macrophage polarization [124] it can be conjectured that these cells sense the fabricated pore size and that their

behavior can be modulated as desired through this particular graft parameter. It must also be mentioned that while this study enabled us to understand the underlying mechanism of graft degradation, the effect of volume degradation can be enhanced *in vivo* by the presence of cells, especially macrophages. This phenomenon is currently under investigation in our group and is being included in the G&R framework to improve its predictive capability for use in rational design of TEVGs.

2.5 Conclusion

In summary, this work provides much-needed experimental data required to guide computational G&R modelling in the field. It is the first study that takes a physics-based approach to informing G&R computational tools with physical mechanisms of degradation and erosion of these grafts using a controlled environment. It also serves as an essential complement to our ongoing *in vivo* study of neoartery formation using the PGS core studied here as replacement vessels in the carotid artery of rats [52]. These results are of value not only for the use of G&R frameworks as predictive tools but also for understanding the fundamental mechanisms responsible for successful in-host remodeling of TEVGs as translational medical devices.

Authors' Contributions

A.M.R conceived, led the project and oversaw writing of the manuscript. P.S.G performed the design and analysis of *in vitro* experiments, computational analysis and took a major role in writing the manuscript. A.M.R and P.S.G carried out the theoretical analysis of graft erosion and

interpretation of results. K.L fabricated the grafts required for the experiments. B.N.P performed analysis of the enzyme concentration required to achieve an appropriate rate of graft degradation. Y.W advised with the preliminary design of the experimental study.

3.0 Determine the Evolution of Cellular Content, ECM, and Mechanical Properties during Neoartery Formation in Young Rats

The work in this chapter was largely reproduced from the following manuscript:

Lee, Kee-Won, Piyusha S. Gade, Liwei Dong, Zhaoxiang Zhang, Ali Mubin Aral, Jin Gao, Xiaochu Ding et al. "A biodegradable synthetic graft for small arteries matches the performance of autologous vein in rat carotid arteries." *Biomaterials* 181 (2018): 67-80.

3.1 Introduction

In our prior work, we successfully elicited G&R in a young healthy rat abdominal aorta model through the implantation of a porous, synthetic, bilayered graft [31], [98]. In order to translate this success to small diameter and mature animal models, there is a need to understand the mechanobiology of the remodeling process in these young rats. There is also a critical need to understand the remodeling process in the context of initial graft properties. Correlation of quantifiable mechanics and biological parameters to initial graft properties like degradation rate and mechanical properties can aid iTEVG design. The objective of this aim to a) develop a mechanistic understanding of the remodeling process in young rats and, b) compare the effects of remodeling to the surgical gold standard – vein graft.

We set out to design an iTEVG that could withstand arterial pressure immediately upon implantation and leverage the natural regenerative capabilities of the host to transform the structure into an arterial conduit *in vivo*, bypassing cell harvesting and culture completely. We use a

relatively fast-degrading and highly porous tube as the major component [31] to enable rapid cell infiltration and host remodeling. The polymer, poly(glycerol sebacate) (PGS), is elastomeric and promotes elastin synthesis [102]. The tubular core is surrounded by a slow-degrading and thin sheath made of poly(caprolactone) (PCL) to increase suturability and avoid graft dilation. Multi-layered and bi-layered designs have been previously reported in tissue engineered vascular structures made of collagen gels [125], poly(ester urethane)urea [126], and PCL micro and nanofibers [127], [128]. The composition of our bi-layered graft is different in that > 90% of the graft is made of PGS. This design induces the host to replace the acellular scaffold with a structurally sound vascular conduit in a rat abdominal aorta at 3 months [31] and further matched the elastin content while maintaining good patency in a 1-year follow-up [98]. Recent studies using the fast-degrading material support our approach, demonstrating cell infiltration and vascular remodeling and inhibited calcification in mouse and rat aorta [129], [130]. However, the aorta is a large-diameter artery with a high blood flow and its hemodynamics and mechanical properties are quite different from small-diameter arteries. The small diameter increases the risk of early graft stenosis and thrombosis [131], [132] and the low blood flow affects long-term patency of the grafts [133]. Thus, we examined whether our design would meet the more stringent requirement of grafting rat carotid arteries. Furthermore, we compared the performance with the autologous graft from external jugular veins because the vein is the largest source for small artery grafting clinically.

Previous studies of degradable synthetic grafts in small arteries have used the common carotid artery because it is easily accessible and long enough to implant and monitor the graft [134]. Compared to the aorta, the common carotid has a smaller diameter, lower blood flow and is more muscular and stiffer. Acellular grafts made of PCL and chitosan enhances cell infiltration and arterial remodeling in carotid arteries and supports the feasibility of using iTEVGs in the

peripheral arterial circulation [135]. However, the presence of significant graft materials at the terminal time point makes it difficult to predict outcome upon complete degradation of the graft material. We chose 3 months as a terminal time point for this study because very little graft material is left and the remodeled conduit consists mostly of host tissues. The key data are patency, morphological change, inflammatory responses, cellular organizations, ECM production, and mechanical properties.

3.2 Materials and Methods

3.2.1 Graft Fabrication and Characterization

3.2.1.1 Graft Fabrication

The PGS inner core was fabricated as described previously in Section 2.2.1 . To fabricate the outer sheath, PCL (M_n = 80,000 Da) (Sigma-Aldrich, St. Louis, MO) was dissolved in 2,2,2-trifluoroethanol (ThermoFisher Scientific, Waltham, MA) at 14% w/vol and electrospun onto the rotating cured PGS-salt tubes size = 22 gauge, distance between the needle and aluminum col- using the following conditions: applied voltage = ± 12 kV, needle lector = 30 cm, distance between the mandrel and aluminium collector = 10 cm, infusion rate = 29 ml/min, and mandrel rotating speed = 80 rpm. The thickness of PCL outer sheath was controlled in a targeted range of 20 - 25 µm by varying time and monitored using a high- speed laser micrometer (LS-7070M, Keyence Corp., Itasca, IL). After electrospinning, PGS-PCL-salt tubes were dried in a vacuum chamber for 24 h and residual salt was dissolved in a series of two 10mLwater baths (first bath for 24 h and

second bath for 48 h). Final grafts were lyophilized, sterilized with a gamma irradiation (dose = 25 kGy), and soaked into the heparin solution (100 U/mg) for 5 min before implantation.

3.2.1.2 Graft Characterization: Gel Permeation Chromatography (GPC)

The molecular weights of the electrospun PCL sheets before and after gamma irradiation were examined using Waters Ambient Temperature GPC equipped with Gramm column and tetrahydro- furan (THF) as stationary and mobile phases (Waters Corporation, Milford, MA). Three different locations of the PCL sheets and the gamma-irradiated PCL sheets were taken for GPC analysis. The samples were prepared in THF at 1.5 mg/mL and filtrated through 0.2 mm syringe filter before the test (n = 3). Polystyrene was used as the standard polymer to calibrate the molecular weight.

3.2.1.3 Differential Scanning Calorimetry (DSC)

The crystallinity of electrospun PCL was measured before and after gamma sterilization. Five-milligram portions (n = 3) were scanned in a Q1000 MDSC (TA Instruments, New Castle, DE) operating in unmodulated mode. Samples were heated at 10ºC/min from 25 ºC to100 ºC. Crystallinity (X_c) was calculated as:

$$X_c = \frac{\Delta H_f}{\Delta H_f^o} \qquad \textbf{Equation 3-1}$$

where, $\Delta \boldsymbol{H_f}$ is the measured heat of fusion and $\Delta \boldsymbol{H_f^o}$ is the heat of fusion of purely crystalline PCL, taken as 136 J/g.

3.2.1.4 Uniaxial Tensile Test

Electrospun PCL sheets before and after gamma sterilization were cut using the dog-bone cutting die (TestResources Inc., Shakopee, MN). The mechanical properties were measured according to the standard method (ASTM D412) using an electromechanical testing machine (Insight, MTS Systems, Eden Prairie, MN) equipped with a 5N load cell. Uniaxial tensile force was applied to dog-bone specimens (gauge length = 7 mm, and width of narrow section = 1 mm) for three samples with an average length of 28 mm, average width of 5 mm which were extended until failure at a rate of 5 mm/min while recording the force. Ultimate tensile stress, linear elastic modulus, and strain at complete failure were calculated from the stress-strain curves.

3.2.1.5 Scanning Electron Microscopy (SEM)

The morphology of the iTEVGs was examined using SEM. Grafts were cut into 2 mm segments transversely, mounted onto aluminum stubs, sputter-coated with gold, and observed with a field emission SEM (6330F, JEOL, Tokyo, Japan). Inner diameter, wall thickness and PCL sheath thicknesses of the graft were measured from cross-sectional SEM images using ImageJ software (National Institutes of Health (NIH), Bethesda, MD).

3.2.1.6 X-ray Micro-Computed Tomography

Porosity and pore size distribution of grafts were measured using X-ray micro-computed tomography (micro-CT) as described in Section 2.2.4 .

3.2.2 Graft Implantation

All procedures involving animals were approved by the Institutional Animal Care and Use Committee at the University of Pittsburgh following NIH guidelines for the care and use of laboratory animals. Male Sprague Dawley rats (8 to 9 weeks old; 225-250 g, $n = 50$, Charles River Laboratories, Wilmington, MA) were used in this study. Eight rats were used to characterize carotids and external jugular veins ($n = 4$ each) for cell and ECM content and dimensions. For graft implantation, 42 rats were randomly divided into two groups for implantation of iTEVGs and autologous vein grafts. The 21 rats in each group were randomly divided into three groups of 7 rats for each time point (day 14, 30, and 90). The time points were selected based on our previous study demonstrating near complete graft material degradation within 90 days. Rats were anesthetized with isoflurane inhalation (5% for induction, then 1-3% for maintenance), and their limbs were fixed in the supine position.

Experimental group: The midline of the neck was cut longitudinally. Blunt dissection created the operating space, exposing left sternocleidomastoid and sternohyoid. The left sternocleidomastoid was retracted to the lateral side, then the left common carotid artery was exposed, clamped, and transected it at 2 mm proximal to the bifurcation of internal and external carotid artery; a segment of 5 mm common carotid artery was removed as well. The graft (10-mm long) was interpositioned by end-to-end anastomosis using interrupted 10-0 polyamide monofilament sutures (AROSurgical, Newport Beach, CA).

Control group: To compare with iTEVGs, the autologous external jugular vein was used as a control. The skin incision was made in the same way as described above. The left external jugular vein was exposed, ligated all branches, and harvested as 10-mm long segment. The left common carotid artery of the same rat was exposed, clamped, and transected as mentioned above. The

external jugular vein was interpositioned by end-to-end anastomosis using running 10-0 polyamide monofilament sutures. No anticoagulation and antiplatelet treatments were administrated during and after implantation. The contralateral right common carotid artery was used as an age-matched healthy control. Both antibiotic (Baytril, 10 mg/kg) and analgesic (Buprenorphine, 0.1 mg/kg) medications were given until 72 h after implantation. To measure dimensions of native vessels, native common carotid arteries and external jugular veins (n = 4 each) were explanted, cut as 2-mm thickness, and viewed with a stereomicroscope (SMZ745T, Nikon Instruments Inc., Melville, NY). Both inner diameter and wall thickness were measured from cross-sectional images using the NIS-Elements software (Nikon).

3.2.3 Patency Monitoring

The blood flow was checked with a flow coupler monitor (GEM1020M, Synovis Micro, Birmingham, AL) at 5, 10, 15, and 30 min after removing clamps. A high-frequency ultrasound imaging system (Vevo2100, FUJIFILM Visualsonics, Toronto, Canada) was used to monitor the inner diameter and flow velocity of mid-grafts and contralateral native carotids at day 14, 30, 60 and 90 after implantation. Animals were anesthetized with 1-2% isoflurane via precision vaporizer and 1 L per minute gas flow and placed on a custom-built platform with a warming pad in a position. The hair on the neck area was removed with hair removal cream and ultrasound gel (AccuGel, Lynn Medical, Wixom, MI) was then applied to the skin. Transcutaneous ultrasound imaging was performed on the neck using a linear array transducer MS 550 centered at 40 MHz. B-mode, color Doppler mode, and PW mode images along the long axis and middle region of the graft and native carotids were measured through the cardiac cycle recorded from ECG leads and stored for offline analysis. Cine loop images were later analyzed using a high-frequency ultrasound

imaging system (Vevo2100) software for overall patency, inner diameter changes, and flow velocity at and around the graft. Both the inner diameter and flow velocity were obtained by averaging end-diastolic and end-systolic inner diameter and flow velocity measured from B-mode and PW mode images, respectively.

3.2.4 Histology and Immunofluorescence Staining

All explanted grafts and native carotids were rinsed with PBS, fixed in 10% formalin for 1 h at 4°C, and dehydrated in 30% sucrose solution at 4°C for 24 h. Tissue sections were embedded in optimal cutting temperature compound (Sakura Finetek, Torrance, CA), frozen at -80°C for 2 h, and cryosectioned to 8-µm thickness. Tissue slides were stained with H&E, Masson's trichrome, Verhoeff-van Gieson, and Alizarin red to examine cell presence and infiltration, collagen, elastin, calcium, respectively. All histological images were representative of three independent sections per group (n = 4) and captured with an inverted microscope (Eclipse Ti-E, Nikon). The luminal area and wall thickness of both grafts and native carotids were measured from H&E staining images with a high-power magnification (60×) using the NIS-Elements software (Nikon). Tissue sections (8-µm thick) were fixed with 4% paraformaldehyde for 1 h at 4°C and permeabilized with 0.2% Triton X-100 for 5 min at room temperature. Tissue sites on slides were blocked with 5% normal goat serum (NGS) (Sigma-Aldrich) for 24 h at 4°C, incubated with primary antibodies in 1% NGS for 45 min at 37°C, were rinsed twice with PBS, followed with the corresponding secondary antibodies in 1% NGS for 45 min at 37°C. Antibodies used are described in Table 4**.** Nuclei were counterstained with 4',6-diamidino-2-phenylindole (DAPI) (Life Technologies, Carlsbad, CA) at room temperature for 20 min. Tissue slides without primary antibodies were used as negative controls.

Table 4: Antibodies used.

Primary and secondary antibodies used for immunofluorescence staining and Western blotting.

Primary	Dilution	Company	Secondary	Dilution	Company
Immunofluorescence staining					
CD11b	1:100	Abcam	Alexa 647 α-mouse	1:400	Invitrogen
CCR2	1:50	ThermoScientific	Alexa 594 α-rabbit	1:400	
CD68	1:100	EMD Millipore	Alexa 488 α-mouse	1:400	
iNOS	1:100	Abcam	Alexa 594 α-rabbit	1:400	
CD206	1:100	Abcam	Alexa 594 α-rabbit	1:400	
vWF	1:200	Abcam	Alexa 594 α-rabbit	1:400	
αSMA	1:500	Sigma	FITC- conjugated		
calponin	1:100	Abcam	Alexa 647 α-mouse	1:400	Invitrogen
MHC11	1:100	Abcam	Alexa 594 α-rabbit	1:400	
Ki67	1:100	Abcam	Alexa 594 α-rabbit	1:400	
collagen I	1:100	Abcam	Alexa 594 α-rabbit	1:200	
collagen III	1:100	Abcam	Alexa 594 α-rabbit	1:200	
elastin	1:100	Santa Cruz Biotechnology	Alexa 488 α-mouse	1:400	
fibrillin-1	1:500	Dr. Dieter P. Reinhardt (from McGill University)	Alexa 594 α-rabbit	1:200	
Western blotting					
eNOS	1:200	Santa Cruz Biotechnology	HRP-conjugated rabbit IgG	1:1000	R&D systems
TM	1:1500	Abcam		1:100000	
VCAM-1	1:200	Santa Cruz Biotechnology		1:1000	
p-Akt (Ser473)	1:2000	Cell Signaling Technology		1:20000	
ICAM-1	1:200	Santa Cruz Biotechnology	HRP-conjugated mouse IgG	1:1000	
p-ERK1/2	1:1000	Santa Cruz Biotechnology		1:20000	
β-actin	1:50000	Sigma		1:2000	

3.2.5 Endothelial Cell Examination

The grafts and native carotids were explanted at day 90, cut longitudinally by using microscissors, and fixed with minute pins. For SEM, samples were fixed with 2.5% glutaraldehyde for 2 h at room temperature, washed with PBS, and dehydrated in graded series of ethanol. After the critical-point drying, samples were mounted onto aluminum stubs, sputter-coated with gold, and observed with a field emission SEM. For en face immunofluorescence staining, samples were fixed with 4% paraformaldehyde at 1 h and permeabilized with 0.2% Triton X-100 for 5 min at room temperature. Samples were blocked with 5% NGS for 24 h at 4°C, incubated with the mouse anti-CD31 (1:200, Abcam, Cambridge, MA) primary antibody, and then incubated with Alexa Fluor 594 goat anti-mouse IgG (1:400) secondary antibody. Immunofluorescence images were captured with the inverted microscope.

3.2.6 Western Blot Analysis

The grafts and native carotids were homogenized in cold RIPA buffer (Cell Signaling Technology, Danvers, MA) containing protease inhibitor cocktail. The homogenized tissues were centrifuged at 14,000×g for 10 min at 4°C and protein contents of the supernatants were measured by Pierce 660nm Protein Assay (ThermoFisher Scientific). Equal amounts (20 µg) of proteins were separated on 8% SDS/PAGE gels and transferred onto polyvinylidene fluoride membranes (ThermoFisher Scientific). Membranes were blocked with 5% bovine serum albumin (EMD Millipore, Burlington, MA) and incubated with primary antibodies at 4°C with shaking at 90 rpm overnight. After washing with Tris-buffered saline, membranes were probed with secondary antibodies at room temperature for 2 h. Antibodies used are described in Table 4**.** HRP-based

detection was performed using Pierce ECL Western Blotting Substrate (ThermoFisher Scientific, Waltham, MA). Membranes were stripped and reprobed, and blots were visualized by X-ray film exposure with the use of a quality X-ray processor (AX700LE, Alphatek, Salem, WI). The intensity of blots was quantified using ImageJ software (NIH) and normalized to that of β-actin.

3.2.7 Biochemical Assays

Collagen quantification. Collagen contents of grafts and native carotids were measured using the Sircol Insoluble Collagen Assay kit (Accurate Chemical & Scientific Corp., Westbury, NY). Tissue segments (3-mm long) were minced finely, weighed to obtain wet weight, and then digested with the Fragmentation Reagent at 65 °C for 2 h 30 min to convert the insoluble collagen to denatured soluble collagen. Collagen content in pooled supernatants was measured following the manufacturer's instructions and normalized to tissue wet weight (μg/mg).

Elastin quantification. Elastin contents of grafts and native carotids were measured using a Fastin Elastin Assay kit (Accurate Chemical & Scientific Corp.). Tissue segments (3-mm long) were minced finely, weighed to obtain wet weight, and then digested with 0.25M oxalic acid at 100 °C for 1 h three times to extract the mature insoluble elastin into the solution supernatant. Elastin content in pooled supernatants was measured following the manufacturer's instructions and normalized to tissue wet weight (μg/mg). A sample size of $n = 4$ was used for graft explants as well as native carotids. All samples were tested in triplicate during the same assay run. Bare iTEVGs were used as a negative control.

3.2.8 Mechanical Evaluation

Suture retention strength measurement. Suture retention strength of grafts and native vessels was measured using a uniaxial testing machine (Insight, MTS Systems, Eden Prairie, MN) equipped with a 5 N load cell according to ISO 7198. Both bare grafts and explanted external jugular veins and native carotids were cut longitudinally by microscissors to obtain rectangular samples (length = 10 mm, width = 4 mm). A single 9-0 Nylon suture (AROSurgical) was inserted through the 2 mm of the edge of each sample and tied to form a loop. The non-sutured end of each sample and the suture loop were secured to separate clamps in the testing machine and the suture was pulled at the rate of 50 mm/min with recording the force. Grafts were tested in the dry state, but native vessels were tested in the wet state using saline at room temperature. Suture retention strength was defined as the maximum force recorded before the suture was pulled through each sample. A sample size of $n = 5$ was chosen for grafts and native vessels.

Biaxial inflation test. Circumferential mechanical properties of the explanted grafts were measured using a custom-designed biaxial inflation testing device (Figure 18).

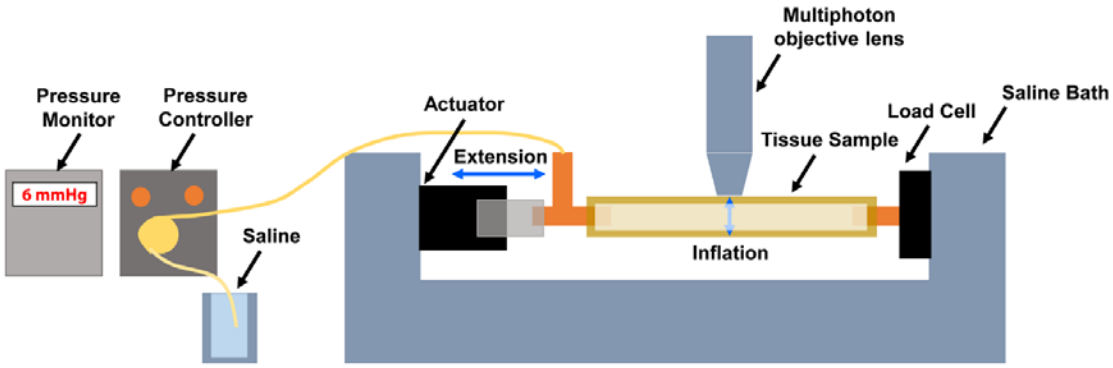

Figure 18: Schematic of biaxial – inflation mechanical testing device mounted under a multiphoton microscope.

The biaxial load is applied to the cannulated vessel using the actuator for applying axial stretch and pressure controller to pressurize the vessel. The multiphoton microscope objective lens is used to image the vessel from the outer wall down to the lumen at pressures of 0 and 120 mmHg.

Entire segments of grafts were mounted on the device by suturing them on cannulae and immersed in a water bath maintained at 37˚C. For local strain measurement, 350-400 μm microspheres (Zephyrtronics Inc., Pomona, CA) were lightly glued on the surface of grafts and tracked using a video camera (EO-5012C, Edmund Optics, Barrington, NJ) which captures images at 5 megapixels and 6 frames per second giving a final pixel size of 2.2 × 2.2 μm to obtain local axial strain measurement. Both axial and circumferential strains were calculated by analyzing these images using a custom code in MATLAB (R2014b, Mathworks, Natick, MA). The load was measured using a high precision load cell (MDB-5, Transducer Techniques, Temecula, CA) mounted on one end of the device and axial strain controlled using a computer-controlled actuator (ANT-25LA, Aerotech Inc., Pittsburgh, PA). Testing consisted of four preconditioning cycles during which the grafts were stretched to the *in vivo* axial strain level and cycled from 0-120 mmHg. Following

preconditioning, the grafts were tested at the following axial strain levels: 0, 10, 20%, *in vivo* strain and 40% axial strains by performing three inflation cycles from 0-120 mmHg at each strain level. High-strain modulus was calculated by fitting a line to the high strain region of the stress-stretch curve with an $R^2 > 0.98$. Compliance was calculated as

$$C\ (\%/100mmHg) = \frac{\Delta D}{D_0}/\Delta P \qquad \textbf{Equation 3-2}$$

where ΔD is the change in the inner diameter of the sample. The outer diameter is measured and thickness calculated using the isovolumetric deformation assumption. D_0 is the inner diameter at 70 mmHg and ΔP is 40 mmHg.

Burst pressure measurement. Explanted grafts and native carotids (10-mm long, n = 3 each) were cannulated and pressurized with PBS using 20 mL syringe at an infusion rate of 5 mL/min until failure. The luminal pressure was measured using a pressure transducer (PX309-100G5V, Omega Engineering Inc., Stamford, CT) with a range of 0-5000 mmHg. The data were recorded using a data acquisition system (PowerLab 8/30, ADInstruments, Colorado Springs, CO).

Collagen fiber imaging under biaxial loads. Explanted grafts and native carotids (10 mm long, n = 3 each) were cannulated and mounted on the biaxial inflating testing device (Figure 18). The device was then mounted directly under a multiphoton microscope (FV1000 MPE, Olympus, Center Valley, PA) objective lens to image the vessel under specified inflated pressures and axial load. In particular, specimens were axially stretched to their respective measured *in vivo* strains and imaged at two pressures; 0 mmHg (no load) and 120 mmHg (maximum physiologic load). An excitation wavelength of 800 nm and 1.12 NA 25× MPE water immersion objective was used for

all samples. SHG signal was collected using a 400 nm emission filter with $\pm$ 50 spectral bin. Planar images were taken starting from the outer wall, moving toward the lumen at 2 μm intervals. Collagen fiber recruitment was quantified through fiber tortuosity using the manual filament tracing function in Imaris (Bitplane, Switzerland). Fibers were manually traced on 2D images generated from projections of stacks of 2D imaging data taken across the thickness of the sample within a central region ($200 \times 100\ \mu m$). This region was chosen such that it was possible to image through the entire wall thickness of the sample. Straightness is defined as such that a straightness value of one represents fully straightened collagen fiber and less than one represents fibers with some curvature/undulation. Similarly, collagen fiber orientation was quantified using the manually traced fibers mentioned above. Angles of $\theta = 0°$ and $90°$ represent fibers aligned in the circumferential and longitudinal direction, respectively.

3.2.9 Statistical Analysis

All measured data were reported as a mean ± SD. A log-rank test (for survival curve) and an unpaired, two-tailed Student's *t*-test were performed to compare two groups. A one-way analysis of variance (ANOVA) with Tukey's multiple comparisons was performed to compare three groups. Statistical analysis was performed using Prism version 7 (GraphPad Software, La Jolla, CA) to assess the statistical significance at $P < 0.05$.

3.3 Results

3.3.1 Graft Characterization

The porous PGS core and the electrospun PCL sheath can be seen in the SEM image of a representative iTEVG, (Figure 19A) with an inner diameter of 768 ± 24 μm matching that of the vein graft, and significantly larger than that of the native common carotid artery (referred to as a carotid) (P = 0.0037) (Figure 19B).

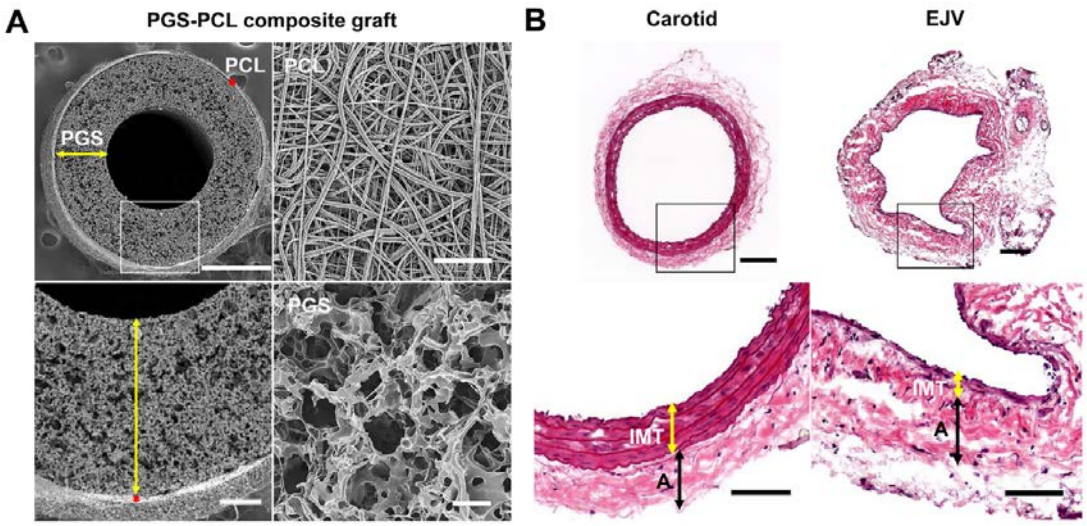

Figure 19: Morphology of the iTEVG and native vessels.

(A) Cross-sectional SEM images of the PGS-PCL bi-layered iTEVG. The bottom row represents the partial magnification of the box shown in the top row (left). Scale bars, 500 μm (top, left), 10 μm (top, right, and bottom, right), 100 μm (bottom, left). (B) Representative images for H&E staining in the middle region of the explanted native common carotid artery and external jugular vein (top row), and the magnification of the box region shown in the top row (bottom row). Carotid, common carotid artery. EJV, external jugular vein. IMT, intima-media thickness. A, adventitia. Scale bars, 200 μm (top row), 100 μm (bottom row).

The wall thickness was 391 ± 23 μm, significantly larger than that of the carotid ($P < 0.0001$) and vein ($P = 0.0074$). The PCL sheath thickness was 23.6 ± 14 μm. MicroCT revealed a total porosity of 72.8 ± 1.9 % and the average pore size of 26.6 ± 3.2 μm, corresponding well to a calculated porosity of 75% and salt particles with diameters of 25-32 μm. Pore interconnectivity was greater than 99 %.

3.3.2 Neoarteries Showed Comparable Patency to Vein Grafts

We interpositioned both the synthetic and vein grafts (n = 21 each) in the left common carotid artery of Sprague Dawley rats and kept the right carotid as a control (Figure 20A).Newly formed microvessels in the outer wall of both grafts suggested graft integration into the host. Ultrasonography at days 14, 30, 60, and 90 demonstrated open lumen and blood flow of the remodeled neoarteries similar to those of vein grafts and the native common carotid artery (referred to as a "carotid" in all figures) at day 90 (Figure 20B). The overall patency was 90.5% (19/21) for the neoarteries and 100% (21/21) for vein grafts, and there was no statistical difference (Figure 20C). One neoartery developed distal thrombosis at day 6 and one ruptured at day 9. The inner diameter of neoarteries and vein grafts was similar but significantly larger than that of native carotids at all time points ($P < 0.05$) (Figure 20D). At day 90, the inner diameter tended to be smaller in the vein graft (0.98 mm) than in the neoarteries (1.13 mm), although this difference is statistically insignificant. The flow velocity of both grafts was similar to that of native carotids (contralateral) except that the vein graft displayed a significantly lower flow at day 14 ($P = 0.013$) (Figure 20E). Thus, the neoarteries provided patency and stability equivalent to the vein at 3 months.

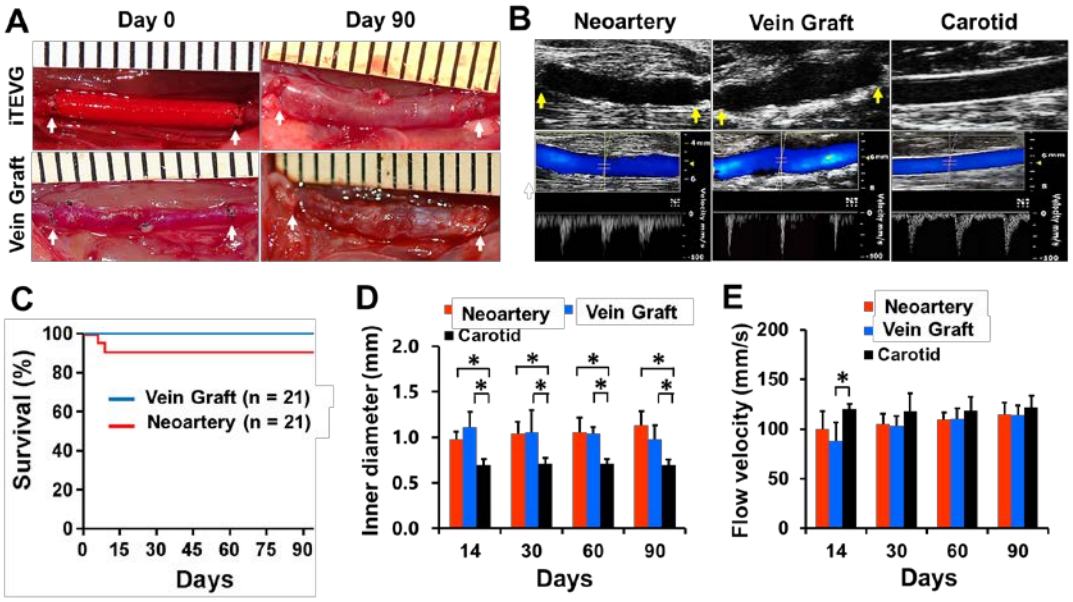

Figure 20 Graft implantation and patency.

(A) Gross appearance of the grafts at day 0 and 90 post-implantation. Arrows indicate suture lines. Day zero is the graft (row 1) and native vein (row 2) immediately after implantaion. (B) Representative ultrasound images of both grafts and native artery at 90 days of remodelin. B-mode (top row), color Doppler and pulse wave (PW) modes (bottom row). Arrows indicate suture lines.. (C) Survival plot showing the overall patency of the grafts. There is no statistical difference between the two remodeled grafts (P = 0.15). (D) The inner diameter measured by B-mode images. (E) Flow velocity measured in the middle region of the remodeled grafts and native carotids by PW mode images. Data in (D) and (E) are means ± standard deviation (SD) (n = 5). * represents P < 0.05.

3.3.3 Neoarteries Exhibit Outward Remodeling

We examined mid-sections of the remodeled grafts using histology and morphometry to assess cell infiltration, organization, and morphological changes. H&E staining showed a substantial and early cell infiltration in iTEVGs followed by cell and ECM organization (Figure 21A). A dense luminal cell layer and little remaining synthetic materials were visible in the wall at day 14. Cells distributed throughout the wall and were denser in the outer wall at day 30. Circumferentially-organized cells and ECM were observed in the wall with a distinct medial-like layer at day 90. The distribution of cells and ECM was asymmetric near the lumen but resembled native carotids. Conversely, vein grafts showed disrupted endothelium at the luminal surface, and cell infiltration from the outer wall at day 14, followed by increased cell density in the lumen at day 30. At day 90, dense and disorganized cells and ECM were observed within the inner wall.

Morphometrical analysis indicated that the luminal area increased gradually in neoarteries, but decreased in vein grafts with time (Figure 21B). At days 14 and 30, there was no significant difference in the luminal area between the neoarteries and vein grafts. However, the vein displayed a trend of decreasing luminal area and became significantly smaller than that of the neoarteries at day 90 ($P = 0.036$). Both grafts had significantly larger luminal area and wall thickness than native carotids at all time points ($P < 0.001$). However, the wall thickness increased in vein grafts but decreased in neoarteries so the latter approached the thickness of native carotids over time while the former thickened (Figure 21C).

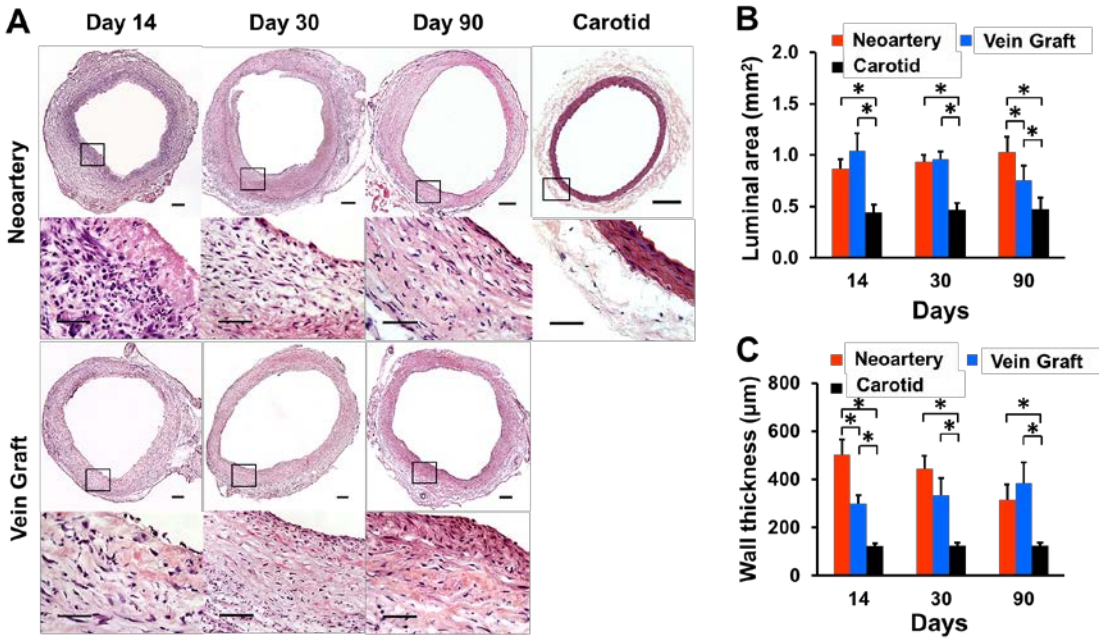

Figure 21 Histological and morphological assessments at middle regions.

(A) Representative images for H&E staining in the middle region of grafts and native carotids at each time point. The bottom row represents the magnification of the box region shown in the top row. Scale bars, 200 μm (top row) and 50 μm (bottom row). (B) Luminal area. (C) Wall thickness. Both (B) and (C) were measured by using H&E stained images from three independent sections per sample. Data in (B) and (C) are means ± SD (n = 4). * represents P < 0.05.

Furthermore, while the remodeled PGL-PCL grafts showed consistent luminal area and wall thickness throughout the graft at all time points, the remodeled vein graft showed distinct change in both the luminal area and wall thickness along the vessel at the early time point (Figure 22A). At day 14, the luminal area of the remodeled vein graft was minimal at the proximal region and became significantly larger toward the distal region (P = 0.008, middle and 0.0003, distal) than that of the remodeled PGS-PCL graft (P = 0.007, distal) (Figure 22B). In contrast, the wall thickness of the vein graft was maximal at the proximal region and became significantly smaller

toward the distal region ($P < 0.0001$, middle and distal) than that of the neoarteries ($P < 0.0001$, middle and distal) (Figure 22C). At day 90, remodeled vein grafts had a significantly smaller luminal area ($P < 0.0003$) and thicker walls ($P < 0.002$) in the anastomotic regions than neoarteries.

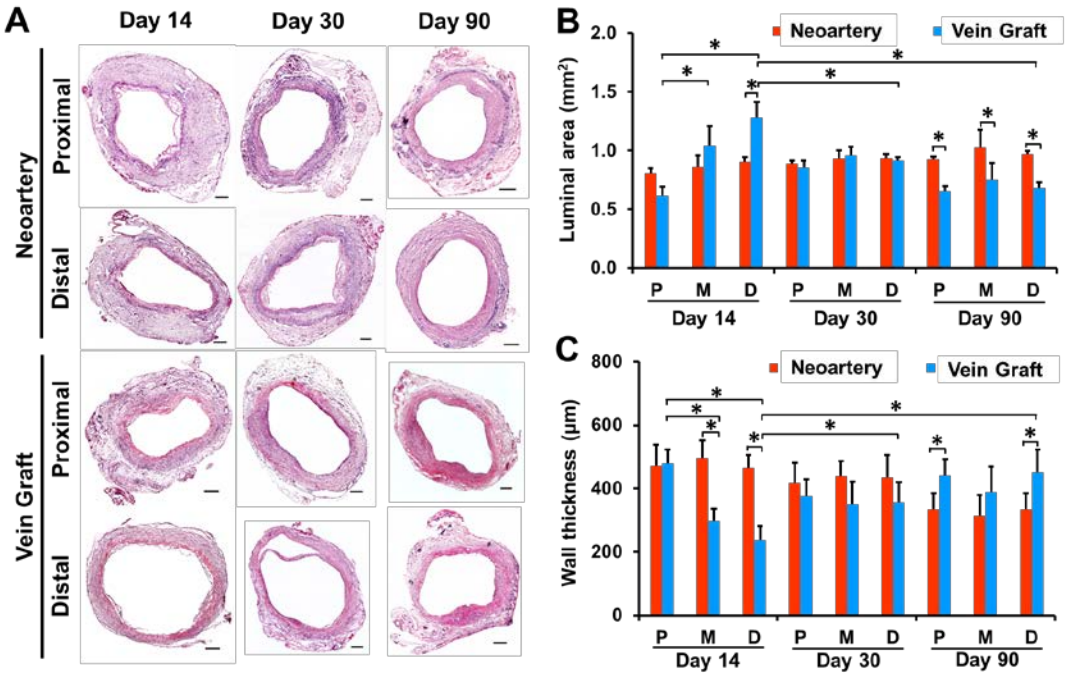

Figure 22 Histological and morphological assessments of grafts at anastomotic regions.

(A) Representative images for H&E staining in both proximal and distal regions of remodeled grafts at each time point. Scale bars, 200 μm. (B) Luminal area. (C) Wall thickness. P, proximal. M, middle. D, distal. Both (B) and (C) were measured by using H&E stained images from three independent sections per sample. Data in (B) and (C) are means ± SD (n = 4). * represents P < 0.05.

3.3.4 Remodeled Neoarteries Exhibit Heightened Monocyte Recruitment Markers at 90 Days

We evaluated monocyte infiltration into the grafts to assess the initial host response. We stained mid-section of grafts with C-C chemokine receptor type 2 (CCR2) and CD11b, markers for monocyte recruitment, adhesion, and migration. The expression of CCR2 and CD11b were highest at day 14 and decreased thereafter in both grafts (Figure 23A and Figure 23C). Many $CCR2^+$ cells infiltrated remodeled PGS-PCL grafts at day 14, but were almost absent at day 30, and disappeared at day 90. $CD11b^+$ cells were dispersed through the wall at day 14 and limited to the abluminal area thereafter. Conversely, in remodeled vein grafts, $CCR2^+$ cells dispersed throughout the wall at day 14 and persisted at the lumen and the abluminal areas at day 90. Quantification of the fluorescent-positive cells revealed that the neoarteries had more $CCR2^+$ cells at day 14 ($P = 0.015$) but less at days 30 ($P = 0.0003$) and 90 ($P = 0.002$) than vein grafts (Figure 23B).On the other hand, more $CD11b^+$ cells were detected in neoarteries than the vein grafts at days 14 ($P = 0.033$) and 90 ($P = 0.009$), (Figure 23D).

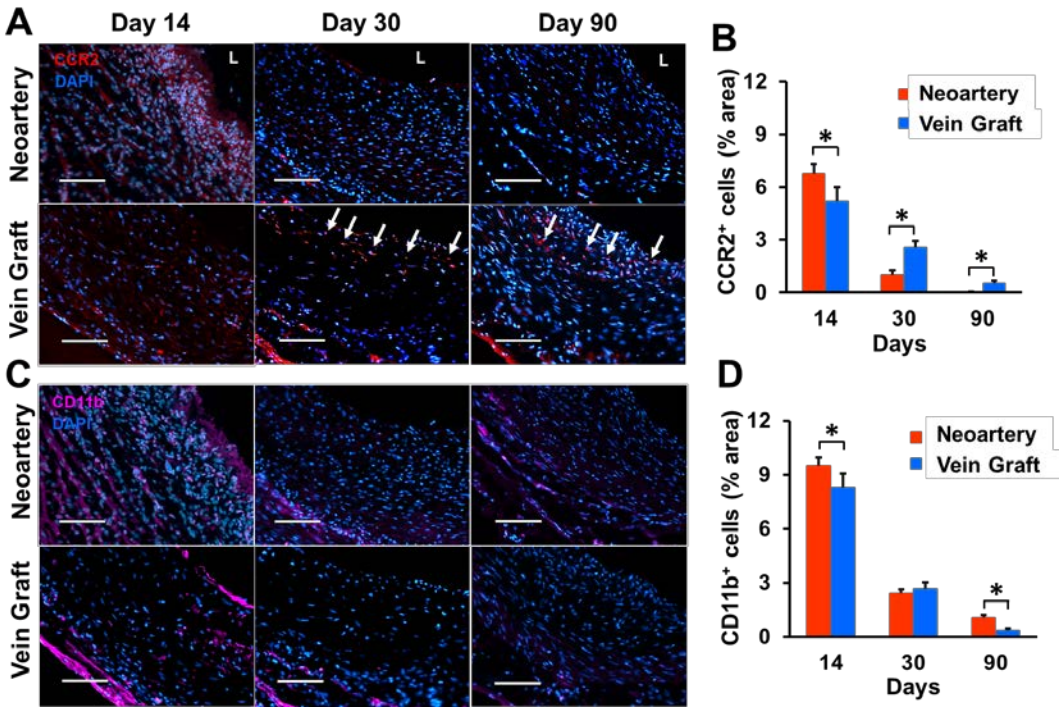

Figure 23: Infiltration of inflammatory monocytes.

(A) Representative images for immunofluorescence staining with the monocyte recruitment marker CCR2. Arrows denote CCR2+ cells. L, lumen. (B) Quantification of the results shown in (A). (C) Representative images for immunofluorescence staining with the monocyte adhesion, migration marker CD11b. (D) Quantification of the results shown in (C). Scale bars, 100 μm (A and C). Data in (B) and (D) are means ± SD (n = 4). * represents P < 0.05.

3.3.5 Remodeled Neoarteries Exhibit Similar Macrophage Distribution to Vein Grafts at 90 Days

We stained mid-sections of remodeled grafts with CD68, inducible nitric oxide synthase (iNOS), and CD206, markers of the newly recruited, pro-inflammatory (M1), and alternatively activated (M2) macrophages, respectively. Consistent with CD11b expression, both CD68 and

iNOS expression were highest in the lumen at day 14, decreased markedly thereafter, and were limited to the abluminal area in both grafts (Figure 24A and Figure 24C). Remodeled neoarteries showed significantly more $CD68^+$ cells than vein grafts at day 14 ($P = 0.034$) (Figure 24B). There was no significant difference in the $iNOS^+$ cells between remodeled neoarteries and vein grafts at all time points (Figure 24D). Conversely, CD206 expression was minimal at day 14 and increased gradually with time (Figure 24E). At day 14, $CD206^+$ cells in remodeled neoarteries were significantly less than that in vein grafts ($P < 0.0001$); however, no difference was observed at later time points (Figure 24F). The ratio of $iNOS^+$ to $CD206^+$ cells was significantly higher in remodeled neoarteries than in vein grafts at day 14 ($P < 0.0001$) but showed no significant difference thereafter (Figure 24G). These results show that neoarteries enabled early infiltration of the classically activated macrophages, followed by a phenotype switching to the alternatively activated macrophages.

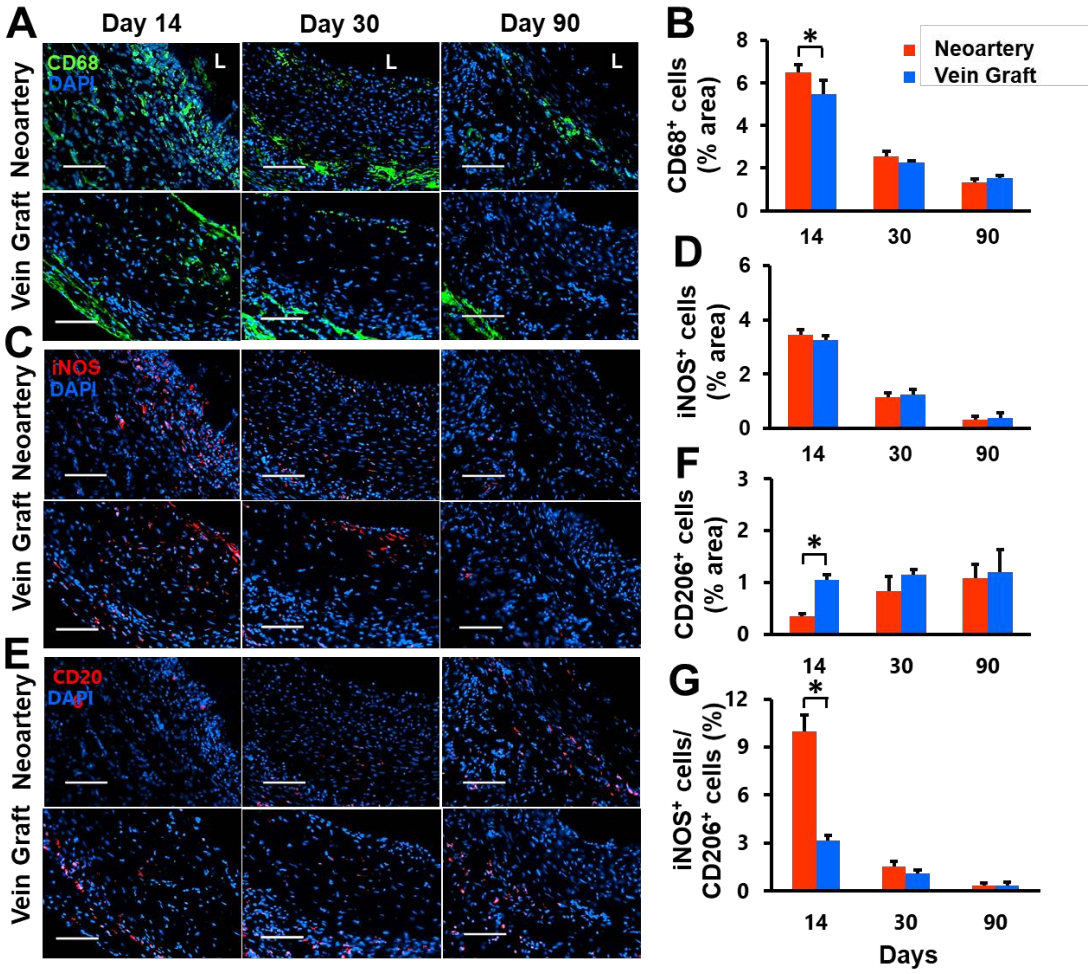

Figure 24: Macrophage infiltration and polarization.

(A) Representative images for immunofluorescence staining with the pan-macrophage marker CD68. L, lumen. (B) Quantification of the results shown in (A). (C) Representative images for immunofluorescence staining with the M1 macrophage marker iNOS. (D) Quantification of the results shown in (C). (E) Representative images for immunofluorescence staining with the M2 macrophage marker CD206. (F) Quantification of the results shown in (E). (G) The area ratio of iNOS+ to CD206+ cells representing the M1/M2 macrophage ratio. Scale bars, 100 μm (A, C, and E). Data in (B), (D), (F) and (G) are means ± SD (n = 4). * represents P < 0.05.

3.3.6 Endothelial Cells Cover Neoarterial Luminal Surface by 1 Month

We examined the luminal surface of the remodeled grafts using SEM and immunofluorescence staining with EC markers CD31 and vWF to assess EC coverage. At day 14, no ECs appeared for the remodeled neoarteries. Remodeled vein grafts showed disrupted endothelium in the luminal surface. At day 30, ECs covered the luminal surface of both grafts as demonstrated by vWF expression (Figure 25A). SEM images showed that ECs completely covered the lumen of both grafts at day 90 and were aligned in the flow direction, resembling that of native carotids (Figure 25B).

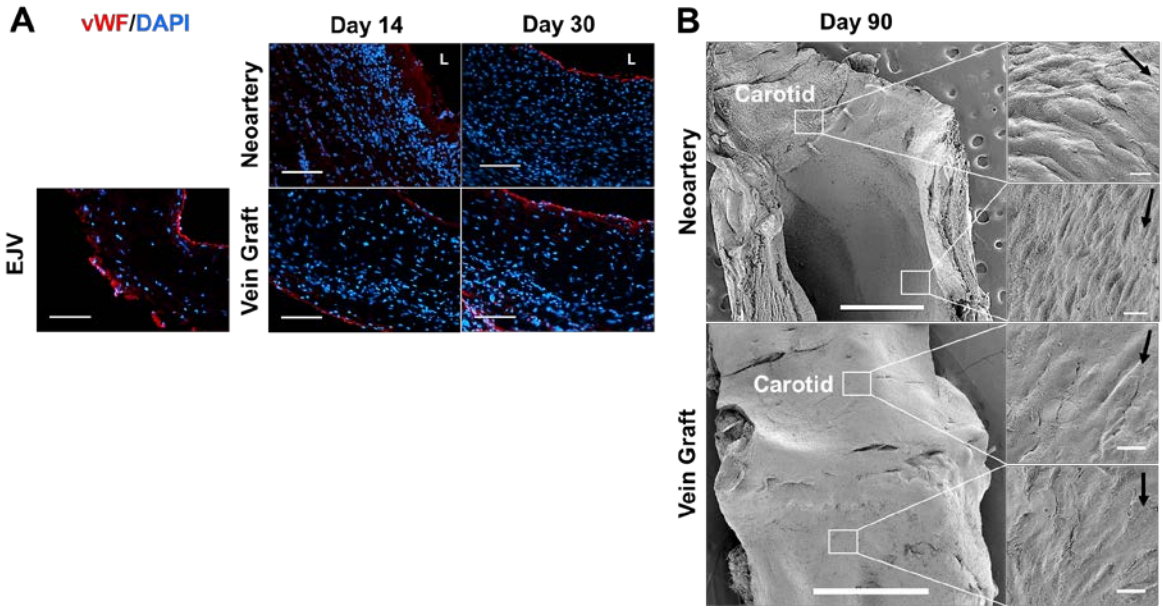

Figure 25: Endothelial cell coverage in vein graft and neoarteries.

(A) Representative images for immunofluorescence staining with the endothelial cell (EC) marker vWF. The external jugular vein (EJV) image (bottom, left) represents ECs of the vein graft before interposition to the carotid artery. L, lumen. Scale bars, 100 μm. (B) Longitudinal SEM images showing the lumen of the neoartery (top row) and vein graft (bottom row) at day 90. Arrows indicated the flow direction. Scale bars, 1 mm (top and bottom, left), 10 μm (top and bottom, right).

Tightly-bound ECs with cobblestone-like morphology were clearly observed in neoarteries. $CD31^+$ and vWF^+ cells in the luminal surface confirmed EC coverage in both grafts (Figure 26A). Western blot analysis indicated that both the remodeled neoarteries and vein grafts expressed endothelial nitric oxide synthase (eNOS) and thrombomodulin (TM), but did not express vascular cell adhesion protein-1 (VCAM-1) and intercellular adhesion molecule-1 (ICAM-1), indicating quiescence (Figure 26B). There were no significant differences in eNOS and TM

expressions between the remodeled neoarteries and vein grafts (P = 0.98 and 0.50) (Figure 26C). However, eNOS and TM expressions in both grafts were significantly lower than in native carotids ($P < 0.05$).

We stained mid-section of grafts with smooth muscle contractile phenotypic and cell proliferating markers. Alpha-smooth muscle actin $(SMA)^+$ cells were observed in the middle of the wall at day 14 and dispersed at day 30 in both grafts. More αSMA^+ cells were organized near the outer layer in the remodeled neoarteries. In contrast, more αSMA^+ cells were present near the lumen in the remodeled vein grafts. At day 90, the neoarteries showed a dense, concentric cell layer expressing calponin and myosin heavy chain, markers of contractile VSMCs (Figure 26D). There was no evidence of proliferating VSMCs, indicated by a negative expression of Ki67. On the contrary, remodeled vein grafts contained numerous proliferating αSMA^+ and $Ki67^+$ cells near the lumen. Alpha-SMA^+ cells were disorganized in the wall and the expression of calponin and myosin heavy chain was weaker than neoarteries. We further investigated the activation of Akt and extracellular signal-regulated kinases 1 and 2 (ERK1/2) (Figure 26E). These are protein kinases of phosphatidylinositol 3-kinase (PI3K)-Akt-mammalian target of rapamycin (mTOR) and Ras-mitogen-activated protein kinase (MAPK) cascades, both of which are major signaling pathways of VSMC proliferation. Western blot analysis indicated that the expression of phosphorylated-Akt and ERK1/2 was significantly higher in the remodeled vein graft than in the neoarteries (P = 0.0036 and 0.0072) and native carotids (P = 0.0008 and 0.016) at day 90 (Figure 26F). These results correlated with more proliferative VSMCs in the vein graft at day 90. Taken together, the neoarteries were closer to native carotids than remodeled autologous vein grafts in terms of VSMC phenotype and organization.

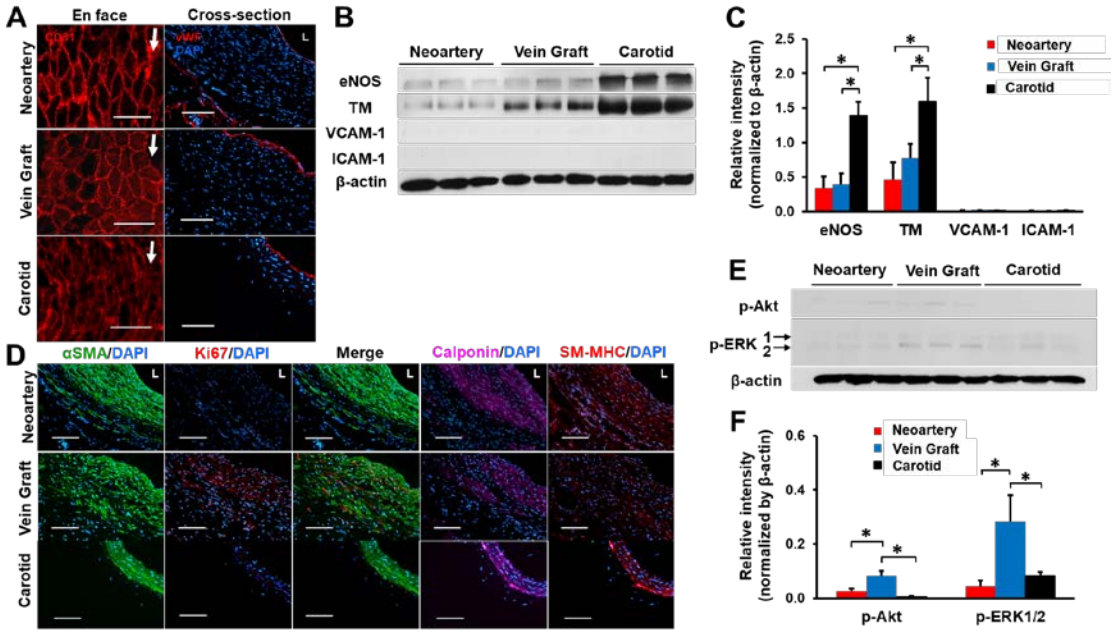

Figure 26: Arterial-like tissue remodeling at day 90.

(A) Representative images for en face (left) and cross-sectional (right) immunofluorescence staining with EC markers, CD31 and vWF. Arrows indicate the flow direction. L, lumen. Scale bars, 100 μm. (B) Immunoblots of grafts and native carotids for eNOS, TM, VCAM-1, and ICAM-1. (C) Quantification of the relative intensity of each blot normalized to β-actin expression. Data are means ± SD (n = 3). * represents P < 0.05. (D) Representative images for immunofluorescence staining with VSMC phenotype markers, αSMA, calponin, and smooth muscle-myosin heavy chain (SM-MHC), and proliferation marker Ki67. L, lumen. Scale bars, 100 μm. (E) Immunoblots of p-Akt (Ser473) and p-ERK1/2. p-ERK1, 44 kDa (top). p-ERK2, 42 kDa (bottom). (F) Quantification of the relative intensity of each blot normalized to β-actin expression. Data are means ± SD (n = 3). * represents P < 0.05.

3.3.7 Remodeled Neoarteries show Comparable ECM Levels to Remodeled Vein Grafts

ECM proteins provide mechanical support for the vessel and guide cellular differentiation and functions. We examined collagen and elastin using histology, immunofluorescence staining, and multiphoton microscopy. Masson's trichrome and Verhoeff-van Gieson staining showed collagen fibers spanning the wall and some elastic fibers near the lumen in both grafts. Remodeled neoarteries had similar organization and distribution of ECM protein assemblies to native carotids with circumferentially organized collagen and elastin near the outer wall and the lumen, respectively. However, remodeled vein grafts had thick collagen fibers in the entire wall and aggregated elastin near the lumen. Alizarin red staining revealed that there is no calcification in either graft (Figure 27A). Immunofluorescence staining revealed the expression of collagen I and III across the entire wall of both grafts, in contrast to native carotid where collagen I and III were segregated to the adventitia and medial layers respectively. Furthermore, the remodeled neoarteries expressed elastin and fibrillin-1. Vein grafts displayed weaker expression of fibrillin-1 in the lumen than the remodeled neoarteries. Biochemical assays indicated that both grafts contained comparable densities of collagen (Figure 27B), but significantly less elastin than native carotids ($P < 0.0003$) (Figure 27C). As implanted, the iTEVGs contain no ECM but have similar collagen and elastin contents to the vein graft at 3 months: these were 88% and 23% of those in native carotids, respectively.

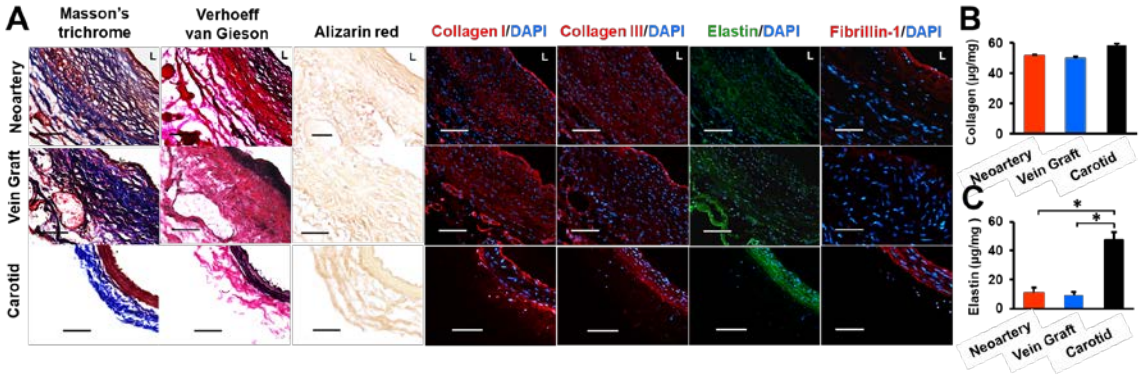

Figure 27: ECM protein deposition and quantification at day 90.

(A) Representative images for histology and immunofluorescence staining with collagen and elastin markers. Masson's trichrome, Verhoeff-van Gieson, Alizarin red staining show collagen (blue), elastin (black), but no calcium (red) deposition, respectively. L, lumen. Scale bars, 100 μm. (B) Quantification of total collagen using Sircol Insoluble Collagen assay. (C) Quantification of elastin using Fastin assay. Data in (B) and (C) are means ± SD (n = 4). * represents P < 0.05.

3.3.8 Neoarteries Exhibit Similar Compliance to Vein Grafts due to Collagen Fiber Re-orientation

We evaluated mechanical properties of grafts and native carotids using suture retention, biaxial inflation – extension, compliance, and burst pressure tests. Suture retention strength of both bare grafts and explanted external jugular veins was similar (P = 0.058), but significantly lower than that of native carotids (P < 0.0001 and 0.0024) (Figure 28A). There was no significant difference in the mechanical performance of the two types of grafts; both lacked a toe-region leading to a lower range of stretch in the loading curves compared with native carotids and veins. At physiological values of pressure, the intramural stress within both grafts was in the range of 40-

50 kPa (Figure 28B). Both grafts were significantly stiffer compared with native carotids as shown by the high strain modulus (P = 0.031) (Figure 28C). There was no significant difference in the burst pressure, a marker of bulk strength, between all three groups **(**Figure 28D**)**, demonstrating that both types of grafts were capable of withstanding the arterial pressure by 3 months post-implantation. However, compliance of both grafts was significantly lower than that of native carotids and veins ($P < 0.05$) (Figure 28E).

We assessed the microstructural response to loading of each of the groups using second harmonic generation (SHG) imaging for collagen fibers and two-photon excitation for elastin fibers (Figure 28F). The first main difference between the groups was the lack of visible elastin fibers in both grafts as compared to native carotids. Secondly, there was a difference in collagen fiber load bearing mechanism between the two grafts. In native carotids, collagen fibers bear biaxial load by two mechanisms – (a) recruitment (straightening) and (b) change in orientation (Figure 28G). However, vein grafts did not exhibit collagen fiber recruitment or fiber re-alignment upon loading. Rather, most collagen fibers remained aligned in the axial ($\pm$60 - $\pm$90˚) direction and very few in the circumferential (-30 to +30˚: 14% 0 mmHg vs. 16% 120 mmHg) direction upon pressurization. In contrast, 13% of collagen fibers in the remodeled neoarteries were crimped under zero pressure and were recruited upon pressurization. Furthermore, fiber re-alignment measurements showed that neoarteries behaved similarly to native carotids with a significant ($P <$ 0.001) change in fiber re-alignment upon pressurization. Fibers re-aligned from the longitudinal to the circumferential direction (-30 to +30˚: 15% 0 mmHg vs 57% 120 mmHg) upon pressurization. These findings suggest that the remodeled neoarteries enabled the remodeling of collagen fibers to bear biaxial load upon extension and pressurization.

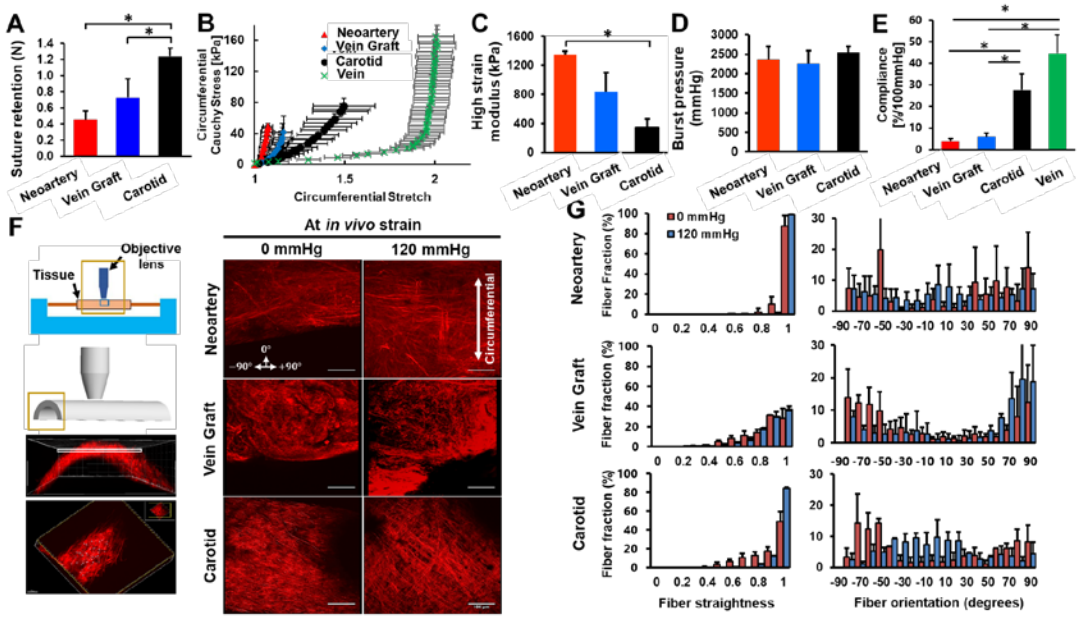

Figure 28: Assessment of mechanical response.

(A) Suture retention strength of bare grafts and native vessels before implantation. (B) Circumferential stress-stretch curves. (C) High strain moduli. (D) Burst pressure. (E) Compliance. (F) Schematic of biaxial inflation device used with a multiphoton microscope to image collagen fibers (left). Planar images were obtained starting from the outer wall, moving down to the inner wall with images stacked to obtain projection images of collagen fibers across the thickness of the sample. Scale bars, 100 µm. Note the difference in collagen fiber density, morphology and orientation between samples (right). (G) Collagen fiber straightness and orientation quantified in each slice across sample thickness and normalized to a total number of traced fibers. A value of 1 represents completely straightened (recruited) fibers. Orientation was measured from θ = 0° to 90° with θ = 0° being the circumferential direction. Data in (A) - (E) are means ± SD (n = 5 for A and n = 3 for B - E). Data in (B)-(G) were obtained from explanted grafts and native carotids at day 90. * represents P < 0.05.

3.4 Discussion

To date, all tissue-engineered grafts in clinical trials are cell-based, needing human cells for seeding polymeric scaffolds or creating cell sheets. Using banked allogeneic cells greatly reduces waiting time for grafts; however, isolation, expansion, and seeding of recipient endothelial or endothelial progenitor cells are still necessary. In a 1-month pig study, decellularized tissue-engineered matrix showed better patency rate than autologous internal jugular vein grafts, resisting luminal occlusion and intimal hyperplasia. The dense collagenous matrix appears to inhibit host cell infiltration and ECM content was not reported. Decellularized porcine small intestine submucosa showed patency and arterial-like tissues similar to saphenous vein in a canine carotid model for 6 months. However, this xenogeneic graft was prone to acute thrombosis, despite systemic administration of heparin. No ECM contents or mechanical data were reported.

The iTEVG reported here relies on the host cells to infiltrate and remodel the iTEVG after implantation as it is a degradable. Compared with autologous veins and current tissue-engineered grafts, these iTEVGs avoid donor-site morbidity and immunogenicity, reduce fabrication cost and time, and ease storage and transport requirement. This approach poses its own challenges but offers the potential to combine the advantages of tissue-engineered grafts and conventional synthetic grafts.

Ultrasonography data indicated that the 90-day patency was similar for the remodeled PGS-PCL and the autologous vein grafts studied here. One implanted PGS-PCL graft developed a distal thrombosis at day 6 and one ruptured at day 9. Since the rupture was mainly due to a defect of the PGS core, we believe that defect-related failure will decrease significantly for larger and thicker grafts used in clinical applications and by the quality control steps in manufacturing. Compared with previous studies using acellular micro-fibrous grafts in the rat carotid artery

interposition model, our PGS-PCL grafts displayed slight better patency at 90 days (90.5% of cases) *without* anti-thrombogenic surface modifications. In particular, hirudin-polyethylene glycol (PEG) conjugated grafts had only 83% patency at 1 month and 86% patency at 6 months. Stromal cell-derived factor (SDF)-1α decorated grafts showed 89% patency at 3 months [136]. Despite the anti-thrombogenic surface modification, these grafts with an inner diameter of 1 mm were prone to thrombosis. PCL grafts with an inner diameter of 0.7 mm also showed an overall 73% patency for 72 weeks, dropping to 57% patency for 12 weeks.

At 3 months, the autologous vein grafts showed certain signs of neointimal hyperplasia: reduced luminal area, thickened wall, and many proliferative VSMCs in the wall. None of these were present in the remodeled neoartery. Histological data indicated that early geometrical changes were crucial determinants to long-term patency of vein grafts in bypass. Increased lumen and wall thickness in the vein graft in the first 1 month were usually followed by relative stability. However, decreased lumen and increased wall thickness after 1 month indicated neointimal hyperplasia. Initial lumen dilation of vein grafts was evidenced by maximal luminal area and minimal wall thickness at day 14. Additionally, vein grafts had lower flow velocity than carotids at day 14, but similar thereafter (Figure 20E). After day 14, the narrowing lumen and thickening wall reflected further adaptation processes with corresponding VSMC migration and proliferation (Figure 26D), and ECM deposition in the inner wall (Figure 27A).

The divergence between the vein and the PGS-PCL grafts might be related to the different inflammatory responses. The PGS-PCL grafts induce more extensive early inflammatory response than vein grafts at day 14. There is no difference of M1 macrophages ($iNOS^+$) in both grafts. After 14 days, the population of pro-inflammatory cells subsides in the neoarteries, whereas M2 macrophages ($CD206^+$) increase. This finding suggests a resolution of inflammation and

macrophage polarization towards a healing outcome. On the contrary, $CCR2^+$ cells persist to day 90 in vein grafts (Figure 24A and Figure 24B). CCR2, a monocyte chemoattractant protein (MCP)-1 receptor, mediates monocyte migration from bone marrow to peripheral blood. $CCR2^+$ cells, classified as inflammatory monocytes, extravasate to inflamed tissues in the early inflammatory phase. $CCR2^+$ cells enhance angiogenesis and tissue repair, however, excessive expression of MCP-1/CCR2 induces VSMC proliferation, leading to intimal hyperplasia in vein grafts. This is consistent with our observation of VSMC proliferation and a narrower lumen in the vein graft at 90 days (Figure 22B and Figure 26D).

Short-term recruitment of bone marrow-derived circulating monocytes has been achieved in acellular grafts by a burst release of exogenous MCP-1. Here, the graft design induces an initial influx of bone marrow-derived circulating monocytes, initiating inflammation-mediated vascular remodeling. $CD11b^+$ and $CD68^+$ cells remain near the abluminal surface of the neoarteries after day 14 (Figure 23C and Figure 24A). This could be caused by the continued presence of the small amount of PCL in the outer layer. Conversely, vein graft shows densely packed $CD11b^+$ and $CD68^+$ cells near both the luminal and abluminal surfaces at day 14, suggesting that living cells and ECM inhibit infiltration of these cells into the vessel wall. After day 14, $CD11b^+$ cells almost disappeared. It is likely that the slow degrading PCL sheath contributes to the extended presence of resident monocytes ($CCR2^-$, $CD11b^+$) and their differentiation to tissue macrophages ($CD11b^+$, $CD68^+$). Tissue-resident macrophages have similar functions to M2 phenotypes that play a fundamental role in the resolution of inflammation and tissue homeostasis [137]. We found that both $CD68^+$ and $CD206^+$ but few $iNOS^+$ cells were observed in the same abluminal area in the neoarteries at day 90 (Figure 24A, C, and E). In the remodeled grafts, the distribution and organization of VSMCs correlate directly with the morphology and organization of ECM proteins.

Thick, disorganized collagen fibers and aggregated elastin are present in vein grafts alongside randomly orientated VSMCs. On the other hand, the remodeled neoarteries have collagen and elastin aligned circumferentially alongside VSMCs at 3 months, resembling the organization in native carotids (Figure 27A). The newly synthesized elastin in the remodeled neoarteries co-exists with fibrillin-1 and is equivalent to 23% of that found in native carotids. Several studies have reported elastin production in small artery grafting using pre-clinical animal models. Decellularized engineered allografts contained elastin corresponded to 8.8% of an ovine femoral artery at 6 months. Porcine small intestine submucosa grafts loaded with heparin and VEGF showed a varied range of elastin contents in an ovine carotid artery model at 3 months, but no fibrillar elastin was observed. However, elastin fibers were not visible under MPM for either graft. The functional requirements of replacement vascular grafts have changed from just sufficient suture retention strength and burst pressure to requiring functional adaptability and sound microstructure-function relationship. There is also a pressing need to understand the mechanical cues that govern ECM deposition and the manifestation of these cues into a structural response to gain a mechanistic understanding of the long-term graft remodeling. As the first step toward this, we used nondestructive SHG testing to understand the microstructural behavior of collagen loading. An important mechanism for compliance in the native arteries is the gradual recruitment and re-orientation of collagen fibers which leads to their nonlinear stress-strain relationship. At sub-physiological loads, elastin fibers and the surrounding matrix are the main load-bearing components while collagen fibers are engaged at physiological levels. While the origin of a crimp (waviness) in collagen fibers is unknown, native arteries synthesize collagen at various levels of crimp. These undulations are one mechanism for enabling high compliance followed by stiffening at higher loads. In our neoarteries, some collagens exhibit crimp; however, most fibers are already

straightened at low pressures (Figure 28G), which is one of the main causes of a higher graft stiffness. This diminished crimp might be attributed to the fact that collagen fibers are being rapidly synthesized to bear load to compensate for the degradation of the graft material. Furthermore, as collagen fibers are continually turning over, it is possible that over a longer time frame, the level of crimp will increase.

We recognize that our neoarteries exhibited a significantly lower compliance at lower strains than that of native carotids and veins (Figure 28E), likely because of the low elastin content at 90 days. However, this does not inevitably preclude elastin synthesis at later timepoints as evidenced by comparable elastin production by neoarteries to the native aorta seen at 1 year in our previous work [98]. Thus, the lower compliance in our grafts than in native carotids and veins is not necessarily a sign of maladaptive remodeling. Furthermore, collagen fibers in our grafts exhibit native-like functional behavior and are capable of recruitment and re-orientation during pressurization, suggesting that collagen is exhibiting adaptive remodeling. In contrast, vein grafts lack recruitment and re-orientation of collagen fibers upon loading which is more typical of scar-like collagen. Furthermore, vein grafts also show extensive remodeling with stiffening in both the low and high strain regions as compared to the native vein prior to implant. Consistent with the functional characteristics, histological and SHG imaging reveal thicker walls and dense collagen, which, coupled with high levels of proliferating VSMCs, indicate a fibrotic remodeling response in the vein grafts. This work represents the first step towards a detailed mechanical and biological evaluation of remodeling grafts that requires a long-term study.

The observations in this study are limited to the rat model and the 3-month follow-up window. Rats enable a high-throughput, cost-effective study to assess cell infiltration. However, rats have different regenerative potentials, hemodynamics, and physiology than humans. This study uses

young rats; thus, the effect of aging on host remodeling remains unknown. Additionally, methodological limitations include performing multiphoton microscopy only under *in vivo* measured strains and two pressure levels. Future studies should include analysis of multiple loading configurations to completely characterize the biaxial properties of the evolving grafts. To our knowledge, this is the first report of a neoarteries that performs comparably to an autologous vein in small artery grafting. We are currently performing a long-term study in a sheep carotid model before the clinical translation of these grafts.

3.5 Conclusion

In summary, we developed biodegradable iTEVGs that do not require cell seeding before implantation and compared their performance with autologous vein grafts in a rat carotid artery model for 3 months. Compared with autologous vein grafts, our iTEVGs have: (1) similar patency without anti-thrombogenic surface modifications; (2) consistent morphological changes without any signs of stenosis; (3) extensive but transient infiltration of circulating inflammatory monocytes, leading to quickly-resolved inflammation and arterial-like tissue remodeling; (4) remodeled wall with circumferentially organized, contractile, non-proliferating VSMCs; and (5) recruitment and re-orientation of newly synthesized collagen fibers upon mechanical loading. The critical next step of this study is to test our design in large animals and aged animals; both are currently under investigation.

Authors' Contribution

KL and PSG designed and conducted the small animal study. LD performed the graft surgical implant and explant, and MUN performed ultrasonography. KL fabricated the grafts and performed the histological and biochemical assessment of neoarteries, and JG performed immunoblotting. PSG performed the mechanical analysis, two photon imaging and image quantification. All authors contributed to writing, discussion, and interpretation of results in the manuscript. We also thank Xiaozhou Fan for assistance with ultrasonography, Dr. Michael W. Epperly for gamma sterilization, and Brandon B. Risley for assistance with GPC analysis.

4.0 Data-Driven Growth and Remodeling Computational Tool for iTEVG Modeling

4.1 Introduction

The scope of this chapter is to develop a G&R theoretical model to predict the evolution of an iTEVG to a neoartery in the host. As outlined in chapter 1.5, constrained mixture theory-based G&R tools have been employed to understand salient features of arterial remodeling, aneurysm formation and neotissue formation in the venous circulation. These tools are based on the knowledge that vascular tissues adapt their structure and function to achieve a certain homeostatic stress state. In chapters 2.0 and 3.0, we obtained biological and mechanical data to understand the final homeostatic condition for *i*TEVGs. In this chapter, we utilize these data to translate this tool to neoartery formation in the arterial circulation. This chapter will outline the G&R framework in which the evolving neoartery is idealized as a thick-walled cylindrical tube. The chapter begins with a discussion of the relevant kinematics, followed by outlining the constitutive formulation for mass production and degradation, and describing the mechanical response of these constituents. Finally, we will provide the solution procedure for the governing equations.

4.2 Constitutive Framework

4.2.1 G&R Formulation

Three fundamental assumptions govern G&R mechanics – (i) that the evolving iTEVG is modeled as a mixture comprising of PGS, PCL, collagen, elastin, and VSMCs. (ii) This mixture is constrained, i.e. all constituents at a material point are subject to the same motions, and (iii) mass per unit current volume ($\bar{\rho}$) is assumed to be constant throughout the G&R process.

G&R occurs across time $\tau \in [0, s]$. We denote the reference configuration at time $s = 0$ as κ_0 and the changing configuration of the body at arbitrary time τ by $\kappa(\tau)$. The current configuration is then $\kappa(s)$. Infinitesimal material segments are mapped from κ_0 to $\kappa(\tau)$ through the deformation gradient tensor $\mathbf{F}(\tau)$, Figure 29.

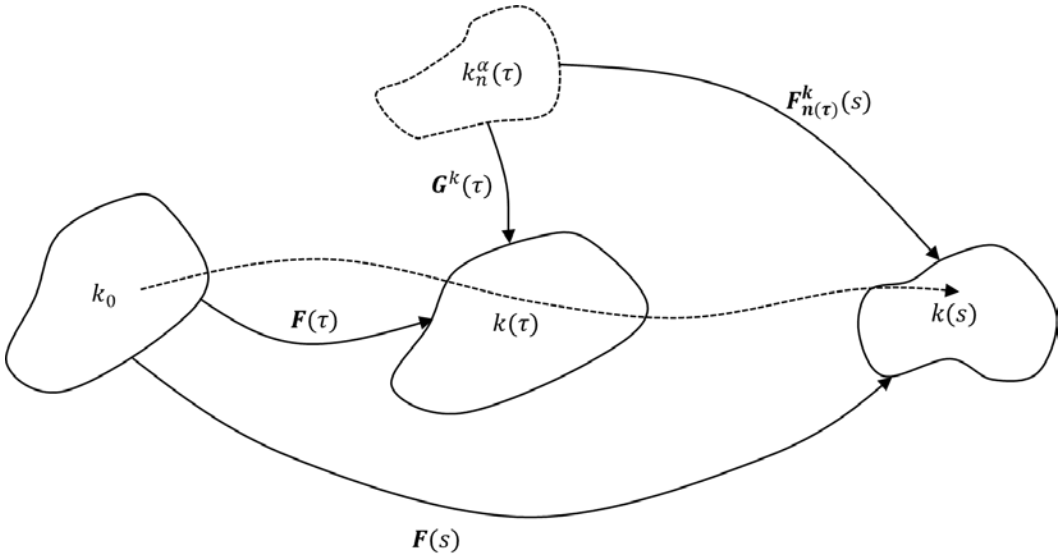

Figure 29: Schematic of configurations describing the G&R kinematics.

The cohort-specific, stress-free natural configuration is denoted as $k_{n(\tau)}^{\alpha}(\tau)$ and the deposition stretch tensor as $\boldsymbol{G}^{k}(\tau)$.

In general, the constituents deposited at time τ will not be deposited in a stress-free configuration. In defining the constitutive response of this material, it is therefore useful to introduce an additional reference configuration $\kappa_{n(\tau)}^{\alpha}$ that is related to κ(τ) through a deposition pre-stretch tensor denoted as $\boldsymbol{G}^{\alpha}(\tau)$, Figure 29. The pre-stretch tensor is defined such that the stress-free configuration is shifted by the deposition pre-stretch relative to the current configuration. Note that each constituent can be deposited at its own pre-stretch and hence the rep-stretch tensor has the additional superscript α. Our approach thereby captures pre-stretches imposed by cells on the constituents they synthesize during the incorporation of newly secreted material into the ECM. The deformation gradient used to map material elements of individual constituent α from its natural, stress-free configuration $\kappa_{n(\tau)}^{\alpha}$ to the current G&R configuration at

time s (see Figure 1) is denoted by $\boldsymbol{F}^{\alpha}_{n(\tau)}(s)$. The right Cauchy Green tensor for each cohort of constituent α deposited at time τ and surviving to time s is

$$\boldsymbol{C}^{\alpha}_{n(\tau)}(s) = \left(\boldsymbol{F}^{\alpha}_{n(\tau)}(s)\right)^{T} \boldsymbol{F}^{\alpha}_{n(\tau)}(s) \qquad \textbf{Equation 4-1}$$

where,

$$\boldsymbol{F}^{\alpha}_{n(\tau)}(s) = \boldsymbol{F}(s)\boldsymbol{F}^{-1}(\tau)\boldsymbol{G}^{\alpha}(\tau) \qquad \textbf{Equation 4-2}$$

4.2.2 Governing Equations

In this framework, growth is fundamentally described by tracking the evolution of mass density of the N individual constituents. For a constituent α, the mass density per unit reference and current volume is denoted by ρ^{α} and $\overline{\rho^{\alpha}}$ respectively. The total mass density can then be written as

$$\rho = \sum_{\alpha=1}^{n} \rho^{\alpha}(\tau) \qquad \bar{\rho} = \sum_{\alpha=1}^{n} \overline{\rho^{\alpha}}\,(\tau) \qquad \textbf{Equation 4-3}$$

The mass of the mixture in an arbitrary subregion of the body V at current time s can then be written as

$$M(s) = \int_{v(s)} \bar{\rho} dv = \int_{v(0)} \rho dV$$ **Equation 4-4**

where

$$dv = JdV$$ **Equation 4-5**

It then follows that

$$\rho(\tau) = \bar{\rho} J(\tau)$$ **Equation 4-6**

It thus follows from equation Equation 4-6, that $\rho(0) = \bar{\rho}$. Although $\bar{\rho}$ is constant, equation Equation 4-6 also shows that mass per unit reference volume (ρ) is a function of time τ.

It must be emphasized that while $\bar{\rho}$ is constant, $\overline{\rho^{\alpha}}$ is not. The mass density per unit reference volume evolves due to the degradation and deposition of material and is represented as

$$\rho^{\alpha}(s) = \rho^{\alpha}(0) Q^{\alpha}(s) + \int_0^s m^{\alpha}(\tau) q^{\alpha}(s - \tau) d\tau$$ **Equation 4-7**

where $Q^{\alpha}(s)$ is the survival function and represents the survival fraction of material present in the original reference configuration (i.e. PGS, PCL). $m^{\alpha}(\tau)$ and $q^{\alpha}(s-\tau)$ are, respectively, mass density production rates per unit reference volume and survival fraction at time s of material deposited at time τ.

Furthermore, we assume that for every constituent α, there exists a strain energy function per unit reference volume κ_0 with uncoupled responses, such that $W(s) = \sum_{\alpha=1}^{n} W^{\alpha}(s)$, where,

$$W^{\alpha}(s) = \frac{\rho^{\alpha}(0)}{\rho(s)} Q^{\alpha}(s)\widehat{W^{\alpha}}\left(\boldsymbol{C}^{\alpha}_{n(0)}(s)\right) + \int_0^s \frac{m^{\alpha}(\tau)}{\rho(s)} q^{\alpha}(s-\tau)\widehat{W^{\alpha}}\left(\boldsymbol{C}^{\alpha}_{n(\tau)}(s)\right) d\tau \qquad \textbf{Equation 4-8}$$

We can then calculate the Cauchy stress as follows

$$\boldsymbol{\sigma}(s) = -p(s)\boldsymbol{I} + 2\boldsymbol{F}(s)\frac{\partial W(s)}{\partial \boldsymbol{C}(s)}\boldsymbol{F}^{T}(s) + \boldsymbol{\sigma}_{act}(s) \qquad \textbf{Equation 4-9}$$

Where, $p(s)$ is the Lagrange multiplier enforcing the incompressibility constraint and $\boldsymbol{\sigma}_{act}(s)$ is outlined in section 4.2.6 .

4.2.3 Kinematics of Cylindrical Deformation

We model the iTEVG as an axisymmetric thick-walled cylinder undergoing finite extension and inflation. We introduce cylindrical polar co-ordinates (r, θ, z) and (r, t, z) representing the graft pre/post-implantation, and the experimentally loaded configuration respectively. Throughout the remainder of this work, we will consider motions for which the radial displacement depends at most upon radial position and time, and axial displacement depends, at most, upon time. For such motions, the deformation gradient tensor with respect to cylindrical polar coordinates is diagonal. In particular, the deformation gradient for motions from the un-implanted state κ_0 to the *in vivo*, loaded configuration immediately after surgery $\kappa(s = 0)$ (i.e., the acellular graft pressurized and stretched to normal physiological conditions) is

$$\boldsymbol{F} = diag\left[\frac{\partial r(0)}{\partial r_0}, \frac{r(0)}{r_0}, \frac{l(0)}{l_0}\right] \qquad \textbf{Equation 4-10}$$

where, r_0 and $r(0)$ are radial positions in configurations κ_0 and $\kappa(s = 0)$, respectively, and $l(0)$ and l_0 are the implanted and un-implanted axial lengths respectively. The deformation gradient tensor for motions from the implanted configuration to the current configuration is

$$\boldsymbol{F}(s) = diag\left[\frac{\partial r(s)}{\partial r(0)}, \frac{r(s)}{r(0)}, \frac{l(s)}{l(0)}\right] \qquad \textbf{Equation 4-11}$$

The axial stretch $\lambda(s) = l(s)/l(0)$ is prescribed in the *in vivo* configuration at all G&R times s, where $l(s)$ is the current *in vivo* axial length. Since the density of the newly deposited material is constant, namely $\bar{\rho}(s) = \bar{\rho}(0) = \rho(0)$, the mass of an infinitesimal material particle can be expressed in the following equivalent forms,

$$\overline{\rho(s)}dv|_{k(s)} = \rho(0)J(s)dv|_{k(0)} = \rho(s)dv|_{k(0)} \qquad \textbf{Equation 4-12}$$

It follows that the current radial position $r(s)$ can be expressed as a function of an original (before G&R) position within the arterial wall and local volumetric changes, i.e.

$$r(s) = \sqrt{\frac{2}{\lambda(s)}\int_{r_i(0)}^{r(0)} rJ(r,s)dr + r_i^2(s)} \qquad \textbf{Equation 4-13}$$

where, $r_i(s)$ and $r_i(0)$ are the current and original radii respectively.

At any intermediate time $s = \tau$ during our simulation, we may pause the G&R process and enter an experimental mode whereby we numerically simulate a set of experimental protocols against which to compare the predictions of the model to laboratory results. Accordingly, we define an additional deformation gradient tensor

$$F_1(\tau) = diag\left[\frac{\partial R(\tau)}{\partial r(\tau)}, \frac{R(\tau)}{r(\tau)}, \frac{1}{\Lambda(\tau)}\right] \qquad \textbf{Equation 4-14}$$

which describes the motion from the loaded, *in vivo* configuration at time τ to the unloaded, excised configuration at time τ. In this case, at a fixed intermediate time τ, the incompressibility constraint requires

$$R(\tau) = \{\Lambda(\tau)[r^2(\tau) - r_i^2(\tau)] + R_i^2(\tau)\}^{1/2} \quad \textbf{Equation 4-15}$$

4.2.4 Constituent Production and Degradation

4.2.4.1 PGS and PCL Degradation

The mechanical properties of PGS and PCL are the primary drivers of early G&R response. Motivated by the *in vitro* studies performed in Section 2.3.4.1, we prescribed the following functional form to prescribe the loss of mechanical strength of PGS and PCL.

$$W^{PGS}(s) = \frac{\beta(s)}{2}[I_1 - 3] = \zeta(s)\left[\frac{\beta_0^{PGS}}{2}(I_1 - 3)\right] \quad \textbf{Equation 4-16}$$

Where $\beta_0^{PGS} = 34.43\ kPa$, and $\beta_0^{PCL} = 350\ kPa$ based on the works of Eshraghi and Das who determined the modulus based on uniaxial tensile testing of dog-bone shaped specimens at a displacement rate of 50 mm/min[138].

4.2.4.2 Production of Load Bearing Constituents in Phase I

Data obtained from iTEVG neoarterial development in young and aged hosts was used to develop the functional form of mass production. Notwithstanding the complex phenomenon governing ECM deposition, we assumed that αSMA^{+} synthetic cells (VSMCs and fibroblasts) were the primary producers of collagen and hence prescribed the following form for mass of collagen deposition per unit time per mass of synthetic cells.

$$m_1^{\alpha}(s) = m_{\infty}^{\alpha}\left\{\exp\left(\mathrm{k}_{\mathrm{syn}}(s - offset)\right)\right\} \qquad \textbf{Equation 4-17}$$

4.2.4.3 Production of Load Bearing Constituents in Phase II

Following initial rapid deposition of collagen through synthetic VSMCs under the influence of PGS degradation, the production of fibrillar constituents are assumed to depend upon several mechanical factors. Since neoarterial G&R is guided by homeostatic stresses, we propose a function for intramural and shear stress-mediated rates of mass density production for VSMCs and collagen.

$$m_2^{\alpha}(s) = \frac{\rho^m(s)}{\rho(s)}\xi^m(s)m_{\infty}^{\alpha}(\Upsilon_{\sigma}\{K_{\sigma}^{\alpha}, \Delta\sigma^{\alpha}\} + \Upsilon_{\tau}\{K_{\tau}^{\alpha}, \Delta\tau_w\})/2 \qquad \textbf{Equation 4-18}$$

Where $m_{\infty}^{\alpha}$is the homeostatic mass density production rate, $\xi^m(s)$ is the synthetic ability of VSMCs, and $\Upsilon_{(.)}$ are mechanobiological scaling functions that depend on deviations of transmural

and shear stress from their homeostatic values. The total mass production is a summation of the two phases

$$m^{\alpha}(s) = m_1^{\alpha}(s) + m_2^{\alpha}(s)$$

Intramural Stress Dependence

The mechanobiological scaling functions must capture some of the salient qualitative features of remodeling. Mass production should be negligible for low deviations of intramural stress from homeostatic levels and saturate at higher deviations. The function should reach a maximum sensitivity of K_{σ}^{α} at some intermediate levels of stress deviation. One possible function that captures this behavior is the piecewise sinusoidal function that is dependent on deviations of stress levels from their desired homeostatic levels (Figure 30).

$$\Upsilon_{\sigma}(K^{\alpha}, \Delta\sigma^{\alpha}) = \begin{cases} 0 & \forall\, \Delta\sigma \in (-\infty, l_{neg}), \\ \frac{1}{2} * \left(1 + \sin\left(\omega_{neg}\left\{\Delta\sigma^{\alpha} + b_{neg}\right\}\right)\right) & \forall\, \Delta\sigma \in [l_{neg}, 0), \\ \frac{1}{2} * \left\{\{\Upsilon_{max}^{\alpha} + 1\} + \{\Upsilon_{max}^{\alpha} - 1\}\sin\left(\omega_{pos}\left\{\Delta\sigma^{\alpha} - b_{pos}\right\}\right)\right\} & \forall\, \Delta\sigma \in [0, l_{pos}), \\ \Upsilon_{max}^{\alpha} & \forall\, \Delta\sigma \in [l_{pos}, \infty) \end{cases}$$

Equation 4-19

Where $\omega_{neg} = 2K^{\alpha}$ and $\omega_{pos} = 1.5 + 2K^{\alpha}/(\Upsilon_{max} - 1)$

Saturation limits $l_{neg} = -\pi/\omega_{neg}$ and $l_{pos} = \pi/\omega_{pos}$. Υ_{max}^{α} is the maximum scaling value and offsets $b_{neg} = \frac{\pi}{2\omega_{neg}}$ and $b_{pos} = \frac{\pi}{2\omega_{pos}}$.

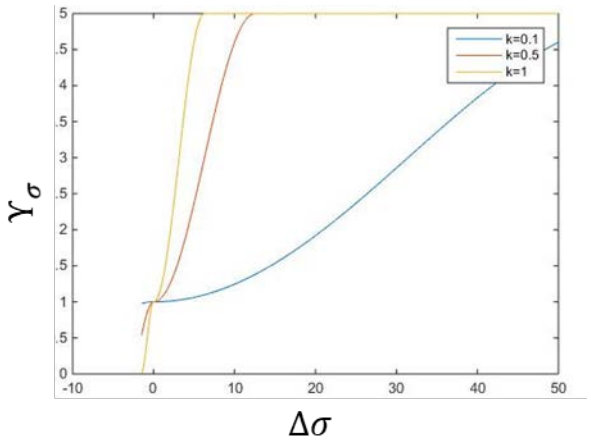

Figure 30: Mechanobiological scaling function modulating mass deposition in response to deviations in transmural stress at different values of k.

$\Delta\sigma^\alpha(s) = \frac{\sigma^\alpha(s)}{\sigma^\alpha(0)} - 1$, which represents the change distortional stress borne by each constituent family where

$$\sigma^\alpha(s) = ||\boldsymbol{\sigma}^\alpha_{dis}(s)\boldsymbol{m}^\alpha(s)|| \qquad \textbf{Equation 4-20}$$

And $\boldsymbol{m}^\alpha(s)$ is unit vector describing fiber orientation. The Cauchy stress distribution resulting from isochoric distortions for a constituent family is

$$\boldsymbol{\sigma}_{dis}^{\alpha}(s) = 2J(s)^{-1}\boldsymbol{F}(s)\frac{\partial W_{dis}^{\alpha}(\overline{\boldsymbol{C}(s)})}{\partial \boldsymbol{C}(s)}\boldsymbol{F}^{T}(s) \qquad \textbf{Equation 4-21}$$

Where $\overline{\boldsymbol{C}(s)} = J^{-\frac{2}{3}}(s)\boldsymbol{C}(s)$ is the modified right Cauchy-Green tensor.

Shear Stress Dependence

The shear-stress dependent function $\Upsilon_{\tau w}(\Delta\tau_w)$ captures the emerging behavior of signaling pathways involving various endothelium-derived factors (e.g., growth factors, mitogens, inhibitors, etc.) which affect the synthesis of ECM and the proliferation of myocytes (Figure 31). We assume that these factors, and by consequence the function $\Upsilon_{\tau w}$, are spatially uniform in the neoartery. Similar to the case for intramural-stress driven G&R, we postulate the form

$$\Upsilon_{\tau}(K^{\alpha}, \Delta\tau_w) = \begin{cases} \{\Upsilon_{max}^{\alpha} + 1\}\Delta\tau_w^2 + 1 & \forall \Delta\tau_w \in [-1,0), \\ \frac{1}{2}\left(1 + \cos\left(\omega_{pos}\Delta\tau_w\right)\right) & \forall \Delta\tau_w \in \left[0, l_{pos}\right), \\ 0 & \forall \Delta\tau_w \in \left[l_{pos}, \infty\right) \end{cases} \qquad \textbf{Equation 4-22}$$

Where, $\Delta\tau_w = \frac{\tau_w(s)}{\tau_w^h} - 1$; $\tau_w(s)$ and τ_w^h are the current and homeostatic shear stress respectively.

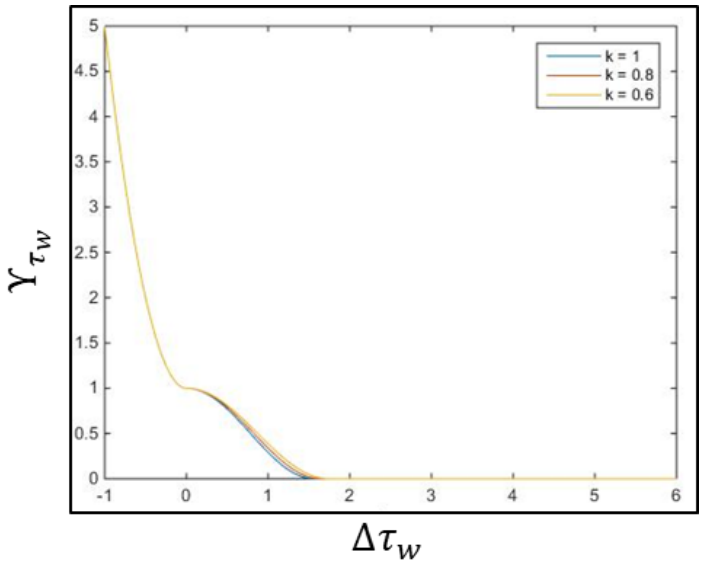

Figure 31: Mechanobiological scaling function modulating mass deposition in response to deviations in wall shear stress at different values of k.

This relation thereby couples the local chemical concentrations to the active response which may be a function of radial position and captures the aggregate mitogenic and synthetic effects of a host of chemical agonists released by the endothelium in response to changing wall shear stress. No deviation from homeostatic values of shear and transmural stress maintains the mass production levels to their homeostatic values and values increase with increase in deviation from homeostasis (Figure 32).

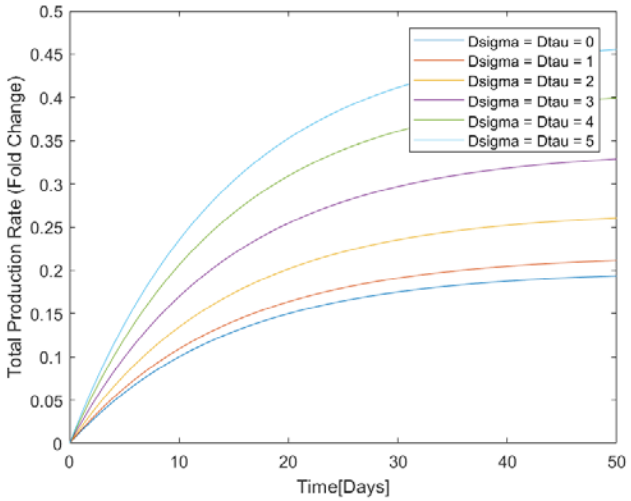

Figure 32: Fold rate of mass production as a function of deviation from homeostatic wall shear stress and transmural stress.

4.2.5 Degradation of Deposited Constituents

As outlined in section 1.5, continuous collagen degradation and deposition (turnover) is one of the fundamental mechanisms of maintaining arterial homeostasis. In order to model this phenomenon, we introduce a survival function that models how much of the constituents deposited during at time τ survive to the current time s.

$$q^{\alpha}(s-\tau) = \exp(-\int_{\tau}^{s} K_q^{\alpha}(\tau)d\tau) \qquad \textbf{Equation 4-23}$$

where, $K_q^\alpha = K_{qh}^\alpha\left(1+\Delta\zeta^\alpha(s)\right)^2$ are the evolving cohort specific rate parameters for mass removal, and K_{qh}^α is the homeostatic rate parameter. This enables us to model mass degradation as a function of the cumulative change of cohort-specific tension level, with

$$\Delta\zeta^\alpha(s) = \left(\frac{\partial\widehat{W}^\alpha}{\partial\lambda_n^\alpha}\left(\frac{\lambda_{n(\tau)}^\alpha(s)}{\frac{\partial\widehat{W}^\alpha}{\partial\lambda_n^\alpha}(G_h^\alpha)}\right)\right)^{-1}$$

being the normalized difference between fiber tensions at times s and deposition time τ within an individual cohort of constituent α. G_h^α is the homeostatic deposition stretch and $\lambda_{n(\tau)}^\alpha$ is the fiber stretch.

4.2.6 Mechanical Properties of Load Bearing Constituents

Collagen Fibers and Passive Smooth Muscle Cells

Collagen and the passive response of VSMCs are modeled using the four-fiber family model with the following strain energy function

$$\widehat{W^\alpha}(\tau) = \frac{c_2^\alpha}{4c_3^\alpha}\left[\exp\left(c_3^\alpha\left\{I_{4_{n(\tau)}}^{\ \alpha}(\tau)-1\right\}^2\right)-1\right] \qquad \textbf{Equation 4-24}$$

where c_2^α and c_3^α are mechanical constants, $I_{4_{n(\tau)}}^{\alpha}(\tau) = \boldsymbol{\eta}^\alpha(\tau).\boldsymbol{C}(s).\boldsymbol{\eta}^\alpha(\tau)$, and $\boldsymbol{\eta}^\alpha(\tau) = \boldsymbol{F}^{-1}(\tau)\boldsymbol{G}^\alpha(\tau)\boldsymbol{M}_{n(\tau)}^\alpha$. The deposition stretch tensor for the fibrillar constituents is the structural tensor $\boldsymbol{G}^\alpha(\tau) = G_h^\alpha(\tau)\boldsymbol{m}^\alpha(\tau) \otimes \boldsymbol{m}^\alpha(\tau)$, where $G_h^\alpha > 1$ is the scalar homeostatic stretch imposed upon the fiber oriented in the direction $\boldsymbol{m}^\alpha$ at time τ.

Elastin

Elastin is modeled as Neo-Hookean material with the strain energy function,

$$W^e(\tau) = \frac{c^e}{2}\left(I_{1_{n(\tau)}}^e(\tau) - 3\right) \qquad \textbf{Equation 4-25}$$

where c^e is a shear modulus and $I_{1_{n(\tau)}}^e(\tau)$ captures the effects of deposition stretches and motions subsequent to the incorporation of elastin. $I_{1_{n(\tau)}}^e(\tau) = tr\boldsymbol{C}_{n(\tau)}^e(s)$, $\boldsymbol{C}_{n(\tau)}^e(s)$ $(\boldsymbol{F}_{n(\tau)}^e(s))^T(\boldsymbol{F}_{n(\tau)}^e(s))$ and, $\boldsymbol{F}_{n(\tau)}^e(s) = \boldsymbol{F}(s)\boldsymbol{F}^{-1}(\tau)\boldsymbol{G}^e(\tau)$. $\boldsymbol{G}^e(\tau) = \boldsymbol{I}$ is the deposition stretch tensor at time τ.

Active Smooth Muscle

We model the active part of the Cauchy stress due to the contractile properties of VSMCs as follows

$$\boldsymbol{\sigma}_{act}(\tau) = f_{act}(\tau)\boldsymbol{e}_\theta \otimes \boldsymbol{e}_\theta \qquad \textbf{Equation 4-26}$$

where and $\boldsymbol{e}_\theta$ is the direction of VSMC orientation and $f_{act}(\tau)$ is a scalar function have the form

$$f_{act}(\tau) = \frac{\rho^m(\tau)}{\rho(\tau)} T_{max}[1 - \xi^m(\tau)][1 - e^{-C^2(\tau)}] \quad \textbf{Equation 4-27}$$

where $\rho^m(\tau)$ is the evolving VSMC mass density, T_{max} is the maximum contractile force generated by VSMCs and $1 - \xi^m(\tau)$ captures the complementary relationship between contractile and synthetic VSMCs. Here we assume a binary representation of VSMC phenotype, recognizing that when more data is available, this representation can be generalized. $C(\tau)$ is the ratio of vasoconstrictors and vasodilators and has the following form

$$C(\tau) = C_b - C_s \Delta\tau_w(\tau) \quad \textbf{Equation 4-28}$$

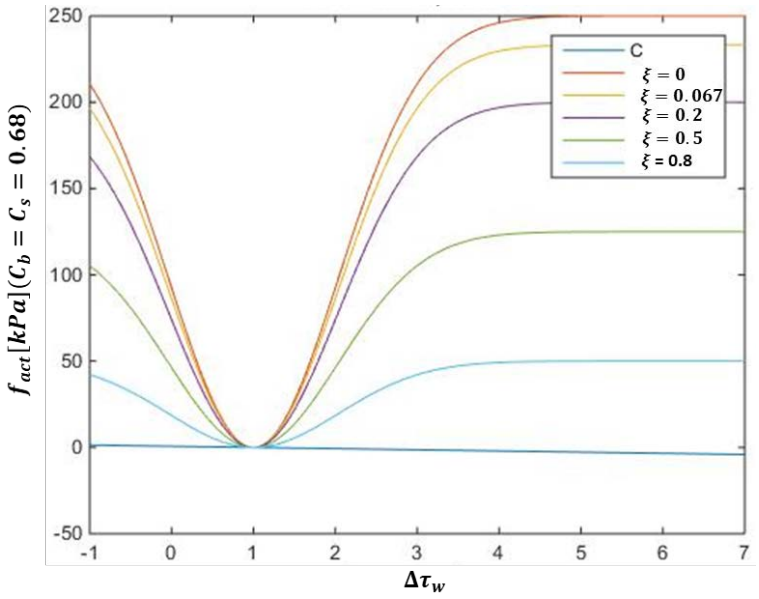

Figure 33: Active force as a function of deviation from homeostatic wall shear stress at different levels of synthetic ability.

As synthetic ability tends 1 (fully synthetic cells) active force generation tends to 0.

f_{act} enables VSMCs to maintain a basal tone at homeostasis and increases vasoactivity with changes in the ratio of vasoconstriction and dilation factors (Figure 33).

Table 5 summarizes the main parameters in the G&R model along with the dimensions. These parameters will be tailored using experimental data in future chapters to model neoarterial remodeling in young and aged hosts.

Table 5: Dimensions of parameters in G&R model

Variable	Definition	General Units [MLT]
$\boldsymbol{\rho}$	Mass density per unit reference volume	$M^1L^{-3}T^0$
$\boldsymbol{\rho^{\alpha}}$	Mass density per unit reference volume of individual constituent	$M^1L^{-3}T^0$
$\boldsymbol{\bar{\rho}}$	Mass density per unit current volume	$M^1L^{-3}T^0$
$\boldsymbol{\overline{\rho^{\alpha}}}$	Mass density per unit current volume of individual constituent	$M^1L^{-3}T^0$
$\boldsymbol{Q^{\alpha}}$	Survival fraction of originally existing material	$M^0L^0T^0$
$\boldsymbol{m^{\alpha}}$	mass density production rate per unit reference volume	$M^1L^{-3}T^{-1}$
$\boldsymbol{q^{s-\tau}}$	Survival fraction at time s of material deposited at time τ	$M^0L^0T^0$
$\boldsymbol{\beta_0^{PGS}}$	PGS shear modulus at time $s = 0$	$M^1L^{-1}T^{-2}$
$\boldsymbol{\zeta}$	Damage function	$M^0L^0T^0$
$\boldsymbol{k_{syn}}$	ECM synthesis rate parameter	$M^0L^0T^{-1}$
$\boldsymbol{\xi^m}$	Synthetic VSMC ability	$M^0L^0T^0$
$\boldsymbol{\tau_w^h}$	Homeostatic wall shear stress	$M^1L^{-1}T^{-2}$
$\boldsymbol{c_2^{\alpha}}$	Fung constant	$M^1L^{-1}T^{-2}$
$\boldsymbol{c_3^{\alpha}}$	Fung constant	$M^0L^0T^0$
$\boldsymbol{G_h^{\alpha}}$	Homeostatic stretch imposed on fibers	$M^0L^0T^0$
$\boldsymbol{c^e}$	Elastin shear modulus	$M^1L^{-1}T^{-2}$
$\boldsymbol{f_{act}}$	Force generated by VSMCs	$M^1L^{-1}T^{-2}$
$\boldsymbol{T_{max}}$	Maximum stress generated by VSMCs	$M^1L^{-1}T^{-2}$
$\boldsymbol{C_b, C_s}$	Vasoconstrictor, vasodilator constants	$M^0L^0T^0$

4.3 Solution Procedure

Neglecting body forces for the quasi-static condition, the balance of linear momentum requires

$$div\ \boldsymbol{\sigma}(s) = 0 \qquad \textbf{Equation 4-29}$$

According to the kinematic assumptions and the material symmetries outlined in Section 4.2.3 , all shear terms vanish, and the global equilibrium equation for this special case is

$$P(s) = \int_{r_i(s)}^{r_a(s)} \frac{\sigma_{\theta\theta}(s) - \sigma_{rr}(s)}{r}\, dr \qquad \textbf{Equation 4-30}$$

where $P(s)$ is the transmural pressure, $r_i(s)$ and $r_s(s)$ are the current inner and adventitial radii, respectively, and $\sigma_{\theta\theta}(s)$ and $\sigma_{rr}(s)$ are the circumferential and radial components of the Cauchy stress, respectively. The Lagrange multipliers vanish in the integrand, and the solution depends only upon the motions and transmural pressure. We therefore calculate the time-varying inner radius which satisfies the global radial equilibrium equation via the secant method.

Spatial integration is performed using the Gauss-Legendre quadrature method, and temporal integrations of strain-energy functions and kinetics are performed using the trapezoidal rule. Evolving mechanical properties and geometry drive mass kinetics, and G&R advances via finite differences in time.

4.4 Conclusions

This chapter describes the mathematical formulation of the G&R theory as applied to iTEVG formation. We provide the forms of constitutive equations for mass kinetics and mechanics of each of the constituents in the mixture. Furthermore, we provide the solution procedure to solve for the evolving morphology and mass density of each constituent. In the next chapter, we will inform this computational model with experimental data specific to young and old neoarterial (YN and ON) remodeling and use it to predict long-term remodeling and understand key mechanisms driving G&R.

Contributions

Dr. Arturo Valentin (AV), a previous postdoctoral researcher in our group, Dr. Anne M. Robertson, and Dr. Paolo Zunino developed the general G&R theoretical framework. AV also developed the first version of the kinematic computational formulation and solution procedure.

5.0 Role of Age in the Biological and Mechanical Evolution of Neoarteries: *In Vivo*, *Ex Vivo* and *In Silico* Study

5.1 Introduction

Synthetic vascular grafts have been an integral tool of vascular surgery as a treatment for atherosclerosis for half a century [139]. However, there remains an urgent need to develop small caliber (<6mm) vascular graft substitutes, especially for the older (>75 years) population where atherosclerosis prevalence rates are as high as 80% [140]. iTEVGs have previously shown successful remodeling in the rat aorta [31]; Chapter 3.0 shows that these grafts can also elicit neoartery formation in the rat carotid artery. Nevertheless, these studies were conducted in young, healthy animals. Translating this success of iTEVGs from young to old animals, across species, or even across different sites in the body is not a trivial task due to the large number of graft (porosity, degradation rate, wall thickness etc.) and system parameters (cellular infiltration, rate of ECM deposition etc.) governing the remodeling response. Hence, there is an unmet need for a sophisticated approach to iTEVG design that can reduce the time and cost for clinical translation.

It is well known that aging elicits changes in vascular biology, ECM, and mechanical response of arteries. For example, older arteries exhibit increased stiffness [141], dilatation [41] and intimal thickening due to VSMC, macrophage and mast cell proliferation [142], [143]. Furthermore, there is reduction in mature elastin formation with age due to an age-associated reduction in lysyl oxidase [144] and increase in Ca^{2+} content [145]. On the other hand, there is an increased production of immature collagen with increased cross-linking in aged arteries which in turn leads to increased tensile strength as the fibers are more susceptible to nonenzymatic glycation

and oxidation [146]. Additionally, as outlined in Section 1.4, there is a change in the remodeling response of old arteries to mechanical cues. While these studies show that arterial structure, function and remodeling are highly age-dependent, very little is known about the effect of aging and diseased conditions on tissue engineered vascular graft development. While some studies have looked at the effects of diabetes and hypercholesteromelia on PCL [147] and PG10 grafts [148], the impact of aging on iTEVG development has not been evaluated.

The G&R model outlined in Chapter 4.0 can be used to aid iTEVG design in old hosts by determining salient mechanisms guiding remodeling. However, in order to improve the fidelity of predictions, there is first a need to acquire age-specific experimental data. Thus, the overall goal of this chapter is twofold – (a) To translate neoartery formation to the clinically relevant aged animal model, and (b) To use a combined theoretical and experimental approach to understand the fundamental differences in remodeling with age and develop a tailored G&R model that can be used for rational design of iTEVGs in older animals. The rationale behind the proposed work is that it is only with a mechanistic G&R tool of this kind, coupled with our rich experimental dataset, that it will be possible to rationally design optimal iTEVG properties for various animal models and ultimately human clinical trials.

5.2 Methods

5.2.1 Graft Fabrication, Implantation and Harvesting

iTEVGs were fabricated using methods described previously [149], [150]. Briefly, the PGS core was formed using a solvent casting and salt leaching method, followed by electrospinning a PCL sheath around the PGS core. The final dimensions of the graft were: inner diameter = 800μm, PGS wall thickness = 330μm, PCL thickness = 20 μm, length = 1cm. Grafts were finally lyophilized, sterilized with gamma irradiation, and soaked in a heparin solution (100 U/mg) for 5 min before implantation.

All procedures involving animals were approved by the Institutional Animal Care and Use Committee at the University of Pittsburgh following NIH guidelines for the care and use of laboratory animals. Male and female Sprague Dawley rats (young = 8 to 9 weeks old; n = 38, old = 18 months old; n = 38, Charles River Laboratories, Wilmington, MA) were used in this study. TEVGs were implanted in both, young and aged groups using interposition, end-to-end anastomosis grafting, using interrupted 10-0 polyamide monofilament sutures (AROSurgical, Newport Beach, CA) [149]. A high-frequency ultrasound imaging system (Vevo2100, FUJIFILM Visualsonics, Toronto, Canada) was used to monitor the inner diameter and flow velocity mid-graft at days 14, 30, 60, 90 and 180 days after implantation. Remodeled neoarteries were harvested at 3, 7, 14, 60, 90- and 180-days post-implant for the young animals, and days 90 and 180 for the old animals.

5.2.2 Mechanical Testing with Simultaneous Multiphoton Imaging

Explanted young and old neoarteries (YNs, ONs) were tested using our custom-designed biaxial-inflation system that is compatible with the multiphoton microscope (MPM) as previously described [151]. Briefly, *in vivo* axial strain was calculated using the distance between anastomosis pre and post-explant. The inner and outer diameters were measured using a thin excised segment of the neoartery under a dissection scope prior to testing. Entire neoartery segments were mounted on cannulae and 350-400 μm beads were glued along their length. The vessel was then immersed in a saline bath within the biaxial testing device which was placed under the multiphoton microscope (Olympus FV 1000 Multiphoton) for collecting second harmonic excitation from collagen fibers and two photon emission signals from elastin fibers. A 1.12-NA 25× multiphoton excitation (MPE) water-immersion objective was placed on top of the mid-neoartery segment for imaging. Preconditioning was performed by first pressurizing the neoarteries to 80mHg and stretching them from the unloaded to the *in vivo* axial strain level four times. This was followed by stretching neoarteries to the *in vivo* axial strain and cyclically pressurizing them from 0-120 mmHg four times. Following preconditioning, the grafts were tested at the following axial strain levels: 0, 10, 20%, *in vivo* strain and 40% axial strains by performing three inflation cycles from 0-120 mmHg at each strain level. The deformation of the vessels was recorded during testing using a video camera (EO-5012C, Edmund Optics, Barrington, NJ) which captures images at 5 megapixels and 6 frames per second. Force was measured using a high precision load cell (MDB-5, Transducer Techniques, Temecula, CA) mounted on one end of the device and axial strain controlled using a computer-controlled actuator (ANT-25LA, Aerotech Inc., Pittsburgh, PA). Outer diameter and axial length were calculated from the raw images using a custom MATLAB (R2014b, Mathworks, Natick, MA) script. MPM imaging was performed by capturing sequential

scans at 2um thickness intervals at two pressure levels – 7mmHg and 120 mmHg, at each of the four axial strain levels used during mechanical testing. SHG signal from collagen was collected using backscatter epifluorescence detectors and 350- to 450-nm Chroma emission filters with a 50 spectral bin.

5.2.3 Data Processing and Image Analysis

5.2.3.1 Stress-Strain Analysis

The inner diameter of the deformed neoarteries was estimated assuming incompressibility of the vessel using the measured unloaded inner and outer diameter, and the deformed outer diameter and length. Together with the assumption of an isochoric deformation, the inner diameter can be estimated using

$$d_i = \sqrt{d_o^2 - \frac{L}{l}(D_o^2 - D_i^2)}$$ **Equation 5-1**

Where, d_o is the loaded outer diameter, D_o and D_i are the unloaded outer and inner diameters and L, l are the unloaded and loaded lengths respectively.

This data was used to calculate the mean circumferential and axial Cauchy stress:

$$\sigma_\theta = \frac{P(r_o + r_i)}{2h};\ \sigma_z = \frac{f}{\pi(r_o^2 - r_i^2)}$$ **Equation 5-2**

where, P is the transmural pressure, r_o and r_i are the loaded outer and inner radii, $h = r_o - r_i$ is the wall thickness and $f = f_t + P\pi r_i^2$ is the total axial force supported by the vessel wall with f_t being the force measured by the load cell.

Circumferential and axial stretch were calculated as follows:

$$\lambda_\theta = \frac{r_o + r_i}{R_o + R_i}; \qquad \lambda_z = \frac{l}{L} \qquad \textbf{Equation 5-3}$$

where, R_0 and R_i are the unloaded outer and inner radii and other variables were previously defined. The stretch is calculated mid-surface, appropriate for the thin walled vessels.

5.2.3.2 Collagen Fiber Orientation and Recruitment

Collagen fiber orientation was quantified using CT-FIRE [152] to trace and extract collagen fiber metrics. The first step of this method is to apply a threshold to form a binary image. Next, a distance transform is performed to yield the distance from each foreground pixel to the nearest background pixel. Then, the maximal ridges formed by the distance transform are searched to create a list of nucleation points. Branches are formed by extending the fiber from each nucleation point based on fiber trajectory. Short fiber branches are then pruned, and closely associated fibers are connected based on adjustable parameters such as the minimum fiber length, fiber direction, and the distance between adjacent fibers. Each of the planar images, obtained at 2um intervals, was analyzed using the following settings: fiber minimum length = 30, image resolution = 300 dpi and maximum fiber width = 0.5. A central region of interest was chosen such that it was possible to go through the entire wall thickness and avoid edge artifacts (Figure 34).

Fiber angles and straightness values were obtained for each image and heat maps were used to display the values across the wall thickness. Angle $\theta = 0°$ and $90°$ represent fibers aligned in the circumferential and longitudinal direction, respectively. A straightness value of one represents a fully straightened collagen fiber and a value less than one represents a crimped (wavy) fiber.

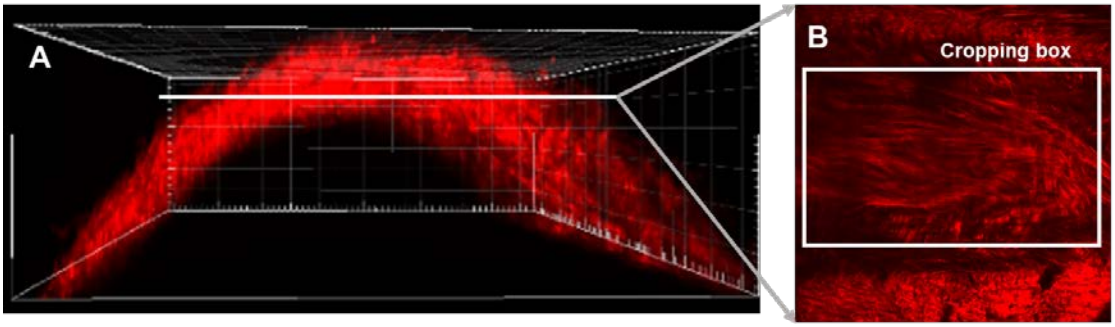

Figure 34: Methodology for selecting image regions for quantifying collagen fiber orientation. 3D reconstruction of collagen fibers imaged using multiphoton microscopy, (B) cross section image with cropping region.

5.2.3.3 Collagen Fiber Density

Collagen fiber density was calculated using 2µm stacks of MPM images. Four non-overlapping regions of interest were randomly selected from different regions of the image for each slice such that each region of interest was completely covered with collagen fibers. Following this, a custom-written MATLAB (Natick, MA, USA) code was used to segment the collagen fibers from the background followed by calculating the area of the segmented region. Collagen areal

density was then calculated as the ratio between the segmented area and total ROI area and summed across all the slices.

5.2.4 Histology, Immunofluorescence and Biochemical Analysis

Neoarteries were fixed in 10% formalin for 1 h at 4°C, and dehydrated in 30% sucrose solution at 4°C for 24 h. Tissue sections were embedded in optimal cutting temperature compound (Sakura Finetek, Torrance, CA), frozen at -80°C for 2 h, and cryosectioned to 8-µm thickness. Tissue slides were stained with H&E and images captured with a high-power magnification (60×) using the NIS-Elements software (Nikon).

As previously described [153], tissue sections (8-µm thick) were fixed with 4% paraformaldehyde for 1 h at 4°C and permeabilized with 0.2% Triton X-100 for 5 min at room temperature. Tissue sites were blocked with 5% normal goat serum (NGS) (Sigma-Aldrich) for 24 h at 4°C, incubated with primary antibodies in 1% NGS for 45 min at 37°C, rinsed twice with PBS, followed with the corresponding secondary antibodies in 1% NGS for 45 min at 37°C. Antibodies used are described in Table S1. Nuclei were counterstained with 4',6-diamidino-2-phenylindole (DAPI) (Life Technologies, Carlsbad, CA) at room temperature for 20 min. Tissue slides without primary antibodies were used as negative controls. The total number of immunofluorescent-positive cells in each sample was calculated as (the area size of the positive staining for each marker / the area size of DAPI positive staining) × 100 and expressed as a percentage of the area. Collagen and elastin content were measured using the Sircol Insoluble Collagen Assay kit (Accurate Chemical & Scientific Corp., Westbury, NY) and the Fastin Elastin Assay kit (Accurate Chemical & Scientific Corp.) respectively.

5.2.5 Endothelial Cell Examination

Endothelial cell coverage and morphology was assessed using SEM and en face immunofluorescence staining as outlined in section 3.2.1.5.

5.2.6 Tailoring G&R Tool with Experimental Data

The final mechanical homeostatic states of YN and ONs were defined as the mechanical properties of the arteries at the final time point. In particular, data obtained from the biaxial inflation experiments for the neoarteries were used to determine best-fit parameters for a two-fiber hyperelastic constitutive model.

$$W = \frac{c}{2}(I_1 - 3) + \sum_{k=1}^{2} \frac{c_1}{4c_2}\left(\exp\left[c_2\left(\lambda^{k^2} - 1\right)^2\right] - 1\right) \quad \textbf{Equation 5-4}$$

where, I_1 is the first invariant of the right Cauchy-Green tensor, c is a material parameter with units of kPa and $k = 1{,}2$ denotes the dominant two fiber directions which were calculated from multiphoton microscopy imaging of collagen fibers (refer to section 5.2.3.2).

Mechanical homeostatic parameters and final time points, along with data from histological assessment up to six months were then used to determine rate constants for our G&R tool. Predictions from the model were validated against experimental measurements of mass deposition, changes in morphology and mechanical response over the course of six-months. This validated tool was then used for parametric studies to assess the impact of various parameters on neoartery

formation over the course of a year. For example, we used the tool to understand the role of two main rate parameters – graft degradation rate and ECM deposition rate on ON formation making it possible to develop strategies for attaining stable long-term remodeling in aged hosts.

5.3 Results

5.3.1 Successful Remodeling Six-Months Post-Implant for both Young and Aged hosts

Pre-implantation, our graft comprised of a solvent cast, salt leached PGS core (inner diameter = 768 $\pm$ 24µm, wall thickness = 391 $\pm$ 23µm, porosity = 72.8 $\pm$ 1.9%) and an electrospun PCL sheath (23 $\pm$ 14µm) (Figure 35A). By six-months post implant, the iTEVGs had visibly remodeled into neoarteries in both young and aged hosts, without any visible signs of adverse remodeling (Figure 35B). We can see a translucent arterial structure with vasa vasorum on the adventitial surface of the neoarteries in both young and aged hosts. Successful remodeling of these grafts was observed, with primary patency rates of 90.6% and 81.25% in young and aged hosts respectively (Figure 35C).

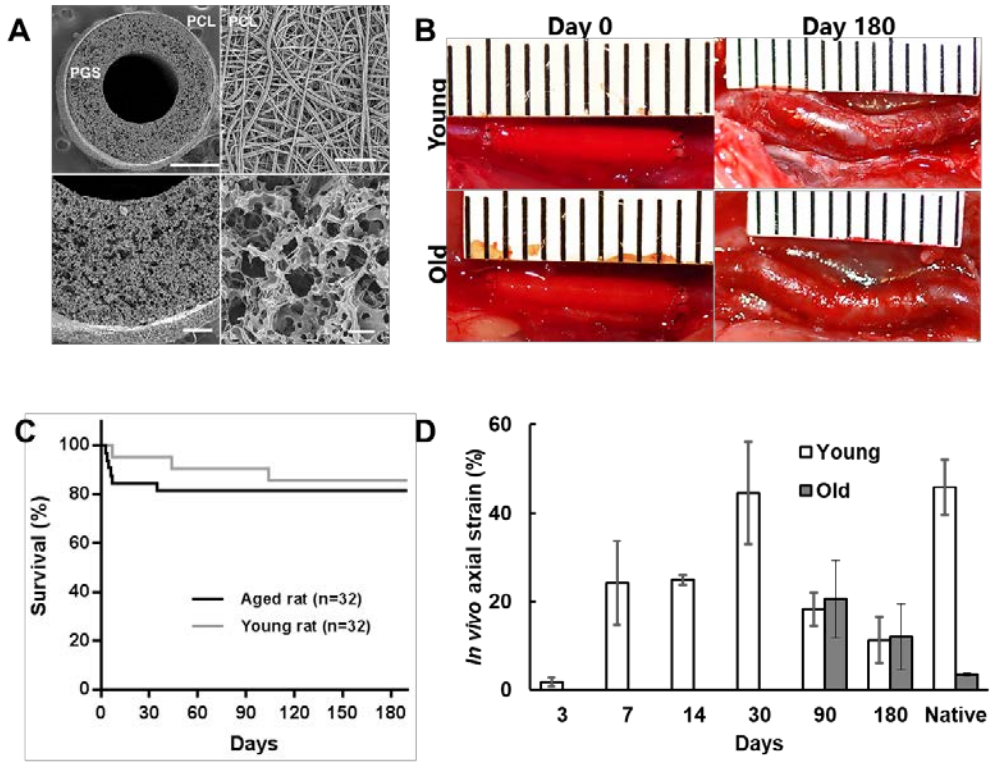

Figure 35: Neoartery development in young and aged hosts

Scanning electron microscope image of bilayered graft comprised of a solvent cast salt leached PGS core and electrospun PCL sheath. (B) Gross images of interposition grafts immediately after, and 180 days post-implantation, (C) Survival curve, (D) *in vivo* axial strain in young and aged hosts over 180 days post-implantation.

Six old rats in the study died due to natural causes. For both the young and old hosts, the primary modes of graft failure in the iTEVGS were rupture and dilation. Rupture (n = 1, 4 for YN, ON respectively) for both the groups was observed at early time-points, between days 4 – 7, while dilatation (n = 2, 1 for YN, ON respectively) occurred anywhere between 35 – 105 days post-implant. The PGS grafts were implanted at no axial strain. As remodeling commences, there was an increase *in vivo* axial strain increased over one-month followed by a decrease until six months

post implant in young hosts. There was no significant difference in *in vivo* axial strain at three and six months with age Figure 35D.

Histological H&E evaluation showed heightened cell infiltration in YNs starting at day 7 post-implantation. Starting one-month post-implantation, there was an associated collagen deposition and formation of a bi-layered YN (Figure 36A). This response is delayed in old hosts wherein a bi-layered neoartery is seen only at six months post-implantation along with heightened cellular infiltration. Morphological evaluation based on the histology images shows that young hosts maintained their wall thickness over time while old hosts showed significantly increased wall thickness and reduced luminal area at three and six months (Figure 36B, C).

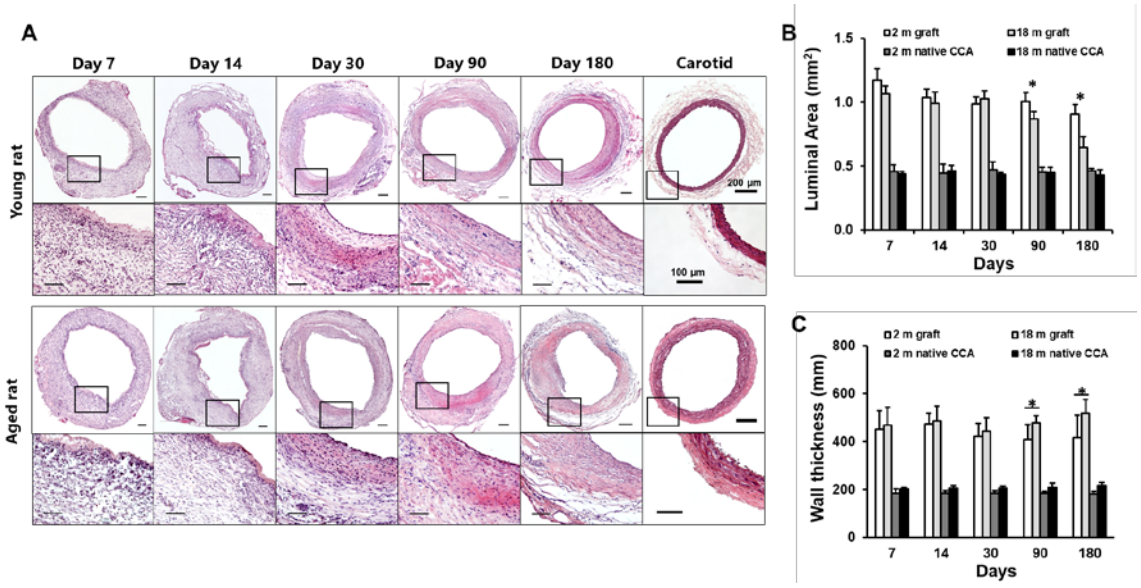

Figure 36: Histological and morphological assessment of neoarteries in young and aged hosts. (A) Representative H&E images of neoarteries at each time point. Scale bar = 200 µm, 100µm in the main and zoomed in images respectively. (B) Luminal area and (C) Wall thickness quantified using H&E images for young and aged hosts.

5.3.2 Phases of Neoarterial Remodeling

5.3.2.1 Two Phases of Cellular Remodeling in Young and Aged Hosts

The neoarteries exhibited two phases of cellular remodeling. Phase I lasted for 14 days post-implant and was marked by a peak in the inflammation (M1 macrophage) response. This was followed by phase II wherein the M1 response is virtually resolved in young hosts. In this section we outline the cellular and mechanical evolution of neoarteries in both phases along with the differences in remodeling response with age.

Phase I (Day 0 – 14)

Phase I cellular remodeling response for both young and aged hosts was dominated by a heightened inflammatory cell infiltration comprising primarily of neutrophils and M1 macrophages (Figure 38). ONs exhibited significantly higher M1 infiltration than YNs (Figure 38B). Importantly, the M1 response for YNs was almost completely resolved by the end of phase I, whereas M1 macrophages continued to proliferate in ONs. M2 macrophages were virtually absent in this phase across both age groups. The YNs also show increased vascularization starting at day 7 based on the gross appearance of the neoarteries, while ONs demonstrated delayed vascularization (Figure 37). VSMCs are the other dominant cell type seen in neoarterial remodeling. Both YNs and ONs displayed increased VSMC infiltration over time. ONs had significantly more αSMA+ cells by the end of phase I in comparison with YNs (Figure 39B).

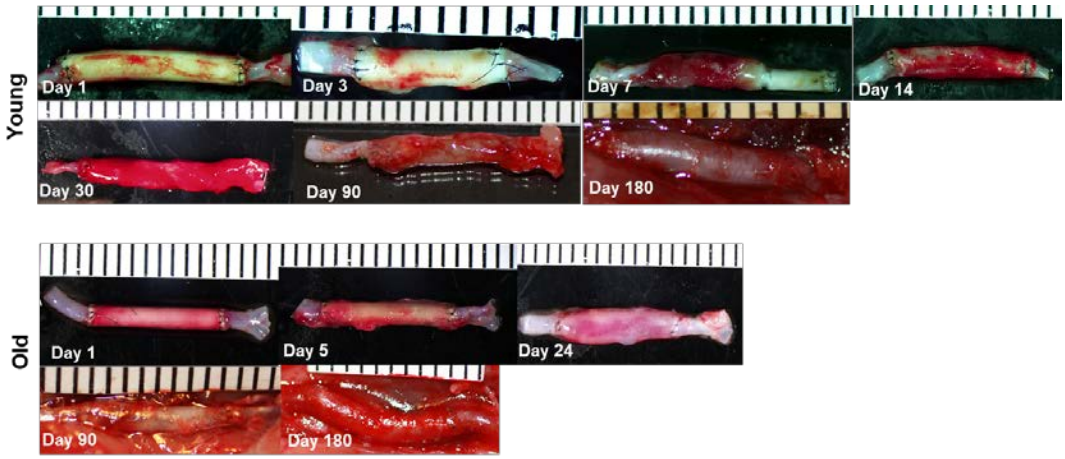

Figure 37: Images of gross remodeling of neoarteries in young and old hosts over the course of six months.

Phase II (post Day 14)

For YNs, phase II remodeling response was comprised of a significant reduction of the M1 response accompanied by a switch in macrophage phenotype to M2 macrophages (Figure 38) along with increased vascularization (Figure 37). While there was a reduction in the M1 response in ONs, they still exhibited statistically higher number of M1 macrophages than YNs in phase II. Furthermore, ONs also showed statistically lower levels of M2 macrophages from days 90 through 180 than YNs. Continuing on the same trend as phase I, there was increasing VSMC proliferation in both age groups with ONs exhibiting significantly higher number of αSMA+ cells in comparison to YNs (Figure 39B). This led to an intimal hyperplasia like accumulation of αSMA+ cells in the intimal region of ONs causing them to have increased wall thickness (Figure 39). In contrast, YNs did not have increased wall thickness at six months and presented αSMA+ cells in the luminal as well as adventitial regions of the wall.

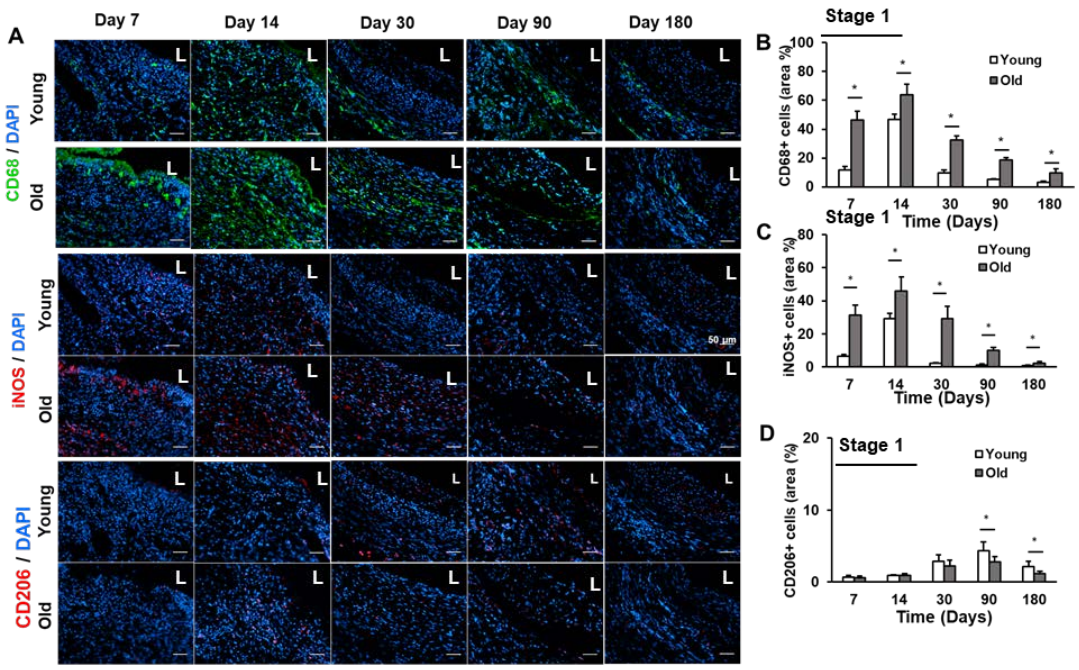

Figure 38: Macrophage staining and quantification.

Representative images of (A) macrophages (CD68 positive cells), M1 macrophages (iNOS positive cells), and M2 macrophages (CD206 positive cells). Scale bar = 50μm and L indicates lumen. Quantification of area fraction occupied by (B) all macrophages, (C) M1 and (D) M2 macrophages over time in young and aged hosts.

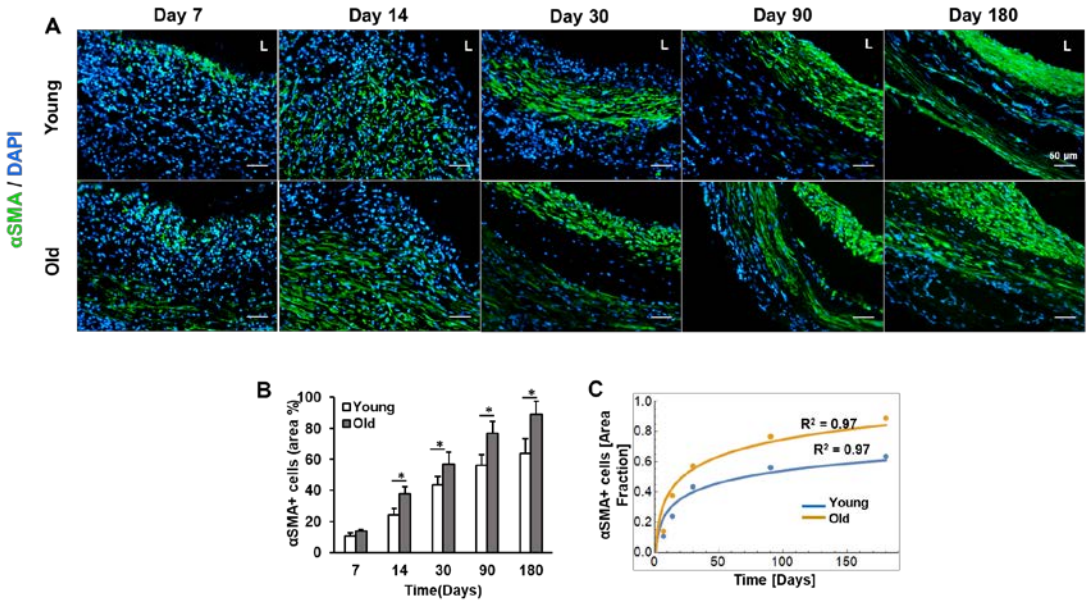

Figure 39: Smooth muscle cell staining and quantification

Representative images for smooth muscle cells (αSMA positive). Scale bar = 50μm and L represents the lumen. (B) Quantification of VSMC area fraction as a function of time. (C) Best-fit line for VSMC area over time.

5.3.2.2 Two Phases of Mechanical Remodeling in Young Hosts

The two phases of cellular remodeling in neoarterial formation were accompanied by a concurrent two-stage mechanical remodeling response for both the circumferential and axial mechanical response of YNs.

Phase I (Day 0 – 14)

Phase I is dominated by fast degradation of the PGS core which leads to a drastic reduction in stiffness of the iTEVG (Figure 40). We also observed collagen deposition as early as 6 days presumably due to the presence of αSMA+ cells (VSMCs and myofibroblasts). This rapid loss of

load bearing ability by the graft was compensated by the rapid deposition of sparse, disorganized, scar-like collagen (Figure 41, row 1) leading to a stiffening of the YN response. YNs in phase I lack of distinct collagen fiber layers that are typical of native arteries and exhibit a uniformly disorganized structure across the wall thickness (Figure 41, row 1).

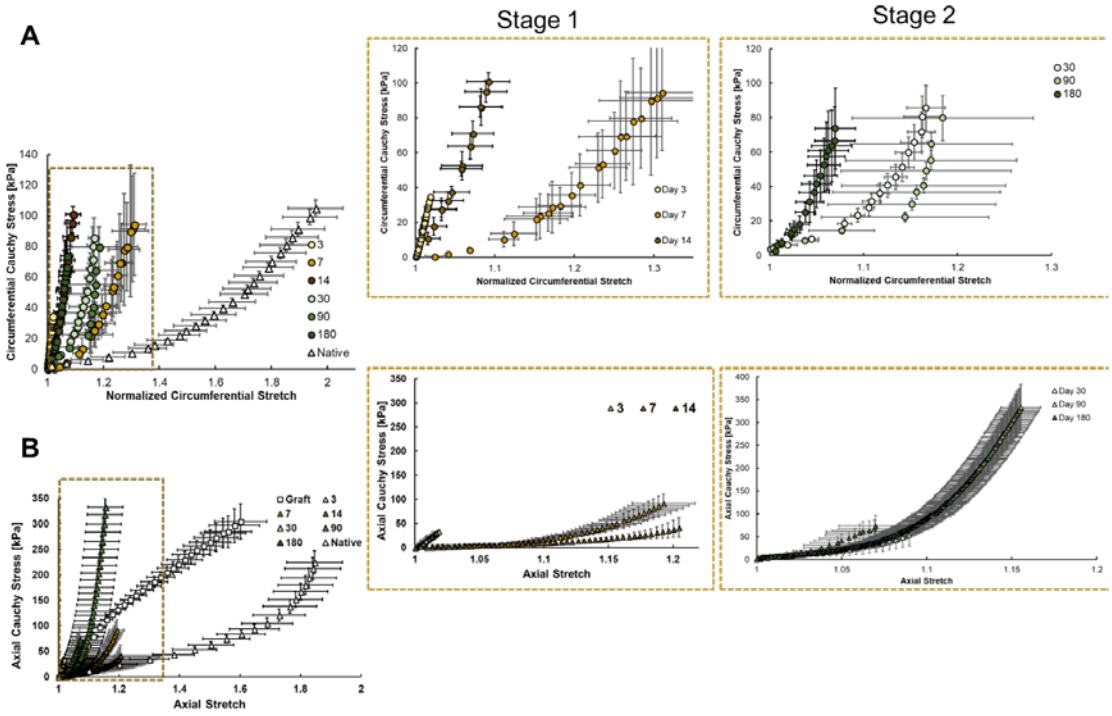

Figure 40: Mechanical stages of remodeling in young hosts.

(A) Circumferential and (B) Axial stress-stretch response as a function of G&R time. Note the two stages of remodeling observed. Stage 1 corresponds to rapid softening due to graft degradation followed by rapid ECM deposition at Day 14 that compensates for the loss of load bearing ability by the graft. Stage 2 is dominated by minor adjustments in the stress-stretch response, potentially due to environmental bio-chemo-mechanical cues.

Phase II (post Day 14)

Phase II response is dominated by change in collagen microstructure and ECM deposition in response to local microenvironment (bio-chemo-mechanical stimuli). This phase exhibits a non-monotonic change in the circumferential and axial stress-strain mechanical response in which there is an initial softening (day 14 – 90) followed by stiffening at day 180. The deviations in mechanical response tend towards a particular set point indicating that the neoarteries are potentially remodeling to achieve a constant homeostatic stress state (Figure 40A, B insets). The YN parameters of the four-fiber family model also demonstrate the non-monotonic mechanical response (Table 6) observed in Figure 40.

Table 6: Parameters of four-fiber family model for young and old neoarteries as a fuction of G&R time

Young							
Days	**c (kPa)**	**c11 (kPa)**	**c21**	**c12 (kPa)**	**c22**	**c13 (kPa)**	**c23**
14	867.33	1939.27	3.897	76700	7.253	25772	0.0007
30	369	130000	19.6	52500	10.8	17900	0.316
90	0.298	212539	11.453	234152	20.36	4873	20.63
180	0.034	76411	330.37	363323	41.83	5831	86.91
Old							
90	157.69	1743.37	8.742	56588	15.43	1652	14.96
180	108.72	10308	5.704	878933	169.77	20909	15.52

Remarkably, as early as one month, the YN microstructural remodeling leads to the formation of a bi-layered wall structure. In particular, these walls display an adventitia-like layer with thin fibers on the abluminal side (Figure 41, row 2). Below this, is a media-like layer which is comprised of crimped collagen fibers that are recruited upon loading, behavior that is typical of native arteries[12]. Furthermore, these collagen fibers also exhibit fiber re-orientation upon loading, especially fibers in the adventitial layer (Figure 42, row 2). These adventitia and media-like layers persist up to three months (Figure 42, row 3). YNs at three months also exhibit a very high degree of fiber re-orientation in all layers of the wall from the axial to circumferential direction (Figure 42, row 3). At six months, the YN s exhibit a different response from those at one and three months. Remodeling in YNs leads to the loss of two layers seen at earlier time-points and leads to the formation of a dense, thin, isotropic collagen fiber structure across the entire wall thickness (Figure 41, row 4). These neoarteries do not exhibit crimped collagen fibers or fiber re-orientation even in the unloaded states (Figure 42, row 4).

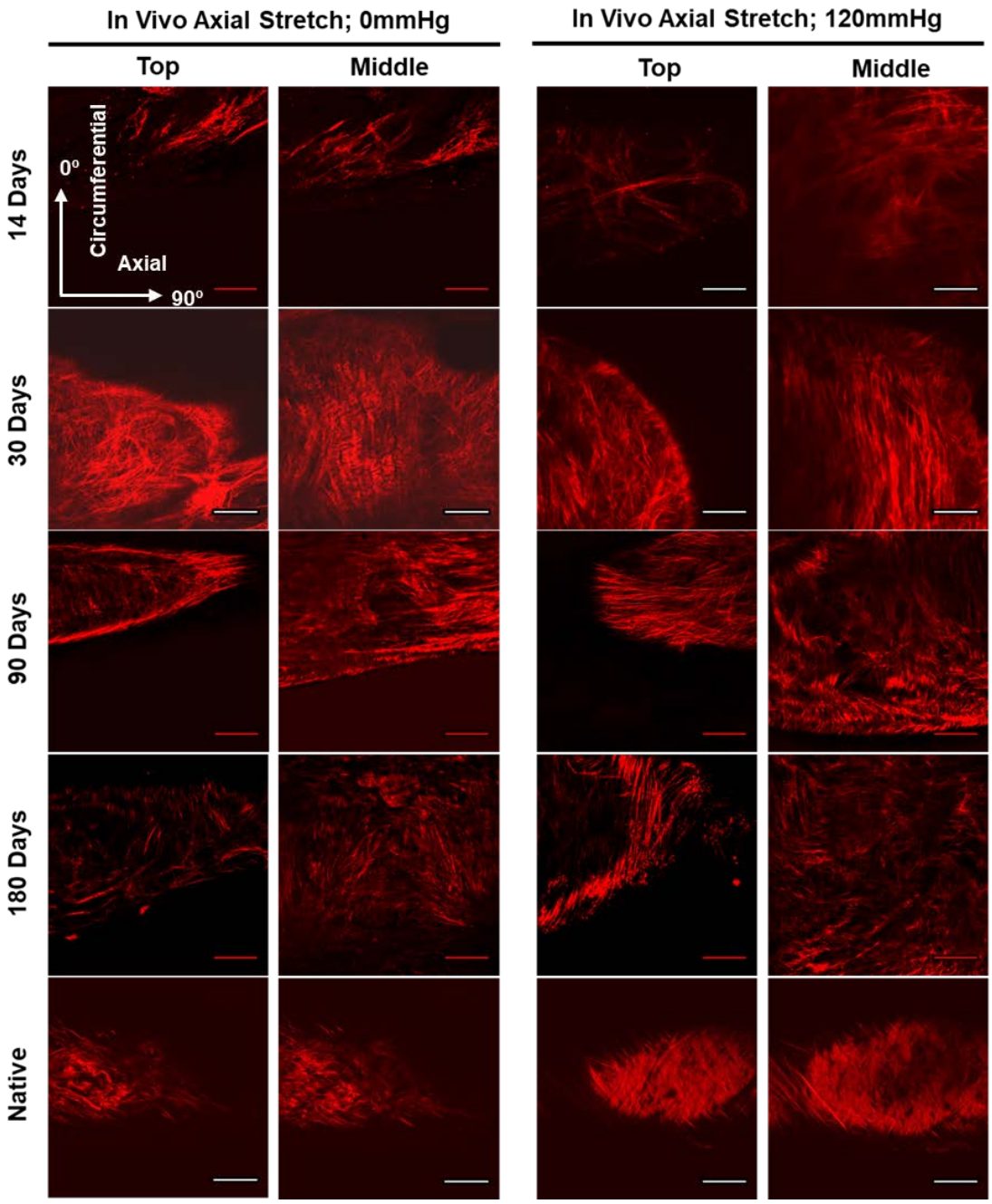

Figure 41: Second harmonic generation images of collagen fibers imaged at *in vivo* axial stretch in young hosts as a function of time.

Collagen fibers imaged at the unloaded (0mmHg) and loaded (120mHg) states across the wall thickness. Note the differences in collagen fiber structure, orientation and waviness in the top and middle layers. Scale bar = 100µm.

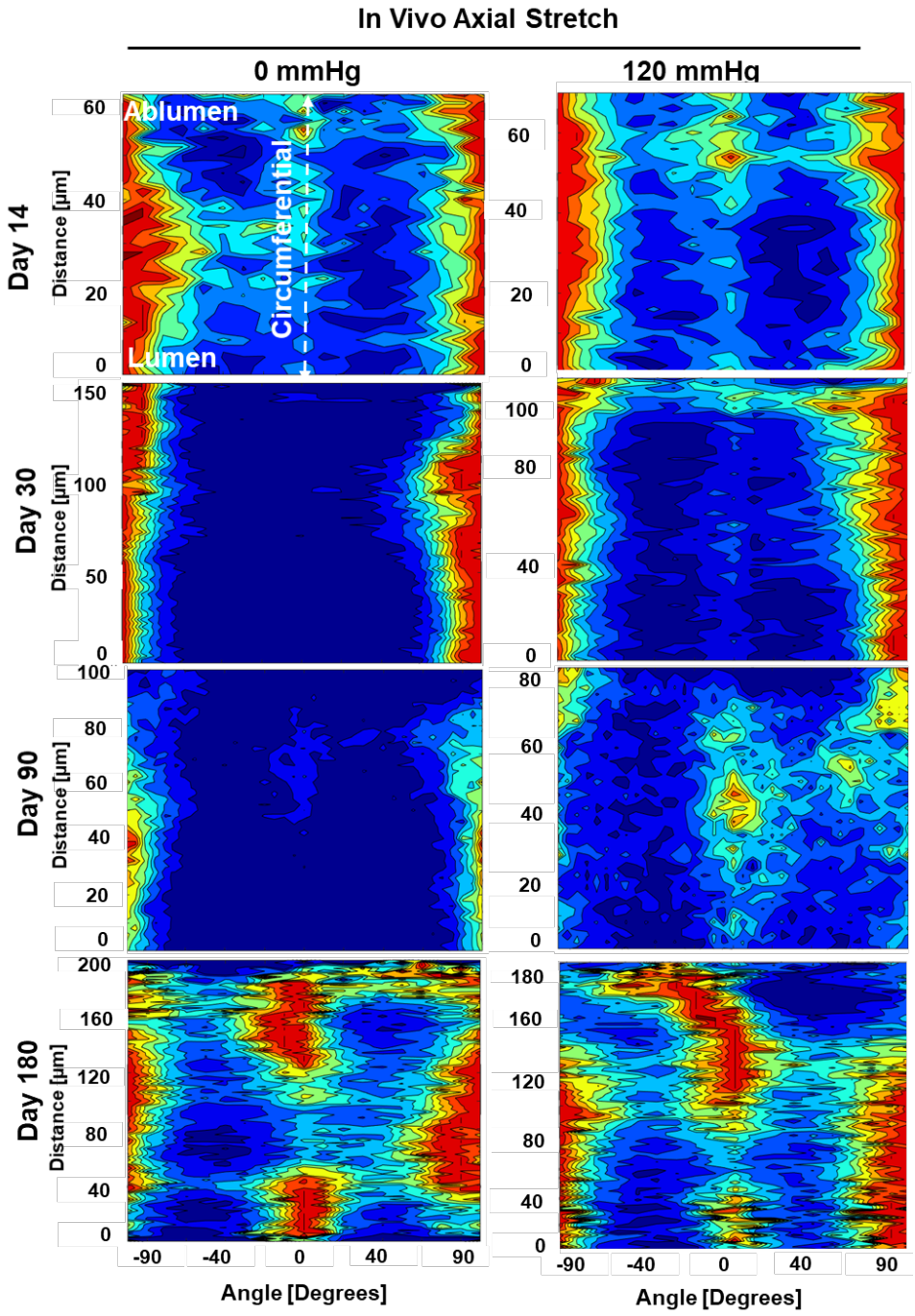

Figure 42: Collagen fiber orientation in young hosts as a function of time.

Collagen fiber orientation quantified using CT-Fire across wall thickness and normalized as a fraction of total traced fibers. 0µm represents the luminal side and 0º represents the circumferential collagen fiber orientation.

ONs exhibit dense, fused collagen fibers that do not have any preferential direction at three months (Figure 43, Figure 44). Furthermore, these fibers do not undergo reorientation or straightening upon loading. At six months, ONs exhibit a highly heterogeneous response with some exhibiting a similar microstructural response as that seen at three months while others forming a bi-layered neoartery. Figure 43 shows one such bi-layered neoartery at six months which displays an outer adventitial layer with thin fibers orientated in two preferential directions followed by an inner medial layer which had circumferentially aligned crimped collagen fibers that straighten upon loading.

Table 7: Comparison of collagen microstructure characteristics in young and old neoarteries

Days	Scar-like	Bi-layered	Isotropic	Crimped fibers	Fiber straightening	Fiber reorientation
	Young					
7	✓			✓		
14	✓					
30		✓		✓	✓	
90		✓		✓	✓	✓
180			✓			
	Old					
90			✓	✓		
180			✓	✓		

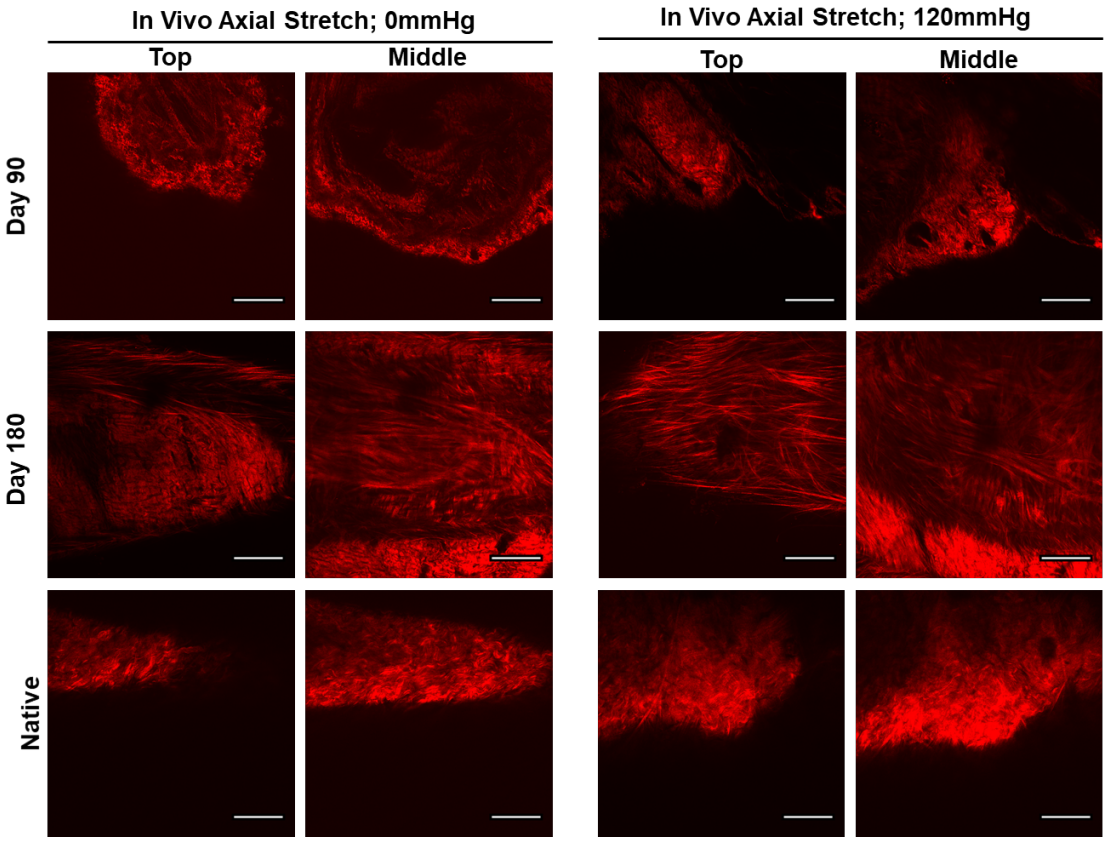

Figure 43: Second harmonic generation images of collagen fibers imaged at *in vivo* axial stretch in old hosts as a function of time.

Collagen fibers imaged across the wall thickness in a neoartery under *in vivo* axial stretch at two inflation levels- the unloaded (0mmHg) and loaded (120mHg) states. Note the differences in collagen fiber structure, orientation and waviness in the top and middle layers. Scale bar = 100μm.

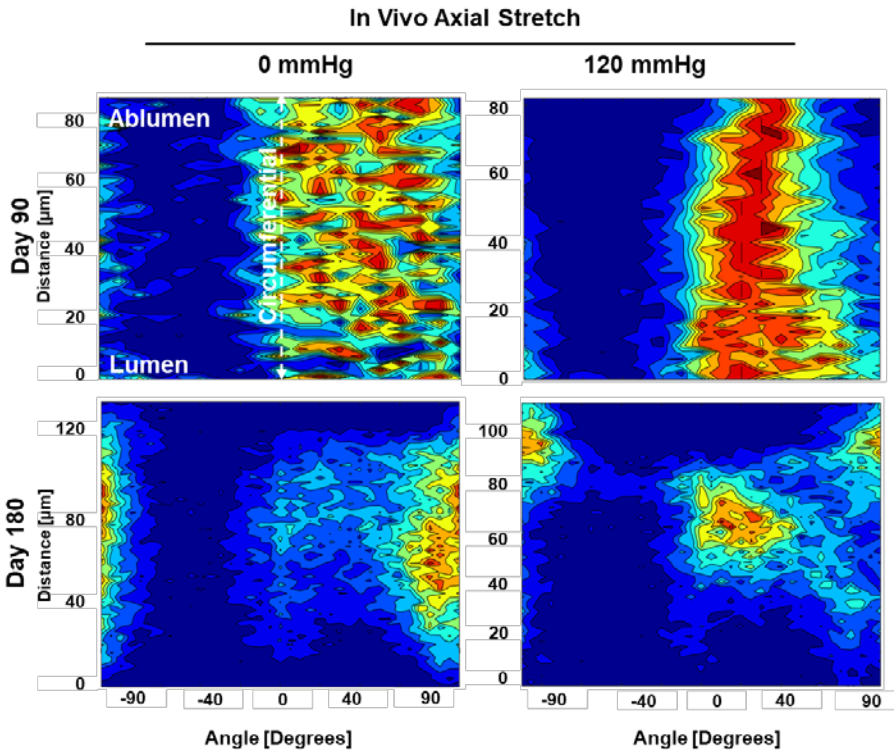

Figure 44: Collagen fiber orientation in old hosts as a function of G&R time. Neoarteries are extended to *in vivo* axial stretch at two pressure levels. Collagen fiber orientation quantified using CT-Fire across wall thickness and normalized as a fraction of total traced fibers. 0μm represents the luminal side and 0° represents the circumferential collagen fiber orientation.

The change in collagen architecture over time includes an increase in collagen fiber density in both YN and ONs and (Figure 45) could potentially be one of the mechanisms causing the observed increase in stiffness.

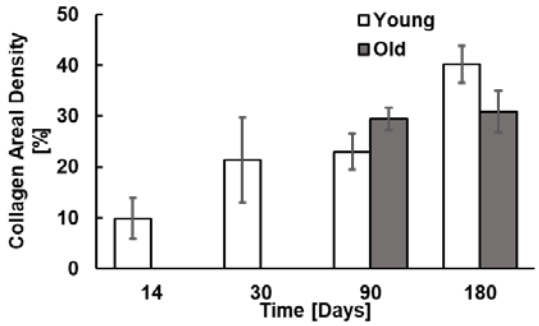

Figure 45: Collagen areal density in young and aged hosts over time.

Collagen fiber density quantified by segmenting area occupied by collagen fibers in multiphoton images across wall thickness normalized by total area. Data available for two time points in older rats.

5.3.3 Differences in End-Stage Remodeling with Age

One of the main differences in end-stage remodeling with age is the VSMC response. The presence the of Ki67 positive, proliferative VSMCs in the intimal region of neoarteries in ONs confirm the presence of hyperplasia-like remodeling at six months post-implant (Figure 46). In contrast, YNs demonstrated a significantly lower number of proliferating cells that did not lead increased wall thickness in the luminal region. . While proliferative VSMCs are observed only in ONs, both YNs and ONs exhibit contractile VSMCs in the medial and adventitial regions.

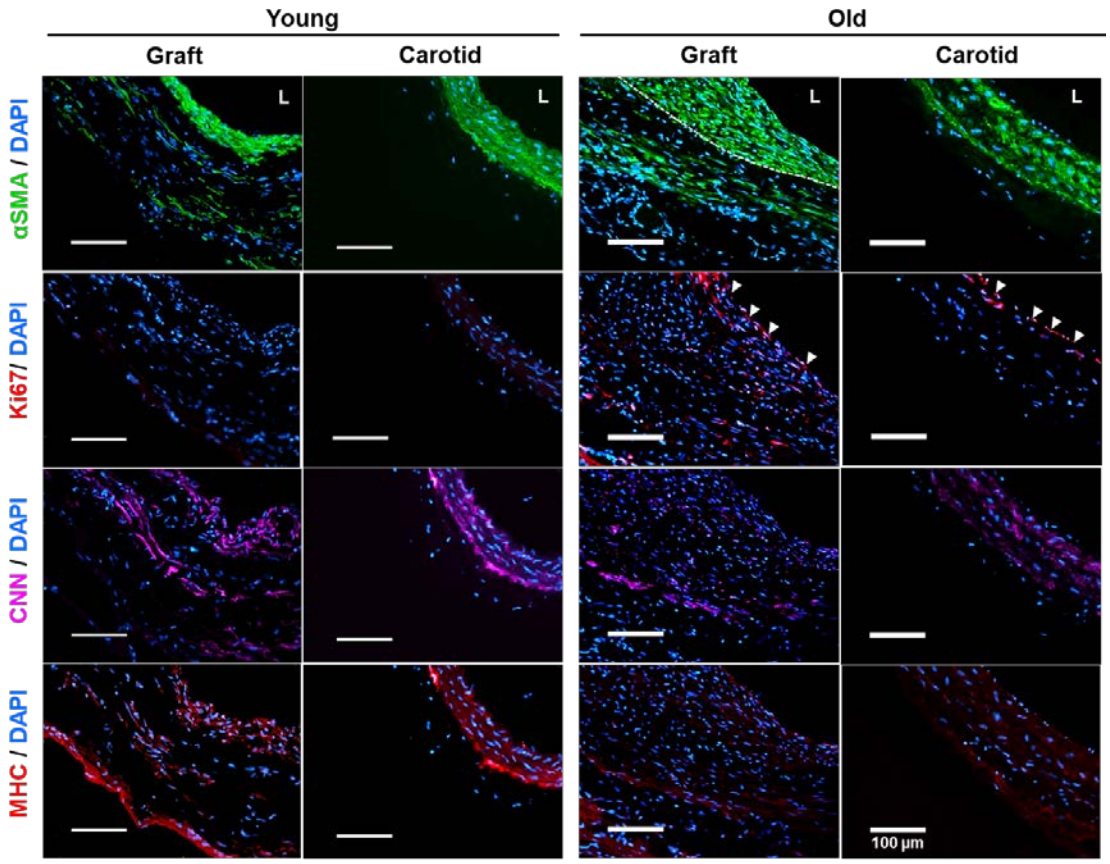

Figure 46: Difference in end-stage cellular response with age.

Representative images of smooth muscle cells (αSMA positive cells), proliferative VSMCs (Ki67 positive cells), and, contractile VSMCs (CNN, MHC11 positive cells) in young and aged hosts at 180 days post-implant.

SEM and CD31 staining confirm the presence of a fully endothelial covered lumen in both YN and ONs at six months. This endothelial lining is oriented in the direction of blood flow as is expected in arterial remodeling.

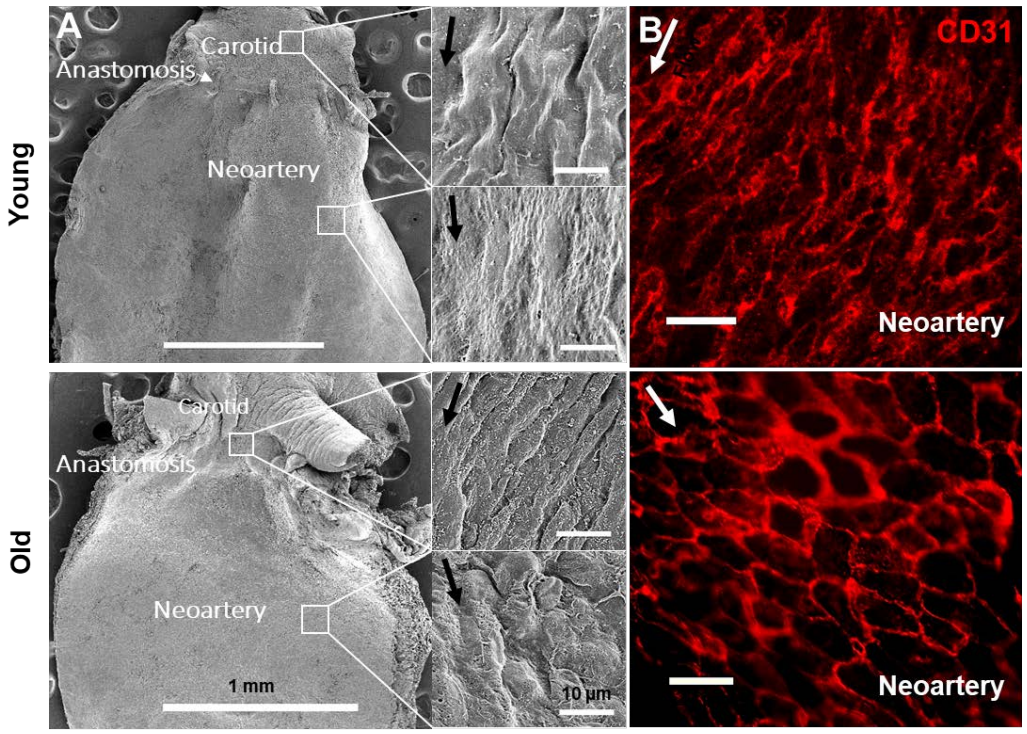

Figure 47: End stage (180 days) endothelial cell response in young and aged hosts. Representative images of endothelial cell coverage, stained en-face, on the lumen of young and old neoarteries using (A) scanning electron microscopy, and (B) CD31 staining, scale bar = 10µm.

Gross ECM evaluation in serial sections using histological methods revealed that collagen I was present in the inner third of the neoarterial walls in both YN and ONs. Interestingly, collagen III was present throughout the wall thickness of YNs while it occurred only in the outer layer of ONs (Figure 48, row 4). Both the YN and ONs lacked the presence of organized, cross-linked elastin.

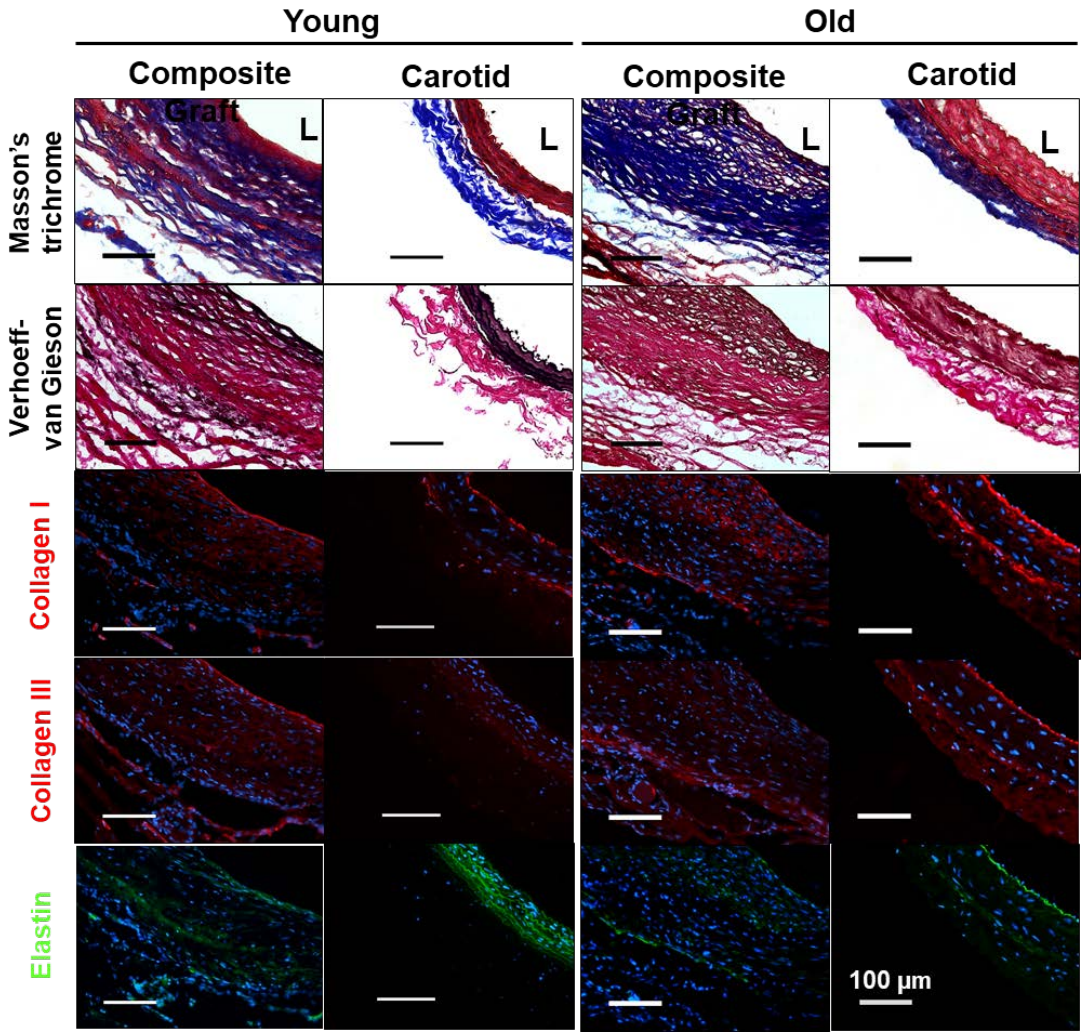

Figure 48: Difference in end stage (180 days) ECM deposition.

Representative images of collagen, including collagen I and III, and elastin architecture as stained using Mason's Trichrome and Verhoeff Van Gieson staining. L indicates lumen.

While both the YNs and ONs stiffened over time, YNs exhibited a 27% higher compliance and 47% lower high strain modulus as compared to ONs (Figure 49). As mentioned earlier, this trend can partially be attributed to the higher collagen fiber density and loss of crimped collagen fibers that are capable of straightening and re-orienting upon loading across both age groups. Furthermore, the significantly increased VSMC proliferation and the presence of calcification in ONs could also contribute to the increase in stiffness.

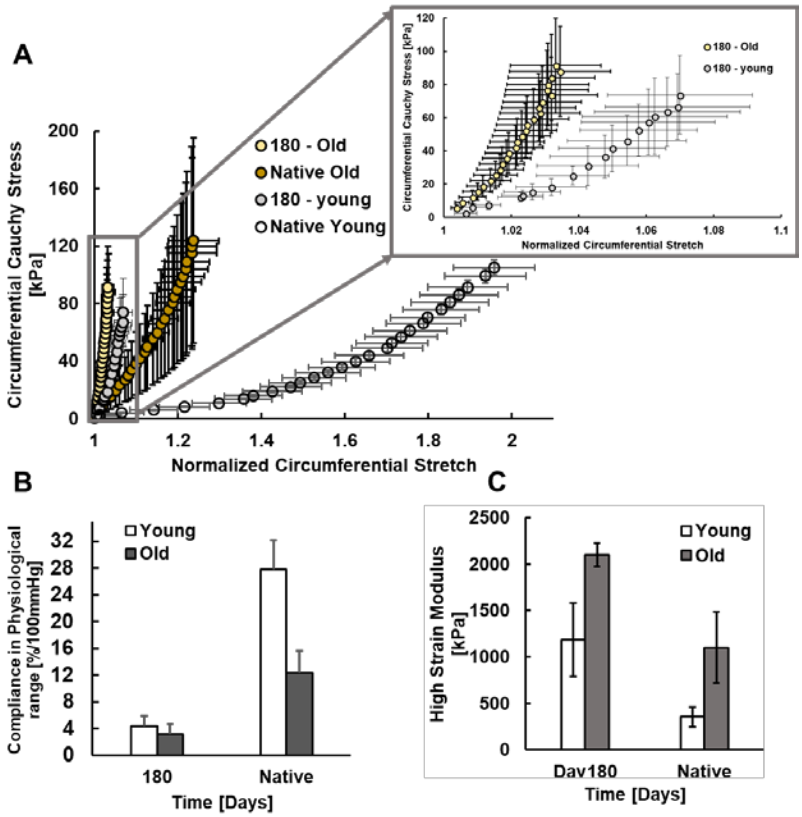

Figure 49: End stage mechanical response with age.

Circumferential stress-stretch curve and (B) compliance of young and old neoarteries at 180 days post-implantation

5.3.4 Validation of G&R Tool

Using data obtained from Chapters 2.0, 3.0, and 5.0, we informed our G&R tool with experimental rate parameters specific to YN and ON remodeling. Table 8 outlines a summary of the main parameters driving the G&R tool.

Table 8: Summary of important G&R parameters in young and old neoarterial remodeling.

Class	Role	Value(s)	
Measured	Initial conditions	P = 93 mmHg, $\tau_w^h = 0.5\ Pa$, $\lambda(0) = 1$, $porosity_{PGS} = 72\%, \rho_{PGS} = \frac{1100kg}{m^3}, \rho_{PCL} = \frac{1145kg}{m^3}$,	
	Initial morphological parameters	$a_h = 800\ \mu m$, $h_{core} = 330\ \mu m$, $h_{sheath} = 16\mu m$	
		Young	**Old**
	Degradation Kinetics	$s_{0.5}^{PGS} = 14\ days, s_{0.5}^{c} = 70\ days$	$21\ days, s_{0.5}^{c} = 50\ days$
	Production kinetics	$k_{syn} = 0.117\ d^{-1}$	$k_{syn} = 0.162\ d^{-1}$
	Mechanical	$c^{PGS} = 34.43kPa$, $c^{PCL} = 0.15MPa$, $c11 = 76411$, $c21 = 330.37$, $c12 = 363323$, $c22 = 41.83$, $c13 = 5831$, $c23 = 86.91$	$c^{PGS} = 34.43kPa$, $c^{PCL} = 0.15MPa$, $c11 = 10308$, $c21 = 5.7$, $c12 = 878933$, $c22 = 169.77$, $c13 = 20909$, $c23 = 15.52$
Assumed	Vasoactivity	$T_{max} = 500\ kPa, C_s = 0.68, C_b = 0.68$	
	Production kinetics	$K_\sigma^\alpha = 1, K_\tau^\alpha = 1$	
	Turnover Kinetics	$K_{qh}^c = \frac{\ln(2)}{70} days^{-1}$	
	Deposition Stretches	$G_h^c = 1.08, G_h^m = 1.2, G^e = 1$	

Predictions from the tailored computational G&R tool were compared with the experimentally observed values for collagen mass deposition and wall thickness over time in both YN and ONs (Figure 50A, B). The tool correctly predicts the reduced collagen deposition observed in phase I followed by increase in collagen deposition over the course of six months. The model also accurately predicts the increase in collagen deposition in ONs versus YNs. The trends in morphological remodeling, i.e. evolution in neoarterial wall thickness is also captured by the model. It correctly predicts that YNs maintain a relatively constant wall thickness over time, whereas ONs have a significantly increased wall thickness at later time-points (three to six months post-implant).

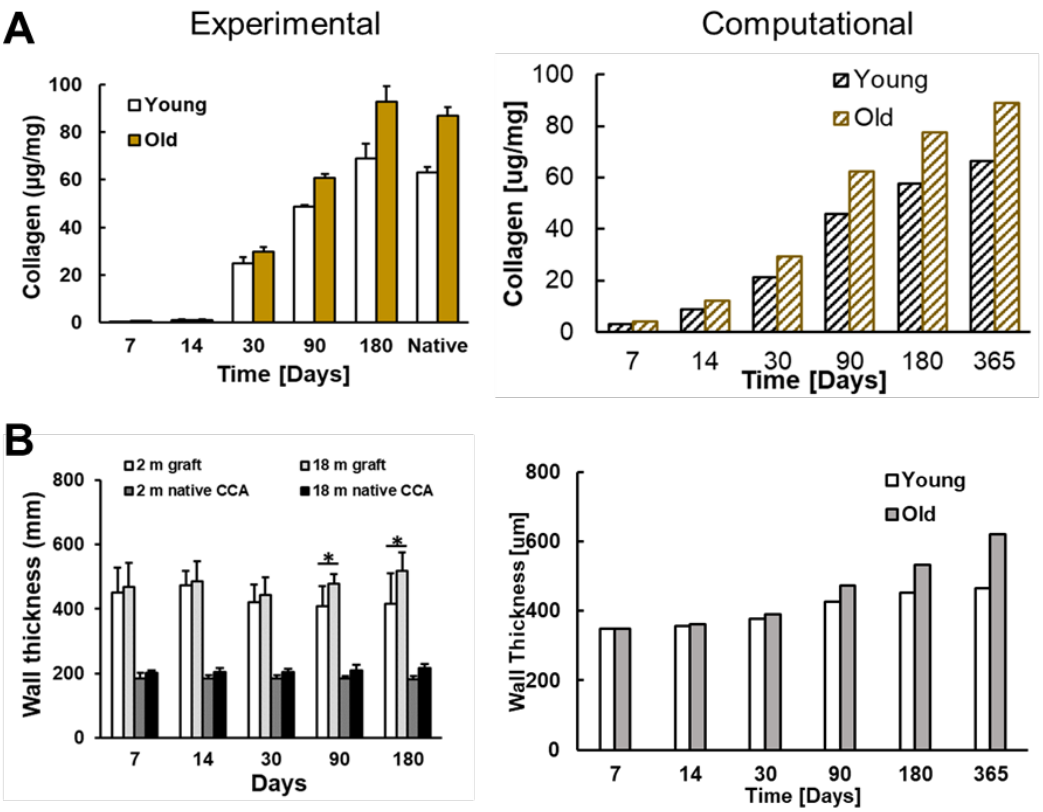

Figure 50: Validation of G&R tool: ECM deposition and morphology

Experimentally observed and computationally predicted (A) collagen mass fraction, (B) wall thickness over 180 days post-implantation.

The pre-implant response of iTEVGs is governed by the stiff PCL sheath which renders the entire graft to be stiffer than native arteries. Following remodeling, the neoartery starts exhibiting the typical nonlinearity associated with native arteries. This phenomenon of transitioning from a stiff, linear graft to a nonlinear stress-strain response, was observed in our G&R simulations (Figure 51). While our G&R model accurately predicts salient governing features of neoarterial remodeling across both age groups, it does not capture the non-monotonic stress-strain response observed in phase II of remodeling. Collagen deposited in both phase I and

II is modeled with the same material parameters. We also do not include a recruitment stretch for collagen fibers in the constitutive equations. Future work will address these limitations and develop these constitutive formulations.

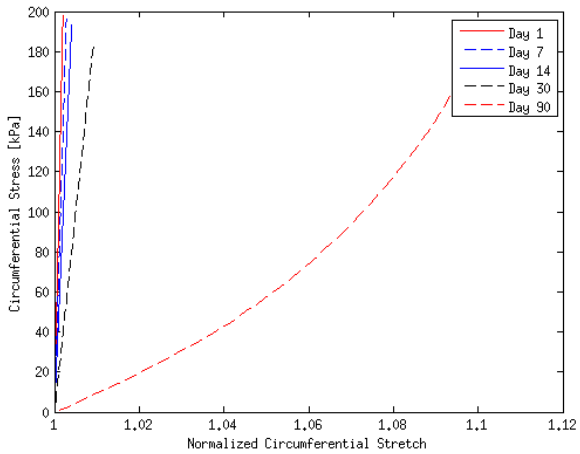

Figure 51: Predicting evolving stress-strech response in neoarteries over time.

The G&R predicts the nonlinear stress-stretch response observed in neoarteries at later time-points.

5.3.5 Primary Drivers of Neoarterial Remodeling: Parametric Study

An *in situ* design strategy relies on the graft-host interaction to develop functional neoarteries. Therefore, the role of graft, as well as host response parameters on remodeling must be understood in order rationally tailor the grafts to specific host targets. In this section, we use the informed G&R computational tool to identify and investigate some of the salient mechanisms driving neoarterial formation in young and aged hosts.

5.3.5.1 Graft Degradation

Appropriate degradation properties of biodegradable grafts are critical for the success of their clinical applications. The degradation rate of PGS grafts can be tuned by adjusting the cross-linking density of PGS and PCL fibers during the curing process [154]. This enables fine-tuning the degradation rate to achieve the desired long-term remodeling response. In this section we report results of parametric studies evaluating the role of degradation rate.

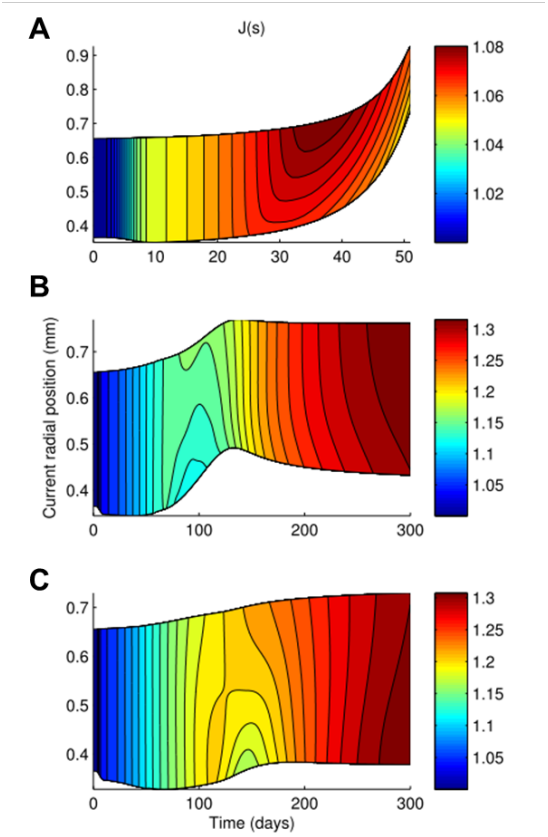

Figure 52: Role of graft degradation half-life on remodeling of neoarteries over time. Predicted time-course of fold-changes in total mass deposition for PGS half-lives of (A) 7 days, (B) 14 days, and, (C) 21 days. Note the unbounded (aneurysmal) growth for short degradation half-life of 7 days.

5.3.5.2 Varying the Degradation Half-Life of the PGS Core can Significantly Alter the Remodeling Morphology, and Mass Density of Neoarteries.

Very fast degradation rates ($S_{0.5}$ = 7 days) lead to unstable remodeling and dilatation of the graft starting as early 30 days (Figure 52A) whereas slightly slower degrading grafts with half-lives of 14 and 21 days show stable remodeling up to a year post-implant (Figure 52B, C). This is presumably because the rate of collagen deposition cannot compensate for the rapid loss of load bearing ability of the degrading graft at very high degradation rates. However, slower degrading grafts can lead to chronic inflammation and osteogenesis[155][130], which are both undesirable outcomes of remodeling. Thus, we determine that there exists an "optimal" degradation rate of 14 days wherein iTEVGs undergo stable remodeling to develop neoarteries. Collagen Turnover Rate

Collagen turnover rate is another major player in wound healing in regeneration. Rapid healing is associated with increased collagen turnover rates [156] and collagen half-lives are organ-specific [157]. In our study, we find that increased collagen turnover rate of 50 days leads to inward, stenotic type remodeling whereas a collagen turnover rate of 70 days leads to stable remodeling at one-year post-implant with PGS degradation half-life of 14 days. Additionally, increased collagen turnover is a hallmark of regeneration and wound healing and leads to increased collagen content. This increased collagen in turn leads to increased to thickening of the neoarterial wall causing stenotic remodeling as observed in Figure 53.

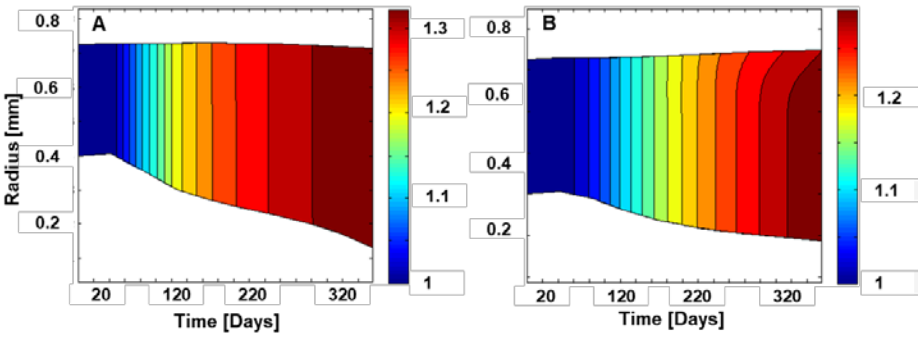

Figure 53: Time-course of fold-changes in mass deposition (J(s)) for collagen turnover rates of (A) 50, (B) 70 days in young neoarteries.

5.3.5.3 Hypertension

Increased wall thickness is the biomechanical manifestation of hypertension. Our simulations suggest that the G&R tool can capture this increased wall thickness observed during hypertension (sustained blood pressure = 180mmHg) (Figure 54). This sustained increased in blood pressure leads to an inward, stenotic remodeling as opposed a to fairly constant wall thickness observed at healthy mean arterial pressure (93mmHg).

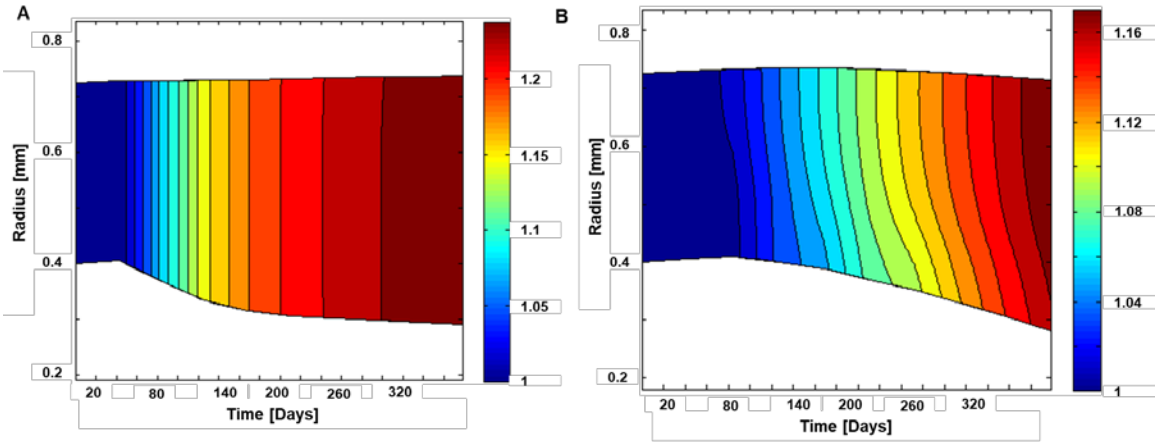

Figure 54: Effect of hypertension on young neoarterial remodeling.

Time course of fold-changes in mass deposition at normal (93mmHg) mean arterial pressure and (B) increased blood pressure (180 mmHg) at a degradation half-life of 14 days.

5.3.6 Combined Role of Graft Degradation and ECM Deposition for Old Neoarterial Remodeling

We used our informed G&R tool to understand the interplay of graft degradation and ECM deposition for improved TEVG design in old hosts. We observe that ONs can fail through stenosis (inward remodeling) with a high graft degradation half-life ($S_{0.5}$) of 7 and 14 days and a high deposition rate (Figure 55A, B). This stenosis can be mitigated by reducing the ECM deposition rate at high PGS degradation rates (Figure 55A, B)). However, simulations demonstrate a practically feasible method to avoid stenosis is to increase the degradation half-life to 21 days, which leads to non-stenotic remodeling at most ECM deposition rates (Figure 55C). ECM deposition can be controlled not only by varying graft degradation but also changing graft porosity

or chemically modifying the graft material to induce higher cell infiltration[130]. Thus, our results indicate that a balance of medium degradation half-life combined with lower ECM deposition rate is required for stable long-term remodeling in old hosts.

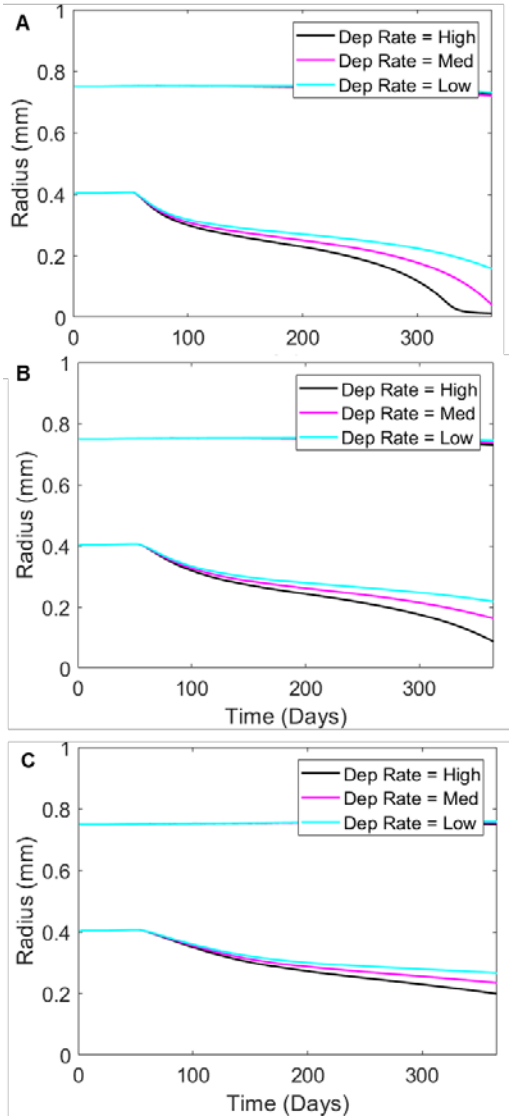

Figure 55: Combined role of ECM deposition and graft degradation on remodeling of old neoarteries over time.

Predicted current radius over time for polymer degradation half-lives of (A) 7 days, (B) 14 days, and, (C) 21 days and different levels of ECM deposition.

5.3.7 Adverse Remodeling in iTEVGs

Aneurysmal type remodeling leading to rupture, and calcification, were the two main modes of adverse remodeling seen in neoartery formation (Figure 56). As discussed in section 5.3.5.1, one of the primary reasons for aneurysmal remodeling is the PGS degradation rate. Regional variations in degradataion rate can arise from variations in degradation rate between grafts. Another cause could be heterogeneity in the host response. Even though the hosts were chosen to have the same genotypic, alterations in their phenotypic response can lead to altered remodeling responses. These factors must be taken into consideration for future studies.

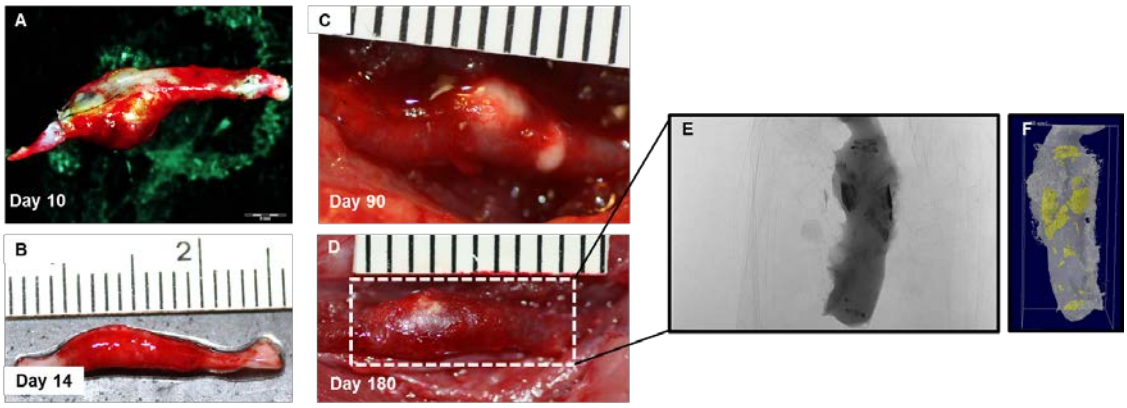

Figure 56: Modes of adverse neoarterial remodeling.

Dilatation (A, B) and calcification (C, D) are the primary modes of adverse remodeling at early and late time-points respectively. (E) Shadow projection of the micro-CT scan of neoartery in (D) and (F) 3D reconstruction of the micro-CT scan. Yellow represents calcification and grey represents tissue.

Since calcification is one of the major modes of adverse remodeling, there is a pressing need to understand the role, cause, and effect of calcification on iTEVG remodeling. 83% of old and 16% of young microCT scanned neoarteries exhibited calcification formation in later timepoints. As a first step toward determining the role of calcification in remodeling, we developed tools and methodologies for analyzing the distribution and size of calcification in a parallel model system with similar modes of failure – human cerebral aneurysms [158]. We further developed protocols for simultaneous imaging of calcification and collagen fibers in intact specimens (details in Appendix B)[159]. In the next chapter we employ these tools to study the prevalence and role of calcification in human cerebral aneurysms (CA). CAs are focal dilatations of the arterial wall caused due to loss of arterial elastin. CAs also have to undergo rapid remodeling in order to compensate for the loss of elastin. There is remarkable diversity in the remodeling response of CAs with some walls remodeling to be stronger than others [160]. Thus, they represent a model system in which the role of calcification in remodeling can be assessed. Understanding the role of calcification in this system can provide us guidance for future studies as well as for designing mitigating strategies for successful long-term neoarterial remodeling.

5.4 Discussion

To our knowledge, this is the first study that translates neoartery formation to old animals, determines factors responsible for *in situ* recapitulation of ECM structure and function, and systematically investigates the role of iTEVG and host parameters in long-term remodeling.

5.4.1 Two Phases of Remodeling

We observe that G&R in is a nonlinear process with an initial graft degradation and inflammation dominated phase followed by a phase of microenvironment driven mechanical remodeling toward a homeostatic state (Figure 57). Both young and old hosts exhibit these two phases, albeit with different rates. Porous PGS grafts lose about 50% of their mass *in vitro* under enzymatic degradation by 8 days [150]. *In vivo*, this passive degradation is combined with inflammation-driven active degradation which leads to a very rapid loss of load bearing by the PGS core. This loss of load bearing ability is compensated by rapid, scar-like, disorganized collagen fiber deposition starting at day 6. These collagen fibers are highly sparse and crimped at 6 and remodel to develop straightened collagen fibers as the PGS continues to degrade until day 14. The key cellular players that guide this response in phase I are M1 macrophages and some VSMCs and myofibroblasts that deposit collagen. Normal wound healing occurs in three stages – inflammation, proliferation, and tissue remodeling [161]. Macrophages seem to be key regulators in the wound healing response and have many functions including host defense, the promotion and resolution of inflammation, the removal of apoptotic cells, and the support of cell proliferation and tissue restoration [162]. In our study, we observed that ONs exhibited statistically higher levels of M1 macrophages as compared with YNs in phase I. While reports on the nature of wound healing

suggest that rates of wound healing are slower in aged hosts and are accompanied by delayed cell infiltration [42], [163], the role of macrophages in old hosts is still unclear. Some studies suggest that macrophages in old hosts have impaired remodeling [164], while others report reduced M1 and M2 expression with age [165]. Yet other studies find increased macrophage expression in aged hosts [166], [167]. Further studies are needed to address the role of macrophages in iTEVG formation in both young and aged hosts.

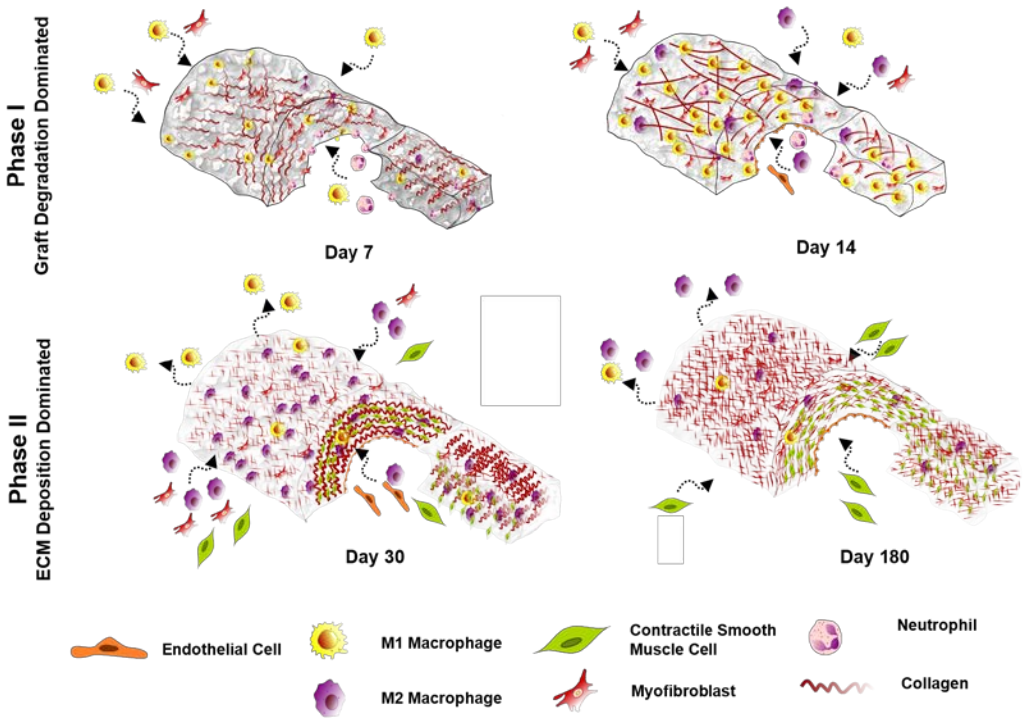

Figure 57: Schematic of phases of neoarterial growth and remodeling in young hosts.

Phase I (Day 0 – 14) remodeling is dominated by graft degradation and heightened inflammatory cell infiltration (particularly, neutrophils and M1 macrophages). Phase II (post Day 14) is dominated by ECM deposition and remodeling in response to mechanobiological cues. Phase II also exhibits increased M2 macrophage, myofibroblast, and contractile smooth muscle cells organization along with change in collagen fiber architecture over time. Neoarteries at day 30 exhibit two distinct layers of collagen fibers – thin, isotropic, adventitial fibers, and crimped, circumferentially oriented medial fibers. Day 180 displays an increased density of isotropically oriented fibers with circumferentially aligned VSMCs.

The transition between the phase I and phase II at day 14 was marked by a dramatic reduction of M1 macrophages and a switch in phenotype to M2 macrophages. While the M1 response was practically resolved in YNs, ONs exhibited a heightened and chronic M1 macrophage infiltration that is reduced, but still not resolved even at six months. Furthermore, ONs also exhibited statistically lower M2 macrophage infiltration. YNs exhibit a non-monotonic mechanical response over time, presumably due to microstructural collagen remodeling. We observed that the collagen microstructure evolves from a scar-like disorganized, sparse structure to a bi-layered YN that has an outer adventitial layer with thin fibers and an inner layer comprised of crimped collagen fibers that are circumferentially aligned, typical of native arteries (Figure 57). One of the main mechanisms eliciting collagen fibers to bear load is the gradual recruitment of crimped collagen fibers upon loading [12], a behavior that is exhibited by one month YNs. This contributes to reduction in stiffness and development of a toe-region in the mechanical response of YNs at one month. This bi-layered YN continues up to three months at which point collagen fibers not only display recruitment, but also reorientation in the circumferential direction upon loading. While these changes tend toward native artery-like remodeling, these YNs demonstrate a very stiff response A major limitation of this study is the lack of mechanical and microstructural data about ONs in phase I. At three months, ONs exhibited a dense collagen network, and a lack of both fiber recruitment and reorientation, making them significantly stiffer than YNs. At six months, the ONs have a highly heterogeneous response with some neoarteries displaying a bi-layered structure with thin adventitial fibers and crimped medial fibers that are recruited upon loading. Aged native arteries exhibit a compromised homeostatic state as evidenced by increased stiffness, increased collagen content, and increased GAG content [141]. It is therefore, reasonable to expect an altered homeostatic state in ONs. However, since the end-point of this study was six

months post-implantation, future studies need to determine the trajectory of remodeling in ONs over longer times.

5.4.2 Altered States of End Stage Remodeling

While both the YN and ONs exhibited altered states of remodeling they maintained the general trends typical of their respective native arteries. For example, while neoarteries across age had significantly increased stiffness at six months, ONs had a higher stiffness than YNs. This is typical of native arteries, wherein old native carotids have higher stiffness as compared to young native carotids[141]. Furthermore, the heightened inflammatory as well as intimal hyperplasia-like remodeling seen in ONs at six months is typical of aged blood vessels. It is interesting to note that while inflammation (M1 macrophage infiltration) is resolved by six months in YNs, they also were associated with significantly stiffer YNs. This could potentially be due to the presence of proliferating VSMCs that deposit collagen. Future studies will determine if these YNs continue to remodel and form a bi-layered structure with increased compliance at later time points or if this constitutes a stable but altered state of homeostasis.

5.4.3 G&R Models for Rational Design of iTEVGs

In order to guide future studies, we developed a G&R computational model that can elucidate the salient mechanisms guiding remodeling. Parametric studies indicated that graft degradation, ECM deposition, collagen turnover rate, and collagen deposition pre-stretches are important factors controlling long-term G&R responses. High degradation half-lives can lead to failure from neoarterial dilatation, while reduced collagen turnover rates can lead to stenotic

remodeling. Since conditions such as hypertension can be modeled using our G&R tool, future work can combine this tool with optimization strategies to determine parameters that lead to normal remodeling under various pathological conditions. Furthermore, an important finding is that the interplay of graft degradation and ECM deposition are crucial factors that need to be controlled to achieve stable long-term G&R in ON remodeling. Biochemical evaluation show that ONs exhibit higher ECM deposition which, as our simulations suggest, coupled with slower polymer degradation half-life (faster graft degradation rate) can lead to stenosis. Thus, our results indicate that a balance of medium degradation half-life combined with lower ECM deposition rate is required for stable long-term remodeling.

5.4.4 Conclusion

In summary, we assessed the longitudinal remodeling process of TEVGs in young and aged hosts and observed that they remodel in two similar phases, but, at altered rates. We determined that both YN and ONs have altered remodeljng response in comparison with their respective native arteries. Nevertheless, YNs potentially demonstrate a relatively homogeneous response between samples to develop a stable neoartery at six months as evidenced by the reduction in inflammation and potentially stable proliferating VSMCs. In contrast, age seems to first and foremost confer heterogeneity in remodeling response of ONs. This leads to favorable remodeling in some, whereas altered and potentially unstable remodeling in others. We established that the remodeling response is highly non-monotonic in both YN and ON, not just in terms of cellular content, but also in terms of mechanical response. Future studies are needed to assess long-term remodeling to determine fate of these neoarteries. We used this knowledge to tailor our G&R computational tool and applied this tool to assess salient mechanisms guiding arterial remodeling. We determined key

iTEVG and host parameters that need to regulated to have a stable long-term remodeling response. These studies have identified the next directions for future studies to reach our long-term goal of clinical translation of in host tissue engineering of vascular grafts to patients.

Contributions

Keewon Lee, a postdoctoral researcher in Dr. Wang's group performed the histological, biochemical staining, and imaging in this chapter. Dr. Liwei Dong performed the surgical iTEVG implantation and explantation.

6.0 Pathological Growth and Remodeling: Calcification in Human Cerebral Aneurysms

The work in this chapter was submitted in the following manuscript:

Piyusha S. Gade, Riikka Tulamo, Keewon Lee, Fernando Mut, Eliisa Ollikainen, Chih-Yuan Chuang, Bong Jae Chung, Mika Niemelä, Behnam Rezai Jahromi, Khaled Aziz, Alexander Yu, Fady T. Charbel, Sepideh Amin-Hanjani, Juhana Frösen, Juan Cebral, Anne M. Robertson. " Calcification in human intracranial aneurysms is highly prevalent and displays both atherosclerotic and non-atherosclerotic types." *ATVB, Under Review*.

6.1 Introduction

Patient specific treatment planning for unruptured intracranial aneurysms (IAs) remains a complex issue for both clinical and scientific reasons. Clinically, there is a need to balance the risk of intervention with the potential risk of rupture [168]–[171]. The main morphological and anatomical factors that are clinically implicated in higher risk of IA rupture are posterior circulation [172], high aspect ratio [173], surface irregularities like lobulations [174], and size (>7mm) [171], [174], [175]. Although these factors correlate with increased risk, they are not exhaustive or specific enough to impact clinical decision making for the vast majority of IAs. For example, while large IA size (>7mm) is often used as a metric of increased rupture risk, 38% of smaller IAs rupture[176] and there is no minimum size that alone guarantees structural integrity of the IA wall.

Aneurysms rupture when structural components of the wall, largely collagen fibers, are unable to withstand loading from transmural pressure. IA wall weakening is attributed to a variety of physical causes including enzymatic degradation of collagen fibers due to inflammation or wall remodeling, insufficient levels of collagen fiber deposition due to a dearth of intramural VSMCs, and localized stress concentrations from, for example, calcifications in the IA wall [160], [177]–[179]. This diversity of causes can confound current efforts to identify statistical associations between rupture risk and rupture related factors such as sac geometry and patient characteristics. Hence, there is a crucial need to complement current efforts with studies that directly look for physical causes of IA wall failure and identify the possibly distinct pathologies responsible for these wall changes.

It is well known that physical inclusions such as those formed from calcifications will alter the mechanical stress in a manner that is dependent on the inclusion size and material properties of the surrounding matrix [179]–[183]. The potential medical implications of these inclusions are seen, for example, in atherosclerotic lesions of extracranial arteries where micro-calcifications are associated with rupture of fibrous caps but macro-calcifications are associated with mechanical stability of the cap [183], [184].

Vascular calcification is now known to arise from at least two different pathological processes which lead to different types of wall changes [185]. The most highly studied is a slow, inflammation driven, atherosclerotic type pathology of the intima with associated lipid pools [186] and the second is a non-atherosclerotic phosphate-dependent, rapid mineralization in the media [187]–[189]. Distinct therapies are needed for the prevention and possible reversal of these two types of calcification [190].

Despite these advances in understanding vascular calcification pathologies and recognition of their mechanical importance, the role of calcification in IA rupture has received limited attention, likely due to reports of a low prevalence between 1.7 – 29% [174], [181], [191]. However, these rates are based on clinical computed tomography (CT) imaging studies with a typical voxel resolution of 250-300μm that prevents the detection of micro-calcifications.

Our aim in this work is to determine the prevalence, distribution and type (atherosclerotic, non-atherosclerotic) of calcification in IAs and assess differences in occurrence between ruptured and unruptured IAs. We are able to leverage our database of peri-operatively resected human aneurysm samples and use high resolution *ex vivo* imaging techniques that directly image calcification as small as 3μm. As for extracerebral vessels, such knowledge can be leveraged for improved diagnosis and treatment methods once the role of calcification in IA pathology and mechanical strength are understood.

6.2 Materials and Methods

6.2.1 Aneurysm Tissue Harvesting

Aneurysm samples (n = 65) were harvested from aneurysm sacs in consented patients undergoing surgical clipping for treating unruptured (n = 48) and ruptured (n = 17) aneurysms. This study was approved by an Ethics Committee, protocol number IRB REN18010236. Samples were collected from three study sites – Alleghany General Hospital (Pittsburgh, PA, USA), University of Illinois at Chicago (Chicago, IL, USA), and Helsinki University Hospital (Helsinki, Finland). Samples from Alleghany General Hospital and University of Illinois at Chicago were

transported in a dedicated cooled transport container to the University of Pittsburgh in a 0.9% (w/v) saline solution. Samples were then fixed using 4% paraformaldehyde or 3% glutaraldehyde. Samples from the Helsinki University Hospital were snap frozen in the operating room and transported to Pittsburgh after fixation in 10% formalin.

6.2.2 Patient Clinical Data

Patient clinical data was collected as previously described [160]. Briefly, patient age, gender, family IA history, smoking history, diagnosed hypertension, renal failure, diabetes and use of anti-thrombotic and statin medication were obtained from medical records. Patients were considered hypertensive if they were currently being treated for hypertension or if they were previously diagnosed with hypertension but declined treatment. Patients were categorized as non-smokers if they had never smoked cigarettes or had not smoked within the last 5 years. Patients who currently smoked or who had quit within the last 5 years were categorized as smokers. Patients were categorized as having renal failure if they were on dialysis or were either recommended/had previously undergone kidney transplant. Clinical patient data for indication of hypertension, smoking and anti-thrombotic medication was not available for 5,1, and 1 patient respectively. IA size, aspect ratio and presence of bleb/lobulations were calculated from 3D vascular models constructed from 3D rotational angiography or computed tomography angiography images as previously described [192]. Size was calculated from these reconstructed images as the total volume of the IA and aspect ratio as the ratio of aneurysm height and neck width [193]. Geometric parameters could not be analyzed for 11 patients due to the absence of imaging data for vascular reconstruction.

6.2.3 Micro-CT Scanning

Fixed aneurysm tissue samples (n = 65) were scanned using a high resolution (0.35μm) micro-CT scanner (Skyscan 1272, Bruker Micro-CT, Kontich, Belgium) at resolutions of at least 3μm (range: 1 - 3μm) depending on sample size to ensure that micro-calcifications of a minimum size (range of 3 - 9μm) could be captured. For scanning, samples were mounted on wet gauze to minimize dehydration and placed in a 1.5ml clear microcentrifuge tube. This tube was vertically mounted as previously described [194] to ensure the sample remained stationary. Samples were scanned at 50kV and 200μA with a frame averaging of 8, a rotation step size of 0.3 degrees, scanned 180 degrees around the vertical axis. Sample scanning time was maintained at less than 2.5 hours to prevent sample dehydration. A 3D image of the sample was reconstructed using NRecon (Bruker Micro-CT, Kontich, Belgium) with an axial step size equal to the scanned pixel size.

6.2.4 Image Processing of Micro-CT data

6.2.4.1 Aneurysm Tissue and Calcification Mesh Generation

The surface mesh used for analyzing the locations of calcification within the wall was created using Simpleware ScanIP (Synopsys, Mountain View, USA) as previously described [158],[195]. Briefly, 3D reconstructed images from the micro-CT data were segmented into two distinct masks for the regions of calcification and non-calcified tissue. Tissue mask generation included segmentation, Gaussian smoothing, followed by morphological operations to remove surface noise, and connected components filtering. As previously described [195] and detailed in Supplementary Material, calcification was identified by elevated greyscale value relative to the

tissue, validated using Alizarin Red staining in histological sections. The calcification mask was generated as previously described [195] using a combination of thresholding (Otsu multilevel thresholding filter) for segmentation and Boolean operations for subtraction of the calcification mask from the tissue mask. An unstructured triangular surface mesh was then generated for each component. Calcification and tissue volume fraction were calculated using the general properties module in ScanIP. The calcification mask was split into connected components to analyze individual calcification diameter, volume and eccentricity. Two particles connected by only a single vertex were considered to be separate particles, whereas a connection with one or more faces was considered to be a single particle.

6.2.5 Lipid Pool and Calcification Identification using Micro-CT Scanning in Intact Samples

Lipid pools and calcification manifest as regions with distinct peak intensity levels in micro-CT scanning of intact specimens. In the micro-CT images, lipid pools were identified as regions of low intensity (<30) with distinct morphological patterns. Samples were scored for presence or absence of lipid pools using these two criteria. Calcified regions presented with high grayscale values (220-255) in normalized images where 0 represents black and 255 represents white. Calcification was then segmented using either manual thresholding or an automatic multilevel Otsu segmentation technique, followed by region growing that joins connected components using an intensity-based approach.

In order to verify specificity, we compared grey levels of calcification and lipid pools with their respective histological sections using Alizarin Red and Oil Red O (Figure 58). False positives by hemorrhage or capillaries were ruled out by consideration of greyscale, morphology and size.

In particular, hemorrhage regions have a greyscale value similar to that of tissue which lies in the 50 – 80 greyscale regime [196]. Capillaries, if filled with blood, also appear at a similar intensity to that of tissue, thereby distinct from lipid pools and calcification. Additionally, capillaries are morphologically different (circular vs elliptical/irregular shaped) from lipid pools and have smaller diameters (5 – 10um) when compared with the smallest size of lipid pools identified (20um).

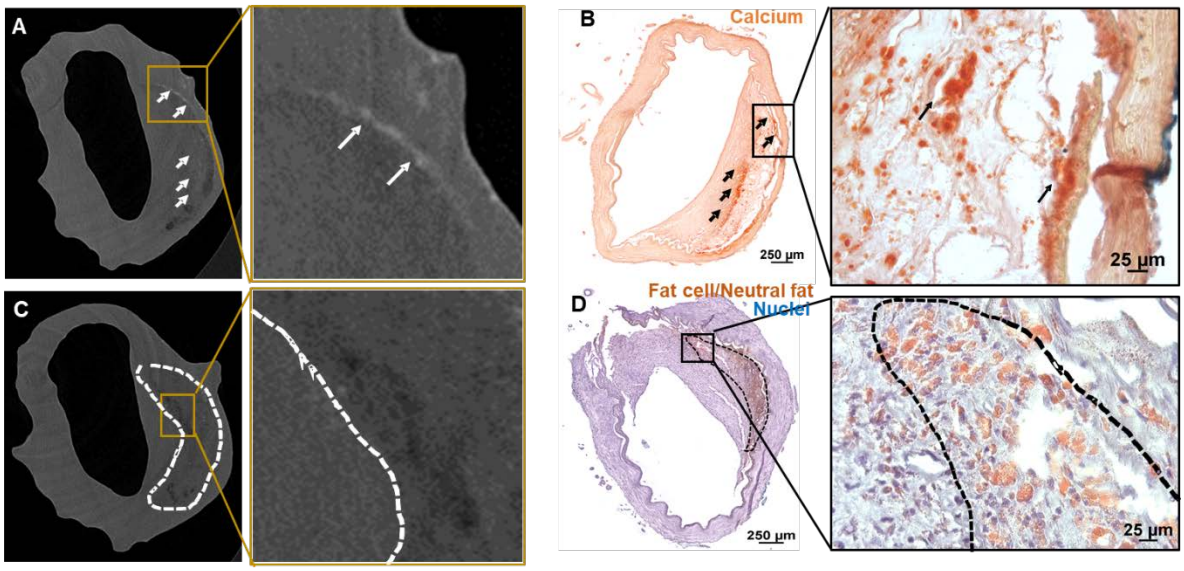

Figure 58: Verification of regions of calcification and lipid pools in control sample of a fresh cerebral artery identified under micro-CT

(A) Cross sections from high resolution micro-CT image of fresh cerebral artery imaged at 2µm resolution. White arrows point to micro-calcifications identified in micro-CT. (B) Alizarin Red staining confirming micro-calcifications (black arrows) as seen in micro-CT with high grayscale values (220-255) on a normalized scale. (C) Lipid pool (white dashed line) visible as low grayscale value in micro-CT image (< 30). (D) Oil Red O staining identifying neutral lipids (concentrated within black dashed line) in same sample. Nuclei were counterstained with hematoxylin.

IA samples in our study were sourced from three sites - Alleghany General Hospital (AGH) (Pittsburgh, PA, USA), University of Illinois at Chicago (UIC) (Chicago, IL, USA), and Helsinki University Hospital (HUH) (Helsinki, Finland). Due to differences in site specific protocols (Finland versus U.S.) as well as differences in plans for further analysis (SEM versus classical histology), three different fixatives were used. Additional studies were performed to determine the role, if any, of each of the fixation methods on micro-CT results. Segments of cerebral artery were scanned before and after fixation for each fixative.

6.2.5.1 Wall Thickness Evaluation

Local wall thickness was assessed using a custom-written code as previously described [158]. Briefly, distance vectors were calculated from the inner to the outer surface elements and from the outer to the inner surface elements. Using these vectors, new "medial points" were introduced half way along these distance vectors. The wall thickness at the medial points was then approximated as the sum of the length of the distance vectors to each surface.

6.2.5.2 Calcification Location Analysis

Calcification was identified as located in the inner, middle or outer third of the wall using a previously developed approach [158]. Calcification location could not be analyzed for four samples for which the IA sample was collapsed, preventing identification of the inner and outer surfaces across the entire sample in these cases.

6.2.6 Visual Scoring of IA Surface Color

Calcification surface mesh was overlaid with the non-calcified tissue and compared with ex-vivo dissection scope images of resected IA samples [158]. The surface color of calcified regions was scored as either being colorless, white or yellow. If a sample presented calcification in multiple color regions, it was scored individually in each of the categories.

6.2.7 Histological and Multiphoton Analysis

Samples were dehydrated in 30% sucrose solution at 4°C for 24 h. Tissue sections were embedded in optimal cutting temperature compound (Sakura Finetek, Torrance, CA, USA), frozen at -80°C overnight, and cryosectioned to 8µm thickness. This was followed by staining sections with H&E, Oil Red-O and Alizarin Red to stain for cell nuclei, lipids and calcification respectively.

6.2.7.1 Neutral Lipid and Free Cholesterol Staining

Tissue cryosections (8-µm thick) were fixed with 4% paraformaldehyde (PFA) for 1 h at 4°C and rinsed twice with PBS. For neutral lipid staining, BODIPY 493/503 (D3922, Thermofisher Scientific, Waltham, MA) was dissolved in dimethyl sulfoxide (DMSO) (D4540, Sigma-Aldrich, St. Louis, MO) at a concentration of 1 mg/ml and diluted to 1:500 with PBS. Tissue sections were stained with 100 µl of the BODIPY working solution, incubated for 30 min at 37°C in the dark, and rinsed twice with PBS. For free cholesterol staining, filipin (F9765, Sigma-Aldrich) was dissolved in DMSO at a concentration of 25 mg/ml and diluted to 1:500 with PBS. Tissue sections were stained with 100 µl of the filipin working solution, incubated for 2 h at room temperature in the dark, and rinsed twice with PBS. Stained slides were viewed using an inverted

microscope with two fluorescence filters: green (for BODIPY, excitation = 450-510 nm) and blue (for filipin, excitation = 340-380 nm). Tissue slides without the staining reagents were used as negative controls. Human cerebral aneurysm tissue that presented with lipid pools on micro-CT images was used for positive controls.

6.2.7.2 Leukocyte and Macrophage Staining

Both leukocytes and macrophages were examined using immunofluorescence staining. Tissue cryosections (8-µm thick) were fixed with 4% PFA for 15 min at room temperature (RT). Tissue sections on slides were blocked with 3% normal goat serum (NGS) (Sigma-Aldrich) and 3% normal horse serum (Vector Laboratories) in buffer solution (3% bovine serum albumin in PBS) for 20 min at RT. incubated with primary antibodies in buffer solution for 30 min at RT, and rinsed with PBS, followed with the corresponding secondary antibodies in buffer solution at RT.

For leukocyte staining, mouse anti-CD45 (clone 2B11 PD7/26, 1:100; Dako, Glostrup, Denmark) was used as a primary antibody, followed by Alexa Fluor 546 goat anti-mouse IgG (1:100, Invitrogen, Carlsbad, CA) as a secondary antibody. For macrophage staining, mouse anti-CD68 (clone EBM11, Dako) was used as a primary antibody, followed by Alexa Fluor 488 goat anti-mouse IgG (1:100, Invitrogen) as a secondary antibody. Nuclei were counterstained with 4',6-diamidino-2-phenylindole (DAPI) (Life Technologies, Carlsbad, CA). Tissue slides without primary antibodies were used as negative controls. Human tonsil was used for positive controls.

6.2.7.3 Calcification Staining in Histological Sections

Micro-calcification was detected using a bisphosphonate-conjugated, near-infrared fluorescent imaging agent, OsteoSense 680 EX (PerkinElmer, Waltham, MA) as described

previously [195]. OsteoSense 680 EX was dissolved in 1.2 ml of PBS and applied to explanted samples for 2 h at room temperature. Samples were rinsed with PBS, fixed in 10% formalin for 1 h at 4°C, and dehydrated in 30% sucrose solution at 4°C for 24 h. Tissue sections were embedded in optimal cutting temperature compound, frozen at -80°C for 2 h, and cryosectioned to 8-µm thickness. Tissue slides were rinsed twice with PBS, mounted with fluorescence mounting medium, and viewed using an inverted microscope with the Cy5 filter (excitation = 630-680 nm). Calcified cerebral vessels were used as positive controls.

6.2.8 Calcification and Collagen Imaging in Intact Sample

Simultaneous imaging of collagen and calcification was performed using two photon microscopy as previously described [195]. Briefly, the entire tissue sample was fixed in 4% PFA for 24h. This was followed by rinsing the sample with PBS. Sample was then incubated in OsteoSense 680EX (diluted 1:50) for 24h. This was followed by rinsing the sample with PBS and imaging with an Olympus two photon microscope (FV 1000, Tokyo, Japan) using the following settings: 1.12NA 259 MPE water immersion lens and 25X objective: 800nm excitation wavelength, dwell time of 8µs/pixel, a scan pixel count of 1024 X 1024 and laser intensity of 7%. Second harmonic signal from collagen was collected using a 350 – 450 nm filter and calcification signal using the fluorescent calcium tracer emission in the 665 – 735 nm channel.

6.2.9 Wall Classification for Presence of Calcification and Lipid Pools

IA walls were classified according to the association of calcification with lipid pools in micro-CT. Type I walls contained calcification without any lipid pools. In Type II walls, both calcification and lipid pools were detected, though never co-localized. In Type III walls, calcification could be found co-localized with lipid pools. Calcifications within and around lipid pools were referred to as "atherosclerotic" (Type III) as is normally seen in peripheral atherosclerosis [197], whereas calcifications distinct from lipid pools or found in the complete absence of lipid pools were referred to as a "non-atherosclerotic" (Types I and II). Calcification particles were subcategorized based on their size. Micro-calcifications were defined by diameters <500μm, meso-calcification by diameters between 500 - 1000 μm and macro-calcifications by diameters >1000 μm.

6.2.10 Statistical Analysis

Statistical analysis was performed using SPSS (IBM SPSS Statistics 25, IBM Corp, North Castle, NY). Proportions were calculated for categorical variables and χ^2 independence test or Fisher's Exact test was used. For continuous variables, median and range or mean were calculated and analyzed using Mann-Whitney U test or independent samples t-test. For normally distributed data, multiple group comparisons were performed using one or two-way ANOVA followed by the Tukey's post-hoc test. For data that violated the assumptions of parametric tests, multiple group comparison was performed using the Kruskal-Wallis test followed by the Mann-Whitney U test with a Bonferroni correction for post-hoc testing. The assumptions of normality and homogeneity of variance were tested using the Kolmogorov-Smirnov and Levene's test respectively.

6.3 Results

6.3.1 Human Cerebral Aneurysms Exhibit High Prevalence of Calcification

High resolution micro-CT revealed the presence of calcification in 78% (51/65) of the IA samples. 60% of samples presented only calcification without associated lipid pools (Types I, II), Table 9. We did not find any significant differences in patient characteristics between calcified and non-calcified samples. None of the patients in our cohort had renal failure and only 9% had type II diabetes. Furthermore, 57% of the IAs were harvested from the MCA and there was no statistical difference in location of the ruptured and unruptured samples.

Table 9: Patient characteristics and prevalence rates for calcification and lipid pools.

	Total (n=65)	Unruptured (n=48)	Ruptured (n=17)	p value
Patient Clinical Characteristics				
Age (years)	57.50 (30 – 79)	58 (30 – 79)	54 (43 – 66)	0.089
Female Sex (%)	50/65 (77)	36/48 (75)	14/17 (82)	0.741
Family History for IAs (%)	15/65 (23)	13/48 (27)	2/17 (12)	0.478
Smoker (%)	23/65 (35)	17/48 (35)	6/17 (35)	1.000
Hypertensive (%)	28/65 (44)	21/48 (44)	7/17 (41)	1.000
Anti-thrombotic medication (%)	14/65 (22)	14/48 (29)	0/17 (0)	0.024*
Statins (%)	16/65 (25)	15/48 (31)	1/17 (6)	0.086
Type II Diabetes	6/65 (9)	5/48 (10)	1/17 (6)	1.000
Size [mm^3]	7.6 (4.6 – 15.6)	7.6 (4.6 – 14.5)	9.2 (4.8 – 15.6)	0.642
Aspect Ratio	1.06 (0.4 – 3.6)	1.05 (0.5 – 2.0)	1.18 (0.4 – 3.6)	0.509
Blebs/Lobulations	19/65 (29)	13/48 (27)	6/17 (35)	0.298
Location				
MCA	37/65 (57)	29/48 (60)	8/17 (47)	0.563
ICA	8/65 (12)	7/48 (15)	1/17 (6)	0.667
ACOM	8/65 (12)	6/48 (13)	2/17 (12)	1.000
PCOM	6/65 (9)	3/48 (6)	3/17 (18)	0.159
Others¥	5/65 (8)	3/48 (6)	2/17 (12)	0.592
Prevalence Rates of Calcification and Lipid Pools in IAs				
Calcification (%)	51/65 (78)	40/48 (83)	11/17 (65)	0.167
Lipid pools (%)	39/65 (60)	29/48 (60)	10/17 (59)	0.783
Both calcification and lipid pools (%)	30/65 (46)	25/48 (52)	5/17 (29)	0.158
Wall Type I, II ("Non-atherosclerotic calcification")	39/65 (60)	28/48 (58)	11/17 (65)	0.380
Wall Type III ("Atherosclerotic calcification")	12/65 (18)	12/48 (25)	0/17 (0)	0.027*

Median and range are given for continuous variables. *P<0.5 (χ^2, Fisher's Exact Test or Mann-Whitney U test). ¥ Other aneurysm locations in this study with a single case include ruptured aneurysms: BA tip, PICA; and unruptured aneurysms: ACA, PCOM-ICA, VA. Abbreviations used: MCA = Middle Cerebral Artery, ICA = Internal Carotid Artery, ACOM = Anterior Communicating Artery, PCOM = Posterior Communicating Artery, BA = Basilar Artery, PICA = Posterior Inferior Cerebellar Artery, ACA = Anterior Cerebral Artery, VA = Vertebral Artery.

6.3.2 Small, Dispersed and Large Aggregated Calcifications Exist throughout the Wall Thickness

Calcification in the form of micro- and macro-calcifications were distributed in all three regions across the IA wall (Figure 59). Calcification in most samples occupied less than 0.1% of the sample volume (Figure 60A) and was approximately ellipsoidal in shape with an average aspect ratio of 0.39 ± 0.21. 77.5% of calcified particles had a major diameter less than 30 μm. However, some calcified particles were as large as 3.87 mm (Figure 60B). For 70% of samples, no particular surface color was associated with calcification presence, even if calcification occupied a large volume fraction of the sample (Figure 59, row 1; Figure 60C, D). Calcification density, size (Figure 61) and area fraction in IA wall all increased with an increasing distance from the lumen, with largest values in the outermost third of the wall (Figure 60E). Additionally, thicker regions in the IA wall tended to have calcification in the outer third of the wall, whereas thinner regions tended to possess calcification in the inner and middle thirds of the wall (Figure 60F). Thick and thin were defined relative to average thickness of the particular specimen.

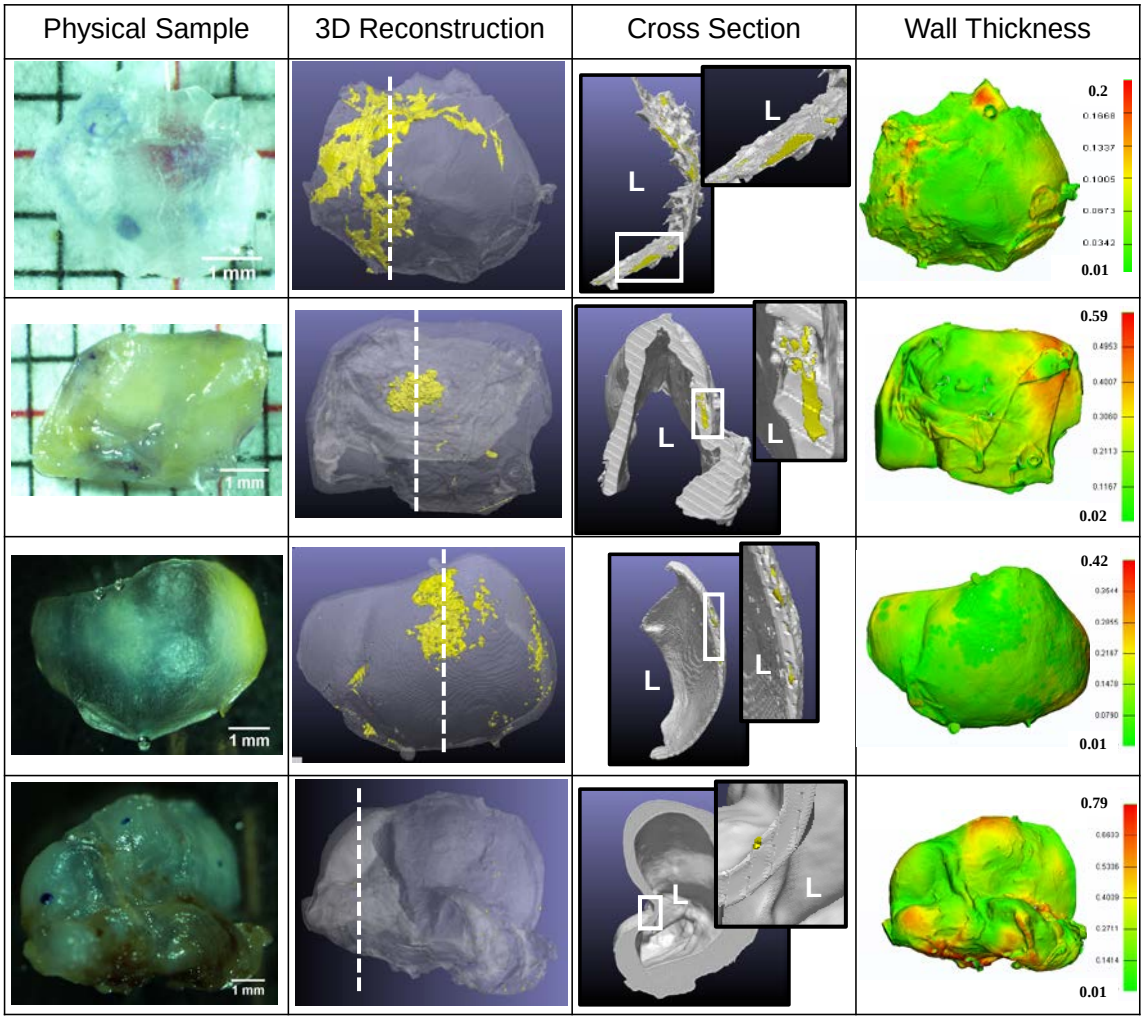

Figure 59: Diversity of calcification morphology, location and tissue surface appearance as seen with high resolution micro-CT for four representative aneurysm samples (Rows 1-4).

3D reconstructed and cross-section images of the micro-CT scans show calcification in yellow and non-calcified tissue in grey. Cross section images are taken at locations indicated by a dashed white line in the 3D reconstruction image. L indicates lumen and insets show calcified region at higher magnification. Wall thickness contours are in mm.

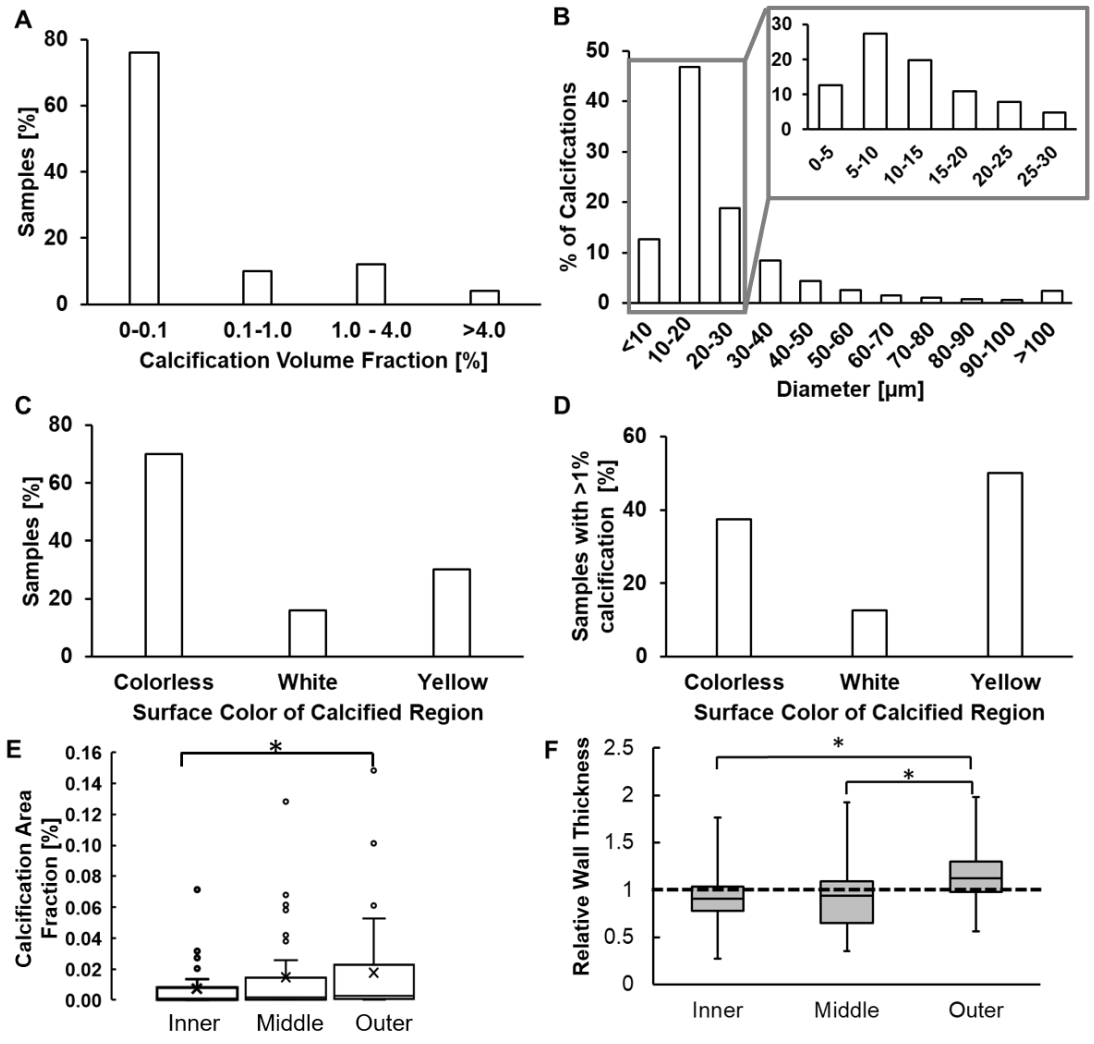

Figure 60: Calcification volume fraction, size, visual manifestation and distribution.

Calcification in human IAs (A) occupies less than 0.1% of sample wall volume, (B) exists mostly as small (< 30µm) micro-calcifications which can exist in clusters and (C, D) does not associate with any specific tissue surface color even when it occupies a large volume.(E) Calcification area fraction increases with increasing distance from lumen (p = 0.016; n = 50). (F) Calcification in the outer third of the wall is found in regions of high relative wall thickness - the ratio of thickness in the calcified region relative to average wall thickness for that specimen (p = 0.0001,0.0001; n = 50) whereas calcification in the inner and middle layer occurs in region of average wall thickness. A relative wall thickness of 1 indicates the calcified wall region has a thickness equal to the average wall thickness of the particular specimen.

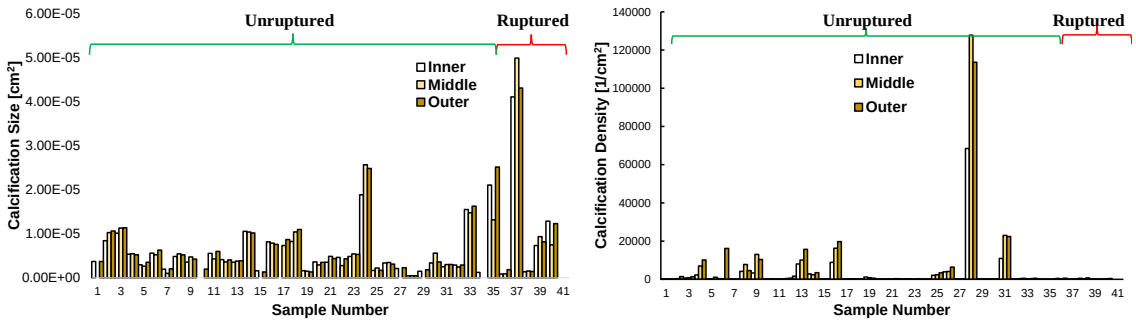

Figure 61: Calcification size and density in wall layers

(A) Calcification size and (B) density both increase with distance from the lumen with highest density and largest size of calcification located in the outer third of the wall.

Qualitatively there was no visual difference in terms of presence, location or morphology of calcification and lipid pools in micro-CT images as a result of fixation (Figure 62A). Additionally, there was no differences in the relative attenuation levels of calcification and lipid pools due to fixation method, (Figure 62B) with calcification remaining in the 220-250 regime and lipid pools and tissue in the < 30 and 50 – 80 respectively. Furthermore, the calcification volume pre and post-fixation were evaluated (using same fixation as for the aneurysm samples, Material and Methods of main text) and found to differ by less than 3% (Table 10).

Table 10: Calcification volume pre and post fixation in three fixatives - 10% formalin, 3% glutaraldehyde and 4% paraformaldehyde

	Pre-Fixation Calcification Volume [mm^3]	Post Fixation Calcification Volume [mm^3]	% Difference pre and post fixation
Formalin	0.000583	0.000585	0.343
Glutaraldehyde	0.0023	0.00236	2.608
Paraformaldehyde	0.0012	0.00122	1.667

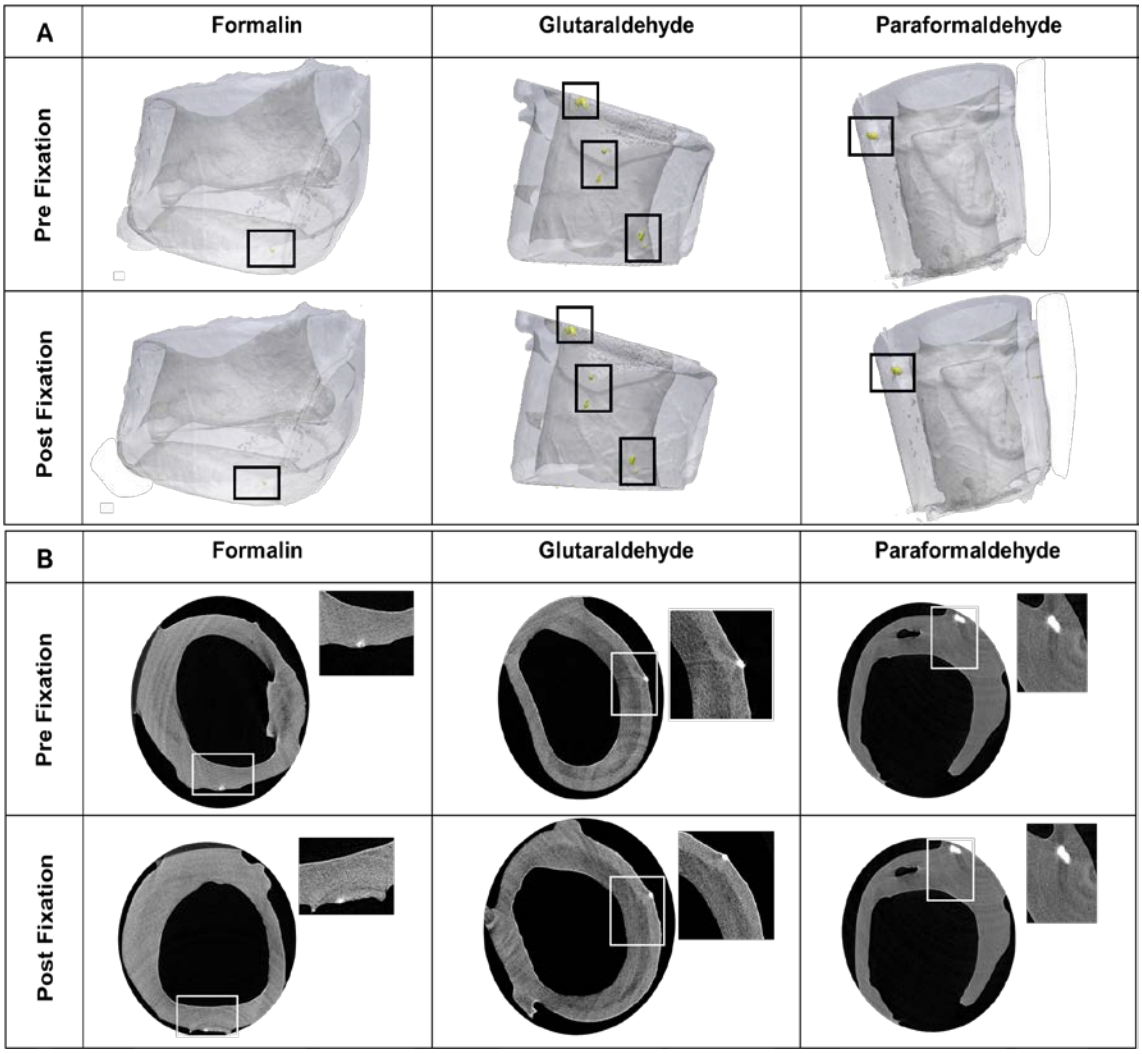

Figure 62: Comparison of cerebral vessels pre and post-fixation with micro-CT scanning.

(A) 3D reconstruction of micro-CT scanned vessels, pre and post fixation in three different fixatives – 10% formalin, 3% glutaraldehyde and 4% paraformaldehyde. Calcification seen in yellow. (B) Cross section micro-CT images of (A) showing calcification in white.

6.3.3 Calcification found in Atherosclerotic and Non-Atherosclerotic Forms

Three IA wall types were identified (Figure 63); 39% (20/51) were Type I walls (calcification without any lipid pools; non-atherosclerotic calcification), 37% (19/51) were Type II walls (calcification that is never co-localized with lipid pools; non-atherosclerotic calcification) and 24% (12/51) were Type III walls (calcification co-localized with lipid pools; atherosclerotic calcification). When subcategorized by calcification particle size, samples with only micro-calcification were the most prevalent accounting for 65% (33/51) of calcified samples. Most micro-calcifications were substantially smaller than the 500 μm upper bound for this category. In particular, 97% of micro-calcifications were less than 90 μm and 78% were less than 30 μm in size. These micro-calcifications could be found either in clusters or as isolated particles (Figure 64C, D). All IA walls with meso- and macro-calcifications also included some (0.5 – 5%) dispersed micro-calcifications.

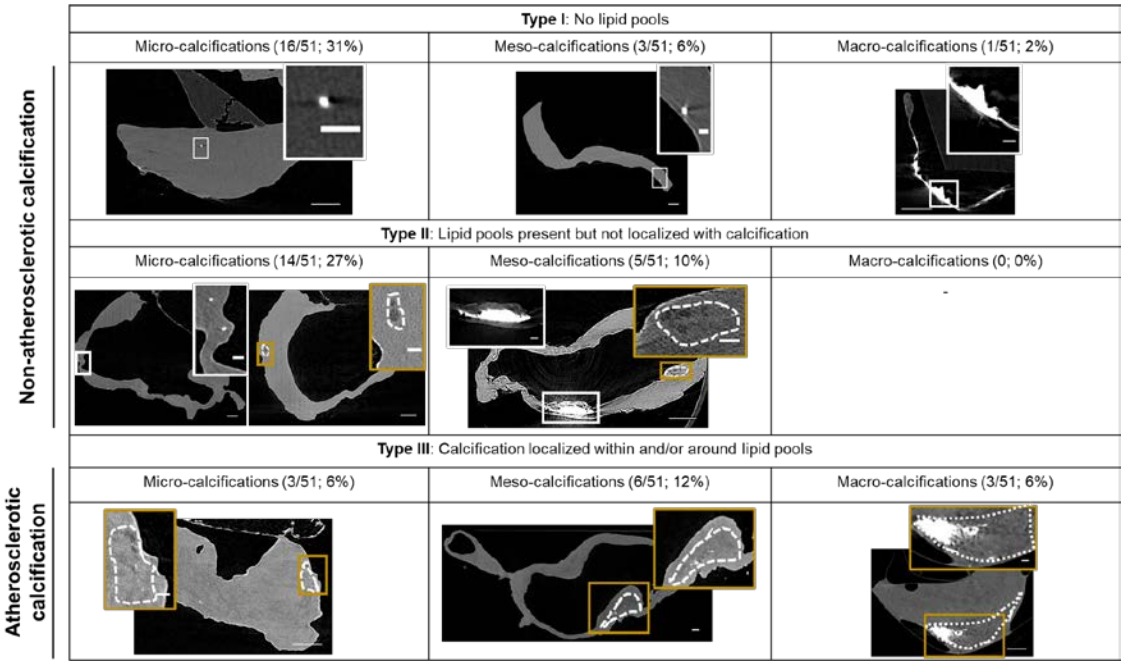

Figure 63: Three main wall types found in aneurysm samples based on the relationship between calcification and lipid pools.

Cross-section micro-CT images of representative calcified wall types present in IAs. Dotted regions indicate lipid pools. White and gold inset images show calcification and lipid pools, respectively, at high magnification. Scale bars correspond to 500µm for main images and 100µm for inset images. L indicates lumen.

The existence of distinct non-lipid, non-inflammation associated calcification in the IA wall was confirmed in a region of Type II wall that had calcification without an associated lipid pool. The region was co-stained with lipid, free cholesterol and inflammatory markers. Both neutral lipids and free cholesterol were absent in the calcified region (Figure 64A), as were inflammatory cells (Figure 64B) such as macrophages and leukocytes. Positive controls are shown in Figure 65.

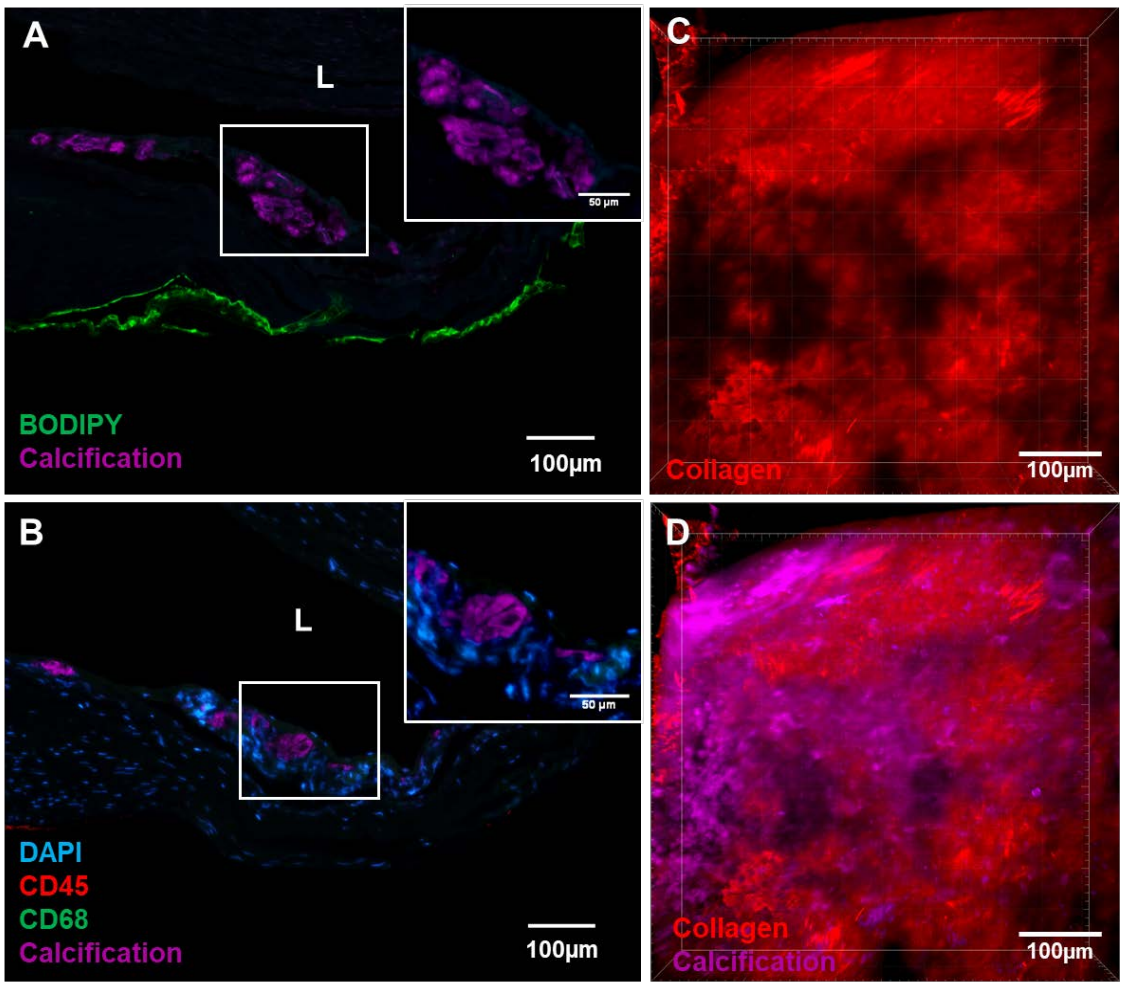

Figure 64: A region from a Type II wall presenting a non-atherosclerotic calcification region without an associated lipid pool.

(A) Calcification (stained with OsteoSense) did not localize with neutral lipid (stained with BODIPY) or free cholesterol (stained with filipin) as typically seen in atherosclerotic plaques. (B) Inflammatory response was also absent as indicated by the absence of both CD45 stained pan leukocyte marker and CD68 stained macrophages at the calcified area. Co-imaging of the relationship between collagen fibers and calcification particles under MPM showed (C) damaged regions of wall devoid of collagen fibers (red signal from second harmonic generation) were (D) filled with clusters of calcification particles (magenta, stained with Ostoesense).

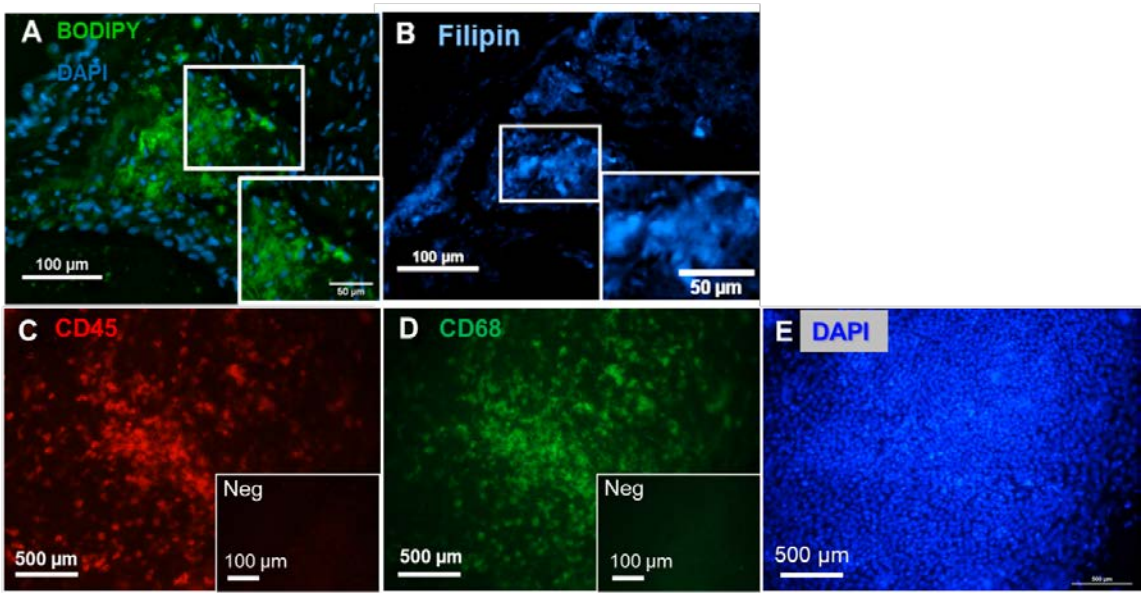

Figure 65: Positive controls for immunofluorescent staining in a human cerebral aneurysm (A-B) and human tonsil (C-E) sample. Free cholesterol and neutral lipids are stained with (A) BODIPY and (B) Filipin respectively. Inflammatory cells are stained using (C) CD45, a pan leukocyte marker and, (D) CD68, macrophage marker. (E) shows the nuclei counterstained using DAPI . Negative controls for CD45 and CD68 (primary antibody omitted) are shown as insets in C, D.

6.3.4 Factors Associated with Ruptured Walls: Small Calcification Volume Fraction, Calcification Size and Non-Atherosclerotic Calcifications

Ruptured IAs exhibited a lower calcification fraction than unruptured samples; a trend which existed across the three regions of the IA wall (Figure 66A). Furthermore, ruptured IAs did not contain macro-calcifications as opposed to unruptured IAs that possessed all sizes of calcification (Figure 66B).

Ruptured samples displayed only non-atherosclerotic calcification (calcification not associated with lipid pools- Types I, II) as opposed to unruptured samples which presented both atherosclerotic and non-atherosclerotic types (p=0.027). We did not find any significant differences in prevalence rates of either calcification or lipid pools between ruptured and unruptured samples, (Table 9).

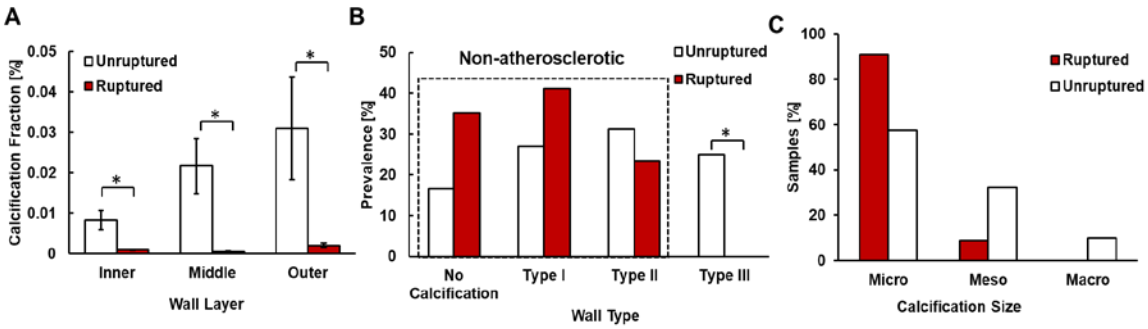

Figure 66: Differences in calcificaiton fraction, wall types and calcification size with rupture status. (A) Ruptured walls have significantly lower calcification fraction than unruptured walls in human IAs, p = 0.005, 0.006, 0.029 for inner, middle and outer thirds of the wall, respectively (n = 50). (B) Ruptured IAs are limited to either having no calcifications or "non-atherosclerotic" calcifications (Type I and Type II walls). No ruptured IAs display "atherosclerotic" calcifications (Type III walls) (p = 0.027*). (C) with micro or meso-calcifications, or Type II walls only with micro-calcifications (n=65), whereas unruptured walls possess all wall types.

6.4 Discussion

This is the first analysis of the prevalence of micro through macro scale calcifications in the IA wall. We found very high prevalence rates of calcification in IA domes (78%), greater than previously reported in imaging [174], [191] and histological [181] studies. We believe this difference is due to the high resolution (1-3μm) *ex vivo* imaging modality used here, which enabled direct, non-destructive evaluation of calcification across the entire intact sample, including particles in the 3-30μm size range.

This work is also the first to consider the possible existence of multiple mechanisms for calcification formation in the IA wall. Calcifications with and without associated lipid pools in extracranial arteries have already been shown to arise from distinct mechanisms. In particular, atherosclerotic intimal calcification of the extracranial arteries is found to be associated with later stages of an atherosclerotic process and is driven by lipid oxidation and inflammation. In contrast, the non-atherosclerotic medial calcification in extracranial arteries is not driven by a lipid oxidation induced inflammatory process but rather is attributed to aging as well as metabolite induced toxic changes that can arise from diseases such as renal insufficiency and diabetes mellitus [187], [188].

Motivated by these results for atherosclerotic and non-atherosclerotic type calcification in extracranial arteries, we introduced three wall types (I-III) to describe calcified IA walls and categorized these as containing “atherosclerotic” or “non-atherosclerotic” calcification. Type I walls (only calcification, no lipid pools) and Type II walls (calcification and lipid pools, not co-localized) contained “non-atherosclerotic” calcification and accounted for 76% of all samples. Type III walls (include calcification that is located within or around lipid pools) are “atherosclerotic" and accounted for 23% of all samples. This Type III atherosclerotic pattern is

similar to later stage (type VII) atherosclerotic lesions in the classification of the American Heart Association (AHA) committee[197] where calcification is spatially associated with lipid pools and is formed through a lipid oxidation driven inflammatory process. Previous histological studies of the IA wall have shown that the VSMC phenotype[198] as well as lipoprotein accumulation and associated foam cell formation [199], [200] in the IA wall resemble changes accompanying peripheral atherosclerosis, further suggesting that some IA calcification shares common pathobiological mechanisms with calcification in atherosclerotic peripheral arteries.

While inflammation driven, atherosclerotic like calcification has previously been studied in IAs[199], [200], the present work is the first to demonstrate calcification in IAs in the absence of lipids, suggesting a second mechanism of calcification formation is possible, potentially similar to non-atherosclerotic calcification in the medial layer of extracranial arteries. In contrast to extracerebral vessels, the non-atherosclerotic calcification was distributed across with entire IA wall. Cerebral arteries lack an external elastic lamina and the internal elastic lamina is additionally nearly universally missing in IAs. The absence of both these natural barriers in IAs could explain the more distributed nature of the non-atherosclerotic IA calcification compared with that in extracerebral vessels.

To further assess the possible similarity of this non-atherosclerotic presentation in IAs with non-inflammatory calcification in extracranial arteries, a region from a Type II wall with calcification distinct from lipid pools was analyzed for lipid and inflammatory markers (Figure 64A, B). The results confirmed that this calcification was not associated with lipids, cholesterol or inflammatory cells and was hence distinct from the typical atherosclerotic pathology outlined by the AHA. This non-inflammatory calcification in the IA wall was located near the IA lumen (Figure 64A, B).

In order to understand the potential mechanism of non-atherosclerotic calcification formation, we assessed the prevalence of renal failure and type II diabetes in our patient cohort since these conditions have been implicated in extracerebral non-atherosclerotic calcification formation [187], [188]. None of the patients in our cohort had kidney failure and only 9% had type II diabetes. Previous studies have also reported the existence of non-atherosclerotic calcification as a distinct form of calcification in the media of internal carotid arteries around the elastic lamina [201] and in peripheral artery disease[202]. Lanzer et al. [187] have conjectured that fragmented elastin can lead to such non-atherosclerotic calcification formation. Unpublished results from our group also show the presence of medial and adventitial calcification in control cerebral vessels. We therefore conjecture that at least some of the non-atherosclerotic calcification in the IA samples was formed due to the degradation of the elastic lamina in the cerebral artery prior to IA formation and would be exacerbated during IA formation. These findings suggest the need for future studies to understand the mechanism of non-atherosclerotic calcification formation. Building on the current work, an extensive evaluation of the prevalence, distribution and potential mechanisms of non-inflammatory calcification in IAs is the subject of ongoing investigation in our group.

Another important and marked finding in our study is that ruptured IAs had a lower calcification fraction and lacked macro-calcifications as compared to unruptured IAs. The role of calcification in rupture is a subject of ongoing investigations. In the extracerebral vasculature, computational modeling studies show that larger calcifications in plaques can contribute to load bearing and hence play a protective role [183], [203]–[205]. Other studies have shown that plaque stress increases with increasing calcification, but only up to a certain limit, after which it plateaus or even reduces [206]. We surmise that larger plaques in IAs area can be protective against rupture, which would be consistent with the lack of larger plaques in ruptured IAs in our study. It has been

conjectured that micro-calcifications could also play a mechanical role in rupture by generating regions of elevated stress (stress concentrations) [183] - leading, for example, to increased rupture risk in fibrous caps of extracranial arteries as well as in abdominal aortic aneurysms. Furthermore, the combined effect of collagen fibers, calcification and lipid pools on wall material properties ultimately dictates the mechanical behavior of soft tissues like the IA wall and this remains an ongoing area of investigation [179], [182]

These potential differences in calcification pathologies and the expected mechanical role of calcification in wall vulnerability suggest a pressing need for further investigation of the multi-faceted role of calcification in the IA wall. We anticipate that calcification will impact IA wall strength through a direct mechanical role as noted above, as well as an indirect pathological role related to aneurysm wall remodeling. For example, the cluster of micro-calcifications seen in the Type II wall (Figure 64C, D) exists within a pocket of distinctly damaged collagen fibers. A structurally deficient region of this kind could potentially reduce the local wall strength, increasing vulnerability to rupture. Hutcheson et al. have also shown that micro-calcifications associate with regions of reduced collagen fibers, and conjecture that collagen acts a scaffold for calcification aggregation[207]. These findings also suggest that the pathology and mechanics of collagen-calcification interaction can determine IA wall strength. Further investigations of the role of calcification in pathological changes of this kind can leverage the recently developed protocols for simultaneous imaging of collagen fibers and calcification particles within intact samples [195]. These studies can be complemented by histological analysis of the IA wall to understand the indirect pathological role of calcification in IA wall remodeling.

The present study also sheds light on recent efforts to infer information about aneurysm walls from intraoperative images. In particular, due to difficulty in obtaining IA samples for

analysis, intraoperative data on the aneurysm wall, such as color of the wall, are being collected as a possible surrogate markers of wall vulnerability [208], [209]. In this context, it is important to note there was no association between the presence of micro, meso or macro-calcifications and color of the aneurysm wall, reflecting a challenge in using intraoperative visual data to assess calcification in the IA wall.

6.4.1 Limitations

Prior studies of combined occurrence rates for lipid droplets and pools in the IA wall based on histological sections, reported prevalence rates of almost 100% [199], [200] . The high-resolution micro-CT used in the present work is able to identify lipid pools across intact IA specimens, though is not suitable for resolving lipid droplets. Therefore, the prevalence rate of 57% for lipid pools is not directly comparable to the results of the prior studies and may reflect the lower threshold for detecting lipids and lipoproteins compared with different histological staining methods. Other limitations of our study include small sample size and selection bias. Tissue was harvested from the aneurysm sac after aneurysm neck clipping only when it was feasible for the patients. Additionally, all aneurysm samples represent only one moment in time in their pathogeneses. Therefore, chronological order of wall changes and causal relationships between the changes remain unclear in this study setting. Nevertheless, we made every effort to include all relevant patient and sample information in order to better understand the population under study.

6.4.2 Conclusion

In summary, we found calcification in intracranial aneurysms is substantially more prevalent than previously reported and manifests as both atherosclerotic and non-atherosclerotic types. Notably, ruptured IAs in this study had significantly lower calcification fraction in comparison with unruptured IAs, and only displayed non-atherosclerotic calcifications. Outside the brain, vascular calcification receives great focus as a potent player in mechanical stability of vessels and a target for pharmacological treatment [190]. Since no prior studies have assessed the prevalence, distribution or morphology of calcification in IAs with high resolution imaging modalities, there is an important gap in knowledge regarding even the presence of calcification in IA walls. Our study bridges this gap and provides a motivation for future lines of investigations into IA pathology and the role of calcification in IA wall rupture that can impact risk assessment and IA treatment. Furthermore, this study provides an understanding of adverse remodeling in an extreme case of IAs. Appendix B also outlines a protocol used to image collagen fiber and calcification simultaneously. Taken together, these studies lay the framework for understanding the role of calcification in neoartery remodeling and designing mitigating strategies for its occurrence.

Authors' Contributions

AMR and PSG conceived of the study and laid out the study design. PSG performed the micro-CT scanning, reconstruction, image processing and data analysis. KL, EO, and CYC performed the histological assessment and PSG performed the two-photon imaging. FM and JC wrote the code to assess calcification location. RT, MK, BRJ, KA, AY, FC, SA, and JF surgically resected the IA samples from patients for analysis. All authors contributed to interpretation of results, discussions, and writing the manuscript.

Appendix A Semi-Automated Salt Packing Device for Improved Repeatability of Graft Fabrication

A.1 Introduction

iTEVG microenvironmental parameters determine host cellular response, which in turn guide signaling pathways that determine long-term neoarterial fate. The iTEVG parameters not only dictate mechanical properties but also determine the initial foreign body response to the graft. In order to systematically investigate the role of host parameters (e.g. age, species etc.), there is a need to first ensure repeatable production of iTEVGs to eliminate variability in outcomes due to batch variability in graft production.

As outlined in earlier chapters, graft fabrication consists of two key steps – i) creating the PGS core (packing salt into an annulus to create a the salt tubes – the negative for the PGS core, followed by adding PGS solution to the salt tubes, then leaching out the salt to recover the PGS core) and ii) electrospinning the PCL sheath around the PGS core. The main element that introduces errors in fabrication is the salt packing stage. The error manifests itself either as gross geometric error in which the graft is not symmetric, or microscopic error, wherein the graft porosity is not repeatable or consistent across its length. Furthermore, the process of salt packing itself is highly inefficient and involves hand packing at the rate of roughly five tubes hour. There are also losses associated with breakage of the packed salt tubes.

In order to overcome these drawbacks, the goal of our work was to develop a machine that autonomously packs the salt tubes and decreases the packing time, while maintaining consistent

thickness and salt density (which determines graft porosity). This appendix will outline the details of the device developed to achieve these objectives.

A.2 Design Requirements and Constraints

A well-designed device must be capable of manufacturing 10 salt tubes/hour while meeting an 80% success rate. In order to be considered successful, a salt tube must meet the following requirements:

1. The inner diameter should range from 0.75 - 0.80 mm.
2. Wall thickness should range from 330 - 350μm
3. Graft length should range from 15mm to 20mm.
4. Total porosity of the tubes should be <= 25%.
5. The 2D pore size distribution of the graft should range from 25-32 μm along the length of the graft.
6. The salt tube must release from a 1.5 mm inner diameter polytetrafluoroethylene (PTFE) mold without cracking.
7. The salt tubes should be axisymmetric.
8. Packing time should be <5min/tube.
9. The device should be modular.
10. The device should have reduced human interaction.

A.3 Device Assembly Units

The salt packing device was developed as an assembly of modular units. This modularity ensured ease of alignment and ease of future improvements to the device. The device can be described in 5 subassembly units - Tube Holder, Mandrel Assembly, Funnel Assembly, Plunger Assembly and the Support Structure. This section describes each of the subassemblies in detail.

Tube Holder

The tube holder is designed as the main housing chamber for PTFE tubes that are individually packed with salt and released from the machine for further processing. It consists of a 3D-printed cylindrical unit that houses 25 PTFE tubes (inner, outer diameter = 1.588mm, 3.175 mm respectively)(Figure 67). Unlike the process of manual process, the holder prevents the PTFE tubes concentric with the mandrel to maintain axisymmetry. The tube holder also has a retaining plate is used to keep the tube flush with the bottom edge of the holder. After packing the tubes can be released using release mechanism for further processes like curing. Rotating the tube holder 90° allows release of the tube through an indentation in the retaining plate from the machine for further processing. A push button switch activates a stepper motor that rotates the holder by 14.4° ($1/25^{th}$ of a revolution) to the next tube.

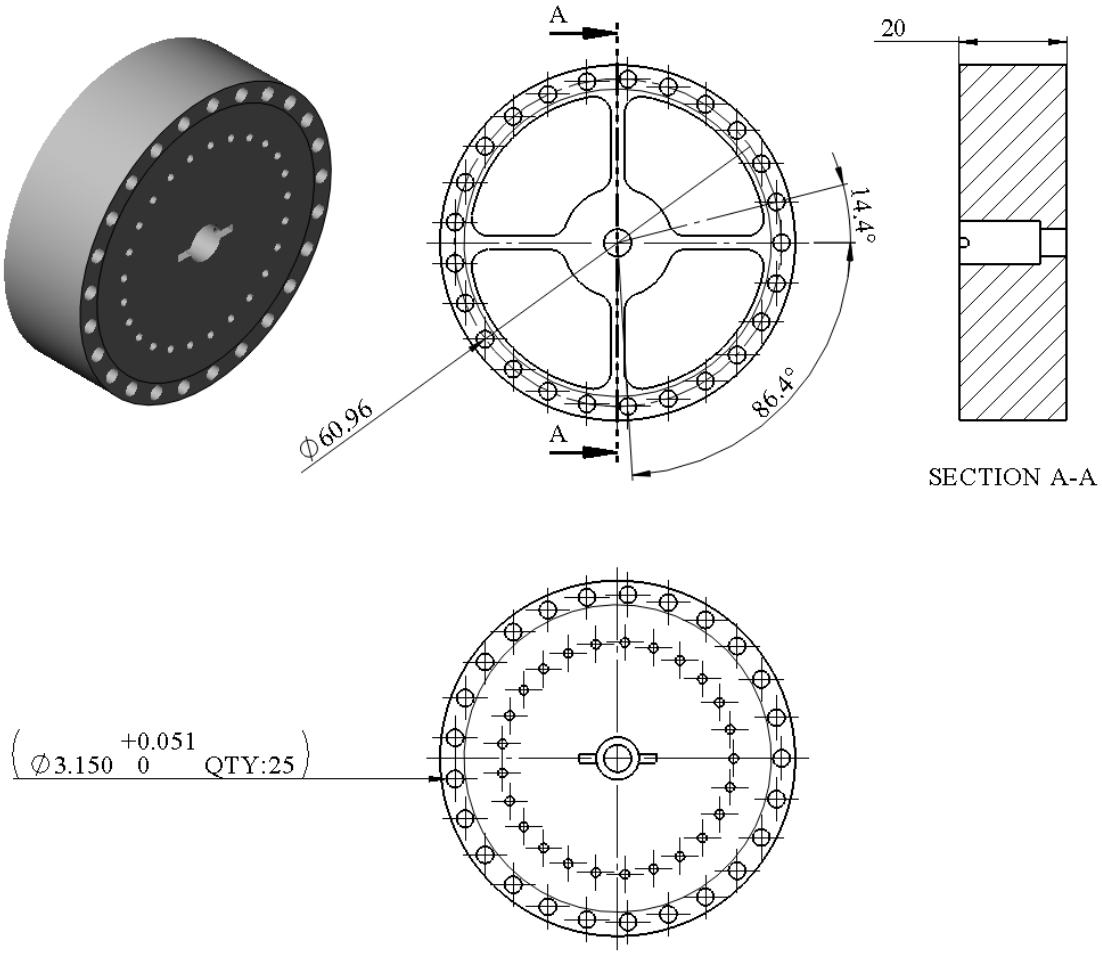

Figure 67: Tube holder assembly.

The assembly holds 25 tubes. Dimensions in mm.

Mandrel Assembly

The mandrel assembly consists of three parts; the inner mandrel, outer mandrel, and plunger holder (Figure 68). The inner mandrel is a 0.79 mm stainless steel 304 wire (McMaster-Carr) that maintains the inner diameter of the salt tube. It is glued into an outer mandrel, which is made from stainless steel 304 and 302 hypodermic tubing (McMaster-Carr) and has an outer

diameter = 1.47mm and inner diameter = 0.81mm. The purpose of the outer mandrel is to pack the salt as the assembly moves downward while the inner mandrel maintains the inner diameter of the tube. These particular materials were chosen made to prevent buckling of the mandrel due to potential misalignment with the PTFE tubing or guide hole.

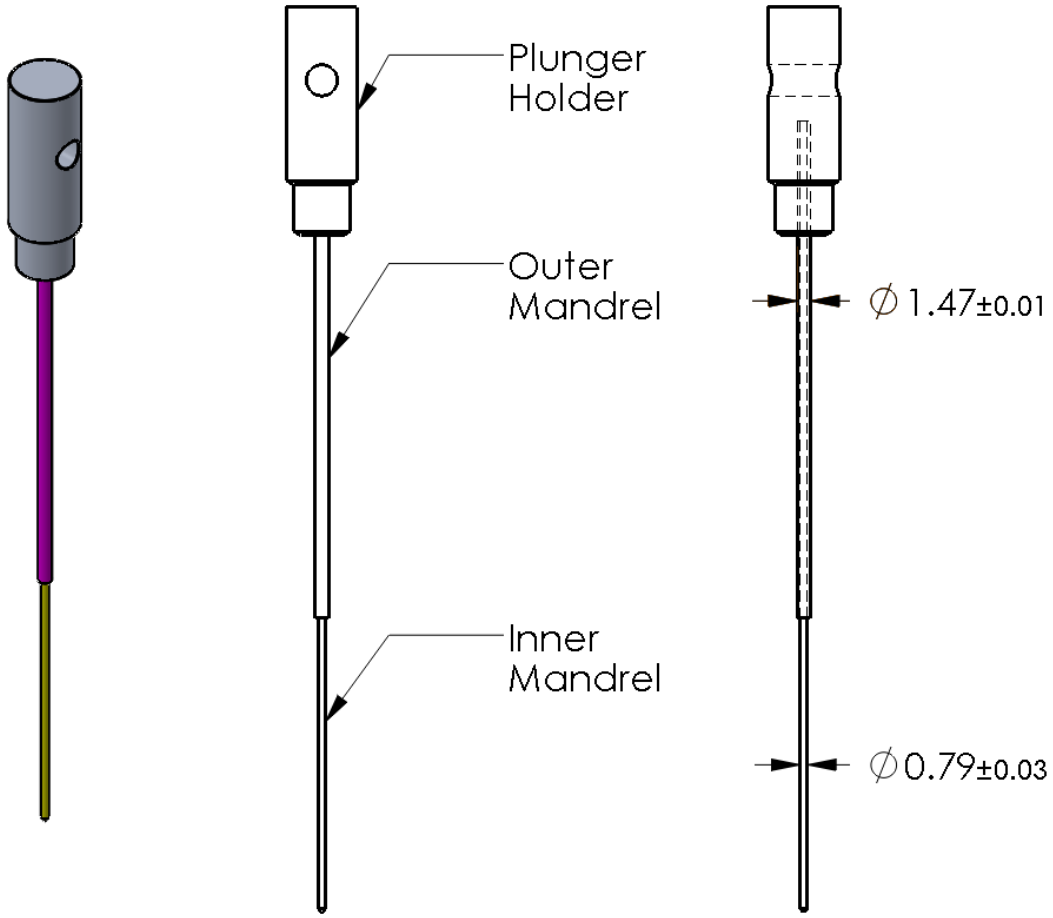

Figure 68: Mandrel assembly.

The assembly is comprised of two mandrels that are press fit and held together in the holder that is attached to the main frame. The diameter of the inner mandrel is equal to the inner diameter of the iTEVG.

Funnel Assembly

The funnel assembly is used to guide a distributed flow of salt particles into the PTFE tubes in which the salt is then packed. The assembly consists of a custom designed, 3D printed funnel and a 20W Dayton Audio exciter (Dayton Audio, OH, USA) connected to a Lepai Tripath Class-T Digital Audio Amplifier (Dayton Audio, OH, USA) (Figure 69). The entire speaker assembly is mounted on the funnel with two 6-32 screws. The screws allow for adjusting the distance between the speaker and funnel via tightening or loosening. The speaker enables creation of a repetitive series of impulses similar to that of a tapping motion shown to best produce salt flow during manual packing [111]. Salt flow is controlled by changing the frequency and amplitude on the speaker and by adjusting funnel to speaker distance.

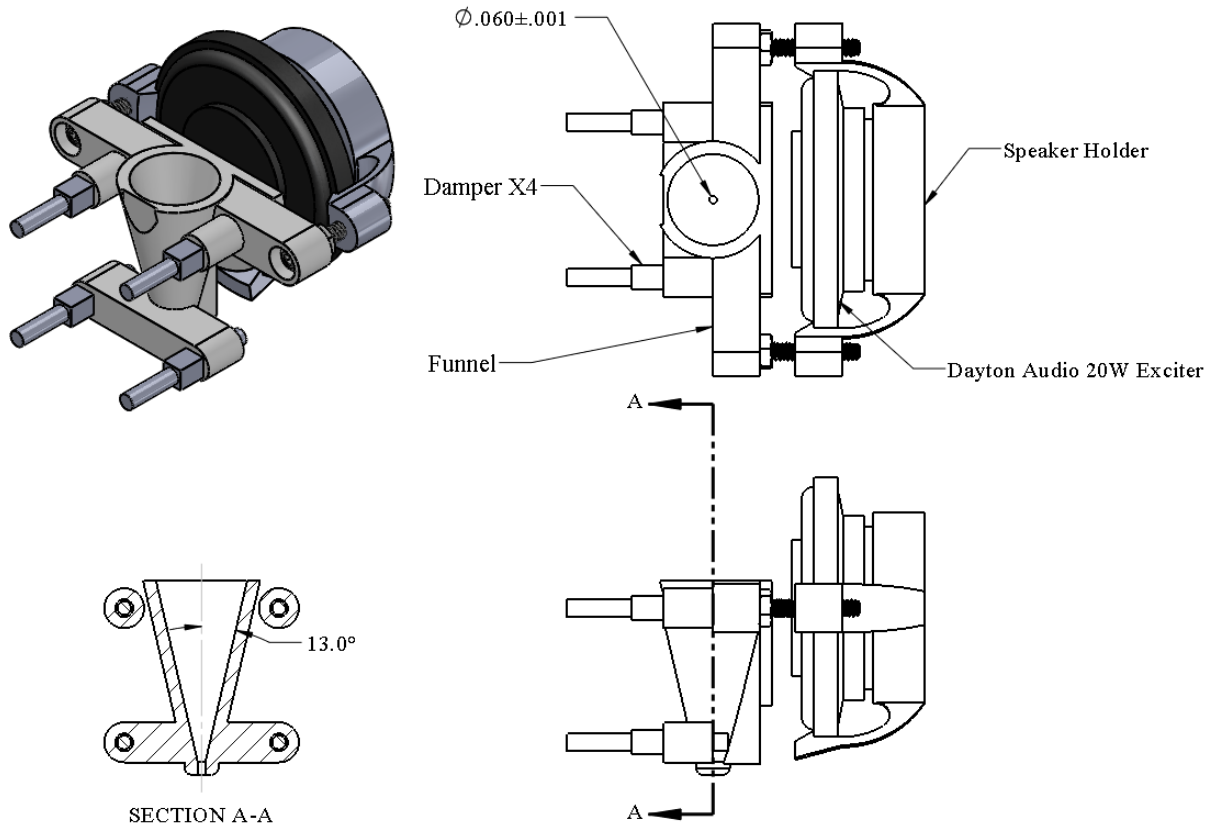

Figure 69: Funnel assembly for salt packing device.

The assembly consists of a 20W audio exciter, holder, damper, and the funnel. Dimensions are in mm.

Plunger Assembly

The plunger assembly houses the mandrel assembly and enables automation of the packing routine. It enables application of force through a linear actuator guided mandrel assembly, centers of the mandrel assembly and stops the packing process when required. The assembly consists of a spring, set screw, bearings and a push button (Figure 70). The set screw-controlled spring is used to regulate the packing force applied through the application of a preload on the spring by tightening the set screw. The switch button is used to stop the packing routine through the push

button activation bolt. The activation bolt is triggered when a tube is entirely packed and the mandrel assembly at the topmost position.

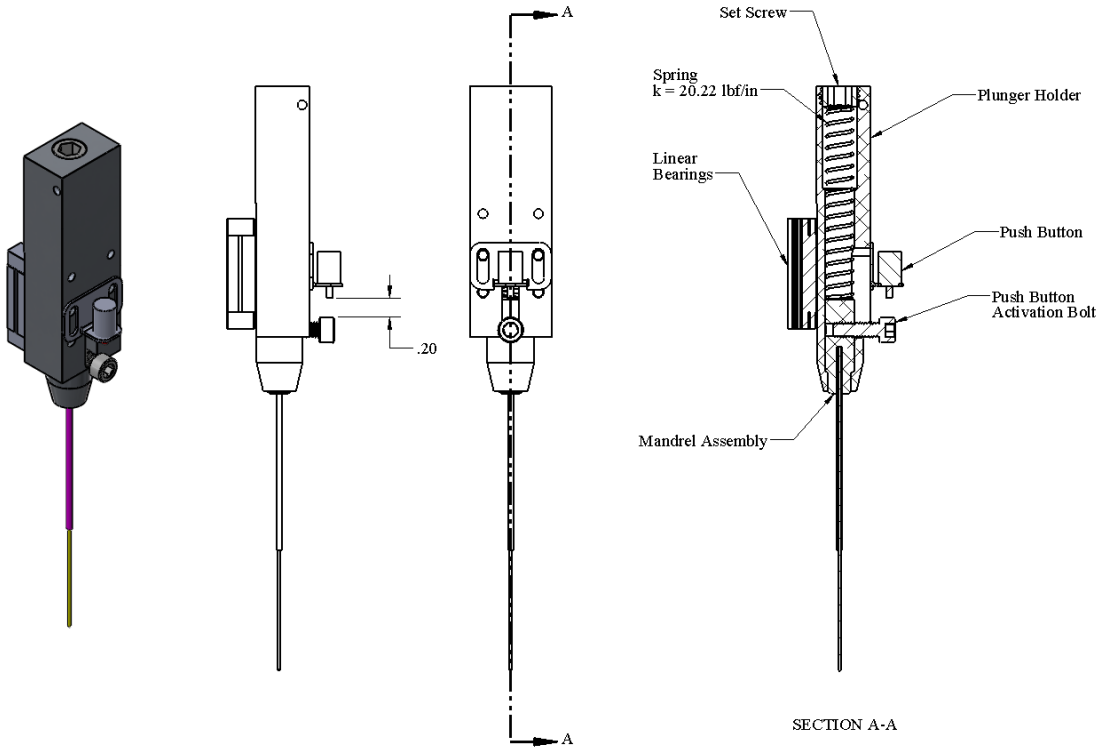

Figure 70: Plunger assembly.

The plunger assembly is comprised of the mandrel assembly, linear bearings, a spring and push button for activation. The assembly enables translation of the mandrel assembly that pack salt crystals and stops when a tube is completely packed.

Main Frame

The main frame features acts as the main supporting structure of the device. It consists three suction cup feet that keep the device anchored to a lab bench and serve as shock absorbers and a linear bearing rail. The main vertical support guides the linear actuator movement. It is reinforced with an aluminum rib to limit mandrel tip deflection to ≤ 0.355 mm. M3x0.5 mm socket head cap screws attach the linear bearing rail to the vertical support and allow adjustability of the rails.

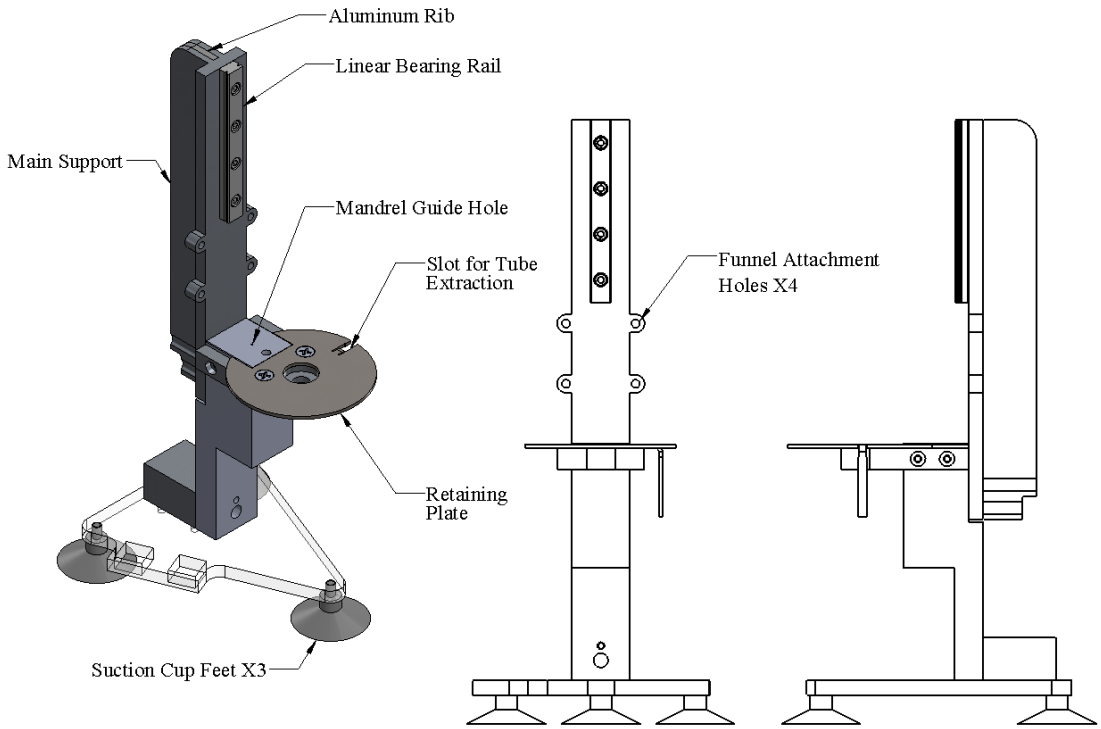

Figure 71: Main frame.

Device Assembly

The 3D and section view of the fully assembled device is shown in Figure 72 and Figure 73. This device is controlled using Arduino hardware and Arduino's Integrated Development Environment (IDE). An Arduino Uno microcontroller translates input signals and controls the motion of the actuator and stepper motor. Figure 74 shows the circuit diagram for controlling the device. All Arduino hardware and software is open source and available for modification.

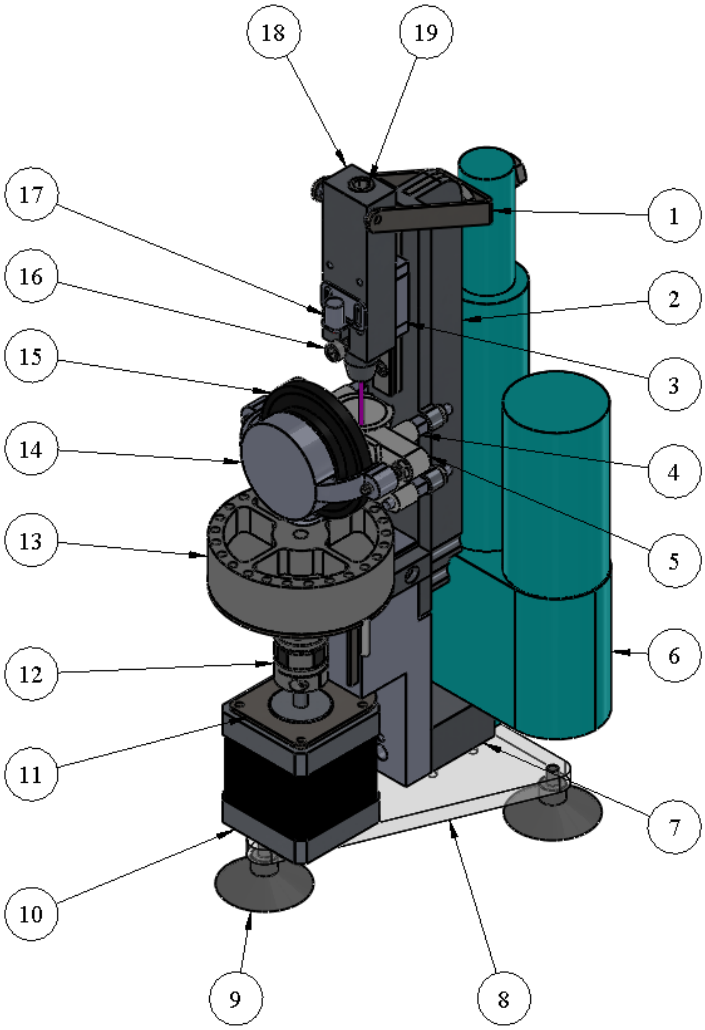

Figure 72: 3D model of semi-automatic salt packing device for iTEVG fabrication.

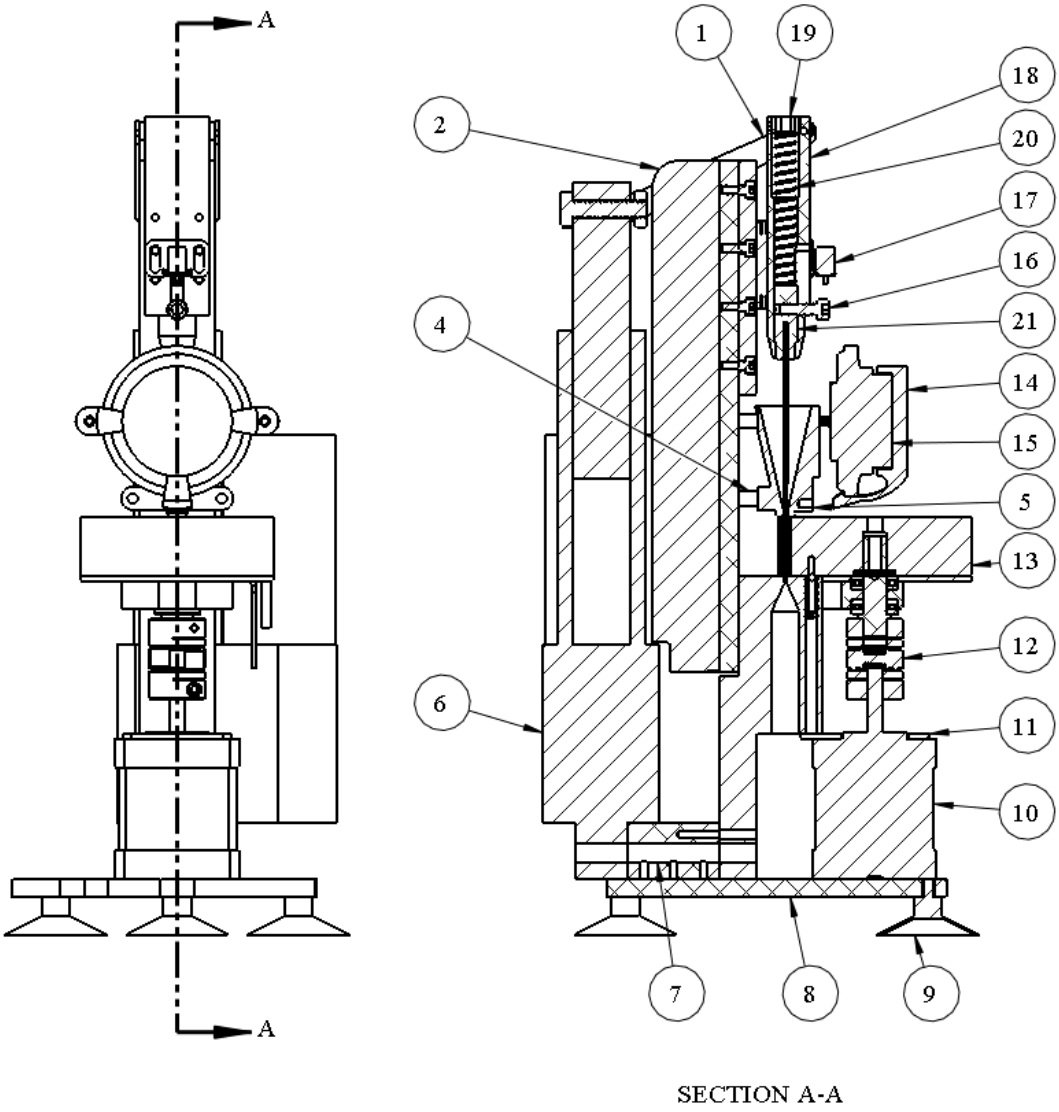

Figure 73: Section view of machine assembly.

Table 11: Part list of components in the semi-automatic salt packing device.

Item Number	Part
1	Actuator Mount
2	Support Structure
3	Linear Bearings (McMaster-Carr)
4	Vibration Damper (McMaster-Carr)
5	Funnel
6	Linear Actuator (Progressive Automation, PA-14P-2-35)
7	Modified Spacer
8	Acrylic Base
9	Suction Cup Feet (3X McMaster-Carr)
10	Stepper Motor, (Sparkfun, 64 oz.in, 0.9 deg/step)
11	Stepper Mounting Plate
12	Shaft Coupler (5mm to 5/16 in, McMaster-Carr)
13	Tube Holder
14	Speaker Holder
15	Speaker (Dayton Audio 20W exciter)
16	Push Button Activation Bolt (McMaster-Carr)
17	Push Button
18	Plunger Holder
19	Set Screw (McMaster)
20	Spring (McMaster)
21	Mandrel Holder

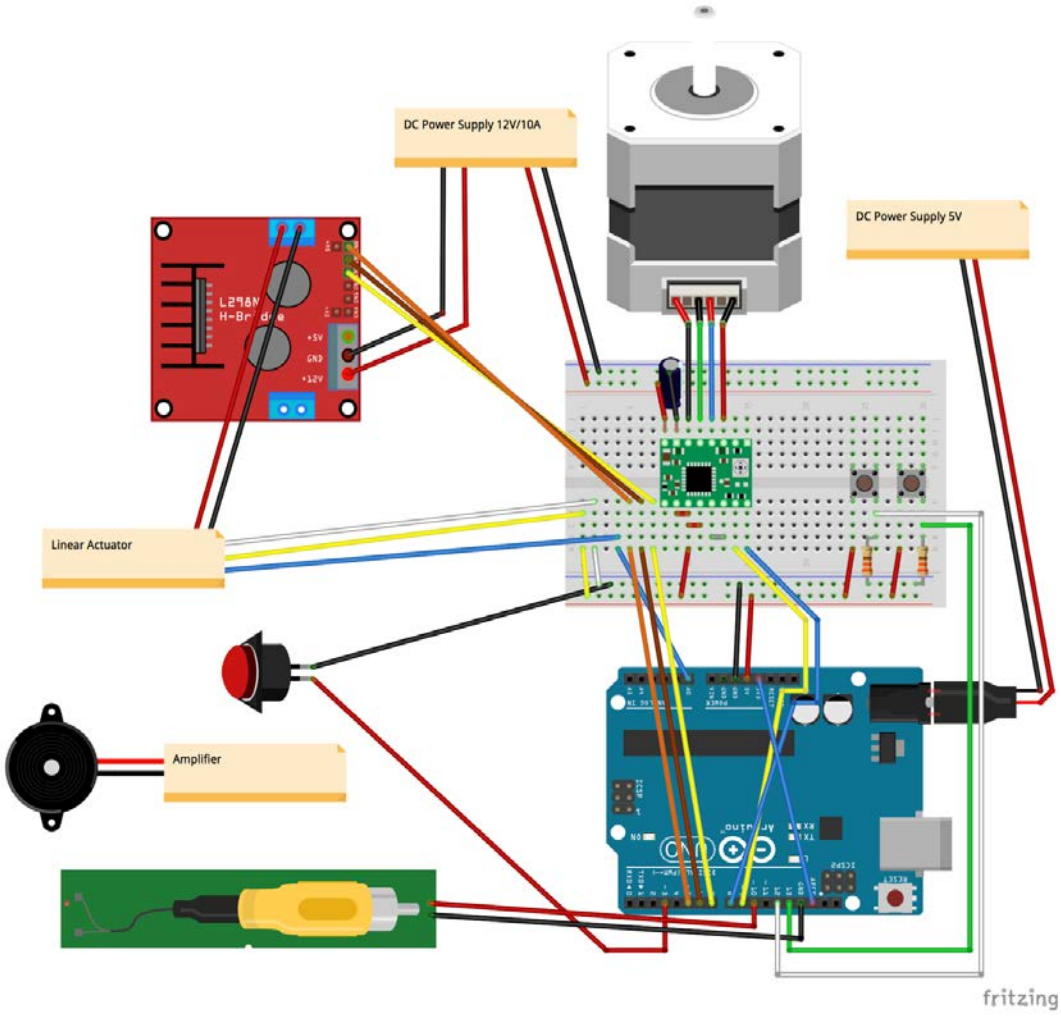

Figure 74: Circuit design for controlling the salt packing device.

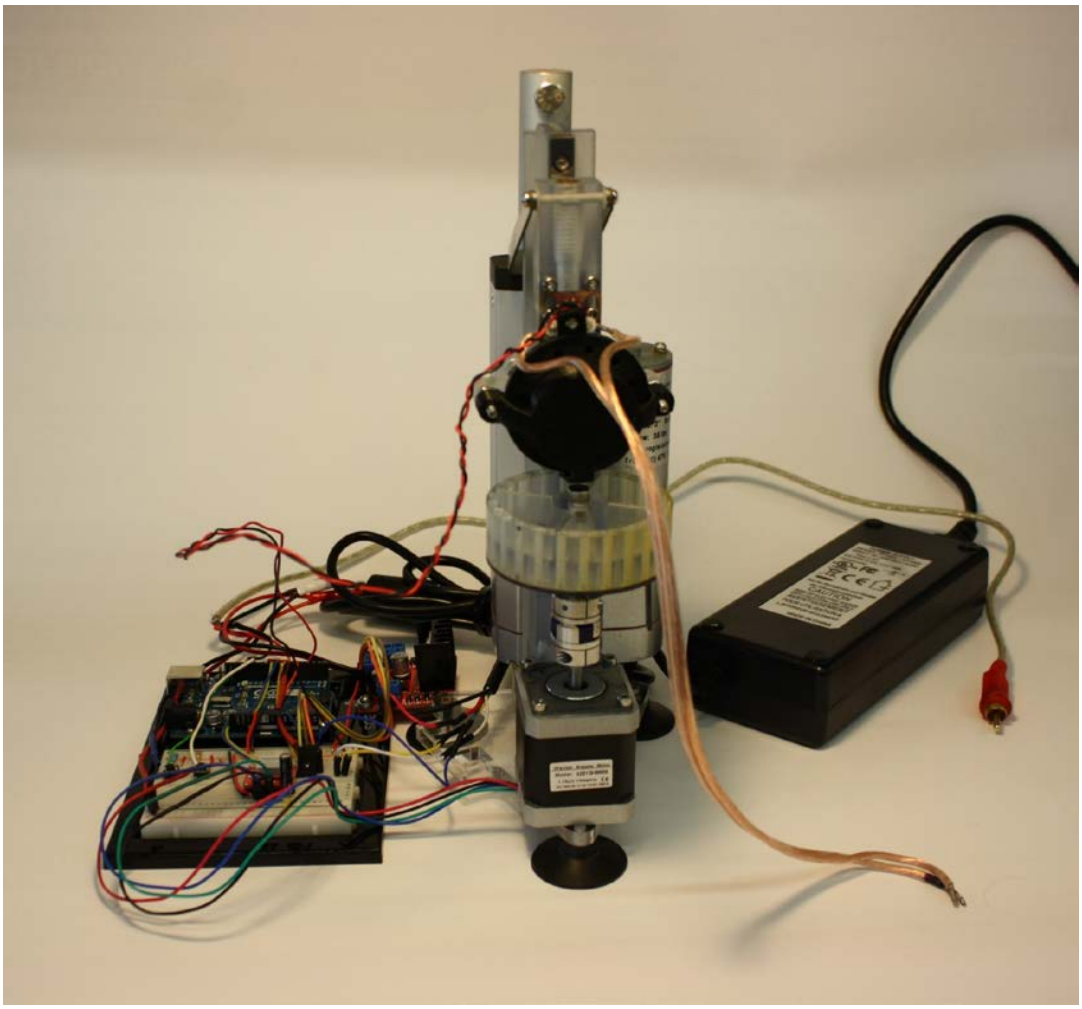

Figure 75: Image of the fully assembled salt packing device.

A.4 iTEVG Fabrication with Assembled Salt Packing Device

Determining Packing force

To achieve the appropriate salt density and thereby, porosity of the grafts, the salt tubes must be packed with the correct compressive force. Packing the tubes too tightly prevents the salt from releasing from the PTFE tube while inadequate force keeps the salt from packing compactly and achieving the correct density. In previous studies, salt tubes were manually packed by "feeling the force". In this section we aimed to determine the appropriate packing force required to achieve a final graft porosity $\geq 75\%$.

The spring and set screw mechanism on the plunger assembly allow for adjusting the packing force. As the set screw is tightened, it preloads the spring and increases the packing force while loosening it reduces the force.

The baseline for packing force was determined with a manual test. Tubes were filled with salt and packed on a scale to quantify downward force during packing. The tubes were then placed in a humidifier and released from the mold. Through a trial and error process, we determined that the optimal force required for packing tubes that did not crack or disintegrate upon release was 15 N. Using this data an appropriate spring with a spring constant $k = 20.22\ lbf/in$ was chosen.

Packing Routine

The packing routine begins by loading salt into the funnel and pressing a button on the breadboard. The exciter vibrates for 500ms, moving some salt into the PTFE tube before the actuator begins its downward motion. As the actuator moves downward (Figure 76a), the wide flange of the mandrel pushes the salt to the bottom of the PTFE tube (Figure 76b). After each compression cycle, the actuator moves the plunger assembly upward to allow more salt to funnel

into the hole. In Figure 76c, note that the smaller diameter of mandrel remains in the guide hole throughout this process to assure symmetry. As the PTFE tube begins to fill up with packed salt, the packing force keeps increasing and the plunger assembly incrementally moves upward toward the push button activation bolt until eventually the plunger assembly hits the push button and stops the actuator movement. This is the end of the packing process for one tube. After this, another button needs to be pressed in order to rotate the tube holder in order to pack the next PTFE tube. This process can be continued until the desired number of tubes are packed. These tubes can subsequently be released during any time after a tube has been packed by pushing against the PTFE tube and sliding it through the indentation in the retainer plate.

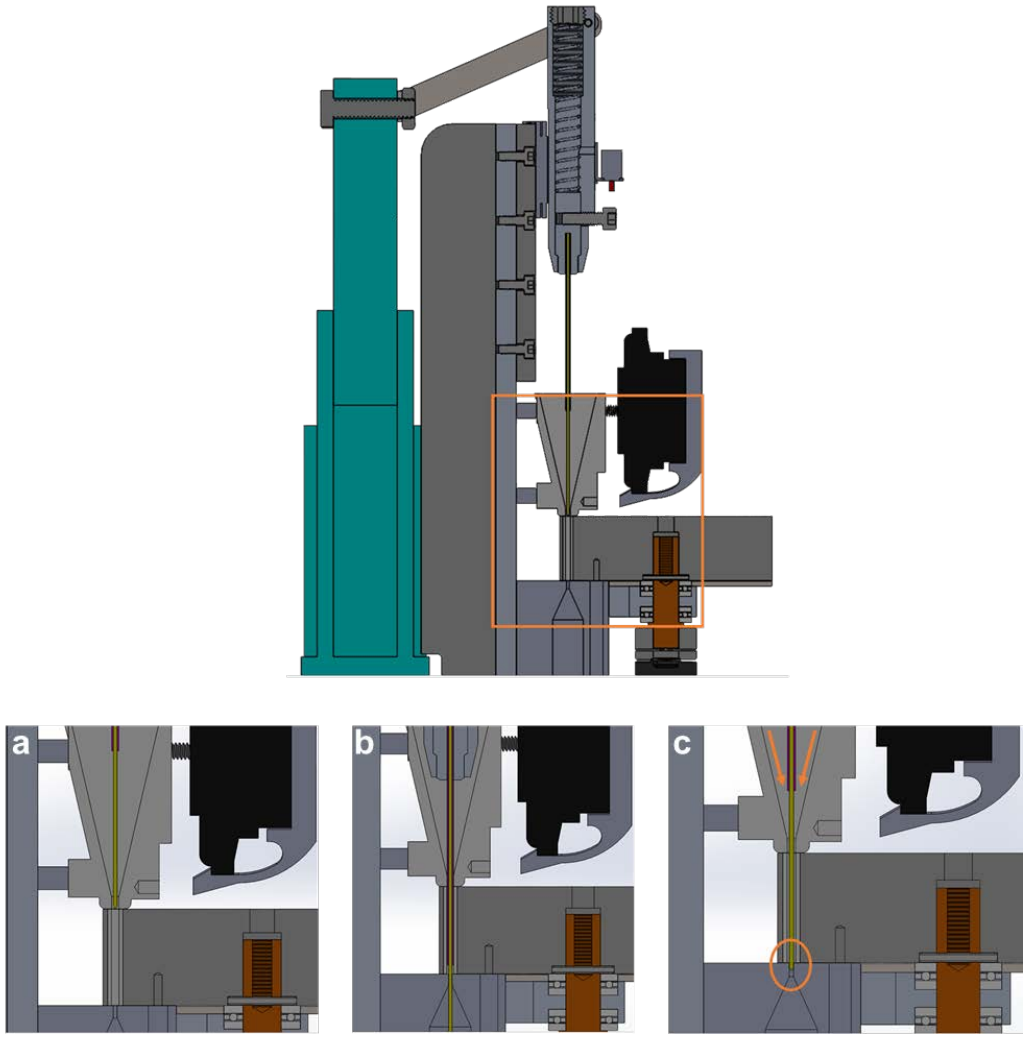

Figure 76: Packing Routine

(a) Actuator at the top of its stroke (top of salt tube), (b) actuator at the bottom of its stroke (bottom of salt tube), (c) salt refill stage. Note that the tip of the mandrel remains in the guide hole of the SLA base to maintain axisymmetry.

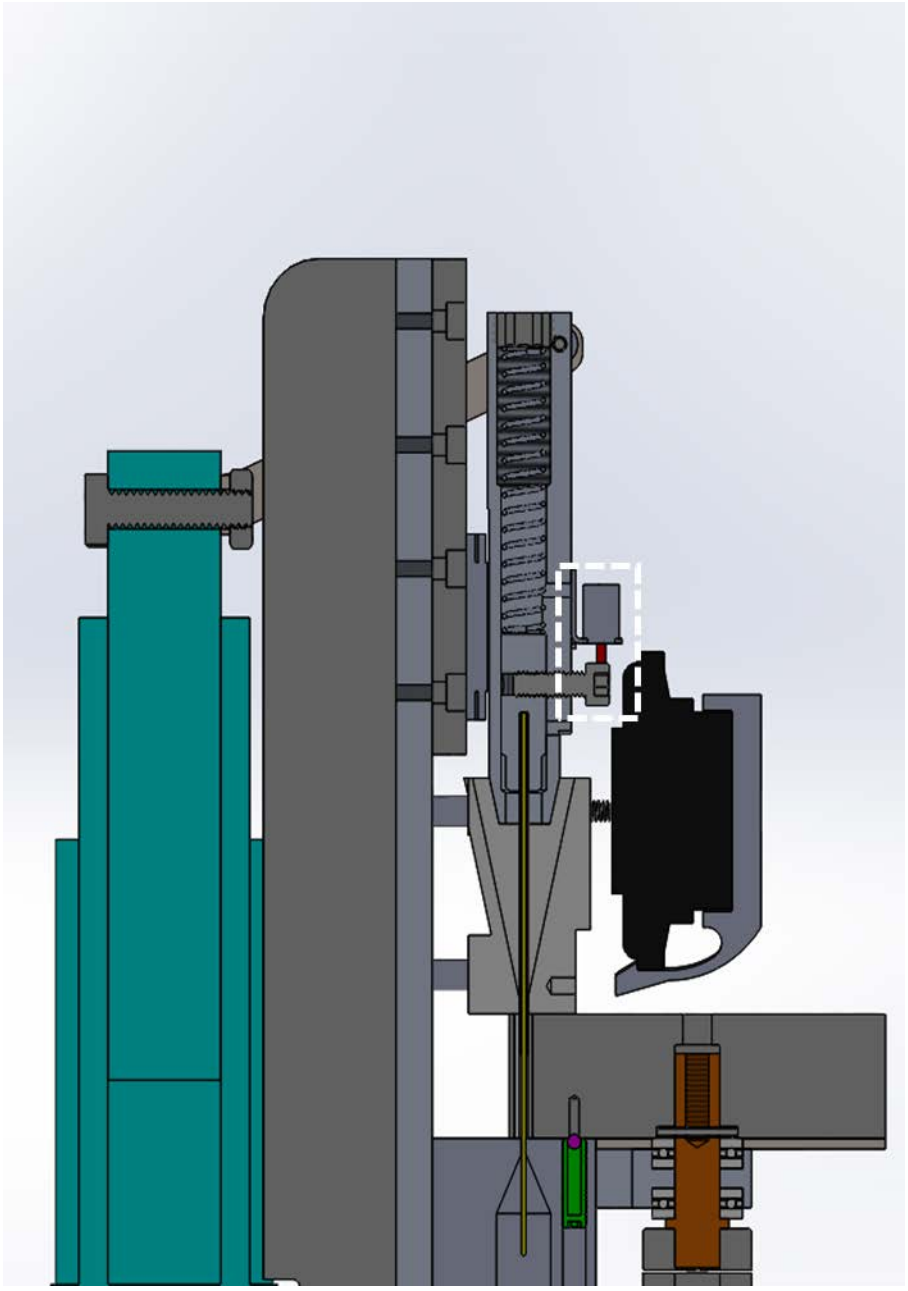

Figure 77: End of packing routine

Contact between the screw and push button drives the actuator upward and ends the packing routine.

The packing routine ends when two conditions are met:

1) The actuator only travels downward to a certain depth
2) The push button is activated
   This state can be seen in the Figure below

A.5 Conclusion

In this chapter, we developed a semi-automatic salt-packing device that is capable of fabricating small diameter (800μm) salt molds at the rate of <5min/mold and >80% yield/batch. The device is capable of packing 25 tubes per session and is comprised of a modular assembly. Furthermore, we determined the ideal packing force required to repeatably achieve a graft porosity of 72% with pore size in the range of 25-32μm. These represent significant developments over the process of manually packing salt tubes which took a significantly longer time with lower yield and unrepeatable salt molds. A major limitation of this work is that these molds are not always axisymmetric. This is due to the high tolerances (20-50μm) required for fabricating these small diameter grafts. This prototype design lays the foundation for the manufacture of the production device. Parts which are currently 3D printed with lower tolerance for the prototype will be machined to tolerances needed to manufacture salt tubes with the required level of axisymmetry.

Contributions

The senior design team (Andrew Lawniczak, Elizabeth Craig, Nathaniel Kissen) fabricated the first version of the design. Abraham Stucky tested the device and programmed the Arduino controller.

Appendix B Simultaneous Imaging of Collagen, Elastin and Calcification in Intact Samples

The work in this chapter was published in the following manuscript:

Gade, Piyusha S., Anne M. Robertson, and Chih-Yuan Chuang. "Multiphoton Imaging of Collagen, Elastin, and Calcification in Intact Soft-Tissue Samples." *Current protocols in cytometry* 87, no. 1 (2019): e51.

B.1 Introduction

Soft biological tissues, such as arteries, heart, bladder, and skin, are layered composites containing collagen and elastin fibers. These load-bearing proteins represent the bulk of the ECM and play a primary role in determining the passive mechanical properties of soft tissues. It is widely acknowledged that cellular phenotype and function are influenced by the properties of this fibrillar architecture. This phenotype, in turn, influences rates of deposition and removal of collagen fibers [31], [210], [211]. Hence, understanding how pathological changes to the ECM alter the stiffness and failure properties of soft tissues is crucial for advancing the treatment of diseases such as cerebral aneurysms, aortic dissection, hypertension, and stroke [212]. A quantitative assessment of these fibers is also important for the design of tissue-engineered soft tissues, including blood vessels and other organs [31], [149] The organization of ECM proteins varies across the wall thickness and generally includes fibers oriented along orthogonal planes. Therefore, there is a great need for effective 3D noninvasive imaging of the fibrous structure of intact soft tissue samples, as 2D histological studies cannot adequately capture this organization.

Multiphoton laser-scanning microscopy (MPM) is a powerful technique that can be leveraged for noninvasive 3D imaging of intact tissue volumes. MPM-induced intrinsic second-harmonic generation (SHG) from ECM proteins such as fibrillar collagen combined with two-photon emission (2PE) of elastin enable high-fidelity imaging without the need for exogenous staining. This approach offers an important advantage over other imaging modalities by enabling simultaneous imaging of the 3D microstructure of both collagen and elastin fibers at relatively large depths (typically hundreds of microns), including the layer-specific inter-relationship of these components. The imaging depth depends on the scattering and absorption coefficients of the tissue, the efficiency of the fluorophore, and the throughput of the optics. Background material on the principals of MPM imaging of biological tissues can be found in various sources [213]–[216].

Although SHG and autofluorescence imaging offers multiple advantages for collagen and elastin fibers, there is a need for complementary protocols for simultaneous imaging of additional wall components using stains and fluorescent probes. Ideally, these protocols would also be effective in fresh samples. Here, we provide such a protocol for simultaneous MPM imaging of calcification along with collagen and elastin fibers that is suitable for both fixed and fresh intact tissue samples. While calcification is a pathology of numerous soft tissue diseases, particular attention has been given to arterial calcification because of its importance as a major predictor of cardiovascular events [217]. Calcification can form in the intima of arteries through a slow, inflammation- driven, atherosclerotic-type process during plaque formation. A second mechanism for calcification is a non-atherosclerotic, phosphate-dependent mineralization in the media that is associated with aging as well as disease pathologies such as diabetes mellitus and chronic kidney disease [187], [202]. Given the involvement of calcification with the ECM, it is important to

understand the location of calcification within the wall as well its physical relationship with collagen and elastin fibers [74].

Since MPM imaging of intact sample volumes is time consuming, it is valuable to identify regions of interest (ROIs) to permit targeted scanning. In the first protocol in this article, we provide a methodology to achieve this objective using microcomputed tomography (micro-CT), which creates a 3D geometric model of the sample along with wall thickness and calcification maps. We demonstrate how these maps can be used to guide the MPM studies. Targeted approaches of this kind are particularly important for unfixed (fresh) tissue samples, which degrade over time. The second protocol provides the methodology for MPM imaging of collagen, elastin, and calcification within the ROIs of the intact specimen. Fiducial markers on the tissue specimen, visible under micro-CT, are then used to identify the ROIs in the sample under MPM. This protocol also provides methods to obtain quantitative data from MPM images, including fiber orientation and waviness, important metrics critical for understanding the mechanical properties of soft tissues.

B.2 Basic Protocol 1: Use of microcomputed Tomography for A Priori Selection of Imaging Location

To scan a square millimeter of tissue (four 500 μm2 regions) of 200 μm thickness by MPM requires on the order of 1 to 2 hr. It is therefore valuable to identify ROIs prior to MPM imaging, particularly for fresh sample analysis. In this first protocol, noninvasive 3D micro-CT scanning of the tissue specimen is performed to generate a 3D geometric model of the sample with a corresponding wall thickness map and 3D calcification map. Regions for focused MPM analysis

are then chosen using the 3D geometric model based on features such as focal areas of calcification. The preferred scan region is located on the fresh tissue sample through the use of fiducial markers (dye and beads) that are visible in the micro-CT model. This protocol is designed for both fresh and fixed tissue samples.

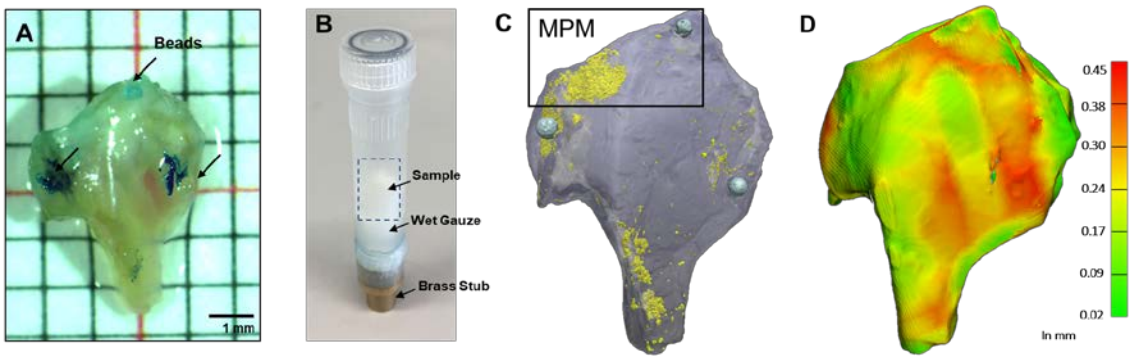

Figure 78: Preparation and assessment of calcification and geometry using micro-CT.

(A) Dissection scope image of a PFA-fixed aneurysm. (B,C) Mounting setup for micro-CT scanning (B) and a 3D reconstructed image of the micro-CT data (C) for an aneurysm sample with calcification (yellow) and tissue (gray). Note the beads on both the physical and reconstructed sample. These beads and dyes serve as physical markers for mapping MPM images to the 3D CT images and the physical samples. (D) Wall thickness map of aneurysm sample constructed from micro-CT data. This map can be used for selecting appropriate ROIs for MPM imaging

Materials

- Tissue sample to be imaged
- Wet gauze
- Tissue dyes: Davidson Marking System dyes (Bradley Products Inc.), preferably blue and/or red (see step 2)

- Dissection microscope (Olympus SZX10)
- 200 to 300µm polystyrene beads (e.g., Polysciences Inc.)
- Loctite 404 glue (McMaster-Carr)
- 1.5-ml clear microcentrifuge tube (e.g., Thermo Fisher Scientific)
- Mounting brass stub
- Desktop microcomputed tomography (micro-CT) scanner (Skyscan 1272, Bruker highest magnification) Corporation, Belgium; resolution = 0.35 µm (16 megapixel X-ray detector)
- Computer hardware and software for image acquisition, reconstruction (NRecon, Bruker Corporation, Belgium), and analysis (Simpleware ScanIP, Synopsys, Mountain View, CA, USA)

Application of fiducial markers

1. Dry the sample using Kimwipes until no excess fluid is visible on the tissue surface.

2. Place the sample under the dissection scope and mark fine dots in a grid structure using the tissue dyes (Figure 78A). This grid structure is visible under MPM analysis and enables the mapping of MPM imaging locations to CT images (step 3). Turn off the dissection scope light and let the sample stand for 5 min to allow the dye to bond to the tissue surface. Turning off the light helps avoid any potential damage to the tissue.

Although in principle, any color of Davidson dye could be chosen for tissue marking, the chemical makeup of each dye is different. Therefore, in addition to having different contrast with the tissue, the different colors of dye also have varying affinity with

the tissue. We found that the blue and red dyes provide the best results for vascular tissues. The yellow and orange dyes do not provide sufficient contrast with the tissue surface color, while the green and black dyes are highly miscible in water and can spread excessively on the tissue surface.

3. Attach marking beads over the dye location using a small amount of Loctite 404 glue (Figure 78A).

Loctite 404 glue was chosen for attaching the beads as the application of this adhesive is easily controlled and little glue volume is needed. These features ensure there is negligible change to tissue material properties. The beads are visible under micro- CT; however, they can detach and separate from the tissue during the preparations for MPM scanning. Although the dye mark cannot be detected under micro-CT, it is more permanent. Therefore, this bead/dye combination guarantees that beads will be visible under micro-CT and that dye marks (and possibly some beads) will be visible under the MPM, while avoiding excessive use of adhesive. This ensures the presence of sufficient markers to register points from the surface of the 3D micro-CT data set to MPM images.

Tissue mounting in micro-CT scanner

4. Place wet gauze or Kimwipes at the bottom of a 1.5ml clear microcentrifuge tube to prevent sample dehydration during scanning. Place the sample vertically on top of the gauze at the center of the tube (or on top of an added piece of Styrofoam, if needed to help position sample) and seal it tightly (Figure 78B).

To ensure maximum field of view, place the sample in the center of tube, symmetrically located with respect to the vertical axis. Alternatively, if the sample is very

small, Glad R? cling wrap can be used to mount the sample on the stub [218]. *This particular brand of wrap has been found to avoid substantial X-ray attenuation.*

5. Place the microcentrifuge tube vertically on the mounting brass stub and seal the tube to the stub using Parafilm sealing film (Figure 78B).

6. Mount the stub onto the micro-CT scanner.

Tissue scanning

7. Scan the sample using the settings outlined here while maintaining a scan time of <2 hr for fixed samples and <1.5 hr for fresh samples to prevent sample dehydration. Note that the settings will vary slightly depending on the sample dimension. Samples image pixel size of 1 to 3 µm, frame averaging of 8 to 10, and rotation step size that have dimensions <1cm × 0.5 cm can be scanned at 50 kV, 200 µA, with an of 0.1° to 0.4°, scanned 180° around the vertical axis. Since this protocol pertains to biologic tissues, no filter is used for scanning. However, aluminum, copper, or a combination of the two can be used for samples with higher density.

A flat-field correction is done prior to every scan to ensure optimal image contrast. Two hours is a conservative estimate for micro-CT imaging affixed tissue samples using this procedure. Thicker samples will dry out more slowly and can be scanned for a longer time if required. If the sample does dry out, the corresponding change in sample volume will generate misalignment artifacts that will be seen during post-processing.

Creation of sample volume and selection of region of interest

8. In order to ensure optimal image quality, correct the images for the most commonly occurring CT artifacts, such as beam hardening and ring artifacts. Then, select

an ROI and corresponding volume of interest for reconstructing raw CT images. The interested reader can reference the NRecon User Manual for further details on image reconstruction.

9. Segment calcification from the reconstructed tissue data set using one of a variety of image processing software (e.g., MATLAB, ITK, VTK, Slicer 3D, etc.). In this protocol, we use Simpleware ScanIP for image analysis owing to the ease with which high-quality surface mesh from CT data can be generated with this software. Segment the calcified regions (regions of relatively high grayscale value) using a combination of thresholding, connected regions filtering, Boolean operations, and Gaussian smoothing to create a calcification mask. Create a second mask for the tissue with beads. To enable 3D visualization of the calcification within the tissue sample, overlay these masks (Figure 78C).

The interested reader is referred to the online Supporting Information for detailed methodology for segmentation and analysis of calcification and tissue.

10. Select the ROI for MPM analysis using the overlaid image based on the scientific objective of the investigation. For example, in Figure 78C, an ROI is selected for a targeted MPM study (rectangle) due to the clustering of calcification in that region.

11. MPM imaging can also be targeted on the basis of geometric features such as sample thickness or interfaces between thick and thin regions. These geometric features can be evaluated from the surface/volume mesh and thickness maps for the sample. In this protocol, we have used Geomagic (3D Systems) for this purpose, using an analysis function for wall thickness maps (Figure 78D).

B.3 Basic Protocol 2: Simultaneous Second-Harmonic Generation and Two-Photon Excitation Imaging of Collagen, Elastin, and Calcification

In this protocol, we describe how to use MPM-induced SHG and 2PE imaging to detect collagen and elastin in soft tissue along with calcification, which is made visible using a far-infrared tracer. Using this technique, it is possible to nondestructively investigate the three-dimensional structural relationship between ECM and calcification. This protocol can be used to image either fresh or fixed tissue samples. We illustrate some key results using a fresh human cerebral artery and a fixed specimen from a human cerebral aneurysm.

Materials

- Osteosense 680 stock solution (see recipe)
- 10X PBS
- Tissue sample to be imaged 4% paraformaldehyde (PFA)
- Custom-made sample chamber (Figure 79) assembled from two threaded metallic rings (e.g., IDEX Health and Science), a silicone gasket (e.g., Roettele Industries), and two 18-mm-diameter round microscope glass coverslips (e.g., Thermo Fisher Scientific)
- Olympus FV 1000 Multiphoton Microscope Spectra-Physics DeepSee Mai Tai Ti:Sapphire laser (Newport Corp.) 1.12-NA 25X multiphoton excitation (MPE) water-immersion objective Backscatter epifluorescence detectors 350 to 450nm emission filters with 50 spectral bin (Chroma Technology)

- Computer hardware and software for 3D reconstruction of MPM images and fiber analysis: e.g., Imaris 9.2 (Bitplane) or CT-Fire, an open source software developed by researchers at the University of Wisconsin Madison [152].

Sample preparation with calcium stain

1. Dilute the Osteosense 680 stock solution (a near-infrared bisphosphonate-based calcium tracer) 1:50 (v/v) with PBS.

2. If staining a fresh sample, incubate the intact sample in the calcium tracer for 24 h at 4°C in dark.

3. If staining a fixed sample, fix the intact sample for 24 h in 4% PFA. Rinse the sample and incubate it with the calcium tracer for 24 h at 4°C in the dark.

4. After incubation, rinse the sample thoroughly with 10X PBS.

5. Mark the tissue as outlined in Basic Protocol 1, steps 1 to 3.

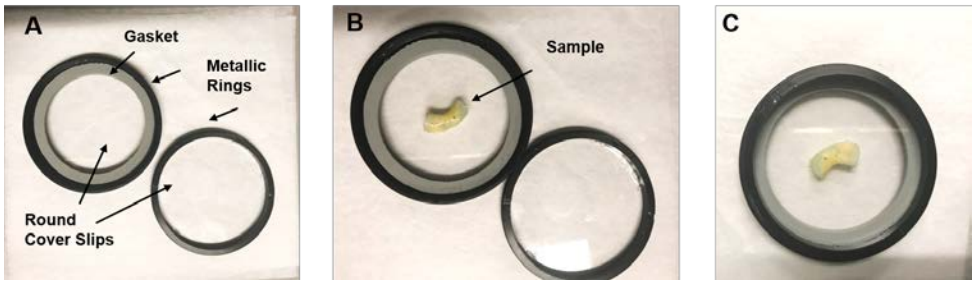

Figure 79: Ring assembly for MPM imaging.

(A) Two threaded round metallic rings with coverslips and appropriately sized gaskets. (B) Sample placed onto one half of the assembly and immersed in 10× PBS. (C) Completed assembly after the two metallic rings are screwed together.

Sample mounting

6. It is important that the sample is securely held during MPM imaging to minimize artifacts from sample movement. As the soft tissue is often composed of layers, it can be advantageous to slightly flatten the tissue so that it can be imaged orthogonally to these layers. For these purposes, we use a simple custom-made chamber that can be placed on the MPM stage (Figure 79), consisting of two concentric metallic rings, with threads on the inner and outer surface, respectively, two round coverslips, and a gasket (Figure 79A), whose thickness determines the internal chamber height. To assemble the chamber, place a round glass coverslip within one ring and place the the second coverslip over the tissue with the metallic ring on top (Figure 79B and C). gasket on the coverslip, followed by the tissue sample. Fill with 10X PBS and place After ensuring that no air bubbles are present, tighten the coverslip-ring assembly.

*Once the chamber is assembled, notations can be marked on the outer coverslip to identify the imaging side (e.g., luminal) and, if desired, a grid can be drawn on the glass to clarify the orientation (*Figure 80A*). The spacing between the rings can be altered by selecting gaskets of different thicknesses.*

As an alternative, hanging-drop slides (Fisher Scientific) of appropriate depth can be used to secure the sample. These are available in varying depths from 1.4 to 3.2 mm. Place the sample in the slide, fill with PBS, and cover with disposable coverslips. However, the sample will generally be held more securely and flattened more effectively with the custom chamber.

Image acquisition

7. Place custom chamber on the microscope stage and add distilled water on the top coverslip of the chamber so that the lens is immersed in water during imaging.

8. Select the appropriate settings for MPM imaging. The following settings work well for imaging collagen, elastin, and calcification with a 1.12-NA, 25X MPE water-immersion lens: 800 nm excitation wavelength, dwell time of 8 µs/pixel, scan pixel count of 1024 × 1024, and laser intensity of 7%.

Further details on the selection of MPM settings can be found in Xie et al. [213]

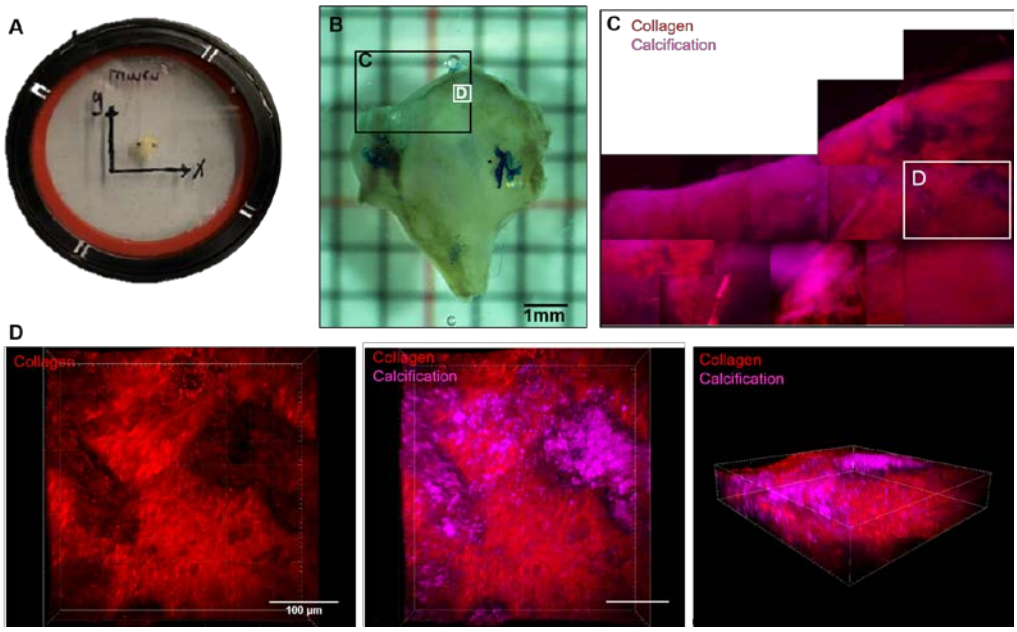

Figure 80: Simultaneous MPM imaging of calcification and collagen.

(A) Aneurysm sample mounted in custom-made device to hold tissue sample steady and flat during the course of MPM imaging. The xand ydirections have been marked manually on the coverslip. (B) PFA-fixed aneurysm sample marked with tissue dye and polystyrene beads. Areas of zoomed images in later panels are indicated. (C) Montage of area C showing projection of 3D stacked MPM images of collagen (red) and calcifi- cation (magenta). (D) Zoomed images of location D. From left, note the degraded collagen fibers in regions that are occupied by calcification. At right, 3D image showing calcification across the scanned section. Each image is a 500 µm × 500 µm projected stack of 2-µm-thick sections.

9. Take sequential scans across the thickness (a z-stack series) at 2µm intervals. The locations of the first and last images of the z-stack series are chosen based on a fast prescan using a coarse setting.

Samples can be scanned from both the luminal and abluminal sides and can typically be imaged to a depth of 200 to 300 µm without optical clearing, depending on the

signal intensity from the components of the ECM. For example, the elastin in the internal elastic lumina of cerebral arteries has strong autofluorescence that can prevent imaging through to the medial collagen fibers for unloaded samples. However, when the cerebral artery is mechanically stretched, the medial collagen can usually be imaged from the luminal side.

10. Collect SHG signal from collagen using backscatter epifluorescence detectors and 350 to 450nm Chroma emission filters with a 50 spectral bin. Collect the intrinsic elastin 2PE signal using a 500 to 550nm filter and calcification signal using the fluorescent calcium tracer signal in the 665 to 735nm range for either fixed (Figure 80C and D) or fresh samples (Figure 81).

The emission range for the calcium tracer provided by the manufacturer was used to select the optimal filter to use for MPM scanning. An excitation wavelength of 800 nm provided good signal quality for the calcium tracer, thereby allowing simultaneous imaging of collagen, elastin, and calcification. As a result, it is possible to see all three components in images and 3D reconstructions where the signals are combined, enabling analysis of the interactions between these three components.

Three-dimensional image reconstruction

11. Create 3D image volumes from the acquired z-stack series of images using software such as Imaris 9.2 (Bitplane) (Figure 80 and Figure 81).

After this point, collagen, elastin, and calcification can be quantitatively analyzed in the individual MPM images, or in the 3D reconstructed stacks as described here.

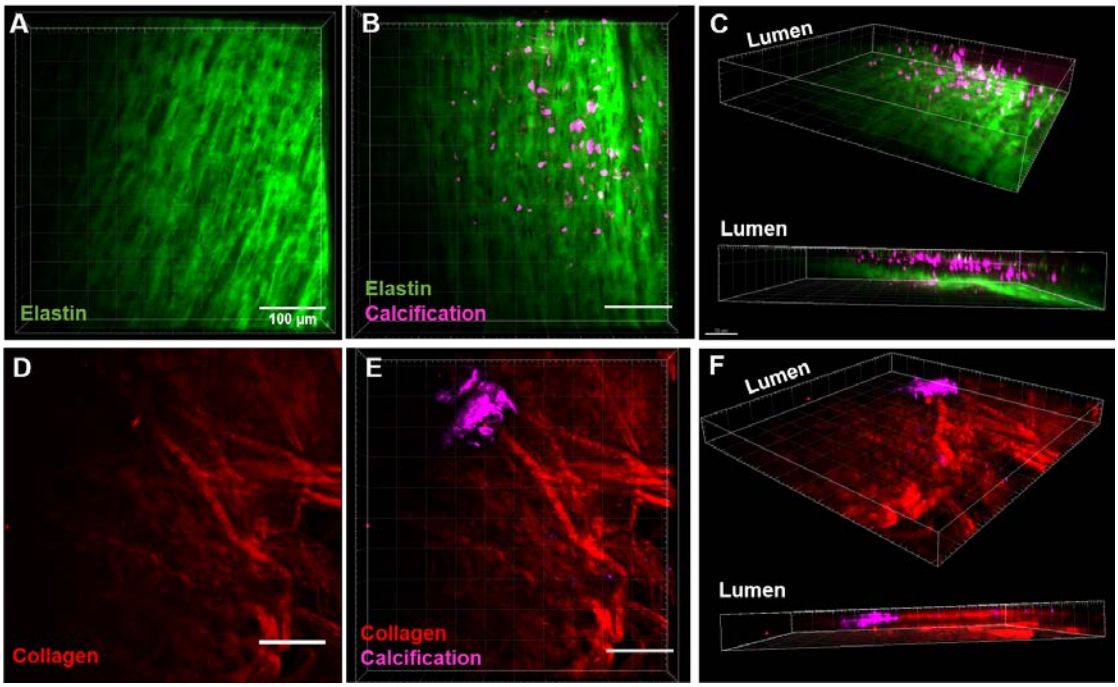

Figure 81: Projections of 3D stacks from MPM imaging of a fresh native human cerebral vessel, imaged en face from luminal (top panel) and abluminal (bottom panel) sides.

(A) Internal elastic lamina (IEL) (green) with visible fenestrations. (B,C) Calcification (magenta) visible on the lumen side along the IEL. (D–F) Thick, wavy adventitial collagen fibers (red; D) and calcification (magenta; E,F) adjacent to the IEL. Each image is a 500 µm × 500 µm projected stack of 2-µm-thick sections.

Quantitative analysis of collagen fiber orientation and waviness

12. Calculate metrics of fiber orientation and waviness on each individual axial slice or by tracing collagen fibers using manual filament tracing (Figure 82A). In this protocol we used the commercial software Imaris 9.2 (Bitplane) to manually trace fibers and thereby ensure that the filament captures the curves of the fibers to obtain accurate measurements of fiber waviness [12]. Waviness and fiber orientation can be determined using built-in

functions within Imaris. The variation of these metrics across the wall thickness can be visualized using, for example, a heat map or rose plot (Figure 82B and C).

Collagen fiber orientation and waviness are important structural features of soft tissues that influence their mechanical function. For example, fiber waviness enables a sample to undergo large deformations with very little load (high compliance), as occurs in arterial collagen fibers. Once the collagen fibers are straightened, they contribute to load bearing, leading to a stiffer response at higher strains [12]. *By obtaining quantitative descriptions of these features, tissue structure can be compared, for example, between treated and untreated tissue or between diseased and healthy tissue. Furthermore, this information can be used to develop mathematical equations (constitutive models) with which to model the mechanical responses of these tissues* [12].

The conformation of the collagen and elastin fibers can be extracted from single planar images either through the manual tracing described here, or through automated methods that include 2D discrete Fourier transform analysis [219], *and a combination of fast Fourier transform and wedge filtering* [220]. *We find the fiber-tracing approach preferable for evaluating the fiber straightness (inverse of waviness) and obtaining average fiber orientation for wavy fibers.*

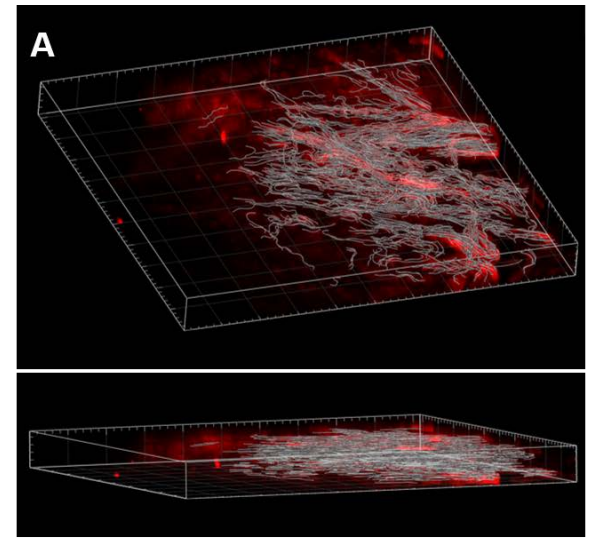

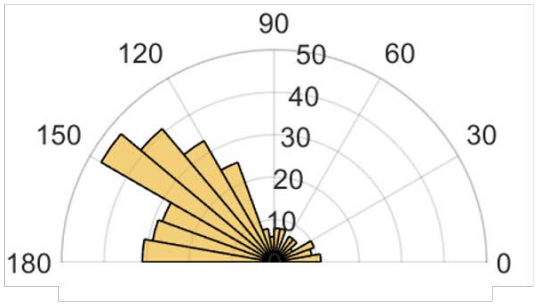

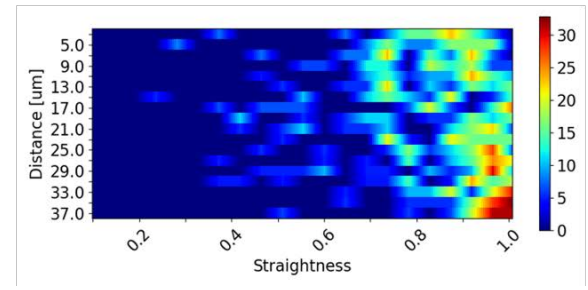

D

	Total Area Across All Slices [mm²]	Area Fraction [%]
Collagen	1.0639	85.11
Calcification	0.1862	14.89

Figure 82: Manual fiber tracing to determine collagen fiber orientation and waviness using Imaris 9.2. (A) Volume projection of collagen fibers (images in Fig. 4D) with fiber tracings. Each image fiber orientation distribution. (C) Heatmap of fiber straightness as seen across the imaged wall is a 500 µm × 500 µm projected stack of 2-µm-thick sections. (B) Circular rose plot of collagen thickness of the sample. Top row represents luminal side and bottom row represents abluminal side of sample. (D) Areal density of calcification and collagen fibers for the volume shown in Figure 4E and F.

Quantitative analysis of collagen and calcification areal density

13. Calculate calcification and collagen areal density by analyzing the separate color channels in each image. Using a custom-written MATLAB script (MATLAB2017A) (see Supporting Information online), load images and separate color channels. Segment each of the constituents (collagen and calcification) using Otsu segmentation [221] in their respective channels. Calculate the area of segmented pixels in each slice and sum up the segmented area across the volume to calculate total areal density in the image volume (Figure 82D).

B.4 Reagents and Solutions

Osteosense stock solution: gently shake or vortex to ascertain that the agent is fully in solution. Keep the stock Add 1.2 ml of 1× PBS to one vial of Osteosense 680 solution (Perkin Elmer) and solution wrapped in aluminum foil at 4°Cfor <2 months.

B.5 Commentary

Background Information Quantitative evaluation of the microstructure of biological tissue samples is essential for understanding tissue function, disease pathologies, disease progression, and the role of therapeutic agents. Classical histological techniques have been instrumental in elucidating the microstructural anatomy of various tissues, which has improved understanding of the related physiology and also contributed to the design of novel treatment strategies of image

alignment [222], montaging [223], and autofocusing have markedly increased the utility of serial sectioning for 3D visualization of tissue microstructure [20]. However, histological techniques are inherently destructive, must be conducted on fixed, processed samples, are associated with a number of artifacts, including tissue shrinkage, changes in morphology, tears, detachment of layers, and folds, and can be applied to only small volumes of tissue [224]. Therefore, there is a great motivation to develop protocols for directly imaging whole volume samples.

MPM leverages the intrinsic SHG and 2PE signals from collagen and elastin, respectively, to provide high imaging depth, typically on the order of hundreds of microns. This is in contrast to confocal imaging, which has significantly smaller imaging depth (<100 μm) due to the lack of localization of imaging to a single spot, which increases out-of-plane emission. However, many tissues, such as the walls of many extracerebral vessels in humans and larger mammals, are thicker than 1 mm and therefore beyond the MPM imaging depth using the approaches described here. Both confocal and MPM imaging depth can be increased by optically clearing the tissue using solutions with refractive indices closer to those of the wall components, reducing light scattering [225]. Although this process cannot be used on fresh tissue samples, it can increase imaging depths in fixed samples by orders of magnitude.

Imaging of intact, fresh specimens using MPM also opens up the possibility of analyzing changes in tissue structure during mechanical loading. For example, using custom-MPM compatible uniaxial and biaxial mechanical testing devices, our group has elucidated the role of collagen fiber waviness in determining the material properties for rabbit carotid artery [12] and rat urinary bladder wall [212], respectively. Thus, MPM is crucial not only for understanding the anatomical microstructure, but also for developing mathematical descriptions of the role of this microstructure in determining the mechanical function of the tissue. These models can be used to

quantitatively compare tissue in health and disease as well as to test hypothesis about the mechanical role of wall components.

Intrinsic MPM-induced SHG and 2PE signals can be combined with fluorescent tracers that do not interfere with the emission range of collagen and elastin to simultaneously image other wall components such as cell nuclei, flavins, NAD(P)H, porphyrins and lipofuscins. A list of stains with their emission spectra is provided by Bestvater et al. [226] In this protocol we introduce the use of a calcium tracer, Osteosense 680 (Perkin Elmer, MA, USA) for use with MPM. This tracer was previously used with confocal microscopy by Hutcheson et al.[207] to study the role of microcalcification in atherosclerotic plaque rupture using collagen fiber SHG signal. Here, we adapted their protocol for MPM analysis of both fresh and fixed samples, enabling simultaneous imaging of calcification and intrinsically fluorescing ECM components (collagen, elastin) up to depths of hundreds of microns. *In vivo* two photon calcium imaging has been extensively used in the neuroscience community to detect neuronal activity at high depth and high resolution [227]–[229]. In this protocol, the focus on complimentary calcium staining is motivated by its role in soft tissue pathologies. For example, ectopic calcification of vascular tissue is associated with cardiovascular risk fac- tors such as hypertension, inflammation and chronological aging [230], [231]. While it has long been understood that large calcification deposits will alter the mechanical and transport properties in arteries, the potential role of even small (micro) calcifications in altering tissue mechanics is being explored in the context of atherosclerotic plaque rupture [183], [207]. This unit provides the techniques necessary for achieving the resolutions required to image the calcification-ECM interaction and ultimately can be used to quantify the effect of calcification on ECM recruitment and mechanical function during loading.

Micro-CT, conventionally used for imaging hard calcified tissue inclusions, has also been used in imaging soft non-calcified tissue, especially in the presence of X-ray contrast agents. Metscher [232] provides a comprehensive overview of various contrast agents suitable for soft-tissue X-ray imaging. While the micro-CT protocol described here was introduced for the purpose of selecting regions of interest within the tissue sample, it can also be used for a variety of applications that re- quire structural assessment. For example, our group has previously demonstrated the use of high-resolution micro-CT to analyze the role of fabrication technique on tissue engineered vascular grafts [154] as well as their *in vivo* and *in vitro* degradation rates [150]. The combination of nondestructive imaging modalities such as micro-CT and MPM offers unique opportunities for targeted assessment of the wall content in heterogeneous materials. The resolutions achieved by both of these techniques for imaging calcification are comparable to that of standard histology, but the nondestructive techniques avoid common artifacts associated with mechanical sectioning and staining of samples. The protocol introduced here uses micro-CT to first image the entire samples to guide the selection of ROIs for detailed study of ECM-calcification inter- faces. Using the micro-CT model of the physical sample, the MPM microstructural data can also be mapped to computational data for blood flow and mechanical loading within the wall [158], [194]. Mapping of this kind is particularly important when there are heterogeneities in the tissue, including those due to disease and structural heterogeneities such as those at the bifurcations of arteries.

B.6 Critical Parameters

Sample stability during imaging

The sample must be held stationary during MPM imaging, either by using a custom chamber such as the device described here or by placing the sample in a slide with a well. Furthermore, clay (Renishaw Inc., part no. A- 1085-0016) can be used to ensure that the device itself is affixed to the micro positioning stage during imaging and that there is negligible device movement.

Sample stability and centering in CT

If the sample cannot be held vertically in the center of the mounting tube, place some Styrofoam (or other material of similar low density) around the sample to ensure that it does not move. Image quality can also be compromised by “movement” caused by the sample drying out; therefore, ensure that wet gauze is placed at the bottom of the tube prior to scanning. If the sample still begins to dry out, wet gauze can also be placed on top of the sample.

Micro-CT scanning time

As outlined in Basic Protocol 1, sample scanning time must be <1.5 h for fresh and <2 h for fixed tissue samples to prevent sample dehydration and image movement artifacts. This can be achieved by (a) reducing scan resolution, (b) reducing scanning rotation angle, and/or (c) reducing frame averaging.

Troubleshooting

Table 12 lists problems that may arise with these procedures as well as their possible causes and solutions.

Anticipated Results

If the protocols outlined above are followed, simultaneous MPM images of collagen, elastin, and calcification can be acquired and mapped to the 3D in silico model of the physical sample that is created from the micro-CT data. These images can help in better understanding the ECM structure and its integrity from either qualitative and/or quantitative analysis. For example, in some cases damaged fibers will be revealed and recognized as representing a disease pathology (Fig. 3C and D). The data can then be used to quantify the local interaction and morphological changes to elastin and collagen due to the presence of calcification. The location of calcification within the wall can be quantified and metrics like the percentage of calcified area in the sample can be calculated [158]. Thus, the micro-CT model can not only serve as a mapping tool but also provide geometric information about the sample and a bulk assessment of calcification burden. In addition to guiding MPM studies of the tissue, the micro-CT data can be used to select regions within the large tissue samples for mechanical testing. For example, guided by the micro-CT data, specimens for mechanical testing can be cut from the larger sample so as to include clusters of micro-calcifications. The tissue specimen will then be well suited for evaluating the impact of these particles on tissue mechanical properties. Quantitative data on collagen fiber orientation and waviness enables the development of structurally motivated constitutive models that mathematically describe the mechanical properties of the tissue sample.

Time Considerations

The time required for this protocol from the time the sample is acquired will vary based on whether the sample needs to be imaged fresh or fixed, its size, and the number of locations that need to be scanned by MPM. For fixed tissue, a fixation time of 24 h followed by 24 h of incubation with calcium tracer adds up to 48 h for sample preparation prior to any imaging. The preparation time for a fresh sample is 24 h. Both fixed and fresh samples can be scanned using micro-CT for <2 h depending on sample size. The MPM scanning time also is the same for fresh or fixed samples and will vary based on the depth and area of scanning: each 500 µm × 500 µm × 200 µm section requires 20 min at the settings outlined in Basic Protocol 2.

Table 12: Troubleshooting Guide for MPM Imaging of Collagen, Elastin, and Calcification

Problem	Possible Cause	Solution
Poor or no calcification signal	Inadequate diffusion of calcium tracer due to high (>450μm) sample thickness.	Increase incubation time with calcium tracer. Check if solution is still viable (is within 2 months of preparation date).
Poor or no collagen, elastin signal and high background noise	Improper laser intensity Improper wavelength Inadequate dwell time Sample movement Inadequate immersion of lens in water	Optimize laser intensity (typical range = 4 – 7%) Optimize wavelength (typical range = 800 – 870 nm) Optimize dwell time (typical range = 4 - 8μs/pixel) Ensure the sample is fixed to stage. Fasten the imaging device to stage using putty Ensure lens is submerged in water

Authors' Contributions

PSG developed the protocol for micro-CT and two-photon imaging of calcification and ECM components. PSG performed the micro-CT scanning, reconstruction, and analysis. CYC and PSG performed the two-photon microscopy. All authors contributed to discussions and writing of the manuscript.

Bibliography

[1] E. G. Lakatta, “Special Review : Clinical Cardiology : New Frontiers Arterial and Cardiac Aging : Major Shareholders in,” *Circulation*, pp. 490–497, 2003.

[2] E. J. Benjamin *et al.*, *Heart Disease and Stroke Statistics — 2017 Update A Report From the American Heart Association*. 2017.

[3] E. J. Benjamin *et al.*, “Heart Disease and Stroke Statistics — 2018 Update A Report From the American Heart Association,” *Circulation*, vol. 137, pp. 67–492, 2018.

[4] U. N. D. of E. and S. A. Division, “World Population Prospects.”

[5] E. G. Lakatta and D. Levy, “Special Review : Clinical Cardiology : New Frontiers Arterial and Cardiac Aging : Major Shareholders in Cardiovascular Disease Enterprises Part I : Aging Arteries : A ‘ Set Up ’ for Vascular Disease,” *Circulation*, pp. 139–146, 2003.

[6] R. Virmani *et al.*, “Effect of Aging on Aortic Morphology in Populations with High and Low Prevalence of Hypertension and Atherosclerosis Communities,” *Am. J. Pathol.*, vol. 139, no. 5, pp. 1119–1129, 1991.

[7] “Chapter 1 : Incidence , Prevalence , Patient Characteristics , and Treatment Modalities,” *2018 USRDS Anuual Data Report, Vol. 2*, vol. 2, 2018.

[8] M. Desai, A. M. Seifalian, and G. Hamilton, “Role of prosthetic conduits in coronary artery bypass grafting,” *Eur. Assoc. Cardio-Thoracic Surg.*, vol. 40, pp. 394–398, 2011.

[9] *Windsor Castle, Royal Collection, RCIN 919027*. .

[10] A. M. Robertson and P. N. Watton, “Chapter 8 - Mechanobiology of the Arterial Wall,” *Transp. Biol. Media*, pp. 275–347, 2013.

[11] *Blausen.com staff (2014). “Medical gallery of Blausen Medical 2014”. WikiJournal of Medicine 1 (2). DOI:10.15347/wjm/2014.010*. Springer Science & Business Media, 2014.

[12] M. R. Hill, X. Duan, G. A. Gibson, S. Watkins, and A. M. Robertson, “A theoretical and non-destructive experimental approach for direct inclusion of measured collagen orientation and recruitment into mechanical models of the artery wall,” *J. Biomech.*, vol. 45, no. 5, pp. 762–771, 2012.

[13] B. Yue, “Biology of the Extracellular Matrix: An Overview,” *J Glaucoma*, 2014.

[14] G. S. Montes, “STRUCTURAL BIOLOGY OF THE FIBRES OF THE COLLAGENOUS AND ELASTIC SYSTEMS,” *Cell Biol. Int.*, vol. 20, no. 1, pp. 15–27, 1996.

[15] E. C. Davis, “Elastic Lamina Growth in the Developing Mouse Aorta,” *J. Histochem. Cytochem.*, vol. 43, no. 11, pp. 1115–1123, 1995.

[16] R. Nissen, G. J. Cardinale, and S. Udenfriend, “Increased turnover of arterial collagen in hypertensive rats.,” *Proc. Natl. Acad. Sci. U. S. A.*, vol. 75, no. 1, pp. 451–453, 1978.

[17] R. J. Mcanulty, “Fibroblasts and myofibroblasts : Their source , function and role in disease,” *Int. J. Biochem. Cell Biol.*, vol. 39, no. 4, pp. 666–671, 2007.

[18] R. J. Mcanulty, J. S. Campa, A. D. Cambrey, and G. J. Laurent, “The effect of transforrmng growth factor fl on rates of procollagen synthesis and degradation in vitro,” *Biochim. Biophys. Acta*, vol. 1091, pp. 231–235, 1991.

[19] M. R. Roach and A. C. Burton, “The reason for the shape of the distensibility curves of arteries,” *Can. J. Biochem. Physiol.*, vol. 35, pp. 681–690, 1957.

[20] M. O’Connell *et al.*, “The three dimensional micro and nanostructure of the aortic medial lamellar unit measured using 3D confocal & electron microscopy,” *Matrix Biol.*, vol. 27, no. 3, pp. 171–181, 2009.

[21] G. A. Holzapfel, J. A. Niestrawska, R. W. Ogden, A. J. Reinisch, and A. J. Schriefl, “Modelling non-symmetric collagen fibre dispersion in arterial walls,” *J. R. Soc. Interface*, vol. 3, pp. 15–35, 2015.

[22] G. Holzapfel and R. W. Ogden, “Constitutive modelling of arteries,” *Proc. R. Soc. A Math. Phys. Eng. Sci.*, vol. 466, no. 2118, pp. 1551–1597, 2010.

[23] H. P. Wagner and J. Humphrey, “Differential passive and active biaxial mechanical behaviors of muscular and elastic arteries: basilar versus common carotid.,” *J. Biomech. Eng.*, vol. 133, no. 5, p. 051009, May 2011.

[24] A. Smits, V. Bonito, and M. Stoddart, “In Situ Tissue Engineering: Seducing the Body to Regenerate Anthal,” *Tissue Eng. Part A*, vol. 22, pp. 1061–1062, 2016.

[25] C. E. T. Stowell and Y. Wang, “Translational design of resorbable synthetic vascular grafts,” *Biomaterials*, vol. 173, pp. 71–86, 2018.

[26] J. J. Stankus, L. Soletti, K. Fujimoto, Y. Hong, D. a Vorp, and W. R. Wagner, “Fabrication of cell microintegrated blood vessel constructs through electrohydrodynamic atomization.,” *Biomaterials*, vol. 28, no. 17, pp. 2738–46, Jun. 2007.

[27] J. H. Lawson *et al.*, “Bioengineered human acellular vessels for dialysis access in patients with end-stage renal disease: two phase 2 single-arm trials,” *Lancet*, vol. 387, no. 10032, pp. 2026–2034, 2016.

[28] N. L’Heureux *et al.*, “Human tissue-engineered blood vessels for adult arterial revascularization,” *Nat. Med.*, vol. 12, no. 3, pp. 361–365, 2006.

[29] J. D. Roh *et al.*, “Tissue-engineered vascular grafts transform into mature blood vessels via an inflammation-mediated process of vascular remodeling.,” *Proceedings of the National Academy of Sciences of the United States of America*, vol. 107. pp. 4669–4674, 2010.

[30] C. K. Hashi *et al.*, “Antithrombogenic property of bone marrow mesenchymal stem cells in nanofibrous vascular grafts,” vol. 104, no. 29, 2007.

[31] W. Wu, R. A. Allen, and Y. Wang, “Fast-degrading elastomer enables rapid remodeling of a cell-free synthetic graft into a neoartery,” *Nat Med*, vol. 18, no. 7, pp. 1148–1153, 2012.

[32] B. H. Wolinsky and S. Glagov, “A Lamellar Unit of Aortic Medial Structure and Function in Mammals,” *Circ. Res.*, vol. XX, pp. 99–111, 1967.

[33] L. C. Y. Wong and B. L. Langille, “Developmental Remodeling of the Internal Elastic Lamina of Rabbit Arteries : Effect of Blood Flow,” *Circ. Res.*, vol. 78, no. 5, pp. 799–805, 1996.

[34] L. Langille and F. W. Keeley, “Adaptations of carotid arteries of young and mature rabbits to reduced carotid blood flow.,” *Am. J. Physiol.*, vol. 256, no. 4 Pt 2, pp. H931-9, Apr. 1989.

[35] B. Langille and F. O’Donnell, “Reductions in arterial diameter produced by chronic decreases in blood flow are endothelium-dependent,” *Science (80-.).*, vol. 231, no. 4736, pp. 405–407, 1986.

[36] H. Wolinsky, “Effects of Hypertension and Its Reversal on the Thoracic Aorta of Male and Female Rats: Morphological and Chemical Studies,” *Circ. Res.*, vol. 28, no. 6, pp. 622–637, 1971.

[37] Z. S. Jackson, A. I. Gotlieb, and B. L. Langille, “Wall tissue remodeling regulates longitudinal tension in arteries,” *Circ. Res.*, vol. 90, no. 8, pp. 918–925, 2002.

[38] Z. S. Jackson, D. Dajnowiec, A. I. Gotlieb, and L. Langille, “Partial off-loading of longitudinal tension induces arterial tortuosity,” *Arterioscler. Thromb. Vasc. Biol.*, vol. 25, no. 5, pp. 957–962, 2005.

[39] J. K. Miyashiro, V. Poppa, and B. C. Berk, “Flow-induced vascular remodeling in the rat carotid artery diminishes with age.,” *Circ. Res.*, vol. 81, pp. 311–319, 1997.

[40] K. Williamson, S. E. Stringer, and M. Y. Alexander, “Endothelial progenitor cells enter the aging arena,” *Front. Physiol.*, vol. 3, no. February, pp. 1–7, 2012.

[41] M. F. O’Rourke and J. Hashimoto, “Mechanical Factors in Arterial Aging. A Clinical Perspective,” *J. Am. Coll. Cardiol.*, vol. 50, no. 1, pp. 1–13, 2007.

[42] A. Gosain, M. D. L. A. Dipietro, and D. Ph, “Aging and Wound Healing,” *World J. Surg.*, vol. 28, pp. 321–326, 2004.

[43] I. M. Conboy and T. A. Rando, “Aging , Stem Cells and Tissue Regeneration ND ES SC CE,” *Cell Cycle*, vol. 4, no. 3, pp. 407–410, 2005.

[44] D. Hachim *et al.*, “Effects of aging upon the host response to implants,” pp. 1281–1292, 2017.

[45] J. D. Humphrey, E. R. Dufresne, and M. a. Schwartz, “Mechanotransduction and extracellular matrix homeostasis,” *Nat. Rev. Mol. Cell Biol.*, vol. 15, no. 12, pp. 802–812, 2014.

[46] C. J. O. Callaghan and B. Williams, “Mechanical Strain – Induced Extracellular Matrix Production by Human Vascular Smooth Muscle Cells,” *Hypertension*, vol. 36, pp. 319–324, 2000.

[47] M. Kjær *et al.*, “From mechanical loading to collagen synthesis , structural changes and function in human tendon,” *Scand. J. Med. Sci. Sport.*, vol. 19, pp. 500–510, 2009.

[48] J. E. Bishop and G. Lindahl, “Regulation of cardiovascular collagen synthesis by mechanical load,” *Cardiovasc. Res.*, vol. 42, pp. 27–44, 1999.

[49] M. Kjaer *et al.*, “Metabolic activity and collagen turnover in human tendon in response to physical activity,” *J. Musculoskelet. neuronal Interact.*, vol. 5, no. December 2004, pp. 41–52, 2005.

[50] D. Thompson, “On growth and form (Edition 1),” *On growth and form.*, p. 793, 1917.

[51] R. Skalak, G. Dasgupta, and M. Moss, “Analytical description of Growth,” vol. 94. pp. 555–577, 1982.

[52] E. K. Rodriguez, A. Hoger, and A. D. McCulloch, “Stress dependent finite growth in soft elastic tissues,” *J. Biomech.*, vol. 27, no. 4, pp. 455–467, 1994.

[53] L. a Taber and D. W. Eggers, “Theoretical study of stress-modulated growth in the aorta.,” *J. Theor. Biol.*, vol. 180, no. 4, pp. 343–57, 1996.

[54] a Rachev and K. Hayashi, “Theoretical study of the effects of vascular smooth muscle contraction on strain and stress distributions in arteries.,” *Ann. Biomed. Eng.*, vol. 27, pp. 459–68, 1999.

[55] M. Epstein and G. A. Maugin, “Thermomechanics of volumetric growth in uniform bodies,” *Int. J. Plast.*, vol. 16, no. 7, pp. 951–978, 2000.

[56] C. Eckart, “The Thermodynamics of Irreversible Processes. IV. The Theory of Elasticity and Aaelasticity,” *Phys. Rev.*, vol. 73, no. 4, pp. 373–382, 1948.

[57] K. R. Rajagopal and A. R. Srinivasa, “Mechanics of the inelastic behavior of materials. Part II: Inelastic Response,” *Int. J. Plast.*, vol. 14, pp. 969–995, 1998.

[58] K. R. Rajagopal and A. R. Srinivasa, “Mechanics of the inelastic behavior of materials - Part I, Theoretical Underpinnings,” *Int. J. Plast.*, vol. 14, pp. 945–967, 1998.

[59] K. R. Rajagopal and A. R. Srinivasa, “A thermodynamic frame work for rate type fluid models,” *J. Non-Newtonian Fluid Mech*, vol. 88, no. February 1999, pp. 207–227, 2000.

[60] D. Ambrosi and F. Mollica, “On the mechanics of a growing tumor,” *Int. J. Eng. Sci.*, vol. 40, no. 12, pp. 1297–1316, 2002.

[61] S. Budday, C. Raybaud, and E. Kuhl, “A mechanical model predicts morphological abnormalities in the developing human brain,” *Sci. Rep.*, vol. 4, pp. 1–7, 2014.

[62] A. M. Zöllner, A. Buganza Tepole, and E. Kuhl, “On the biomechanics and mechanobiology of growing skin,” *J. Theor. Biol.*, vol. 297, pp. 166–175, 2012.

[63] A. B. Tepole, C. J. Ploch, J. Wong, A. Gosain, and E. Kuhl, “Growing skin: A computational model for skin expansion in reconstructive surgery,” *J Mech Phys Solids*, vol. 59, no. 10, pp. 2177–2190, 2011.

[64] D. Ambrosi *et al.*, “Perspectives on biological growth and remodeling,” *J. Mech. Phys. Solids*, vol. 59, no. 4, pp. 863–883, 2011.

[65] J. Humphrey and K. R. Rajagopal, “A constrained mixture model for growth and remodeling of soft tissues,” *Math. Model. methods Appl. Sci.*, vol. 12, no. 3, pp. 407–430, 2002.

[66] J. Humphrey and K. R. Rajagopal, “A constrained mixture model for arterial adaptations to a sustained step change in blood flow.,” *Biomech. Model. Mechanobiol.*, vol. 2, no. 2, pp. 109–126, 2003.

[67] R. L. Gleason and J. Humphrey, “A mixture model of arterial growth and remodeling in hypertension: Altered muscle tone and tissue turnover,” *J. Vasc. Res.*, vol. 41, no. 4, pp. 352–363, 2004.

[68] R. L. Gleason and J. Humphrey, “A 2D constrained mixture model for arterial adaptations to large changes in flow, pressure and axial stretch,” *Math. Med. Biol.*, vol. 22, pp. 347–369, 2005.

[69] A. Valentin, “A Multi-Layered Computational Model of Coupled Elastin Degradation, Vasoactive Dysfunction, and Collagenous Stiffening in Aortic Aging,” *Changes*, vol. 29, no. 7, pp. 997–1003, 2012.

[70] J. D. Humphrey and G. A. Holzapfel, “Mechanics , mechanobiology , and modeling of human abdominal aorta and aneurysms,” *J. Biomech.*, vol. 45, no. 5, pp. 805–814, 2012.

[71] P. N. Watton, Y. Ventikos, and G. A. Holzapfel, “Modelling the growth and stabilization of cerebral aneurysms,” *Math. Med. Biol.*, vol. 26, no. 2, pp. 133–164, 2009.

[72] P. Aparício, M. S. Thompson, and P. N. Watton, “A novel chemo-mechano-biological model of arterial tissue growth and remodelling,” *J. Biomech.*, vol. 49, no. 12, pp. 2321–2330, 2016.

[73] P. Bhogal *et al.*, “The unexplained success of stentplasty vasospasm treatment Insights using Mechanistic Mathematical Modeling,” *Clin. Neuroradiol.*, 2019.

[74] K. S. Miller, Y. U. Lee, Y. Naito, C. K. Breuer, and J. D. Humphrey, “Computational model of the in vivo development of a tissue engineered vein from an implanted polymeric construct,” *J. Biomech.*, vol. 47, no. 9, pp. 2080–2087, 2014.

[75] N. O’ Connor, J. Mulliken, S. Banks-Schlegel, O. Kehinde, and H. Green, “Grafting of burns with cultured epithelial prepared from autlogous epidermal cells,” *Lancet*, vol. 317, no. 8211, pp. 75–78, 1981.

[76] E. K. Rodriguez, “Stress-dependent finite growth in soft elastic tissues,” *J. Biomech.*, vol. 27, no. 4, pp. 455–467, 1994.

[77] Y. C. Fung, “What Are the Residual-Stresses Doing in Our Blood-Vessels,” *Ann. Biomed. Eng.*, vol. 19, no. 3, pp. 237–249, 1991.

[78] S. Baek and T. J. Pence, “On mechanically induced degradation of fiber-reinforced hyperelastic materials,” *Math. Mech. Solids*, vol. 16, no. 4, pp. 406–434, 2011.

[79] T. K. Tonge, J. W. Ruberti, and T. D. Nguyen, “Micromechanical Modeling Study of Mechanical Inhibition of Enzymatic Degradation of Collagen Tissues,” *Biophys. J.*, vol. 109, no. 12, pp. 2689–2700, 2015.

[80] C. M. F. Potter, K. H. Lao, L. Zeng, and Q. Xu, “Role of biomechanical forces in stem cell vascular lineage differentiation,” *Arterioscler. Thromb. Vasc. Biol.*, vol. 34, no. 10, pp. 2184–2190, 2014.

[81] A. J. Engler, S. Sen, H. L. Sweeney, and D. E. Discher, “Matrix Elasticity Directs Stem Cell Lineage Specification,” *Cell*, vol. 126, pp. 677–689, 2006.

[82] D. Dajnowiec and B. L. Langille, “Arterial adaptations to chronic changes in haemodynamic function: coupling vasomotor tone to structural remodelling.,” *Clin. Sci. (Lond).*, vol. 113, pp. 15–23, 2007.

[83] P. Zilla, D. Bezuidenhout, and P. Human, “Prosthetic vascular grafts: wrong models, wrong questions and no healing.,” *Biomaterials*, vol. 28, no. 34, pp. 5009–27, Dec. 2007.

[84] Y. Wang, Y. M. Kim, and R. Langer, “Technical Note In vivo degradation characteristics of poly (glycerol sebacate),” no. 85, 2002.

[85] Y. Wang, G. a Ameer, B. J. Sheppard, and R. Langer, “A tough biodegradable elastomer.,” *Nat. Biotechnol.*, vol. 20, no. June, pp. 602–606, 2002.

[86] S. Gerecht *et al.*, “A porous photocurable elastomer for cell encapsulation and culture,” *Biomaterials*, vol. 28, no. 32, pp. 4826–4835, 2007.

[87] L. E. Niklason, A. T. Yeh, E. a Calle, Y. Bai, A. Valentín, and J. Humphrey, “Enabling tools for engineering collagenous tissues integrating bioreactors, intravital imaging, and biomechanical modeling.,” *Proc. Natl. Acad. Sci. U. S. A.*, vol. 107, no. 8, pp. 3335–3339, 2010.

[88] J. M. Szafron *et al.*, “Immuno-driven and Mechano-mediated Neotissue Formation in Tissue Engineered Vascular Grafts,” *Ann. Biomed. Eng.*, 2018.

[89] P. Alford and J. Humphrey, “Growth & Remodeling in a Thick-Walled Artery Model : Effects of Spatial Variations in Wall Constituents,” *Knowl. Creat. Diffus. Util.*, vol. 7, no. 4, pp. 245–262, 2009.

[90] A. Valentin and J. Humphrey, “A finite element-based constrained mixture implementation for arterial growth, remodeling, and adaptation: Theory and numerical verification A.,” *Int. j. numer. method. biomed. eng.*, vol. 28, no. May, pp. 72–86, 2012.

[91] A. Selimovic, Y. Ventikos, and P. N. Watton, “Modelling the evolution of cerebral aneurysms: Biomechanics, mechanobiology and multiscale modelling,” *Procedia IUTAM*, vol. 10, pp. 396–409, 2013.

[92] P. N. Watton, N. B. Raberger, G. A. Holzapfel, and Y. Ventikos, “Coupling the Hemodynamic Environment to the Evolution of Cerebral Aneurysms: Computational Framework and Numerical Examples,” *J. Biomech. Eng.*, vol. 131, no. 10, 2009.

[93] S. Baek, K. R. Rajagopal, and J. Humphrey, “Competition between radial expansion and thickening in the enlargement of an intracranial saccular aneurysm,” *J. Elast.*, vol. 80, pp. 13–31, 2005.

[94] C. Alberto Figueroa, S. Baek, C. a. Taylor, and J. Humphrey, “A computational framework for fluid-solid-growth modeling in cardiovascular simulations,” *Comput. Methods Appl. Mech. Eng.*, vol. 198, no. 45–46, pp. 3583–3602, 2009.

[95] K. S. Miller, R. Khosravi, C. K. Breuer, and J. D. Humphrey, “A hypothesis-driven parametric study of effects of polymeric scaffold properties on tissue engineered neovessel formation,” *Acta Biomater.*, vol. 11, pp. 283–294, 2015.

[96] A. Valentin, X. Duan, R. Allen, P. Zunino, Y. Wang, and A. Robertson, “A Predictive Computational Model of Arterial Tissue Equivalent Evolution,” vol. 1, no. CanCNSM, pp. 1–2, 2013.

[97] and G. S. Ottenbrite, R. M., A. C. Albertsson, “Discussion on degradation terminology,” *Biodegrad. Polym. Plast. R. Soc. Chem. Cambridge*, vol. 73, no. 92, 1992.

[98] R. A. Allen *et al.*, "Nerve regeneration and elastin formation within PGS based synthetic arterial grafts one-year post-implantation in a rat model," *Biomaterials*, vol. 35, no. 1, pp. 165–173, 2014.

[99] R. Rai *et al.*, "Bioactive Electrospun Fibers of Poly(glycerol sebacate) and Poly(??-caprolactone) for Cardiac Patch Application," *Adv. Healthc. Mater.*, vol. 4, no. 13, pp. 2012–2025, 2015.

[100] R. Ravichandran, J. R. Venugopal, S. Sundarrajan, S. Mukherjee, and S. Ramakrishna, "Poly(Glycerol sebacate)/gelatin core/shell fibrous structure for regeneration of myocardial infarction.," *Tissue Eng. Part A*, vol. 17, no. 9–10, pp. 1363–73, 2011.

[101] M. Radisic *et al.*, "Pre-treatment of synthetic elastomeric scaffolds by cardiac fibroblasts improves engineered heart tissue," *J. Biomed. Mater. Res.*, vol. 86, no. 3, pp. 713–724, 2009.

[102] P. M. Crapo and Y. Wang, "Physiologic compliance in engineered small-diameter arterial constructs based on an elastomeric substrate.," *Biomaterials*, vol. 31, no. 7, pp. 1626–35, Mar. 2010.

[103] J. M. Kemppainen and S. J. Hollister, "Tailoring the mechanical properties of 3D-designed poly(glycerol sebacate) scaffolds for cartilage applications," *J. Biomed. Mater. Res. - Part A*, vol. 94, no. 1, pp. 9–18, 2010.

[104] S. H. Zaky *et al.*, "Poly (glycerol sebacate) elastomer supports osteogenic phenotype for bone engineering applications," *Biomed. Mater.*, vol. 9, no. 2, pp. 1–8, 2014.

[105] C. A. Sundback *et al.*, "Biocompatibility analysis of poly(glycerol sebacate) as a nerve guide material," *Biomaterials*, vol. 26, no. 27, pp. 5454–5464, 2005.

[106] C. Fidkowski, M. R. Kaazempur-Mofrad, J. Borenstein, J. P. Vacanti, R. Langer, and Y. Wang, "Endothelialized microvasculature based on a biodegradable elastomer.," *Tissue Eng.*, vol. 11, no. 1–2, pp. 302–309, 2005.

[107] J. Hu *et al.*, "Electrospinning of poly(glycerol sebacate)-based nanofibers for nerve tissue engineering," *Mater. Sci. Eng. C*, pp. 18–20, 2016.

[108] S. H. Barbanti, C. A. Carvalho Zavaglia, and E. A. De Rezende Duek, "Effect of Salt Leaching on PCL and PLGA (50 / 50) Resorbable Scaffolds 2 . Material and Methods," *Mater. Res.*, vol. 11, no. 1, pp. 75–80, 2008.

[109] P. Aramwit, J. Ratanavaraporn, S. Ekgasit, D. Tongsakul, and N. Bang, "A green salt-leaching technique to produce sericin/PVA/glycerin scaffolds with distinguished characteristics for wound-dressing applications," *J. Biomed. Mater. Res. - Part B Appl. Biomater.*, vol. 103, no. 4, pp. 915–924, 2015.

[110] M. Mattioli-Belmonte *et al.*, “Rapid-prototyped and salt-leached PLGA scaffolds condition cell morpho-functional behavior,” *J. Biomed. Mater. Res. Part A*, vol. 85A, no. 2, pp. 466–476, 2016.

[111] K.-W. Lee and Y. Wang, “Elastomeric PGS scaffolds in arterial tissue engineering.,” *J. Vis. Exp.*, no. 50, pp. 2–6, Jan. 2011.

[112] G. Scott and D. Gilead, *Degradable polymers*, vol. 1. Springer, 1995.

[113] Y. Wang, Y. M. Kim, R. Langer, and C. Truesdell, “Technical Note In vivo degradation characteristics of poly (glycerol sebacate),” *J. Chem. Phys.*, vol. 37, no. 85, p. 2336, 2002.

[114] Q. Chen, X. Yang, and Y. Li, “A comparative study on in vitro enzymatic degradation of poly(glycerol sebacate) and poly(xylitol sebacate),” *RSC Adv.*, vol. 2, p. 4125, 2012.

[115] G. A. Ateshian, “The Role of Mass Balance Equations in Growth Mechanics Illustrated in Surface and Volume Dissolutions,” *J. Biomech. Eng.*, vol. 133, no. 1, p. 011010, 2010.

[116] K. Jiao and K. Jiao, “On solutions for the moving boundary problem describing an eroding vascular graft,” 2017.

[117] A. a Noyes and W. R. Whitney, “The Rate of Solution of Solid Substances in Their Own Solutions,” *J. Am. Chem. Soc.*, vol. 19, no. 12, pp. 930–934, 1897.

[118] “[H._S._Carslaw,_J._C._Jaeger]_Conduction_of_Heat_i(BookZZ.org).pdf.” .

[119] D. R, Boyce W., “Elementary Differential Equations and Boundary Value Problems,” *Statew. Agric. L. Use Baseline 2015*, vol. 1, 2015.

[120] C. Bretti, F. Crea, C. Foti, and S. Sammartano, “Solubility and Activity Coefficients of Acidic and Basic Nonelectrolytes in Aqueous Salt Solutions. 2. Solubility and Activity Coefficients of Suberic, Azelaic, and Sebacic Acids in NaCl(aq), (CH 3) 4 NCl(aq), and (C 2 H 5) 4 NI(aq) at Different Ionic S,” *J. Chem. Eng. Data*, vol. 51, no. 5, pp. 1660–1667, 2006.

[121] K. S. Miller, R. Khosravi, C. K. Breuer, and J. Humphrey, “A hypothesis-driven parametric study of effects of polymeric scaffold properties on tissue engineered neovessel formation,” *Acta Biomater.*, vol. 11, no. 1, pp. 283–294, 2015.

[122] G. A. Holzapfel, *Nonlinear Solid Mechanics : A Continuum Approach for Engineering Science*. 2000.

[123] J. D. Roh *et al.*, “Tissue-engineered vascular grafts transform into mature blood vessels via an inflammation-mediated process of vascular remodeling.,” *Proc. Natl. Acad. Sci. U. S. A.*, vol. 107, pp. 4669–4674, 2010.

[124] L. R. Madden *et al.*, “Proangiogenic scaffolds as functional templates for cardiac tissue engineering.,” *Proc. Natl. Acad. Sci. U. S. A.*, vol. 107, no. 34, pp. 15211–6, Aug. 2010.

[125] C. B. Weinberg and E. Bell, “A blood vessel model constructed from collagen and cultured vascular cells,” *Science (80-.).*, vol. 231, no. 4736, pp. 397–400, 1986.

[126] A. Nieponice *et al.*, “In Vivo Assessment of a Tissue-Engineered Vascular Graft Combining a Biodegradable Elastomeric Scaffold and Muscle-Derived Stem Cells in a Rat Model,” *Tissue Eng. Part A*, vol. 16, no. 4, pp. 1215–1223, 2010.

[127] B. Nottelet *et al.*, “Factorial design optimization and in vivo feasibility of poly(ε-caprolactone)-micro- and nanofiber-based small diameter vascular grafts,” *J. Biomed. Mater. Res. - Part A*, vol. 89, no. 4, pp. 865–875, 2008.

[128] S. de Valence *et al.*, “Long term performance of polycaprolactone vascular grafts in a rat abdominal aorta replacement model,” *Biomaterials*, vol. 33, no. 1, pp. 38–47, 2011.

[129] Y. Pan *et al.*, “Small-diameter hybrid vascular grafts composed of polycaprolactone and polydioxanone fibers,” *Sci. Rep.*, vol. 7, no. 1, pp. 1–11, 2017.

[130] T. Sugiura *et al.*, “Fast-degrading bioresorbable arterial vascular graft with high cellular infiltration inhibits calcification of the graft,” *J. Vasc. Surg.*, vol. 66, no. 1, pp. 243–250, 2017.

[131] M. M. Idu, J. Buth, W. C. J. Hop, P. Cuypers, E. D. W. M. Van De Pavoordt, and J. M. H. Tordoir, “Factors Influencing the Development of Vein-graft Stenosis and their Significance for Clinical Management,” *Eur J Vasc Endovasc Surg*, vol. 17, pp. 15–21, 1999.

[132] A. Schanzer *et al.*, “Technical factors affecting autogenous vein graft failure: Observations from a large multicenter trial,” *J. Vasc. Surg.*, vol. 46, no. 6, pp. 1180–1190, 2007.

[133] M. S. Conte, “The ideal small arterial substitute: a search for the Holy Grail?,” *FASEB J.*, vol. 12, no. 1, pp. 43–45, 1998.

[134] D. D. Swartz and S. T. Andreadis, “Animal models for vascular tissue-engineering,” *Curr. Opin. Biotechnol.*, vol. 24, no. 5, pp. 916–925, 2013.

[135] T. Fukunishi *et al.*, “Tissue-engineered small diameter arterial vascular grafts from cell-free nanofiber PCL/chitosan scaffolds in a sheep model,” *PLoS One*, vol. 11, no. 7, pp. 1–15, 2016.

[136] K. Lee, N. R. Johnson, J. Gao, and Y. Wang, “Human Progenitor Cell Recruitment via SDF-1α Coacervate- laden PGS Vascular Grafts,” *Biomaterials*, vol. 34, no. 38, pp. 1–20, 2013.

[137] L. C. Davies, S. J. Jenkins, J. E. Allen, and P. R. Taylor, “Tissue-resident macrophages,” *Nat. Immunol.*, vol. 14, no. 10, pp. 986–995, 2013.

[138] S. Eshraghi and S. Das, “Mechanical and microstructural properties of polycaprolactone scaffolds with one-dimensional, two-dimensional, and three-dimensional orthogonally oriented porous architectures produced by selective laser sintering,” *Acta Biomater.*, vol. 6, no. 7, pp. 2467–2476, 2010.

[139] D. P. Faxon *et al.*, “Atherosclerotic vascular disease conference: Executive summary: Atherosclerotic vascular disease conference proceeding for healthcare professionals from a special writing group of the American Heart Association,” *Circulation*, vol. 109, pp. 2595–2604, 2004.

[140] D. Mozaffarian *et al.*, *Heart disease and stroke statistics-2016 update a report from the American Heart Association*, vol. 133, no. 4. 2016.

[141] J. Ferruzzi, D. Madziva, A. W. Caulk, G. Tellides, and J. D. Humphrey, “Compromised mechanical homeostasis in arterial aging and associated cardiovascular consequences,” *Biomech. Model. Mechanobiol.*, 2018.

[142] K. Asai *et al.*, “Peripheral Vascular Endothelial Dysfunction and Apoptosis in Old Monkeys,” *Arterioscler. Thromb. Vasc. Biol.*, vol. 20, no. 6, pp. 1493–1499, 2000.

[143] M. Wang *et al.*, “Proinflammatory Profile Within the Grossly Normal Aged,” *Hypertension*, pp. 219–227, 2007.

[144] J. Behmoaras, S. Slove, S. Seve, R. Vranckx, P. Sommer, and M. Jacob, “Differential Expression of Lysyl Oxidases LOXL1 and LOX During Growth and Aging Suggests Specific Roles in Elastin and Collagen Fiber Remodeling in Rat Aorta,” *Rejuvinatiun Res.*, vol. 11, no. 5, pp. 883–889, 2008.

[145] E. G. Lakatta, M. Wang, and S. S. Najjar, “Arterial Aging and Subclinical Arterial Disease are Fundamentally Intertwined at Macroscopic and Molecular Levels,” *Med. Clin. North Am.*, vol. 93, no. 3, pp. 583–604, 2009.

[146] M. Brownlee, “Advanced protein glycosylation in diabetes and aging,” *Annu. Rev. Med.*, vol. 46, pp. 223–234, 1995.

[147] Z. Wang *et al.*, “Differences in the performance of PCL-based vascular grafts as abdominal aorta substitutes in healthy and diabetic rats,” *Biomater. Sci.*, vol. 4, pp. 1485–1492, 2016.

[148] H. Greisler, J. Klosak, E. Endean, J. McGurrin, J. Garfield, and D. Kim, *Effects of Hypercholesterolemia on Healing of Vascular Grafts*, vol. 4. Springer Science & Business Media, 2009.

[149] K.-W. Lee *et al.*, “A biodegradable synthetic graft for small arteries matches the performance of autologous vein in rat carotid arteries,” *Biomaterials*, vol. 181, pp. 67–80, 2018.

[150] P. S. Gade, K. Lee, B. N. Pfaff, Y. Wang, A. M. Robertson, and A. M. Robertson, "Degradation and erosion mechanisms of bioresorbable porous acellular vascular grafts : an in vitro investigation," *J. R. Soc. Interface*, vol. 14, no. 132, 2017.

[151] K. Lee *et al.*, "A biodegradable synthetic graft for small arteries matches the performance of autologous vein in rat carotid arteries," *Biomaterials*, vol. 181, pp. 67–80, 2018.

[152] J. S. Bredfeldt *et al.*, "Computational segmentation of collagen fibers from second-harmonic generation images of breast cancer second-harmonic generation images of breast cancer," *J. Biomed. Opt.*, vol. 19, no. 1, 2018.

[153] K. Lee *et al.*, "A biodegradable synthetic graft for small arteries matches the performance of autologous vein in rat carotid arteries," *Biomaterials*, 2018.

[154] S. H. Lee, K.-W. Lee, P. S. Gade, A. M. Robertson, and Y. Wang, "Microwave-assisted facile fabrication of porous poly (glycerol sebacate) scaffolds," *J. Biomater. Sci. Polym. Ed.*, vol. 5063, no. June, pp. 1–10, 2017.

[155] S. de Valence *et al.*, "Long term performance of polycaprolactone vascular grafts in a rat abdominal aorta replacement model.," *Biomaterials*, vol. 33, no. 1, pp. 38–47, Jan. 2012.

[156] F. J. Meyer, K. G. Burnand, S. Abisi, J. M. Tekoppele, B. Van Els, and A. Smith, "Effect of collagen turnover and matrix metalloproteinase activity on healing of venous leg ulcers," *Br. J. Surg.*, vol. 95, pp. 319–325, 2008.

[157] G. J. Rucklidge, G. Milne, B. A. Mcgaw, E. Milne, and S. P. Robins, "Turnover rates of different collagen types measured by isotope ratio mass spectrometry," *Biochim Biophys Acta*, vol. 1156, no. 1, pp. 57–61, 1992.

[158] F. Mut, P. Gade, F. Cheng, and Y. Tobe, "Combining data from multiple sources to study mechanisms of aneurysm disease : Tools and techniques," *Int J Numer Meth Biomed Engng*, no. April, pp. 1–18, 2018.

[159] C. C. Y. Gade PS Robertson AM, "Multiphoton Imaging of Collagen, Elastin and Calcification in Intact Soft Tissue Samples," *Curr. Protoc. Cytom.*, 2018.

[160] A. M. Robertson, X. Duan, K. M. Aziz, M. R. Hill, S. C. Watkins, and J. R. Cebral, "Diversity in the Strength and Structure of Unruptured Cerebral Aneurysms," *Ann. Biomed. Eng.*, vol. 43, no. 7, pp. 1502–1515, 2015.

[161] R. Sgonc and J. Gruber, "Age-Related Aspects of Cutaneous Wound Healing : A Mini-Review," *Gerontology*, vol. 59, pp. 159–164, 2013.

[162] T. Koh and L. A. DiPietro, "Inflammation and wound healing : The role of the macrophage," *Expert Rev Mol Med.*, vol. 16, no. 2008, pp. 19–25, 2013.

[163] W. H. Goodson and T. K. Hunt, "Wound Healing and Aging," *J. Invest. Dermatol.*, vol. 73, no. 1, pp. 88–91, 1979.

[164] E. Linehan and D. C. Fitzgerald, “Ageing and the immune system: Focus on macrophages,” *Eur. J. Microbiol. Immunol.*, vol. 5, 2015.

[165] S. Mahbub, C. R. Deburghgraeve, and E. J. Kovacs, “Advanced Age Impairs Macrophage Polarization,” *J. Interf. CYTOKINE Res.*, vol. 32, no. 1, pp. 18–26, 2012.

[166] M. E. Swift, A. L. Burns, K. L. Gray, and L. A. Dipietro, “Age-Related Alterations in the Inflammatory Response to Dermal Injury,” *J. Invest. Dermatol.*, vol. 117, no. 5, pp. 1027–1035, 2001.

[167] C. Jackaman, H. G. Radley-crabb, Z. Soffe, T. Shavlakadze, M. D. Grounds, and J. Delia, “Targeting macrophages rescues age-related immune deficiencies in C57BL/6J geriatric mice,” *Aging Cell*, vol. 12, pp. 345–357, 2013.

[168] S. Juvela and M. Korja, “Intracranial Aneurysm Parameters for Predicting a Future Subarachnoid Hemorrhage: A Long-Term Follow-up Study,” *Neurosurgery*, vol. 81, no. 3, pp. 432–440, 2017.

[169] G. J. E. Rinkel, M. Djibuti, A. Algra, and J. van Gijn, “Prevalence and Risk of Rupture of Intracranial Aneurysms : A Systematic Review,” *Stroke*, vol. 29, no. 1, pp. 251–256, 1998.

[170] S. Juvela, M. Porras, and K. Poussa, “Natural history of unruptured intracranial aneurysms: probability of and risk factors for aneurysm rupture,” *J. Neurosurg.*, vol. 108, no. 5, pp. 1052–1060, 2008.

[171] D. O. Wiebers *et al.*, “Unruptured intracranial aneurysms: natural history, clinical outcome, and risks of surgical and endovascular treatment.,” *Lancet*, vol. 362, no. 9378, pp. 103–110, 2003.

[172] R. R. Lall, C. S. Eddleman, B. R. Bendok, and H. H. Batjer, “Unruptured intracranial aneurysms and the assessment of rupture risk based on anatomical and morphological factors: sifting through the sands of data,” *Neurosurg. Focus*, vol. 26, no. 5, p. E2, 2009.

[173] A. Nader-Sepahi *et al.*, “Is aspect ratio a reliable predictor of intracranial aneurysm rupture?,” *Neurosurgery*, vol. 54, no. 6, pp. 1343–1348, 2004.

[174] T. Kirino *et al.*, “The Natural Course of Unruptured Cerebral Aneurysms in a Japanese Cohort,” *N. Engl. J. Med.*, vol. 366, no. 26, pp. 2474–2482, 2012.

[175] M. Korja, H. Lehto, and S. Juvela, “Lifelong rupture risk of intracranial aneurysms depends on risk factors: A prospective Finnish cohort study,” *Stroke*, vol. 45, no. 7, pp. 1958–1963, 2014.

[176] A. E. Lindgren *et al.*, “Irregular shape of intracranial aneurysm indicates rupture risk irrespective of size in a population-based cohort,” *Stroke*, vol. 47, no. 5, pp. 1219–1226, 2016.

[177] T. Hashimoto, H. Meng, and W. L. Young, “Intracranial aneurysms: links among inflammation, hemodynamics and vascular remodeling,” vol. 193, no. 1, pp. 118–125, 2011.

[178] T. Aoki *et al.*, “NF- B Is a Key Mediator of Cerebral Aneurysm Formation,” *Circulation*, vol. 116, no. 24, pp. 2830–2840, 2007.

[179] A. M. Robertson, D. Xinjie, S. Maiti, J. Thunes, P. Gade, and K. et al. Aziz, “Role of calcification in aneurysm failure - a case study,” *Proc. 5th Int. Conf. Comput. Math. Biomed. Eng. 10th-12th April. Pittsburgh, PA, USA*, vol. 1, pp. 52–55, 2017.

[180] R. V. C. Buijs *et al.*, “Calcification as a risk factor for rupture of abdominal aortic aneurysm,” *Eur. J. Vasc. Endovasc. Surg.*, vol. 46, no. 5, pp. 542–548, 2013.

[181] S. H. M. Nyström, “On factors related to growth and rupture of intracranial aneurysms,” *Acta Neuropathol.*, vol. 16, no. 1, pp. 64–72, 1970.

[182] K. Y. Volokh and J. Aboudi, “Aneurysm strength can decrease under calcification,” *J. Mech. Behav. Biomed. Mater.*, vol. 57, pp. 164–174, 2016.

[183] Y. Vengrenyuk *et al.*, “A hypothesis for vulnerable plaque rupture due to stress-induced debonding around cellular microcalcifications in thin fibrous caps,” *Proc. Natl. Acad. Sci.*, vol. 103, no. 40, pp. 14678–14683, 2006.

[184] F. Otsuka, K. Sakakura, K. Yahagi, M. Joner, and R. Virmani, “Has our understanding of calcification in human coronary atherosclerosis progressed?,” *Arterioscler. Thromb. Vasc. Biol.*, vol. 34, no. 4, pp. 724–736, 2014.

[185] L. L. Demer and Y. Tintut, “Inflammatory, metabolic, and genetic mechanisms of vascular calcification,” *Arterioscler. Thromb. Vasc. Biol.*, vol. 34, no. 4, pp. 715–723, 2014.

[186] H. C. Stary, “Natural history and histological classification of atherosclerotic lesions,” *Arterioscler. Thromb. Vasc. Biol.*, vol. 20, pp. 1177–1178, 2000.

[187] P. Lanzer *et al.*, “Medial vascular calcification revisited: Review and perspectives,” *Eur. Heart J.*, vol. 35, pp. 1515–1525, 2014.

[188] K. Amann, “Media calcification and intima calcification are distinct entities in chronic kidney disease,” *Clin. J. Am. Soc. Nephrol.*, vol. 3, no. 6, pp. 1599–1605, 2008.

[189] W. C. O’Neill, K. H. Han, T. M. Schneider, and R. A. Hennigar, “Prevalence of nonatheromatous lesions in peripheral arterial disease,” *Arterioscler. Thromb. Vasc. Biol.*, vol. 35, no. 2, pp. 439–447, 2015.

[190] J. B. Krohn, J. D. Hutcheson, E. Martínez-Martínez, and E. Aikawa, “Extracellular vesicles in cardiovascular calcification: Expanding current paradigms,” *J. Physiol.*, vol. 594, no. 11, pp. 2895–2903, 2016.

[191] S. Bhatia, R. F. Sekula, M. R. Quigley, R. Williams, and A. Ku, “Role of calcification in the outcomes of treated, unruptured, intracerebral aneurysms,” *Acta Neurochir. (Wien).*, vol. 153, no. 4, pp. 905–911, 2011.

[192] J. R. Cebral, M. A. Castro, S. Appanaboyina, C. M. Putman, D. Millan, and A. F. Frangi, “Efficient pipeline for image-based patient-specific analysis of cerebral aneurysm hemodynamics: Technique and sensitivity,” *IEEE Trans. Med. Imaging*, vol. 24, no. 4, pp. 457–467, 2005.

[193] D. M. Sforza, C. M. Putman, and J. R. Cebral, “Hemodynamics of Cerebral Aneurysms,” *Annu Rev Fluid Mech*, vol. 41, pp. 91–107, 2009.

[194] J. R. Cebral *et al.*, “Regional Mapping of Flow and Wall Characteristics of Intracranial Aneurysms,” *Ann. Biomed. Eng.*, vol. 44, no. 12, pp. 1–15, 2016.

[195] P. Gade, A. Robertson, and C. Chuang, “Multiphoton Imaging of Collagen, Elastin and Calcification in Intact Soft Tissue Samples,” *Curr. Protoc. Cytom.*, 2017.

[196] M. Wintermark *et al.*, “High-resolution CT imaging of carotid artery atherosclerotic plaques.,” *AJNR. Am. J. Neuroradiol.*, vol. 29, no. May, pp. 875–882, 2008.

[197] H. C. Stary *et al.*, “A Definition of Advanced Types of Atherosclerotic Lesions and a Histological Classification of Atherosclerosis Atherosclerotic Lesion Types Advanced by Histology Type IV Lesions,” *Circulation*, vol. 92, no. 5, pp. 1355–1374, 1995.

[198] M. Coen *et al.*, “Smooth muscle cells of human intracranial aneurysms assume phenotypic features similar to those of the atherosclerotic plaque,” *Cardiovasc. Pathol.*, vol. 22, no. 5, pp. 339–344, 2013.

[199] E. Ollikainen *et al.*, “Smooth muscle cell foam cell formation, apolipoproteins, and ABCA1 in intracranial aneurysms: Implications for lipid accumulation as a promoter of aneurysm wall rupture,” *J. Neuropathol. Exp. Neurol.*, vol. 75, no. 7, pp. 689–699, 2016.

[200] J. Frösen *et al.*, “Saccular intracranial aneurysm: Pathology and mechanisms,” *Acta Neuropathol.*, vol. 123, no. 6, pp. 773–786, 2012.

[201] A. Vos *et al.*, “Predominance of nonatherosclerotic internal elastic lamina calcification in the intracranial internal carotid artery,” *Stroke*, vol. 47, no. 1, pp. 221–223, 2016.

[202] C. Y. Ho and C. M. Shanahan, “Medial Arterial Calcification: An Overlooked Player in Peripheral Arterial Disease,” *Arter. Thromb Vasc Biol.*, vol. 36, pp. 1475–1482, 2016.

[203] H. Huang, R. Virmani, H. Younis, A. P. Burke, R. D. Kamm, and R. T. Lee, “The impact of calcification on the biomechanical stability of atherosclerotic plaques,” *Circulation*, vol. 103, no. 8, pp. 1051–1056, 2001.

[204] D. E. Kiousis, S. F. Rubinigg, M. Auer, and G. A. Holzapfel, “A Methodology to Analyze Changes in Lipid Core and Calcification Onto Fibrous Cap Vulnerability : The Human Atherosclerotic Carotid Bifurcation as an Illustratory,” *J. Biomech. Eng.*, vol. 131, no. December 2009, pp. 1–9, 2019.

[205] K. K. Wong, P. Thavornpattanapong, S. C. Cheung, Z. Sun, and J. Tu, “Effect of calcification on the mechanical stability of plaque based on a three-dimensional carotid bifurcation model,” *BMC Cardiovasc. Disord.*, vol. 12, no. 1, p. 7, 2012.

[206] Z. Teng *et al.*, “Coronary Plaque Structural Stress Is Associated With Plaque Composition and Subtype and Higher in Acute Coronary Syndrome The BEACON I (Biomechanical Evaluation of Atheromatous Coronary Arteries) Study,” *Circ Cardiovasc Imaging*, vol. 7, pp. 461–470, 2014.

[207] J. D. Hutcheson *et al.*, “Genesis and growth of extracellular vesicle derived microcalcification in atherosclerotic plaques,” *Nat. Mater.*, vol. 15, no. 3, pp. 335–43, 2016.

[208] S. I. Sugiyama *et al.*, “Relative residence time prolongation in intracranial aneurysms: A possible association with atherosclerosis,” *Neurosurgery*, vol. 73, no. 5, pp. 767–776, 2013.

[209] Y. Tobe, “Pathological Engineering for Predicting Transition of Human Cerebral Aneurysms,” 2016.

[210] P. Lacolley, V. Regnault, P. Segers, and S. Laurent, “Vascular Smooth Muscle Cells and Arterial Stiffening: Relevance in Development, Aging, and Disease,” *Physiol. Rev.*, vol. 97, no. 4, pp. 1555–1617, 2017.

[211] K. E. Steucke, P. V Trace, E. S. Hald, J. L. Hall, and P. A. Alford, “Vascular smooth muscle cell functional contractility depends on extracellular mechanical properties,” *J. Biomech*, vol. 48, no. 12, pp. 612–625, 2016.

[212] F. Cheng *et al.*, “Layer-dependent role of collagen recruitment during loading of the rat bladder wall,” *Biomech. Model. Mechanobiol.*, vol. 17, no. 2, pp. 403–417, 2018.

[213] J. Xie, J. Ferbas, and G. Juan, “Three-Dimensional Second-Harmonic Generation Imaging of Fibrillar Collagen in Biological Tissues,” *Curr. Protoc. Cytom.*, vol. 61, no. 6, pp. 1–11, 2012.

[214] K. Padmanabhan, S. E. Andrews, and J. A. J. Fitzpatrick, “Multi-Photon Imaging,” *Curr. Protoc. Cytom.*, vol. 54, no. 2.9, pp. 1–12, 2010.

[215] K. W. Dunn and P. A. Young, “Principles of Multiphoton Microscopy,” *Exp. Nephrol.*, vol. 103, pp. 33–40, 2006.

[216] K. König, “Multiphoton microscopy in life sciences.,” *J. Microsc.*, vol. 200, no. Pt 2, pp. 83–104, 2000.

[217] S. E. P. New *et al.*, “Macrophage-derived matrix vesicles : An alternative novel mechanism for microcalcification in atherosclerotic plaques,” *Circ. Res.*, vol. 113, no. 1, pp. 72–77, 2013.

[218] M. F. Barbe, R. Adiga, O. Gordiienko, N. Pleshko, M. E. Selzer, and B. Krynska, “Micro-computed tomography assessment of vertebral column defects in retinoic acid-Induced rat model of myelomeningocele,” *Birth Defects Res. Part A - Clin. Mol. Teratol.*, vol. 100, no. 6, pp. 453–462, 2014.

[219] C. Bayan, J. M. Levitt, E. Miller, D. Kaplan, and I. Georgakoudi, “Fully automated, quantitative, noninvasive assessment of collagen fiber content and organization in thick collagen gels,” *J. Appl. Phys.*, vol. 105, pp. 1–11, 2009.

[220] a. J. Schriefl, a. J. Reinisch, S. Sankaran, D. M. Pierce, and G. Holzapfel, “Quantitative assessment of collagen fibre orientations from two-dimensional images of soft biological tissues,” *J. R. Soc. Interface*, vol. 9, no. July, pp. 3081–3093, 2012.

[221] N. Otsu, “A Tlreshold Selection Method from Gray-Level Histograms,” *IEEE Trans. Syst. Man Cybern.*, vol. 20, no. 1, pp. 62–66, 1979.

[222] R. Szeliski, “Image Alignment and Stitching: A Tutorial,” *Found. Trends® Comput. Graph. Vis.*, vol. 2, no. 1, pp. 1–104, 2006.

[223] J. C. Fiala, “Reconstruct: A free editor for serial section microscopy,” *J. Microsc.*, vol. 218, no. 1, pp. 52–61, 2005.

[224] V. Rastogi, N. Puri, S. Arora, G. Kaur, L. Yadav, and R. Sharma, “Artefacts : A Diagnostic Dilemma – A Review,” *J. Clin. Diagnostic Res.*, vol. 7, no. 10, pp. 2408–2413, 2013.

[225] M. Muntifering, D. Castranova, G. A. Gibson, E. Meyer, M. Kofron, and A. M. Watson, “Clearing for Deep Tissue Imaging,” *Curr. Protoc. Cytom.*, pp. 1–21, 2018.

[226] F. Bestvater *et al.*, “Two-photon fluorescence absorption and emission spectra of dyes relevant for cell imaging,” *J. Microsc.*, vol. 208, no. 2, pp. 108–115, 2002.

[227] C. E. J. Cheetham, “Multiphoton Intravital Calcium Imaging,” *Curr. Protoc. Cytom.*, pp. 1–29, 2018.

[228] W. Mittmann *et al.*, “Two-photon calcium imaging of evoked activity from L5 somatosensory neurons in vivo,” *Nat. Neurosci.*, vol. 14, no. 8, pp. 1089–1093, 2011.

[229] C. Stosiek, O. Garaschuk, K. Holthoff, and A. Konnerth, “In vivo two-photon calcium imaging of neuronal networks.,” *Proc. Natl. Acad. Sci. U. S. A.*, vol. 100, no. 12, pp. 7319–24, 2003.

[230] E. G. Lakatta, “So! What’s aging? Is cardiovascular aging a disease?,” *Journalof Mol. cell Cardiol.*, vol. 8150, pp. 1–13, 2016.

[231] A. L. Durham, M. Y. Speer, M. Scatena, C. M. Giachelli, and C. M. Shanahan, “Role of smooth muscle cells in vascular calcification: Implications in atherosclerosis and arterial stiffness,” *Cardiovasc. Res.*, vol. 114, no. 4, pp. 590–600, 2018.

[232] B. D. Metscher, “MicroCT for comparative morphology: simple staining methods allow high-contrast 3D imaging of diverse non-mineralized animal tissues,” *BMC Physiol.*, vol. 9, no. 1, p. 11, 2009.